Hazarika, Birinchi Kumar

AN INVESTIGATION OF THE FLOW CHARACTERISTICS IN THE BLADE ENDWALL CORNER REGION

City University of New York PH.D. 1987

PLEASE NOTE:

In all cases this material has been filmed in the best possible way from the available copy. Problems encountered with this document have been identified here with a check mark __✓__.

1. Glossy photographs or pages __✓__
2. Colored illustrations, paper or print __✓__
3. Photographs with dark background __✓__
4. Illustrations are poor copy _____
5. Pages with black marks, not original copy _____
6. Print shows through as there is text on both sides of page _____
7. Indistinct, broken or small print on several pages __✓__
8. Print exceeds margin requirements _____
9. Tightly bound copy with print lost in spine _____
10. Computer printout pages with indistinct print _____
11. Page(s) _____ lacking when material received, and not available from school or author.
12. Page(s) _____ seem to be missing in numbering only as text follows.
13. Two pages numbered _____. Text follows.
14. Curling and wrinkled pages _____
15. Dissertation contains pages with print at a slant, filmed as received _____
16. Other _____

_____

_____

University
Microfilms
International

AN INVESTIGATION OF THE FLOW CHARACTERISTICS IN THE BLADE ENDWALL CORNER REGION

by

BIRINCHI K. HAZARIKA

A dissertation submitted to the Graduate Faculty in Engineering in partial fulfillment of the requirements for the degree of Doctor of Philosophy, The City University of New York.

1987

This manuscript has been read and accepted for the Graduate Faculty in Engineering in satisfaction of the dissertation requirement for the degree of Doctor of Philosophy.

1/26/87

Date

Chair of Examining Committee

Professor R. Rajl

1/28/87

Date

Executive Officer

Professor P. R. Karmel

Professor Y. Andreopoulos

Dr. D. R. Boldman

Professor L. M. Jiji

Professor J. A. Johnson III

Professor M. Levitsky

Supervisory Committee

The City University of New York

ABSTRACT

AN INVESTIGATION OF THE FLOW CHARACTERISTICS

IN THE

BLADE ENDWALL CORNER REGION

by

Birinchi K. Hazarika

Adviser: Professor Rishi Raj

The investigation, reported in this thesis, was undertaken to determine the structure of flow in the blade end wall corner region. The region for the study was simulated by attaching two uncambered airfoils on either side of a flat plate with semicircular leading edge. The initial portion of the flat plate was artificially roughened and free stream turbulence of the order of 1% was introduced in the flow by inserting a grid upstream of the flat plate.

The techniques used in the investigation included flow visualization, static and total pressure measurements with conventional probes, determination of mean velocity profiles and six components of Reynolds stress tensor with inclined single sensor hot wire probe and measurement of power spectra with a single sensor hot wire probe. The measurements

were carried out at six axial stations along the corner and four stations ahead of the leading edge of the airfoil. A large number of data points were located very close to the surfaces forming the corner at the six axial stations in the corner region.

Three streamwise vortices were identified based on the surface streamlines, distortion of total pressure profiles and variation of mean velocity components in the corner. A horseshoe vortex forms near the leading edge of the airfoil. Within a short distance downstream, a corner vortex was detected between the horseshoe vortex and the surfaces forming the corner. Another vortex forms at the rear portion of the corner between the corner vortex and the surface of the flat plate. In the rear portion, very close to the corner the rate of production of streamwise vorticity due to inhomogeneous and anisotropic turbulence was found to be of the same order of magnitude as the net production due to stretching and skewing of the mean vorticity components. The third vortex, therefore, is the stress induced vortex.

Advection by the horseshoe vortex and the corner vortex was found to create low turbulence intensity regions near the surface of the flat plate in the close vicinity of the corner. In this region, turbulent shear stress and production of turbulence are negligibly small. A region of negative turbulent shear stress was also observed near the

region of low turbulence intensity. The growth of stress induced vortices remove the region of low turbulence intensity regions from the vicinity of the flat plate surface.

The effect of the streamwise vorticity on the turbulence structure was found to be opposite to that of the curvature of the airfoil surface in the present investigation. In the close vicinity of the corner the power spectra in the wave number domain at different axial locations were found to be identical even though the energy associated with different frequencies were not the same.

ACKNOWLEDGEMENTS

The author is indebted to his mentor Professor Rishi Raj for his valuable suggestions and help without which it would have been impossible to carry out this investigation. The author also wishes to express his gratitude to Dr. D. R. Boldman of NASA Lewis Research Center, Cleveland, Ohio, for his suggestions and support during this investigation.

The author is grateful to Professor S. B. Menkes and the Mechanical Engineering Department of The City College of CUNY, for providing the experimental and computational facilities and partial financial support to complete this investigation.

The author takes this opportunity to thank Professor P. Ganatos for his consent to let the author use the subroutine SSLAE. The author is thankful to his friends, G. L., Gopalan, Nandan, Nari and Vijay for their help in typing and correcting this thesis and to his colleagues from the Turbomachinery Laboratory of The City College of New York, Karim, Mahmood and Rakesh for extending their moral support.

Acknowledgement is also due to the National Aeronautics and Space Administration for supporting this work through the Contract NAG 3 - 122.

TABLE OF CONTENTS

LIST OF TABLES

LIST OF FIGURES

NOMENCLATURE

Symbols

A	Constant in the logarithmic law of the wall
$A_{i1} \cdots A_{i6}$	Constants in the expressions for equivalent cooling velocity
B	Constant in the logarithmic law of the wall
$B_{i1} \cdots B_{i6}$	Constants in the expressions for fluctuating part of the equivalent cooling velocity
C	Correction for barometer reading
c	Constant of proportionality for velocity
C_{ij}	Transformation matrix
C_p	Pressure coefficient
C_t	Transducer calibration constant
E	Output of linearizer
$\bar{E}$	Time averaged output of linearizer
E_o	Zero intercept of linearizer output line
E_p, E_n	Linearizer output when the velocity vector is in P and N directions, respectively
e'	Output of RMS meter
$F(\kappa)$	Spectral function in wave number domain
f	Frequency in Hz
g	Acceleration due to gravity
H	Shape factor

h	Normal sensitivity coefficient of hot wire probes
h_{tI}	Barometer reading
k	Tangential sensitivity coefficient of hot wire probes
P	Thermodynamic/Static/Stream pressure
$\bar{P}$	Time averaged stream pressure
P_a	Atmospheric pressure
P_o	Stagnation pressure (time averaged)
$P_{o\infty}$	Stagnation pressure of free stream (time averaged)
P_s	Measured stream pressure (time averaged)
q^2	Turbulence energy $(u'^2+ v'^2+ w'^2)/2$
Re_θ	Reynolds number based on momentum thickness
S, S'	Hot wire calibration constants
$\bar{S}_{ij}$	Mean strain rate
s_{ij}	Strain rate fluctuation
t	Room temperature
T_a	Air stream temperature
T, P, N	Hot wire sensor coordinates
$\bar{U}$	Velocity calculated from stagnation probe output
U^*	Friction velocity
U_e	Equivalent cooling velocity

$\bar{U}_e$	Time averaged equivalent cooling velocity
$\bar{U}_\infty$	Undisturbed free stream mean velocity
U, V, W	Velocity components in XYZ coordinates
U_t, U_p, U_n	Velocity components in TPN coordinates
$\bar{U}_1$, $\bar{V}_1$, $\bar{W}_1$	Mean velocity components in $X_1Y_1Z_1$ coordinates
u_1, v_1, w_1	Fluctuating parts of the velocity components in $X_1Y_1Z_1$ coordinates
u_1', v_1', w_1'	RMS values of the fluctuating components $u_1v_1w_1$
U_2, V_2, W_2	Instantaneous velocity components in $X_2Y_2Z_2$ coordinates
$\bar{U}_2$, $\bar{V}_2$, $\bar{W}_2$	Mean velocity components in $X_2Y_2Z_2$ coordinates
u_2, v_2, w_2	Fluctuating part of the velocity components in $X_2Y_2Z_2$ coordinates
u_2', v_2', w_2'	RMS values of the fluctuating components $u_2v_2w_2$
V_t	Transducer output
X, Y, Z	Frame of reference of the test section and distances
X_1, Y_1, Z_1	Frame of reference of the model

X_2, Y_2, Z_2	Frame of reference of the probe

Greek Symbols

α	Probe angle with vertical plane
β	Probe angle with horizontal plane
δ	Boundary layer thickness
δ_a	Boundary layer thickness on airfoil
δ_f	Boundary layer thickness on flat plate
δ^*	Displacement thickness
ϵ_{ijk}	Alternating tensor
ξ	Angle between the velocity vector and the hot wire sensor in the plane of the prongs
θ	Angle of the plane of the prongs/ Momentum thickness
θ_i	Angular positions of the plane of the prongs
κ	Wave number
ν	Kinematic viscosity
ρ	Density of fluid
ρ_a	Density of air in test section

$_1\tau_{ij}$	Reynolds stress tensor in $X_1Y_1Z_1$ coordinates
$_2\tau_{ij}$	Reynolds stress tensor in $X_2Y_2Z_2$ coordinates
$\Phi(\omega)$	Spectral function in frequency domain
ψ	Hot wire slant angle
$\overline{\Omega}$	Mean vorticity
Ω_x, Ω_y, Ω_z	Vorticity in X, Y and Z directions, respectively
$\overline{\Omega}_x$, $\overline{\Omega}_y$, $\overline{\Omega}_z$	Mean vorticity in X, Y and Z directions, respectively
ω	Frequency in rad./s.
ω_i	Vorticity fluctuations

Subscripts

a	Airstream/ Airfoil
c	Constant value
d	Position where depression appears
e	Equivalent
f	Flat plate
i	Probe angular position
i, j, k, l	Tensorial indices
M	Maximum value/ Position where maximum appears
m	Minimum value/ Position where minimum appears
p	Peak value/ Position where peak appears

t, p, n	Hot wire sensor coordinate directions
o	Stagnation condition
1, 2	Coordinate systems/ Measurement at various times
∞	Undisturbed freestream
θ	Based on momentum thickness

Superscripts

$(\bar{})$	Time averaged values
$(\,)'$	Root mean square of the fluctuating part
$(\,)', (\,)'', (\,)'''$	Velocity components in successive coordinate transforms

CHAPTER I

INTRODUCTION

1.1 Statement of the Problem

Flow in the blade endwall corner region is a class of slender three-dimensional shear flows, frequently encountered in fluid dynamic engineering applications. This type of flow is generated, when a boundary layer developed on one body flows past another body attached to the surface of the first body. Flow in the proximity of the junctions of wing and fuselage, stabilizer and rudder, the hub and the tip regions of turbomachinery rotors and stators and the roots of fins in heat exchangers are few examples of this type of flows.

Flow in the blade endwall corner region is different from the type of corner flow occuring in noncircular ducts. The difference between the above mentioned types of flows is due to the variation in the nature of the secondary flows generated. When a vortex sheet is deflected in its own plane, due to pressure gradient or curvature of the streamlines, streamwise vorticity is generated and the secondary flow generated in this manner is known as "secondary flow of the first kind" or "skew induced secondary flow" or "pressure driven secondary flow". When the secondary flow is the result of streamwise vorticity generated due to the lateral gradient

of Reynolds stress in an anisotropic and inhomogeneous turbulent flow it is known as "secondary flow of the second kind" or "stress induced secondary flow".

In the blade endwall corner region, where the boundary layer developing on the wall encounters the leading edge of the blade, a horseshoe shaped vortex is formed. Two legs of this horseshoe vortex are wrapped around the blade. A separation point known as "saddle point" is formed ahead of the leading edge. Two curved "separation lines" start from this point and go around either side of the blade. Depending on the shape of the blade, acceleration or deceleration of the flow will either intensify or attenuate the secondary flow due to the horseshoe vortex. The effect of Reynolds stress on the horseshoe vortex is to diffuse it. The turbulence in the corner region is highly anisotropic and inhomogeneous and leads to the generation of stress induced secondary flow. As the flow proceeds along the corner, it is natural to expect that the strength of skew induced secondary flow will diminish (if the corner does not have large streamwise curvature) and the stress induced secondary flow will predominate.

In a cascade of airfoils two legs of a horseshoe vortex, generated near the leading edge of the airfoil, pass through adjacent flow passages. The leg of the horseshoe vortex passing along the pressure side is reinforced and the leg along the suction side is weakened by the secondary flow inside the wall boundary layer from the pressure side to the

suction side due to the pressure gradient between the suction and the pressure surfaces in the blade passage (Binder and Romey [2]). The pressure side leg of the horseshoe vortex, thus reinforced, becomes a part of the "passage vortex" and the suction side leg is named as the "counter vortex" (Langston [37]). The passage vortex discharges from the trailing edge of the blade row, whereas the counter vortex which is much weaker may dissipate within the passage because of viscous effect. The passage vortex leads to additional losses by sweeping the wall boundary layer to the vulnerable suction surface and may ultimately cause corner stall. In a turbine rotor the trend in the radial flow is inward towards the hub. Therefore, it is very likely that the horseshoe vortex will be driven towards the hub wall. This phenomenon may influence corner stall in the turbine rotor passage. On the other hand, in a compressor rotor the trend in the radial flow is towards the tip, therefore the vortex may weakly influence the stall near the hub but its influence on the flow near the tip may be strong.

Calculations on the wall bounday layers in a cascade, assuming no further losses and using small deflection theory, lead to outlet flow pattern similar to those experimentally observed but provide much lower level of losses. The effect of removal of the upstream boundary layer also contributes to the reduction of loss. Experiments with inlet shear layers similar to the boundary layers passing through cascades with no actual walls inside the cascades,

also produced very small pressure losses (Dunham [11]). At the same time a substantial portion of the losses in compressors and turbines are due to the secondary flows. Contribution of the mainstream secondary flow loss to the total secondary flow losses is relatively small (Lakshminarayana and Horlock [34]). Therefore, it is logical to assume that the major contribution to the secondary flow losses is due to the interaction between the wall boundary layer with the blade rows in the corner region.

From the above observations, it is apparent that more study of the flow in the blade endwall corner region is required to understand the mechanism of secondary flow losses in the turbomachines. The heat transfer from the roots of the fins and the roots of the turbine blades and the size of the fillets required in these locations can be predicted more accurately if the knowledge of the flow in these regions is advanced. The inception of cavitation depends on the presence of the vortices in the critical regions, thus the study of the flow in the blade endwall corner region is required to provide information for the prediction of inception of cavitation at the inner walls of rotors used in a liquid medium.

Unfortunately, not many investigations were carried out in the past on the blade endwall corner region, although extensive investigations have been reported related to the flow in streamwise corners and in noncircular ducts. Few investigations of the three-dimensional flow near the leading

edge of cylindrical surfaces mounted over flat surfaces are also reported. Most of the studies related to the endwall boundary layer losses in turbomachinery involve too many variables and are of little use for modeling a flow other than the particular flow geometry investigated. The investigations of Kubendran [33], Oguz [51], Shabaka [60],Stanbrook [63] and Vasant Ram [66] are the closest to the type of flow in the blade endwall corner region. The models of the blades in these studies generally consisted of two flat surfaces joined by a cylindrical or elliptical leading edge. Nevertheless these investigations provided useful informations towards understanding this complex fluid flow phenomena.

1.2 Analytical Insight to Secondary Flow in Blade Endwall Corner

The flow field in a steady incompressible flow is represented by the continuity and the Navier-Stokes equations given below in Cartesian tensorial notations:

$$U_{i,i} = 0 \tag{1.1}$$

$$U_i U_{i,j} = - P_{,i}/\rho + \nu U_{i,jj} \tag{1.2}$$

In the streamwise coordinates, the component of velocity along the streamwise direction is known as the primary velocity component. The components in the plane normal to the streamwise direction are known as the secondary

velocity components. The flow in the blade endwall corner region falls in the class of flows known as "slender shear layers". In slender shear layers the secondary velocity components are an order of magnitude smaller than the primary velocity components and if they are the results of streamwise vorticity, it is convenient to replace the Navier-Stokes equations for the transverse components by the streamwise vorticity equation.

The vorticity equation is obtained by taking "curl" of the Navier-Stokes equation. The instantaneous vorticity can be decomposed, using Reynolds decomposition, into mean vorticity ($\bar{\Omega}_i$) and vorticity fluctuation (ω_i). The time averaged equation for Ω_i (Tennekes and Lumley [64]) is written as follows:

$$\bar{U}_j \bar{\Omega}_{i,j} = -\overline{u_j \omega_{i,j}} + \overline{\omega_j s_{ij}} + \bar{\Omega}_j \bar{S}_{ij} + \nu \bar{\Omega}_{i,jj} \quad (1.3)$$

where,

$$\bar{\Omega}_i = \epsilon_{ijk} \bar{U}_{k,j}$$

$$\omega_i = \epsilon_{ijk} u_{k,j}$$

$$\bar{S}_{ij} = (\bar{U}_{i,j} + \bar{U}_{j,i})/2$$

$$s_{ij} = (u_{i,j} + u_{j,i})/2$$

In a slender shear layer, with X direction as the

streamwise direction, the transverse velocity components $\bar{V}$ and $\bar{W}$ are an order of magnitude smaller than the streamwise component $\bar{U}$ ($\bar{V}\sim\bar{W}<\bar{U}$). The gradients of $\bar{U}$ in the Y and Z directions are of the same order of magnitude, but the gradients of the streamwise mean velocity components in the X direction are negligibly small ($\partial\bar{U}/\partial Z\sim\partial\bar{U}/\partial Y>>\partial\bar{U}/\partial X$). If all the six components of Reynolds stress tensor are of the same order of magnitude, the equation (1.3) reduces to the following form (Bradshaw, Cebeci and Whitelaw [4]):

$$\begin{aligned}
&\bar{U}\,\partial\bar{\Omega}_x/\partial X + \bar{V}\,\partial\bar{\Omega}_x/\partial Y + \bar{W}\,\partial\bar{\Omega}_x/\partial Z \\
&= \bar{\Omega}_x\,\partial\bar{U}/\partial X + \bar{\Omega}_y\,\partial\bar{U}/\partial Y + \bar{\Omega}_z\,\partial\bar{U}/\partial Z \\
&\quad + (\partial^2/\partial Y^2 + \partial^2/\partial Z^2)(-\overline{vw}) + (\partial^2/\partial Y\partial Z)(\overline{v^2}-\overline{w^2}) \\
&\quad + \nu\nabla^2\bar{\Omega}_x
\end{aligned} \tag{1.4}$$

The first term on the right hand side of equation (1.4) represents stretching or compression of existing streamwise vortex. The second and the third terms represent skewing of the transverse components of vorticity giving rise to streamwise component. These three terms represent the skew induced secondary flow or Prandtl's secondary flow of the first kind. Next two terms are responsible for the stress induced secondary flow or Prandtl's secondary flow of the second kind and the last term represents the diffusion of existing vorticity due to viscosity (Bradshaw et. al. [4]).

In the boundary layer, far upstream of the airfoil, only one vorticity component $\bar{\Omega}_y$ is present as shown in Fig. 1.1. As soon as the presence of the airfoil leading edge is felt, the vortex tube is skewed and it gives rise to the streamwise component $\bar{\Omega}_x$. This action is represented by the second term on the right hand side of equation (1.4). The third term occurs when the flow encounters the surface of the airfoil. Away from the corner the vortex tubes in the boundary layer on the airfoil will have only $\bar{\Omega}_z$ component. In the corner near the flat plate these vortex tubes will be strongly distorted by the velocity gradients $\partial\bar{U}/\partial Y$ and $\partial\bar{U}/\partial Z$. If the streamwise vorticity, thus produced, encounters an accelerating flow the vorticity intensifies and if it encounters a decelerating flow downstream it will attenuate (vortex stretching phenomena), this action is represented by the first term on the right hand side of the equation.

The fourth and the fifth terms on the right hand side of equation (1.4) collectively represent the total effect of the time averaged transport of the vorticity fluctuations and gain or loss of mean vorticity caused by the fluctuating part of the strain rate interacting with the vorticity fluctuations. To produce stress induced secondary flow it is necessary that the anisotropic turbulence be inhomogeneous. These conditions are satisfied in the streamwise corner. In the corner, as one moves from one wall to the other the sense of the vorticity production terms due to the turbulence

alters, that is, the directions of vorticity are in the opposite directions near the two walls for the stress induced vorticity. This phenomena lead to the formation of a pair of contra-rotating vortices.

In case of slender shear layers the continuity and the Navier-Stokes equations contain nine unknowns. Alternatively, if continuity, X direction momentum and X direction vorticity equations are considered, eight unknowns are involved assuming pressure to be a known function of the streamwise direction X. The pressure can be evaluated from inviscid flow consideration (Gessner and Emery [16]). Therefore, additional relationships among the variables are required for the purpose of analysis.

In order to generate appropriate Reynolds stress model to solve the problem analytically or numerically and to verify the assumptions used in arriving at equation (1.4), it is clear that an accurate measurement of the complete flow field is required. The individual terms in the momentum and the vorticity equations could be evaluated based on these measurements.

1.3 Objectives of the Present Investigation

The experimental investigation was undertaken to study the flow field in the corner region formed by attaching an airfoil with its span normal to a flat plate. The specific

objectives of the investigation were:

(a) To carry out flow visualization to establish different regions of interest and to understand overall mean flow structure present in the corner region.

(b) To survey the blade endwall corner region for the total and the static pressure variations and examine the pressure profiles to detect flow distortions due to the presence of vortices.

(c) To measure the components of mean velocity in the corner region and compare the results with the total and the static pressure surveys.

(d) To measure the Reynolds stress tensor in the blade endwall corner region and study the evolving turbulence characteristics along the corner.

(e) To measure the turbulence spectra in the blade endwall corner region and study the effect of the flow on the structural changes of the eddies.

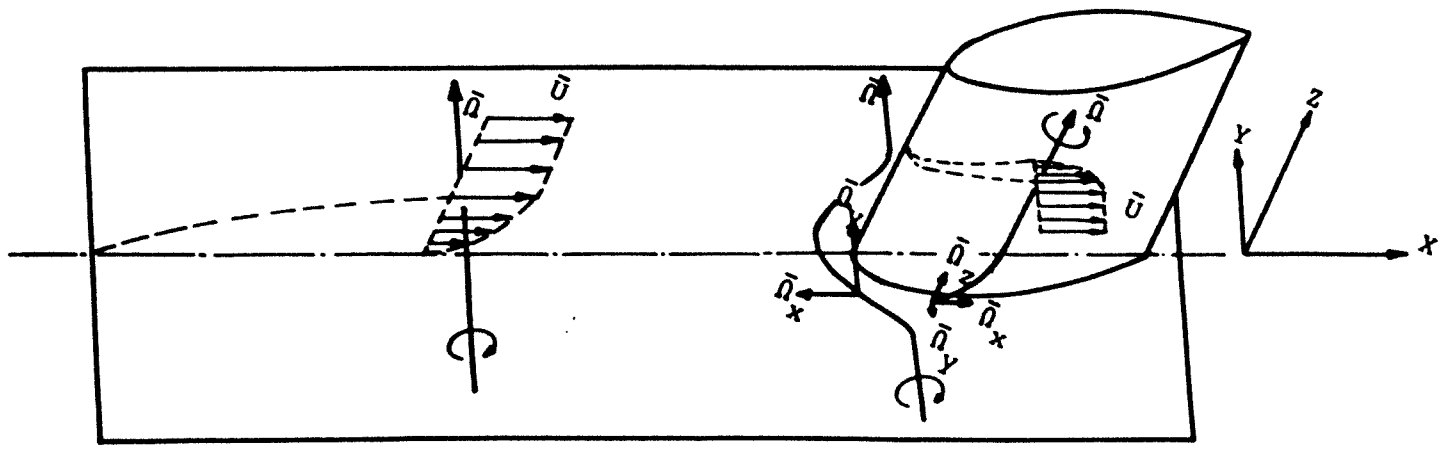

Fig. 1.1 Formation of Skew Induced Streamwise Vorticity

CHAPTER II

LITERATURE SURVEY AND PRESENT STATE OF KNOWLEDGE

The existing literature on corner flows can be divided into two primary groups; laminar and turbulent corner flows. These two groups can be further subdivided into several cases of practical importance to turbomachinery as follows:

(a) Boundary layer starts at the same axial position on the surfaces of both the bodies and,

(i) surfaces of both the bodies are flat

(ii) surface of one body is flat and the surface of the second body is cambered.

(b) Boundary layer developed on the surface of one body is intercepted by the second body and,

(i) surfaces of both the bodies are flat

(ii) surface of the body with the initial boundary layer is flat and the surface of the intercepting body is cambered.

These two subgroups of interest are schematically shown in Fig.2.1 and Fig.2.2.

In case of subgroup (a), when both the shear layers start at the same axial position as in the case of flow

through ducts, the isovels (lines joining equal velocity points) in the initial laminar portion bulge away from the corner as shown in Fig.2.3. However, after the flow becomes turbulent the bulge in the isovels points towards the corner as shown in Fig.2.4. This is due to the anisotropy and inhomogeneity in Reynolds stresses which produces streamwise vorticity in such a manner that a pair of counter rotating vortices across the corner bisector is developed.

In case of subgroup (b), the horseshoe vortex produced near the leading edge will dominate the initial portion of the flow. Further downstream the action of Reynolds stresses and deceleration will diffuse the horseshoe vortex and stress induced secondary flow will start developing. The shape of the leading edge has strong influence on the horseshoe vortex and its development along the corner is dependent on the streamwise curvature of the corner.

2.1 Boundary Layers Start at the Same Axial Position on the Surface of Both the Bodies

2.1.1 Laminar Corner Flows

An extensive literature review of corner flows was carried out by Shabaka [60]. Early theoretical works on corner flow were based essentially on Blasius solution modified for the effect of the perpendicular wall. These

solutions were in error because the effect of streamwise vorticity was either not considered or only minor modifications were made.

Rubin [57] divided the corner into four distinct regions and asymptotic boundary conditions couple the equations governing different regions. A second order perturbation term was retained to account for cross flow. The cross flow, in this case was due to mutual interaction of the two boundary layers. These equations were solved numerically by Pal and Rubin [52] and Rubin and Grossman [58]. Two possible cross flow patterns were predicted; (i) the secondary flow is towards the corner along the walls and away from the corner along the corner bisector and (ii) the secondary flow towards the corner along the corner bisector and away from the corner along the walls.

Zamir [73] formulated the governing equations for corner flow using curvilinear coordinate system coinciding with the flow geometry, that is, along the corner, tangential to the isovels and normal to the isovels. The difficulty involved in numerical solution for this case is that the chosen coordinate system should be a close guess to the flow geometry. By proper choice of similarity variable, these equations were reduced to a single ordinary differential equation for the case of a straight corner. Zamir [71,72] solved this equation numerically in the plane of symmetry for

flow with favorable pressure gradient in a 90° corner. He reported that the streamwise velocity profile on the plane of symmetry is always of separation type with the velocity gradient zero at the corner. With favorable pressure gradient (negative gradient) the secondary flow on the plane of symmetry points away from the corner, but as the pressure gradient approaches zero the secondary flow on the plane of symmetry points towards the corner.

Ghia and Davies [19] assumed that for corner flow, the displacement of the incompressible potential flow is due to the displacement effect of the boundary layer on the flat plates forming the corner. Prandtl-Glauert similarity rule for compressible subsonic and linearized aerofoil theory for supersonic flow were used. The authors pointed out that the cross flow velocity persists even at the infinity because Cartesian coordinate system is not appropriate coordinate system for this type of flow. Ghia [18] tried to correct the deficiency by adopting a suitable formulation such that the asymptotic solution is true at infinity. Numerical solution of the governing equations agreed well with the solution given by Rubin and Grossman [58] except very close to the corner where Ghia [18] found that the secondary flow is directed towards the corner in the plane of symmetry.

Obtaining a thick laminar corner flow, where meaningful measurements can be made with conventional probes,

is difficult. Due to this reason very few experimental investigations are reported for the laminar case. Detailed measurements in laminar corner flow are reported by Zamir and Young [74]. Investigations were carried out in a corner formed by two plates at right angle. The leading edges of the plates were streamline shaped. Wall static pressures were obtained from two rows of holes on the plates running along the corner and velocity profiles were measured with hot wire anemometry. These measurements combined with flow visualization showed that in case of laminar corner flow, secondary flow is towards the corner along the surfaces and away from the corner along the corner bisector. This flow situation gives rise to an isovel pattern bulging away from the corner. The bulge in isovels progressively increase with distance away from the leading edge till the transition takes place. Expected zero skin friction at the corner was not observed due to the practical difficulty in measuring the velocity very near the surface. The boundary layer thickness measured along the corner bisector was of the order of two dimensional boundary layer thickness as predicted by Ghia [18].

Barclay's [1] investigation at a 135° corner with sharp leading edge showed distortions similar to those reported by Zamir and Young [74] but of less severity. However, he found that these distortions were damped at sections away from the leading edge. This difference is

supposedly due to the difference in the leading edge shape in the two cases. Carrier's [7] solution seems to have provided good agreement with the flow in 135° corner although the velocity profile away from the corner suggests existence of slightly favorable pressure gradients.

Zamir and Young [75] found that the shape of the leading edge critically effects the stability of laminar corner flow. Small variations in flow directions, inherently present in the wind tunnels, lead to formation of separation bubbles at the sharp leading edges. If formed, this separation bubble will increase tendency to instability. Favorable pressure gradients help to reduce tendency to instability. It was pointed out that under these circumstances it is unrealistic to expect that the results experimentally obtained using sharp leading edge can be compared with the predictions from theoretical investigations of laminar flow.

2.1.2 Turbulent Corner Flows

The early theoretical work on turbulent corner flow was carried out based on momentum integral solution, assuming nth power law profile for streamwise velocity. Zamir and Young [74], based on the evidence of distortion of primary velocity field and surface flow visualization, reported that after transition from laminar to turbulent flow the rotation

vector of the secondary flow changes its direction. Along the bisector the flow is towards the corner, and along the wall the flow is away from the corner. Since the flow near the corner should be similar to the flow at the corner of ducts, the distortion of isovels could be explained by the findings of Brundrett and Baines [6] in case of non-circular ducts. In the corner, they found strong evidence of a pair of vortices rotating in the opposite directions on either side of the corner bisector. Eichelbrenner and Preston [14] reported the measurements of static pressure taken in a turbulent corner flow. They argued that in the entrance region of a square duct, along each wall, there will be more than two vortices but ultimately when the flow becomes fully developed the progressive collapse of the weak vortices near the center line of the walls, will leave only eight vortices in the whole flow region. The appearance of the vortices is the result of the production of streamwise vorticity caused by the anisotropic and inhomogeneous distribution of Reynolds stresses.

Bragg [5] used similarity analysis and obtained a series of correlations which described the flow for the narrow range of Reynolds numbers for which experimental data were available. Momentum integral methods were difficult to employ because of the form of the terms which must be measured. He surveyed the streamwise mean and turbulent velocities using pitot and single sensor hotwire probes. The wall shear stresses were evaluated from Preston tube measurements in a

90° corner. Although the existence of the secondary flows was clearly indicated by the distortion of isovels, the secondary flows were not investigated by Bragg due to the complications involved. The correlations derived are valid only for limited Reynolds numbers. More data is needed to justify the use of the correlations developed by Bragg at various other Reynolds numbers.

Perkins [55] examined the terms in the streamwise vorticity equation in the flow along a right angle corner. Perkins showed that the method used by Brundrett and Baines [6] gives excessive errors. He, therefore, employed cross hot wires for the measurements. The Reynolds stress components were found to behave in the same manner as those in the corner of a square duct with fully developed turbulent flow. But the magnitudes of these stresses were slightly lower than those found in duct flow. The production of streamwise vorticity due to the gradient of secondary shear stress ($-\rho\overline{vw}$) and anisotropy in transverse normal stress ($\rho\overline{v^2} - \rho\overline{w^2}$) were found to be the same order of magnitude in both cases. However, he did not succeed in separately computing these values with any degree of confidence.

Launder and Ying [41] investigated fully developed turbulent flow in square ducts of varied levels of roughnesses. From these experiments it emerged that the proper normalizing velocity for stress induced secondary flow

is the average friction velocity. Therefore, it is logical to expect that for slowly developing corner flow proper normalizing velocity for secondary flow velocity should also be some kind of friction velocity.

Gessner and Emery [15] proposed a model for Reynolds stresses for turbulent corner flow consistent with Hanjalic and Launder's [25] formulation. Two constants and a length scale needed to be properly selected for using this model in any particular flow situation. These constants and the length scale at a point in the flow related Reynolds stresses to the mean velocity gradients at that point. Gessner and Po [17] used this model to predict the Reynolds stress tensor at the corner of fully developed duct flow. However, a damping factor is required to represent the stresses in the vicinity of the walls and the damping factor model for developing flows could not be derived from this investigation.

Shafir and Rubin [61] carried out theoretical analysis using a two dimensional stream function. They showed that there exists an adverse pressure gradient in transverse direction, which reduces after transition from laminar to turbulent flow and leading to the change in the direction of secondary flow. This analysis also suffers from the lack of closure model for Reynolds stress in the corner flow.

Gessner and Emery [16] proposed a length scale model

for developing flow in a rectangular duct. A damping factor is needed to be known for the near wall calculations. In addition to this, the model can not predict the difference in normal Reynolds stresses in transverse direction with accuracy near the corner. The authors pointed out that it is due to the fact that nearwall pressure strain effect is not introduced in the formulation and a nearwall pressure strain model will be too complicated to introduce in this case.

Gurevich [22] conducted an order of magnitude analysis of flow near a corner formed by a flat plate and concave cylindrical surface. He derived the equation for flow in the corner region in cylindrical coordinate system. One imporant feature of these equations is that they do not contain derivative with respect to the streamwise direction. The equations are valid for a curved surface with large radius of curvature and the influence of streamwise variation of flow field is negligible on secondary flow.

Mikhail and Ghia [44] analyzed compressible turbulent corner flow. They showed a marked influence of mass transfer on laminar corner flow. However, they found the influence to be weak on turbulent corner flow. For asymptotic corner region, anisotropy in turbulent modeling did not show appreciable difference. Calculation by Nakayama et al. [50] reinforced the findings that Launder and Ying's model is adequate for prediction of mean flow field but can not predict

the turbulence quantities and friction coefficients even for fully developed turbulent duct flows.

2.2 Boundary Layer Developed on the Surface of One Body is Intercepted by the Second Body

This class of corner flow is dominated by skew induced secondary flow. Due to the complexity of the problem, very little theoretical investigation has been carried out on this type of flow. The studies on this type of flow are further subdivided into two groups:

(i) A cascade of bodies (blades, vanes) intercepting the incoming boundary layer as occurs in turbomachines,

(ii) Only one body intercepting the incoming boundary layer and the effect due to adjacent bodies (blades, vanes) in the cascade are negligible.

2.2.1 A Cascade of Bodies Intercepting the Incoming Boundary Layer

A comprehensive study of secondary flows in turbomachinery cascade was first carried out by Herzig and Hansen [26]. These studies provided detailed qualitative description of flow in turbomachinery stators. The relative movement of the rotor tip and the endwall was simulated by using a belt moving near the tip of a linear cascade. This

type of simulation could not generate the centrifugal and the Coriolis forces which exist in turbomachinery rotors. However, if the effect of these forces on the vortices are negligible the vortices will have shapes similar to those reported by Herzig and Hansen [26]. The passage vortex inside the cascade bends towards the suction surface due to the pressure gradient in the wall boundary layer. At the same time the passage vortex moves away from the wall into the free stream and ultimately exits from the trailing edge near the suction surface of the adjacent blade in the cascade. During this process the passage vortex ingests low stagnation pressure fluid and results in a high loss core. Accumulation of low energy fluid near the suction surface leads to more pressure loss due to excessive flow disturbance on the already vulnerable suction surface. Another characteristic of the passage vortex is that it resists turning, due to which it may ricochet off the lifting surfaces downstream leading to flow separation in those regions and thereby more loss. Apart from the passage vortex, in the unshrouded rotors, there are scrapping vortex and tip clearance flow. Interaction of all these secondary flows are very complex in nature.

In his review paper Sieverding [62] pointed out that two separation lines may generate ahead of the leading edge from two saddle points and more experimental investigation is required to determine the variation of distance between these two separation lines with flow parameters. The existence of a

corner vortex in the suction side and endwall corner was also pointed out in this paper. The corner vortex may form in the corner between the solid surfaces and passage vortex and may rotate in the opposite sense. It was also mentioned that because of its small size the corner vortex is difficult to visualize but the evidence of the presence of this vortex is felt in the spanwise angle distribution behind highly loaded cascades by a characteristic reduction of the over-turning near the endwall.

Dunham [11] presented a review of methods used to calculate secondary losses in turbomachinery cascades. The methods make use of fluid dynamic and geometric parameters of the machines. Dring [9] used momentum integral method for known profile shapes. His results were found to be comparable with experimental observations on endwall flow visualization results in turbine cascades. The method used by Dring [9] can be used for the prediction of losses in highly favorable pressure gradient endwall flows.

Langston, Nice and Hooper [39] took measurements in a turbine cascade to study the three dimensional nature of the flow field. They reported that a large part of the endwall boundary layer is thin compared to inlet wall boundary layer. The leg of the horseshoe vortex in the pressure side moves away and encounters the suction surface. Most of the loss due to the secondary flow is associated with this leg. The other

leg moves along the suction surface and the loss associated with this leg is small. The inviscid core of the blade passage is also found to be skewed by the passage vortex as it flows downstream. Increase in passage vortex size leads to suction side flow separation and thereby loss of lift. The local film cooling effectiveness on linear gas turbine cascade was reported by Goldstein and Chen [20]. They observed that on the concave surface there is not much change in the effectiveness near the endwall although slight improvement was noticed. The region on the suction surface, which was swept by the passage vortex, as observed from flow visualization study, was not protected by film cooling. Away from this region effectiveness was redistributed by skewing of the cooling jets.

Railly and Sharma [56], in their momentum equation, introduced gradient of apparent stresses to take care of the three dimensional nature of the flow in the blade endwall region. This introduction could not compensate for tip clearance effect. Therefore, their prediction method can be used only for stator rows of turbomachinery. Investigations carried out by Papailiou, Flot and Mathieu [54] show that the three dimensional nature of the endwall flow is not yet well understood and therefore, it is not possible to achieve closure for the momentum integral equation without experimental verification.

Flow visualization and 5-hole probe survey carried out by Marchal and Sieverding [43] supports the phenomenon observed by Herzig and Hansen [26]. Laser light sheet technique used by Marchal and Sieverding [43] for flow visualization was successful in showing clearly the positions of the vortices in the flow passage at different axial locations. It was found that no significant loss is associated with the movement of the wall boundary layer by the passage vortex. However, interaction of the secondary flow with the boundary layer of the blade suction side rsults in a rapid increase in loss. The effect of incoming boundary layer thickness was found to be negligible compared to the interaction between the secondary flow and blade suction side boundary layer and increase in blade loading.

Measurements near the endwall of a turbine cascade were taken by Langston [37]. He analyzed the flow using cross flow boundary layer approach. He found that cross flow near the pressure side of the passage is small whereas cross flow near the suction side of the passage is large. Near the wall, the layer affected by viscous forces were also found to be very thin and cross flow in this layer had the highest value. A relatively simple expression suggested by him was found satisfactory to correlate qualitatively the behavior of the endwall cross flow. Binder and Romey [2] detected mixing loss even beyond three chord length downstream of the trailing edge, indicating presence of vortices even in those sections.

Lakshminarayana and Sitaram [36] presented measurements taken in compressor inlet guide vane (I.G.V.) passage. They found that large cross flow in the passage develops from about 80% of the chord length from the entrance and wall boundary layer becomes thick near the suction side and thin near the pressure side. In this region streamwise velocity profile can be given by logarithemic and power law. However, cross flow profile can not be represented by logarithmic and power laws. A small region near the edge of the boundary layer showed underturning, whereas near the endwall the flow was overturned. Rapid increase in momentum and displacement thickness was observed after the mid chord.

Lasser and Rouleau [40] used laser-Doppler anemometer to measure flow field in a turbine cascade with large flow turning. Secondary flow velocities were found to be as large as 35% of streamwise velocity. The large velocities clearly indicate that commonly used perturbation method can not be used in analyzing such flows. The presence of vorticity and generation of secondary flow in the blade passage strongly influence the wake and the flow field downstream of the trailing edge. Hah [23] presented a numerical scheme which predicted the streamwise velocity porfile as found by Langston et al. [39]. However, he could not predict secondary flow velocity and loss in large part of the flow field. Moore and Ransmayr [45] and Moore and Smith

[46] confirmed that high loss core, in a turbine cascade near the trailing edge, is present not near the endwall but near the midspan. The leading edge shape does not have any detectable effect on the passage vortex.

Investigations of flow near the tip of rotors are reported by Lakshminarayana and Pandya [35], Pandya and Lakshminarayana [53] and Hunter and Cumpsty [31]. These studies indicate that influence of leakage flow is overwhelmingly large in the tip regions compared with the other secondary flow effects. Wagner et al. [68,69] reported the investigations carried out in the downstream of an isolated compressor rotor with a thick boundary layer. Results were similar to those reported by Dring et al. [10] with thin boundary layer, where they did not find any evidence of the horseshoe vortex. At low flow coefficients, the hub corner stall on the suction side of the blade was observed to be the major loss producing mechanism. From the radial and the secondary flow directions and from the distortion of the constant total pressure profiles it appears that there might have been two very weak vortices near the tip. Hunter [30] also reported the accumulation of low energy fluid between the hub surface and the suction surface of turbine blades. In case of the rotor, the high loss core is shifted slightly outwards. However, near the tip of the rotor this high loss accumulation was not observed.

2.2.2 One Body Intercepting the Incoming Boundary Layer

The study of flow at the junction of a flat plate and a cylinder was reported by Vasant Ram [67]. This work was extended by him [66] where two flat surfaces were added on either side of the cylinder to form a wedge with round leading edge simulating a symmetrical airfoil. East and Hoxey [12,13] conducted flow visualization and pressure measurements near the leading edge of a simplified wing body junction and collected data to improve integral calculation method. Hsing and Teng [29], in their experimental investigation, used a model similar to that of East and Hoxey [12,13]. These studies were also confined near the leading edge of the model and provide data for the initial development of the horseshoe vortex. The mean velocity profile reported to follow wall-wake law in the attached flow region, though the constants involved were different. The mixing length was found to vary with pressure gradient and streamline curvature. It was reported that the turbulent stress distributions are similar to those in two dimensional case but the positions and the magnitudes of the peak values are dependent on the streamline curvature and the pressure gradient. The variations were found to be similar in both incompressible and high subsonic cases. Sepri [59], Chu and Young [8] and Young [70] reported investigations carried out in a simplified wing body junction. Flow visualization studies showed that formation of one or more vortices depend on Reynolds number.

Mean values of the three velocity components along with static pressure were measured using a five hole yaw probe near the corner. These measurements were verified using hot wire probe measurements. Stanbrook [63] studied the effect of nose and leading edge shape of the wings in the flow in the wing body junction at subsonic and supersonic free stream velocities. Han et al. [24] studied the effect of horseshoe vortex on the heat transfer from a circular cylinder. The overall heat transfer from the cylinder near the endwall was more due to the horseshoe vortex. However, heat transfer does not increase monotonously with the boundary layer thickness. More understanding of the interaction between the horseshoe vortex and the flow in the separated region is required to explain the circumferential variation of the heat transfer rate in this region.

Shabaka [60] conducted extensive experimental investigations at the corner of an ideal wing body junction formed by a flat plate and a plate with half elliptic leading edge. He measured the distribution of wall static pressure and the shear stresses on both the surfaces. He also measured mean velocity distribution in the corner region. From the measurements and subsequent analysis it was concluded that eddy viscosity and mixing length models are not suitable for the flow in the wing body corners where asymmetrical boundary layers interact. He found that the secondary flow in this case was of skew induced type and there was no evidence of the double vortex pair, characteristic of stress induced secondary

flow. However, it was concluded that the strength of the horseshoe vortex reduces rapidly in the downstream direction due to the diffusive action of the Reynolds stress. The regions of negative shear stress were also found in the corner. The turbulent kinetic energy advection was found to be enhanced by the presence of the secondary flow.

Oguz [51] and Kubendran [33] measured the flow fields in the junctions formed by a flat plate and constant thickness bodies with semi-elliptic leading edges. Oguz [51] found that the effective core of the horseshoe vortex moves closer to the body if the upstream boundary layer thickness is reduced. It was also reported that beyond four undisturbed boundary layer thickness in the transverse direction, the effect of the corner was not felt. Kubendran [33] reported that the strength of the secondary flow vortex increased when the body leading edge was made more blunt. The magnitude and the distribution of the turbulent quantities inside the horseshoe vortex were modified by the vortex. But in the flow region outside the horseshoe vortex the modification was not significant.

Manor [42] studied the effect of yaw and pitch on the stability of a double delta wing aircraft at subsonic speed. Thomson [65] developed analytical method to design wing body configuration such that steep pressure gradients can be avoided. Hornung and Joubert [28] investigated the flow near the upstream side of the region formed by a cylinder on a

flat plate. Murray [49] developed numerical techniques involving successive applications of coordinate transformations involving complex analytic functions to analyse flow in the wing body junction.

Gorski et al. [21] reported the development of a space marching technique to solve the Navier-Stokes equation in the corner. The secondary flow velocities were calculated in the corner of a simplified wing body junction using $k - \epsilon$ model. These results were compared with Shabaka's [60] data and found to be in good agreement. Shabaka's [60] data was established to be an appropriate test case in "The 1980-81 AFOSR-HTTM Stanford Conference on Complex Turbulent Flows". However, an eddy at the corner was observed in this numerical computation and was reported to be due to the secondary flow of the second kind.

From the foregoing review, it is evident that very little basic work is done which will lead to better understanding of the flow in the blade endwall corner region and to the better prediction of the flow in the blade endwall corner region. Whatever work reported in this respect is only of a developmental research nature. Theoretical and experimental work reported was either over-simplified or too complicated to abridge this gap.

One of the most obvious real life situation is the

presence of streamwise curvature. This is present even in the case of non lifting bodies (symmetrical aerofoil, elliptical bodies, struts, etc.) due to the thickness distribution in the flow direction. Streamwise curvature, thus introduced, will give rise to stretching or compressing of the horseshoe vortex depending on the type of curvature resulting in intensification or attenuation of vorticity. The streamwise curvature also leads to streamwise and transverse pressure gradients. It has been observed that the effect of streamwise curvature on turbulence quantities are at least one order of magnitude higher than the rate of strain introduced by the curvature itself . All these factors will contribute to the production of streamwise vorticity and thereby the secondary flow in the corner region. These aspects of streamwise curvatures should be studied for better prediction of the amount of losses directly or indirectly associated with the blade endwall region.

The corner region chosen for the present study was formed by a conventional symmetric airfoil section with its span normal to a flat plate. The flat plate had an initial artificially roughened portion and free stream turbulence was introduced in the flow. The airfoil had circular leading and trailing edges and the thickness distribution in the chordwise direction introduced streamwise curvature. None of the previous studies (References [33], [51] and [60]) had curvature on their blade surface moreover the leading edges of

the blades were elliptic instead of circular as in the subsonic airfoils in common use.

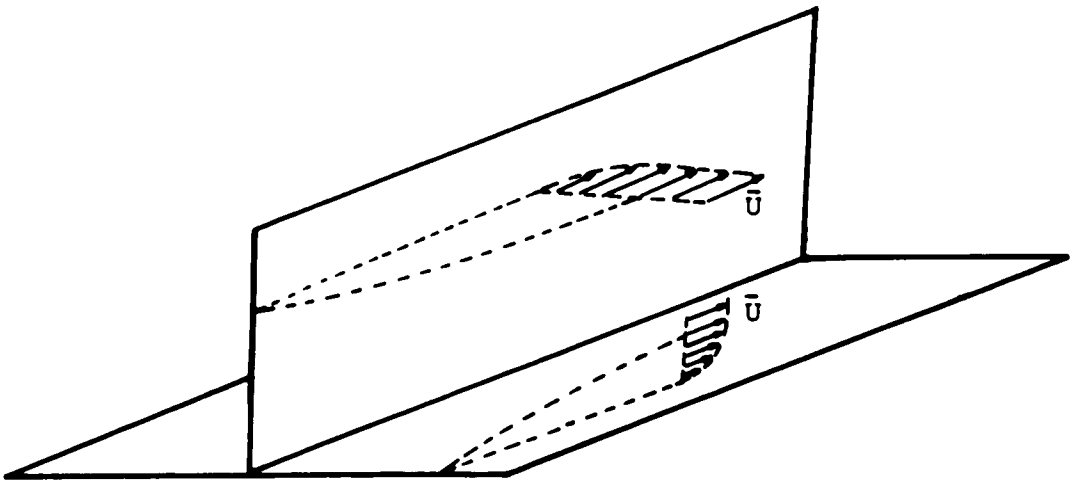

Fig. 2.1 Boundary Layers Start at the Same Axial Location

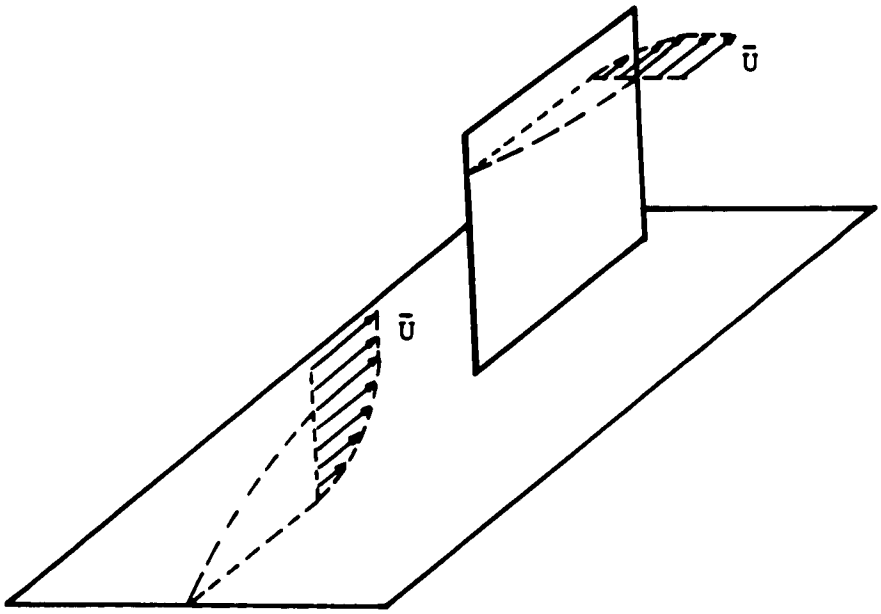

Fig. 2.2 Boundary Layer Developed on one Surface is Intercepted by Another Body

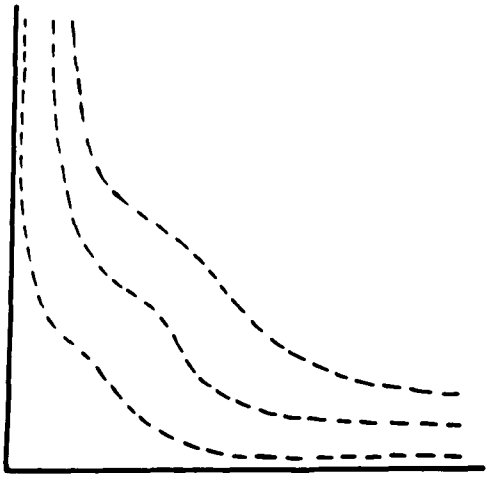

Fig. 2.3 Isovels in Laminar Corner Flow

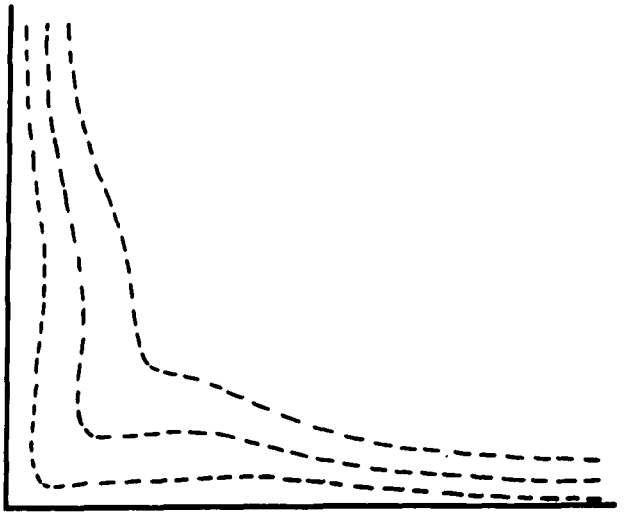

Fig. 2.4 Isovels in Turbulent Corner Flow

CHAPTER III

EXPERIMENTAL EQUIPMENT, INSTRUMENTATION AND METHOD OF MEASUREMENT

The objective of the experimental investigation was to study the development of flow upstream and along the corner formed by an airfoil and a flat plate. The study included the measurements of static pressure, total pressure, turbulence spectra, components of mean velocity and Reynolds stress tensor at suitably located grid points. The details of the experimental arrangements and methods of measurement are described in the following sections.

3.1 Equipment and Instrumentation

3.1.1 Wind Tunnel

A low subsonic open circuit wind tunnel, designed and constructed at the Turbomachinery Laboratory of The City College of the City University of New York, was used for the experiments. A centrifugal blower, fitted with variable inlet guide vanes and driven by a 25 H.P. 1770 rpm A.C. motor, generates the flow in the wind tunnel. Air velocity at 46 cm x 46 cm test section can be varied from about 5 m/s to 35 m/s by adjusting the inlet guide vane setting. Non uniformity of mean velocity profile, in the test section over 36 cm x 36 cm

core was within 0.5% at the maximum flow rate. The turbulence intensity in the test section was found to vary from 0.6% at a velocity of 6 m/s to 0.1% at a velocity of 20 m/s and higher. An inlet filter was used to remove dust from air passing through the tunnel.

3.1.2 Test Model

The flat plate, constructed from two 91 cm long 46 cm x 0.64 cm, 2024T4 bare aluminum plates had four 82.6 cm long 1.3 cm x 0.64 cm aluminum ribs placed lengthwise between the plates and screwed together to produce flat surfaces. The holes were filled with epoxy and sanded down to form smooth surfaces. The leading edge of the plate was made from a 1.9 cm diameter aluminum bar and the trailing edge was made from a 2.5 cm x 1.9 cm bar. There were six static pressure holes on each side of the assembly, three holes in each row lengthwise and two rows on each plate. Twelve polyethylene tubes connected to the wall static holes pass through the space between the plates and emerge from the side near the trailing edge of the flat plate assembly (Fig. 3.1)

Based on a compromise of obtining a thick boundary layer on the airfoil and its stall characteristics NACA 65-015 base profile was chosen for the airfoil. The chord length of the airfoil was 25.4 cm. The leading edge and the trailing edge diameters of the airfoil were 1.27 cm and 0.25 cm,

respectively (Fig. 3.2). The airfoil was made in two sections with 21.9 cm span each and a 0.95 cm hole in the spanwise direction at the position of maximum thickness on the chord line. A threaded rod passing through the holes in the flat plates and airfoils, one on each side of the flat plate, held the entire assembly together. The distance between the leading edge of the flat plate and airfoil was 62 cm. Initial 7 cm from the leading edge of the flat plate was made rough by glueing a strip of sand paper with 0.2 cm grit size and 15 grits/cm^2 to promote early transition to turbulent boundary layer and gain in boundary layer thickness at the measurement points (Fig. 3.3).

The test model assembly was bolted to the test section with the help of two threaded rods. The test section walls parallel to the flat plate were removed 10 cm ahead of the airfoil leading edge to facilitate probe traverse.

3.1.3 Traverse Mechanism and Rotary Device

3.1.3.1 Traverse Mechanism: The traverse mechanism was constructed with two compound slides held perpendicular to each other with the help of an angle plate (Fig.3.4). The assembly was bolted to a table anchored to the floor. A device to rotate the probe about its own axis was bolted to the connecting bar at any required angle to the axis of the bar. The connecting bar was clamped to the compound slide

with its axis perpendicular to the axis of the test section.

The least count of the compound slides were 0.0254 mm. The total traverse distance parallel to the axis of the test section was 33 cm. The traverse was 20 cm perpendicular to the axis in the horizontal and vertical direction. Traverse distances of the probe in all the three directions could be extended by 5 cm by changing the clamping position of the connecting bar on the vertical surface of the compound slide. Subsequent extension in traverse distances were possible by changing the position of the angle plate on the horizontal compound slide.

3.1.3.2 Rotary Devices: Two rotary devices, used to locate the inclined single sensor hot wire at different angular positions, are shown in Figs. 3.5 and 3.6. The first device was used for the preliminary exploratory work. The second one, built on the basis of the experience with the first rotary device, was used for the measurement in the corner region.

The first rotary device (Rotary device 1, Fig. 3.5) was machined from brass stock in two principal components. The base, which was bolted to the connecting bar had a conical hole in which it carried the rotating part in the shape of a frustum of a cone with a hole through its axis and a chuck to hold the guide tube. Three adjustable spring loaded steel

balls were provided to apply sufficient pressure between the base and the rotating part to hold them together snugly, without impeding rotary motion. Two supporting rods, bolted to the base, hold a guide block which had a hole aligned with the axis of the guide tube holder chuck. The protractor mounted on the rotating part and the vernier mounted on the base allowed the change in angle to be measured to the least count of 0.2 degrees. The probe, probe support and guide assembly were held by the guide tube holder chuck and the axis made 45° angle with the connecting bar axis.

The cylindrical, 127 cm long, body of the second rotary device (Rotary device 2, Fig. 3.6) was machined from a 25.4 mm diameter aluminum bar stock. The 38 mm long guide tube holder was also machined from the same bar stock. The guide tube was held in the sliding fit reamed hole of the holder with a nylon screw. The front end of the guide tube emerged from the body through another sliding fit hole. The holder retainers held the assembly together. The friction between the holder and the body could be adjusted with the screws in the retainer ends by forcing two steel balls against the holder base. The circumference of the holder was marked at eight places 45 degrees apart. The body had two indicator marks 180 degrees apart for reference. The body could be bolted to different angle pieces and connecting rod depending on the inclination desired.

3.1.4 Grids

A combination of two grids was used to create free stream turbulence level of 1.5% at 107 cm downstream of the grids (location of the leding edge of the airfoil) to increase the boundary layer thickness on the flat plate and remove the separation bubble on the airfoil which appears in the absence of it. The grids selected for this purpose were 1 mesh 2 mm diameter galvanized iron wire mesh followed by a 4 mesh 0.6 mm diameter galvanized iron wire mesh (Fig. 3.7). The wires of the grids were inclined 45° to each other. The non uniformity in the test section mean velocity introduced by the grids was less than 0.5% at a free stream velocity of 27 m/s.

3.1.5 Probes and Instrumentation

The probes used in these investigations were static and total pressure probes for pressure survey, Kiel probe for reference velocity and inclined single sensor hot wire probe for the components of mean velocity, turbulence intensity and Reynolds stress measurements. Some of the measured values, at locations where the flow was not strongly three dimensional, were verified by normal single sensor hot wire probe (Fig. 3.8).

The static pressure probe, made by United Sensor, was of 1.59 mm diameter, 14d long head type. Total pressure

probe was a square nosed, 0.6 diameter ratio and was made from 0.81 mm stainless tube in the Turbomachinery Laboratory. A miniature sensing head Kiel probe of 1.59 mm diameter head was used to measure the free stream total pressure for reference. All the pressure probes were connected to pre calibrated Validyne pressure transducer and carrier demodulator. The output of the transducer and demodulator was displayed on a DISA 55D31 digital integrating voltmeter through a DISA channel selector. The block diagram of the arrangement of pressure measurements is shown in Fig. A1.

The inclined single sensor hot wire probe had a 0.45 mm long sensor 45° to the probe axis. The prongs were 2.5 mm and 2.18 mm long, mounted on a 0.9 mm diameter 10 mm long front body. The rear body of the probe was 30 mm long and had a diameter of 2 mm. The front and the rear body transition was made over 5 mm length conical portion. The front and the rear body were made by modifying DISA 55A54 and 55D11 probes, respectively. The conical portion was made in a fixture while holding the probes with axes aligned and filled with epoxy. This probe was directly mounted on a DISA 55H21 probe support. The photograph and the sketch of the hot wire probe are shown in Fig. 3.8 and Fig. 3.9, respectively. The probe support was connected to a DISA 55D01 constant temperature anemometer (CTA). Output of the CTA was linearized by a DISA 55D15 linearizer. Output of the linearizer was simultaneously fed to the channel selector and a DISA 55D35 RMS unit. All

outputs were displayed on the digital voltmeter. The block diagram of the setup for turbulence measurements with hot wire is shown in Fig. A3.

The output of the linearizer was also connected to a Panoramic ultrasonic spectrum analyzer of range 10 Hz to 600 kHz to analyze the components of the signal. This spectrum analyzer was a super-hetrodyne receiving device used for visual analysis of the components of the input signals. The output of the tuned receiver was displayed on a cathode ray tube screen. A H.P. model 196 A oscilloscope camera was used to record the output of the spectrum analyzer for future analysis.

3.1.6 Calibration Equipment

All the probes were calibrated in the wind tunnel test section with the model and the grids removed. Thermo Systems Inc. Calibrator Model 1125 was also used to check calibration of the hotwire probes from time to time when it was not possible to remove the model from the test section. This calibration unit was also used to calibrate the pressure transducers against a micromanometer with 0.0254 mm of water pressure resolution. The procedures are described in the Appendix A.

3.1.6.1 Directional Sensitivity Calibration Device: To

determine the directional sensitivities of the inclined single sensor hot wire probe an attachment was designed to be used in the wind tunnel. The device consists of a probe support holder, a swing arm with a clamp and a base as shown in Fig. 3.10. The swing arm was made from a 0.95 cm x 0.95 cm cross section and 29.4 cm long brass bar. The bar was pivoted to the base 1.2 cm from one end and the other end was shaped like a knife edge. The knife edge contains a V-notch for locating the angle. The clamp was at a distance 20.3 cm from the pivot and moved in a 1 cm wide circular arc groove on the base. The swing arm could be clamped at any angular position between 135° to 35° relative to the axis of the test section. The probe support holder, also made from 0.95 cm x 0.95 cm cross section and 22.9 cm long brass bar, was screwed to the swing arm at a point 20.3 cm from the pivot axis and parallel to it. The probe support could be clamped in the holder which was 22 cm above the base. At this position the probe axis is in the horizontal plane. The axis of pivot of swing arm, probe support holder and probe support were on a plane normal to the base. When the plane of the prongs were parallel to the base and thereby parallel to the flow direction, the movement of the swing arm makes the sensor rotate in the plane of the prongs. For calibration of the probe the swing arm support was held in such a position that the pivot axis passed through the midpoint of the sensor, the sensor then rotated around its midpoint.

3.2 Methods of Measurement

All the measurements were conducted at the undisturbed free stream velocity of 27.3 m/s. The maximum variation allowed for the undisturbed free stream velocity was 1.5%. The undisturbed free stream velocity was monitored with the Kiel probe. The sensing head of the Kiel probe was positioned 76 mm above the centre line of the flat plate and 50 mm upstream of the airfoil leading edge. The velocity was calculated on the basis that the undisturbed free stream in the open test section will have stream pressure equal to the atmospheric pressure. The velocity calculated in this manner was also used to normalize the measurements throughout the investigation to eliminate the effect of test section velocity variation on the measured quantities. At the nominal velocity of 27.3 m/s, Reynolds number based on the length of the flat plate upstream of the leading edge of the airfoil was 1×10^6 and Reynolds number based on the airfoil chord length was 4×10^5. In the absence of the airfoil, momentum thickness of the velocity profile at the position of the leading edge was evaluated and the Reynolds number based on this momentum thickness was found to be of the order of 4.5×10^3. Since the velocity profile was artificially thickened and the free stream turbulence was introduced, it was felt necessary to verify that the boundary layer has attained equilibrium ahead of the corner. For this purpose the velocity profile on the flat plate at the axial position of the airfoil leading edge,

in the absence of the airfoil, was surveyed with a pitot tube and two hot wire probes. The survey was carried out at a few transverse locations. The results of the investigations are presented in Chapter IV.

3.2.1 Flow Visualization

Two methods were used for visualization of the flow on the solid surfaces, namely the flat plate and the airfoil surfaces.

3.2.1.1 Surface Oil Film Flow Visualization: A suspension of Lampblack or Titanium Dioxide pigments in #2 Diesel oil with Oleic acid as dispersing agent was generally used in this method. The ratio of the pigment to the oil was determined while doing the experiment. Though the thinnest mixture is considered best from the point of view of flow tracing, but to actually get the flow pattern, somewhat thicker mixture is necessary. This method was useful near the corner to observe the direction of flow in small regions and the overall flow pattern.

A moderately thin mixture of #2 Diesel and Lampblack with a few drops of Oleic acid was in major part of this method. A few times Lampblack was replaced by Titanium Dioxide (TiO_2). A thin layer of the mixture was applied on the flat plate, which was at horizontal position and the

tunnel was started with a preset free stream velocity of 27.3 m/s. The tunnel was allowed to run till all the excess mixture was blown away and a permanent pattern was obtained. Once a well defined pattern was obtained on the surface it was photographed to record all the salient features. The test section was then rotated about its axis through a right angle so that the span of the airfoil was horizontal. A thin layer of mixture was applied on the surface of the airfoil, from the flat plate up to about 100 mm of the span and the tunnel was started with the same setting as the previous run. Tunnel was stopped after permanent pattern was obtained and the airfoil surface was photographed. The salient features of the photographs obtained are discussed in Chapter IV.

3.2.1.2 Surface Streamline Flow Visualization: This method was based on the technique developed by Langston and Boyle [38]. In this technique a matrix of ink dots were made in the region of interest and sprayed with Oil of Wintergreen (Synthetic Methylsalicylate). The air was then allowed to flow over the surface. The ink dissolves in the oil and leaves a fine impression of limiting stream lines. However, the combination of the dye and solvent for the surface used had to be determined for well defined photographs. After conducting experiments with a few different types of dyes, inks, paints, oils and thinners, it was found that good impression on smooth aluminum surface can be obtained from a combination of Polyurethane Oil Enamel Paint and Mineral

Spirit (Paint Thinner). Paints of different colors seem to possess varied adhesive characteristics towards the surface, probably due to the type of dye used. Blue, red and black paints were tested in the experiment conducted.

The inlet guide vanes of the blower in the wind tunnel was adjusted to give undisturbed velocity of 27.3 m/s, with the model in the test section. With the flat plate horizontal, 10.2 mm upstream of the airfoil leading edge 1 mm size dots of blue paint were applied at 3 mm intervals in a row up to 60 mm on either side of the centerline. Paint thinner was sprayed on the surface with an aerosol sprayer to give a continuous film while the paint was wet. Within a few seconds the paint started diffusing into the thinner. The blower was turned on immediately. The excess thinner was swept downstream leaving a thin coat of thinner and faint streaks of paint. The tunnel was turned off after the thinner evaporated leaving streaks of paint. All these streaks were in the region outside the separation line formed by the horseshoe vortex. To show the separation region clearly, dots of red paint were applied in the region inside the separation line. Two rows of blue paint dots were also applied, at 25.4 mm intervals between the rows, on the faint streaks already obtained. Paint thinner was sprayed and the blower switched on as before. This process was repeated till dark streaks were obtained up to the trailing edge of the airfoil.

When the paint was completely dry, the test section was turned 90° about its axis to make the airfoil span horizontal. Dots of red paint were applied near the leading edge along the span of the airfoil. Paint thinner was sprayed and the blower was switched on. The blower was switched off after the paint thinner evaporated and rows of red paint dots, at 25.4 mm chordwise intervals, were applied on the faint streaks obtained. Thinner was sprayed and the process repeated till dark streaks were obtained.

The model was removed from the test section and photographs were taken from different angles. The model was dismantled and all the streaks were traced on tracing papers and photographs of the streaks on the flat plate and the airfoil were separately taken. The discussion of results is presented in Chapter IV.

3.2.2 Upstream Flow Conditions

The velocity profile and the turbulence intensity variation at stations shown in Fig. 3.11 were measured to determine the characteristics of the flow ahead of the leading edge of the airfoil. The locations for these measurements were chosen on the basis of the surface streamlines obtained from the flow visualization studies.

The mean velocity profiles were calculated from the

measurement of total and static pressures. The turbulence intensity was measured by using the inclined single sensor hot wire probe oriented as a normal hot wire and the values were verified by normal hot wire probe. The normal probe was also used for the turbulence spectra measurement ahead of the airfoil. The results are discussed in Chapter IV. The method employed for turbulence spectra measurement is described in Section 3.2.2.3.

3.2.2.1 Static and Total Pressure Measurement: Static and total pressure surveys were carried out in the Z-direction at four stations along the stagnation streamline. Another set of static and total pressure measurements were taken at four locations along the surface streamline passing through a point 101 mm ahead of the leading edge and 11 mm away from the stagnation streamline. At each location, the axis of the sensing head was set parallel to the flat plate and tangential to the surface streamline at that station before the survey was conducted. The output of the transducers connected to the pitot tube and the static pressure probe gave ($P_{O\infty}$- P_a) and (P_s - P_a), respectively. These pressures were expressed as fractions of undisturbed free stream dynamic pressure ($P_{O\infty}$- P_a) measured by the Kiel probe (reference probe). The mean velocity variation is presented in Chapter IV as a fraction of the undisturbed free stream velocity as shown in the following equation.

$$\bar{U}/\bar{U}_{\infty} = [\{(P_o-P_a)-(P_s-P_a)\}/(P_{o\infty}-P_a)]^{1/2} \qquad (3.1)$$

3.2.2.2 Hot Wire Survey: The mean velocity and the turbulence intensity profiles were measured by the normal hot wire and also by inclined single sensor hot wire. The inclined single sensor hot wire probe was used as a normal hot wire probe for this purpose by inserting it at a 45° to the horizontal position and rotating the probe to make the wire parallel to the flat plate and the plane of the prongs normal to the surface streamline direction.

The following equations were used for both the hot wires with appropriate constants E_o and S determined from calibration curves (see Appendix B).

$$\bar{U} = S(\bar{E} - E_o) \qquad (3.2)$$

$$u' = Se' \qquad (3.3)$$

3.2.2.3 Turbulence Spectra: The output from the normal hot wire was fed into the spectrum analyzer and observed during the hot wire survey. Some of the spectra were photographed for quantitative analysis. The spectrum analyzer gives the power spectra in frequency domain (ω). To change it to the wave number (κ) domain, the abscissa and the ordinate scales

need to be changed in the following manner:

$$\kappa = \omega/\bar{U} = 2\pi f/\bar{U} \tag{3.4}$$

and, $$1 = \int_0^\infty \Phi(\omega)\, d\omega/u'^2$$

Therefore,

$$\begin{aligned} 1 &= \int_0^\infty \Phi(\omega)\, d(\bar{U}\kappa)/u'^2 \\ &= \int_0^\infty \bar{U}\, \Phi(\omega)\, d\kappa/u'^2 \\ &= \int_0^\infty F(\kappa)\, d\kappa/u'^2 \end{aligned} \tag{3.5}$$

usually given as

$$\int_0^\infty \{\Phi(\omega)/\bar{U}\}/\{u'^2/\bar{U}^2\}\, d\kappa = 1$$

The scale of the ordinate is chosen to make the area under the trace from spectrum analyzer equal to u'^2, since $\Phi(\omega)$ is a good approximation of $F(\omega)$ for most purposes (Bradshaw [3]), the scale for $\Phi(\omega)$ multiplied by the local mean velocity will give the scale for $F(\kappa)$.

For the measurements upstream of the airfoil leading edge, the frequency range was chosen from 0 to 25 kHz. The attenuation had to be changed when the probe was moved in Z direction because of the change in u'. However, this was not

inconvenient, since for each photograph of the trace on the spectrum analyzer screen the scale was determined separately. The results of these investigations are presented in Chapter IV.

3.2.3 Pressure Measurement in the Corner Region

Static and total pressure measurements in the corner region were carried out at six axial stations (Fig.3.12). The measuring planes were located at X = 25, 76, 127, 152, 203 and 251 mm, downstream of the leading edge of the airfoil, where X was measured along the axis of the test section. At each axial station the probes were traversed in a plane normal to the axis of the test section.

At each axial station the angle plate was rotated about the vertical axis and was bolted down on the horizontal compound slide making the vertical side of the angle plate parallel to the tangential plane of the airfoil at that location. A connecting bar was clamped on the surface of the vertical compound slide. A pressure probe clamp was screwed to the connecting bar. The pressure probe, inserted in the clamp at this position, made 45° angle with the horizontal plane and the axis of the sensing head was tangential to the airfoil surface. The readings of the vertical and the horizontal scale for the position at which the probes make contact with the flat plate surface and with the airfoil

surface were determined by the method of electrical contact. During the traverse the sensing holes of the pressure probes moved in the traverse plane.

The total and the static pressure readings were taken at the grid points shown in Fig. 3.12, while traversing the probes in Y direction at constant Z. The readings were normalized by the total pressure readings taken from the Kiel probe (reference probe) at the same time. The pressure readings taken at each station were plotted for constant Z and variable Y at different values of Z and constant Y and variable Z at different values of Y.

The yaw insensitivity for the type of pitot tube used is about 10 degrees. The estimated secondary flow is not strong enough to create more than 10° of deviation. Therefore, the pressure reading taken from the pitot tube is the total gage pressure. The magnitude of mean velocity at any grid point can be calculated from:

$$|\vec{V}| = \{\bar{U}^2 + \bar{V}^2 + \bar{W}^2\}^{1/2}$$

$$= [2\{(P_o - P_a) - (P_s - P_a)\}/\rho]^{1/2} \qquad (3.6)$$

The results of these investigations are presented and analyzed in Chapter IV.

3.2.4 Three Dimensional Hot Wire Measurements in the

Corner Region

The inclined single sensor hot wire probe was located at the grid points shown in Fig.3.12, to determine the mean velocity components and the Reynolds stress tensor at these points. For a hot wire sensor, the equivalent cooling velocity (U_e) is correlated to the velocity components tangential to the hot wire sensor (U_t), perpendicular to the sensor in the plane of the prongs (U_p) and normal to the plane of the prongs (U_n) as follows:

$$U_e^2 = U_p^2 + k^2U_t^2 + h^2U_n^2 \qquad (3.7)$$

where k and h are tangential and normal sensitivity coefficients, respectively. The method for determination of k and h are illustrated in Appendix B.

For output E_e of the linearizer, the equivalent cooling velocity is given by:

$$U_e = S(E_e - E_o) \qquad (3.8)$$

E_o can be made very small by proper adjustment of the linearizer. By using Reynolds decomposition we get,

$$\bar{U}_e = S(\bar{E}_e - E_o) \tag{3.9}$$

$$u_e' = Se_e' \tag{3.10}$$

Since the equivalent cooling velocity is related only to U_t, U_p and U_n the relationship between T, P and N coordinates and another coordinate system fixed in the coordinate system of the model has to be known. The relationships are developed and shown in Appendix B.

The probe was inserted in the test section in such a manner that the vertical plane passing through the axis of the probe made 15° angle (α) with XZ-plane. On the vertical plane passing through the axis of the probe, the axis of the probe makes 30° angle (β) with the horizontal plane. The angular position θ of the sensor was measured from a plane passing through the axis of the probe and normal to the vertical plane passing through the axis of the probe. This coordinate system passing through the probe axis and the two planes described above are shown in Fig. 3.13, and given by subscript 2 namely X_2, Y_2 and Z_2 system of coordinates. At each grid points eight measurements were taken at the intervals of 45°. Therefore, the angles at which the measurements were taken are:

$$\theta_i = (i-1)\ 45^\circ \quad ; \quad i = 1, 2, ---, 8 \tag{3.11}$$

and the equivalent cooling velocities at the corresponding angular positions (Appendix B) are,

$$U_{ei}^2 = A_{i1}U_2^2 + A_{i2}V_2^2 + A_{i3}W_2^2 + A_{i4}U_2V_2 + A_{i5}U_2W_2 + A_{i6}V_2W_2 \tag{3.12}$$

where,

$$A_{i1} = (1 + k^2)/2$$

$$A_{i2} = \{(1 + k^2)\ \mathrm{Cos}^2\theta_i + 2h^2\ \mathrm{Sin}^2\theta_i\}/2$$

$$A_{i3} = \{(1 + k^2)\ \mathrm{Sin}^2\theta_i + 2h^2\ \mathrm{Cos}^2\theta_i\}/2$$

$$A_{i4} = -(1 - k^2)\ \mathrm{Cos}\theta_i$$

$$A_{i5} = -(1 - k^2)\ \mathrm{Sin}\theta_i$$

$$A_{i6} = (1 + k^2 - 2h^2)\ \mathrm{Sin}\theta_i\ \mathrm{Cos}\theta_i$$

Reynolds decomposition for the instantaneous velocity components and equivalent cooling velocities are as follows:

$$U_2 = \bar{U}_2 + u_2$$

$$V_2 = \bar{V}_2 + v_2$$

$$W_2 = \bar{W}_2 + w_2 \tag{3.13}$$

$$U_{ei} = \bar{U}_{ei} + u_{ei} \quad ; \quad i = 1, 2, ---, 8.$$

Substituting equation (3.13) in equation (3.12), time averaging the resulting equations and neglecting the second and higher order terms of the fluctuating quantities, the following equations were obtained:

$$\begin{aligned}\bar{U}_{ei}^2 + 2\bar{U}_{ei}u_{ei} &= A_{i1}\bar{U}_2^2 + A_{i2}\bar{V}_2^2 + A_{i3}\bar{W}_2^2 + A_{i4}\bar{U}_2\bar{V}_2 + A_{i5}\bar{U}_2\bar{W}_2 \\ &+ A_{i6}\bar{V}_2\bar{W}_2 + 2A_{i1}\bar{U}_2u_2 + 2A_{i2}\bar{V}_2v_2 + 2A_{i3}\bar{W}_2w_2 \\ &+ A_{i4}(\bar{U}_2v_2 + \bar{V}_2u_2) + A_{i5}(\bar{U}_2w_2 + \bar{W}_2u_2) \\ &+ A_{i6}(\bar{V}_2w_2 + \bar{W}_2v_2)\end{aligned} \tag{3.14}$$

$$\begin{aligned}\bar{U}_{ei}^2 &= A_{i1}\bar{U}_2^2 + A_{i2}\bar{V}_2^2 + A_{i3}\bar{W}_2^2 \\ &+ A_{i4}\bar{U}_2\bar{V}_2 + A_{i5}\bar{U}_2\bar{W}_2 + A_{i6}\bar{V}_2\bar{W}_2\end{aligned} \tag{3.15}$$

3.2.4.1 Determination of the Mean Velocity in the Reference Frame of the Probe: The equations (3.15) at the eight different angles of measurement can be written as,

$$\begin{aligned}\bar{U}_{e1}^2 &= (1 + k^2)\bar{U}_2^2/2 + (1 + k^2)\bar{V}_2^2 + h^2\bar{W}_2^2 \\ &- (1 - k^2)\bar{U}_2\bar{V}_2\end{aligned}$$

$$\bar{U}_{e2}^2 = (1 + k^2)\bar{U}_2^2/2 + (1 + k^2 + 2h^2)\bar{V}_2^2/4$$

$$+ (1 + k^2 + 2h^2)\bar{W}_2^2/4 - (1 + k^2)\bar{U}_2\bar{V}_2/\sqrt{2}$$

$$- (1 - k^2)\bar{U}_2\bar{W}_2/\sqrt{2} + (1 + k^2 - 2h^2)\bar{V}_2\bar{W}_2/2$$

$$\bar{U}_{e3}^2 = (1 + k^2)\bar{U}_2^2/2 + h^2\bar{V}_2^2 + (1 - k^2)\bar{W}_2^2/2$$

$$- (1 - k^2)\bar{U}_2\bar{W}_2 \qquad (3.16)$$

$$\bar{U}_{e4}^2 = (1 + k^2)\bar{U}_2^2/2 + (1 + k^2 + 2h^2)\bar{V}_2^2/4$$

$$+ (1 + k^2 + 2h^2)\bar{W}_2^2/4 + (1 - k^2)\bar{U}_2\bar{V}_2/\sqrt{2}$$

$$- (1 - k^2)\bar{U}_2\bar{W}_2/\sqrt{2} - (1 + k^2 - 2h^2)\bar{V}_2\bar{W}_2/2$$

$$\bar{U}_{e5}^2 = (1 + k^2)\bar{U}_2^2/2 + (1 + k^2)\bar{V}_2^2/2 + h^2\bar{W}_2^2$$

$$+ (1 - k^2)\bar{U}_2\bar{V}_2$$

$$\bar{U}_{e6}^2 = (1 + k^2)\bar{U}_2^2/2 + (1 + k^2 + 2h^2)\bar{V}_2^2/4$$

$$+ (1 + k^2 + 2h^2)\bar{W}_2^2/4 + (1 - k^2)\bar{U}_2\bar{V}_2/\sqrt{2}$$

$$+ (1 - k^2)\bar{U}_2\bar{W}_2/\sqrt{2} + (1 + k^2 - 2h^2)\bar{V}_2\bar{W}_2/2$$

$$\bar{U}_{e7}^2 = (1 + k^2)\bar{U}_2^2/2 + h^2\bar{V}_2^2 + (1 + k^2)\bar{W}_2^2/2$$

$$+ (1 - k^2)\bar{U}_2\bar{W}_2$$

$$\bar{U}_{e8}^2 = (1 + k^2)\bar{U}_2^2/2 + (1 + k^2 + 2h^2)\bar{V}_2^2/4$$

$$+ (1 + k^2 + 2h^2)\bar{W}_2^2/4 - (1 - k^2)\bar{U}_2\bar{V}_2/\sqrt{2}$$

$$+ (1 - k^2)\bar{U}_2\bar{W}_2/\sqrt{2} - (1 + k^2 - 2h^2)\bar{V}_2\bar{W}_2/2$$

The foregoing equations can be solved for $\bar{U}_2$, $\bar{V}_2$ and $\bar{W}_2$ in a number of different ways. Four simplest solutions

are,

$$\bar{U}_2 = [\{(1 + k^2 - 2h^2)(\bar{U}_{e3}^2 - \bar{U}_{e7}^2)(\bar{U}_{e1}^2 - \bar{U}_{e5}^2)\}/$$
$$\{2(1 - k^2)^2(\bar{U}_{e2}^2 + \bar{U}_{e6}^2 - \bar{U}_{e4}^2 - \bar{U}_{e8}^2)\}]^{1/2}$$
$$\bar{V}_2 = -(\bar{U}_{e1}^2 - \bar{U}_{e5}^2)/\{2(1 - k^2)\bar{U}_2\}$$
$$\bar{W}_2 = -(\bar{U}_{e3}^2 - \bar{U}_{e7}^2)/\{2(1 - k^2)\bar{U}_2\} \qquad (3.17)$$

$$\bar{U}_2 = [\{(1 + k^2 - 2h^2)(\bar{U}_{e2}^2 + \bar{U}_{e4}^2 - \bar{U}_{e6}^2 - \bar{U}_{e8}^2)$$
$$(\bar{U}_{e1}^2 - \bar{U}_{e3}^2)\}/\{2\sqrt{2}\ (1 - k^2)^2(\bar{U}_{e2}^2 + \bar{U}_{e6}^2$$
$$- \bar{U}_{e4}^2 - \bar{U}_{e8}^2)\}]^{1/2}$$
$$\bar{V}_2 = (\bar{U}_{e1}^2 - \bar{U}_{e5}^2)/\{2(1 - k^2)\bar{U}_2\}$$
$$\bar{W}_2 = -(\bar{U}_{e2}^2 + \bar{U}_{e4}^2 - \bar{U}_{e6}^2 - \bar{U}_{e8}^2)$$
$$/\{2\sqrt{2}(1 - k^2)\bar{U}_2\} \qquad (3.18)$$

$$\bar{U}_2 = [-\{(1 + k^2 - 2h^2)(\bar{U}_{e4}^2 + \bar{U}_{e6}^2 - \bar{U}_{e2}^2 - \bar{U}_{e8}^2)$$
$$(\bar{U}_{e3}^2 - \bar{U}_{e7}^2)\}/\{2\sqrt{2}(1 - k^2)^2(\bar{U}_{e2}^2 + \bar{U}_{e6}^2$$
$$- \bar{U}_{e4}^2 - \bar{U}_{e8}^2)\}]^{1/2}$$
$$\bar{V}_2 = (\bar{U}_{e2}^2 + \bar{U}_{e4}^2 - \bar{U}_{e6}^2 - \bar{U}_{e8}^2)$$
$$/\{2\sqrt{2}(1 - k^2)\bar{U}_2\}$$
$$\bar{W}_2 = -(\bar{U}_{e3}^2 - \bar{U}_{e7}^2)/\{2(1 - k^2)\bar{U}_2\} \qquad (3.19)$$

$$\bar{U}_2 = [-\{(1 - k^2 - 2h^2)(\bar{U}_{e4}^2 + \bar{U}_{e6}^2 - \bar{U}_{e2}^2 - \bar{U}_{e8}^2)$$

$$(\bar{U}_{e2}^2 + \bar{U}_{e4}^2 - \bar{U}_{e6}^2 - \bar{U}_{e8}^2)\}/\{4(1 - k^2)^2$$

$$(\bar{U}_{e2}^2 + \bar{U}_{e6}^2 - \bar{U}_{e4}^2 - \bar{U}_{e8}^2)\}]^{1/2}$$

$$\bar{V}_2 = (\bar{U}_{e4}^2 + \bar{U}_{e6}^2 - \bar{U}_{e2}^2 - \bar{U}_{e8}^2)/\{2\sqrt{2}$$

$$(1 - k^2)\bar{U}_2\}$$

$$\bar{W}_2 = -(\bar{U}_{e2}^2 + \bar{U}_{e4}^2 - \bar{U}_{e6}^2 - \bar{U}_{e8}^2)/\{2\sqrt{2}$$

$$(1 - k^2)\bar{U}_2\} \qquad (3.20)$$

The four sets of values thus obtained were found to be most accurate and they were within 2% of each other. Average of the four values at each grid point was taken as the values of $\bar{U}_2$, $\bar{V}_2$ and $\bar{W}_2$. The results of the mean velocity variations are presented and analyzed in Chapter IV.

3.2.4.2 Reynolds Stress Tensor in the Reference Frame of the Probe: Subtracting equation (3.15) from (3.14), we get,

$$2\bar{U}_{ei}u_{ei} = (2A_{i1}\bar{U}_2 + A_{i4}\bar{V}_2 + A_{i5}\bar{W}_2)u_2 + (2A_{i2}\bar{V}_2 + A_{i6}\bar{W}_2 + A_{i4}\bar{U}_2)v_2 + (2A_{i3}\bar{W}_2 + A_{i5}\bar{U}_2 + A_{i6}\bar{V}_2)w_2 \qquad (3.21)$$

Squaring equation (3.21) and taking time average, the equation can be written as,

$$4\bar{U}_{ei}^2\, u'^2_{ei} = B_{i1}u_2^2 + B_{i2}v_2^2 + B_{i3}w_2^2 + B_{i4}u_2v_2 + B_{i5}u_2w_2 + B_{i6}v_2w_2 \qquad (3.22)$$

where,

$$B_{i1} = (2A_{i1}\bar{U}_2 + A_{i4}\bar{V}_2 + A_{i5}\bar{W}_2)^2$$

$$B_{i2} = (2A_{i2}\bar{V}_2 + A_{i6}\bar{W}_2 + A_{i4}\bar{U}_2)^2$$

$$B_{i3} = (2A_{i3}\bar{W}_2 + A_{i5}\bar{U}_2 + A_{i6}\bar{V}_2)^2$$

$$B_{i4} = 2(2A_{i1}\bar{U}_2 + A_{i4}\bar{V}_2 + A_{i5}\bar{W}_2)(2A_{i2}\bar{V}_2 + A_{i6}\bar{W}_2 + A_{i4}\bar{U}_2)$$

$$B_{i5} = 2(2A_{i1}\bar{U}_2 + A_{i4}\bar{V}_2 + A_{i5}\bar{W}_2)(2A_{i3}\bar{W}_2 + A_{i5}\bar{U}_2 + A_{i6}\bar{V}_2)$$

$$B_{i6} = 2(2A_{i2}\bar{V}_2 + A_{i6}\bar{W}_2 + A_{i4}\bar{U}_2)(2A_{i3}\bar{W}_2 + A_{i5}\bar{U}_2 + A_{i6}\bar{V}_2)$$

Equation (3.22) gives eight equations corresponding to eight angular positions of the probe at each grid point. At each grid point ${}^8C_6$(=28) sets of six simultaneous equations were formed and solved by using Gauss-Jordan elimination method. Average values of mean velocity components described in 3.2.4.1 and values of coefficients A_{ij} calculated in 3.2.4.1 were used in equation (3.22).

3.2.4.3 Transformation to the Frame of Reference of the

Model: For the same setting of the probe axis the value of the angle α was different for different axial stations as shown in Fig. 3.13, however, the angle β was same throughout. The velocity components in the model frame of reference were obtained by using the equations; (see Appendix B)

$$\begin{aligned} U_1 &= (\cos\alpha \cos\beta)U_2 + (-\sin\alpha)V_2 \\ &\quad + (-\cos\alpha \sin\beta)W_2 \\ V_1 &= (\sin\alpha \cos\beta)U_2 + (\cos\alpha)V_2 \\ &\quad + (-\sin\alpha \sin\beta)W_2 \\ W_1 &= (\sin\beta)U_2 + (\cos\beta)W_2 \end{aligned} \tag{3.23}$$

If the Reynolds stress tensor in the reference frame of the probe is given by,

$$2\tau_{ij} = -\rho \begin{bmatrix} \overline{u_2}^2 & \overline{u_2 v_2} & \overline{u_2 w_2} \\ \overline{u_2 v_2} & \overline{v_2}^2 & \overline{v_2 w_2} \\ \overline{u_2 w_2} & \overline{v_2 w_2} & \overline{w_2}^2 \end{bmatrix}, \tag{3.24}$$

the Reynolds stress tensor in the frame of reference of the model is given by,

$$ {}_1\tau_{ij} = -\rho \begin{bmatrix} \overline{u_1^2} & \overline{u_1 v_1} & \overline{u_1 w_1} \\ \overline{u_1 v_1} & \overline{v_1^2} & \overline{v_1 w_1} \\ \overline{u_1 w_1} & \overline{v_1 w_1} & \overline{w_1^2} \end{bmatrix}, \qquad (3.25) $$

and the transformation matrix is given by,

$$ C_{ij} = \begin{bmatrix} (\cos\alpha \cos\beta) & (-\sin\alpha) & (-\cos\alpha \sin\beta) \\ (\sin\alpha \cos\beta) & (\cos\alpha) & (-\sin\alpha \sin\beta) \\ (\sin\beta) & (\ 0\ ) & (\cos\beta) \end{bmatrix} \qquad (3.26) $$

then the elements of the Reynolds stress tensor in the frame of reference of the model can be calculated from,

$$ {}_1\tau_{ij} = C_{ik}\ {}_2\tau_{kl}\ C_{jl} \qquad (3.27) $$

During the measurements, care was taken to see that the velocity components U_2 was always in the positive direction, since that was the only assumption made in solving the equations for mean velocity components.

Out of 28 sets of Reynolds stress tensor obtained, all the sets containing positive values of any of the normal stress terms $(-\rho\overline{u_1^2})$, $(-\rho\overline{v_1^2})$ or $(-\rho\overline{w_1^2})$ were discarded,

because such a case would not be feasible. If the sum of the absolute values of the normal and Reynolds stresses divided by ρ exceed 150 m^2/s^2 in any set of calculation it was ignored because it will amount to more than 20% turbulence intensity for each component of turbulence and correlation coefficients of 0.5 in the present experiment and there was no evidence (from single sensor hot wire measurements) that such large values appear in the corner. The average values of the remaining sets were accepted as the measured Reynolds stress tensor. The results of these investigations are presented and analysed in Chapter V.

3.2.4.4 Turbulence Spectra in the Corner Region: The turbulence spectra at all the six stations shown in Fig. 3.12 were taken at the grid points shown in Fig. 3.14. The inclined hot wire probe was inserted into the wind tunnel with its axis normal to the wind tunnel axis and 45° to the flat plate surface. At each grid points the spectra was checked for two orientations of the sensor, one position was parallel to the Z direction and the other position was parallel to the Y direction. For these measurements the sweep width was kept at 30 kHz. The photographs of the traces were analyzed as described in section 3.2.2.3. To analyze the spectrum for the contribution of different size eddies, in this case, the data were also plotted on a semi-log graph paper for $\omega\Phi(\omega)/u_1'^2$ against ω. The area under the curve between any two values of

ω will represent the fraction of energy contributed towards that turbulence energy by the eddies in that range;

$$\int_o^\infty \omega\Phi(\omega)\ d(\log\omega)/u_1'^2 = \int_o^\infty \Phi(\omega)\ d\omega/u_1'^2 = 1 \quad (3.28)$$

The results are presented and discussed in Chapter V.

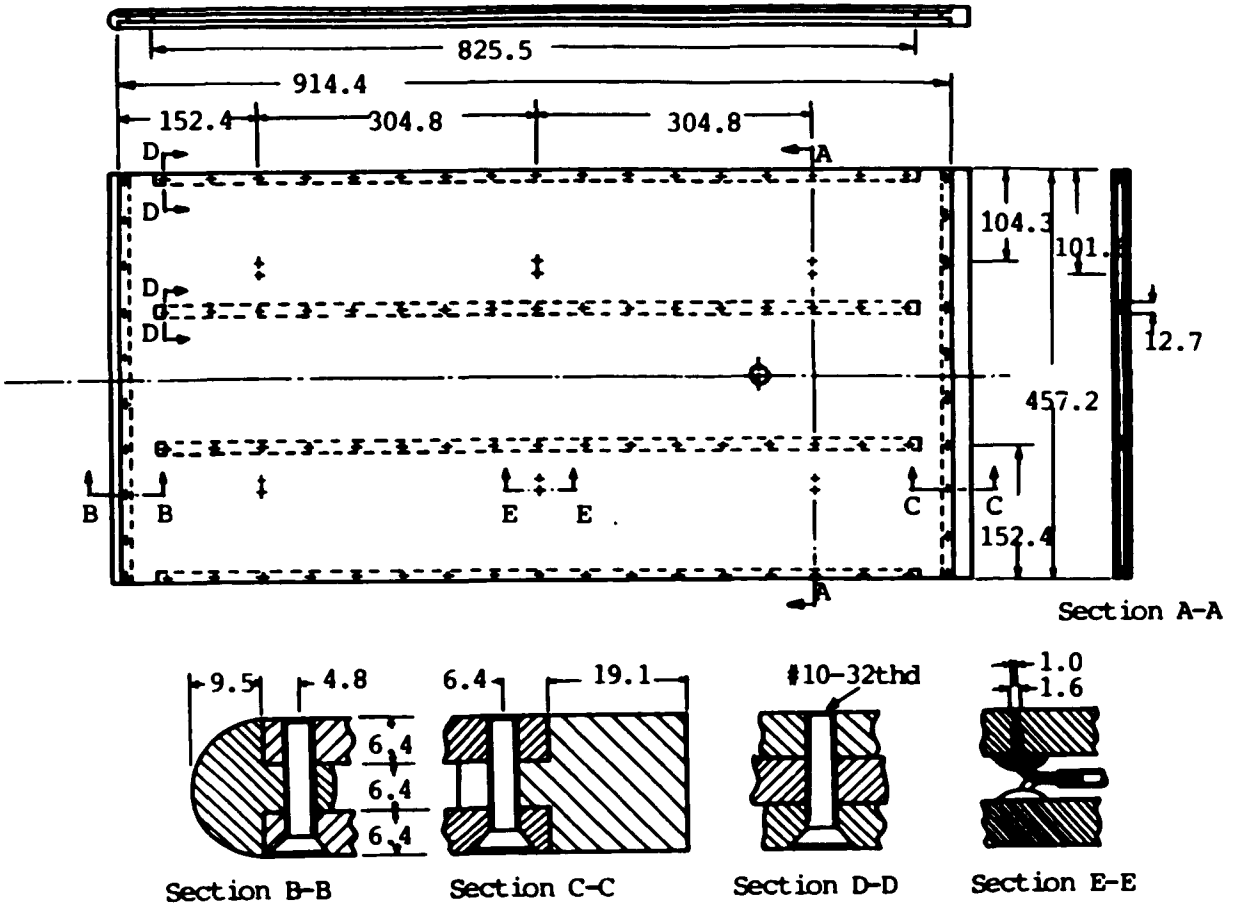

All dimensions are in mm.

Fig. 3.1 Flat Plate Assembly

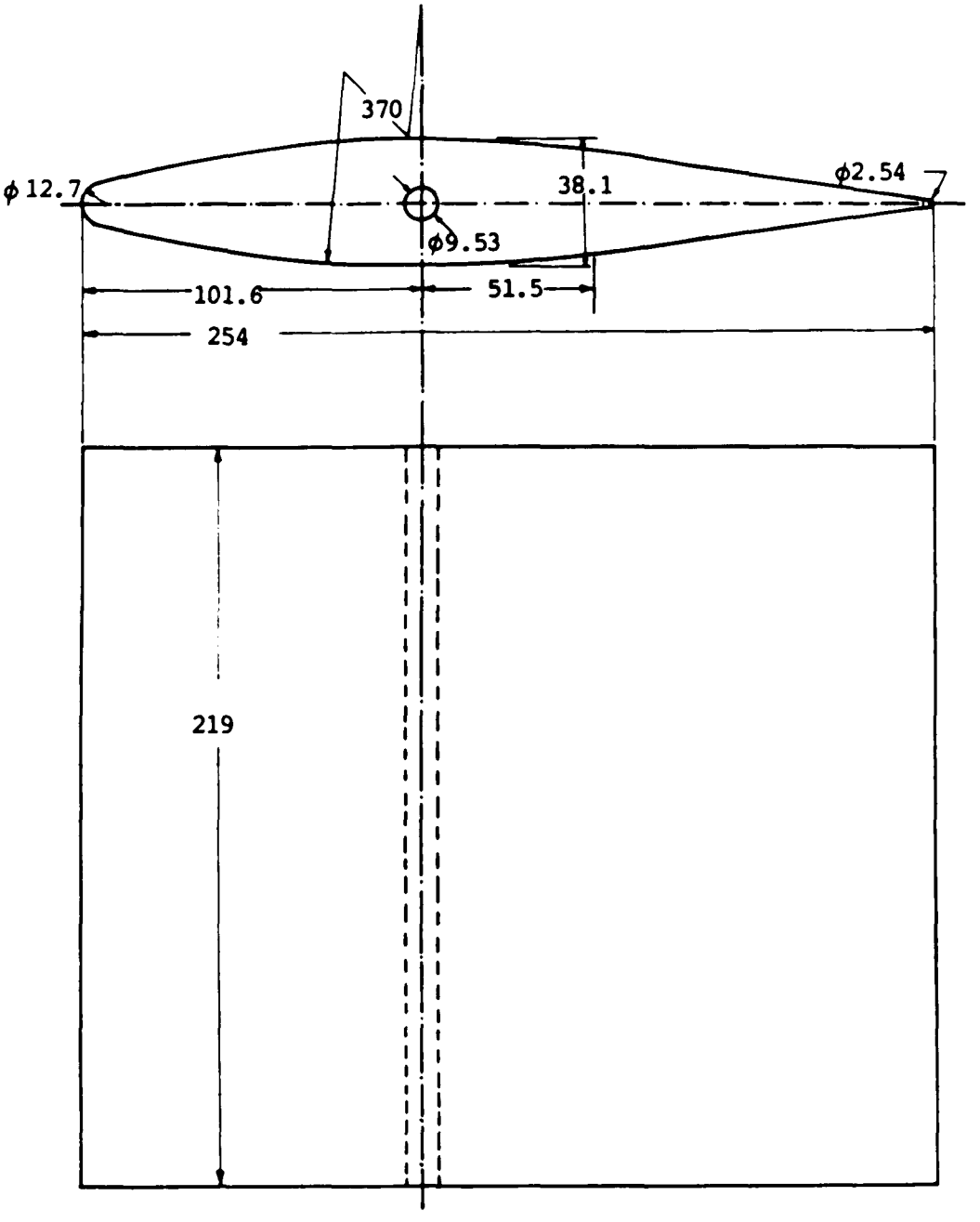

All dimensions are in mm.

Fig. 3.2 Airfoil for the Model

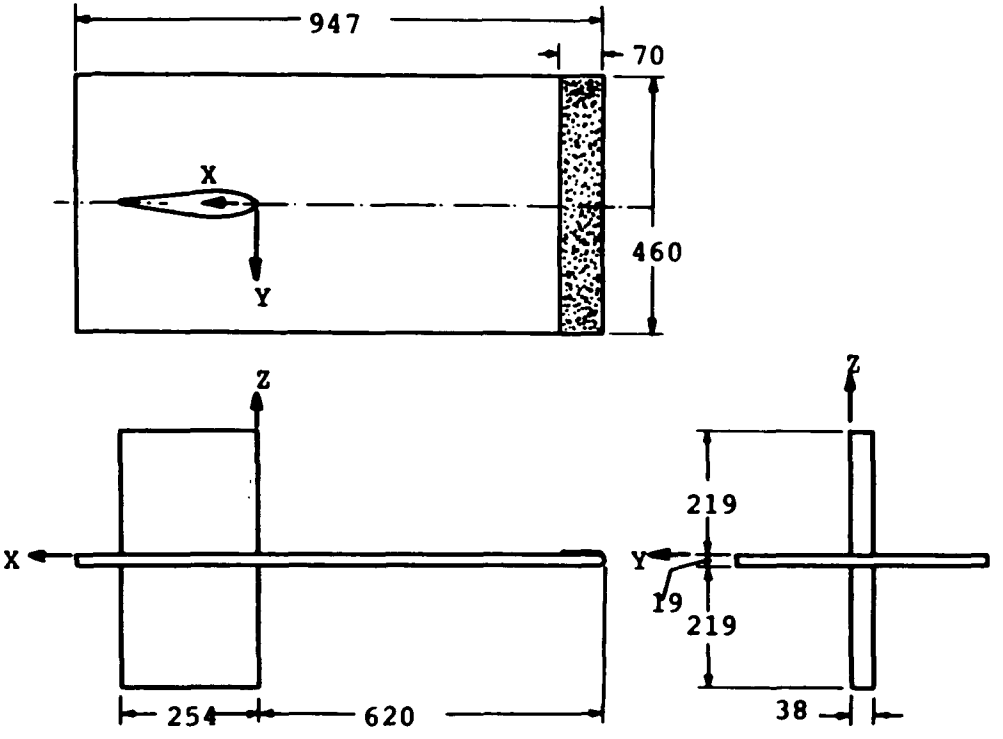

All dimensions are in mm.

Fig. 3.3 Schematic of the Model

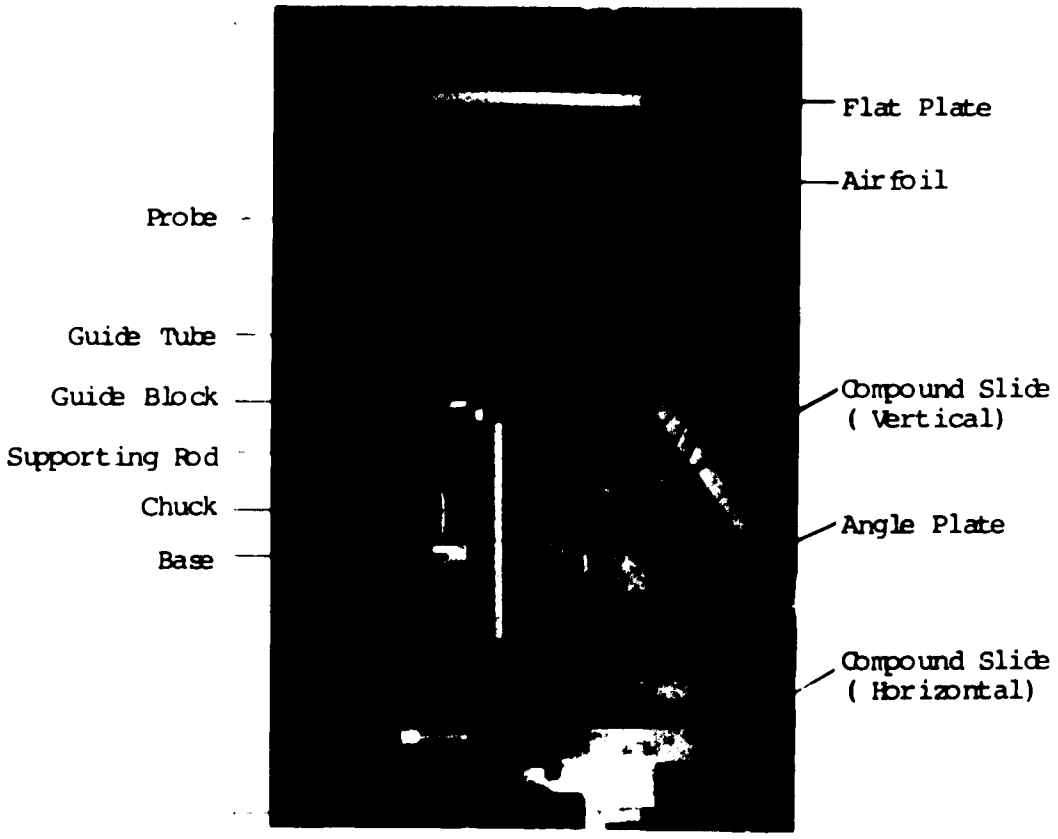

Fig. 3.4 Photograph of the Traverse Mechanism

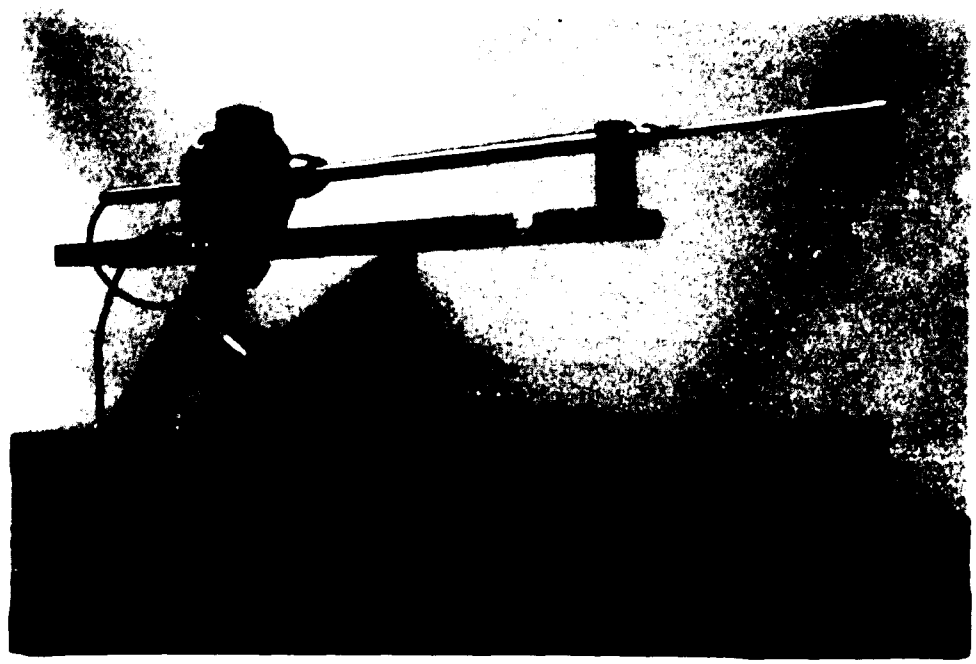

Fig. 3.5 Photograph of First Rotary Device (Rotary Device 1)

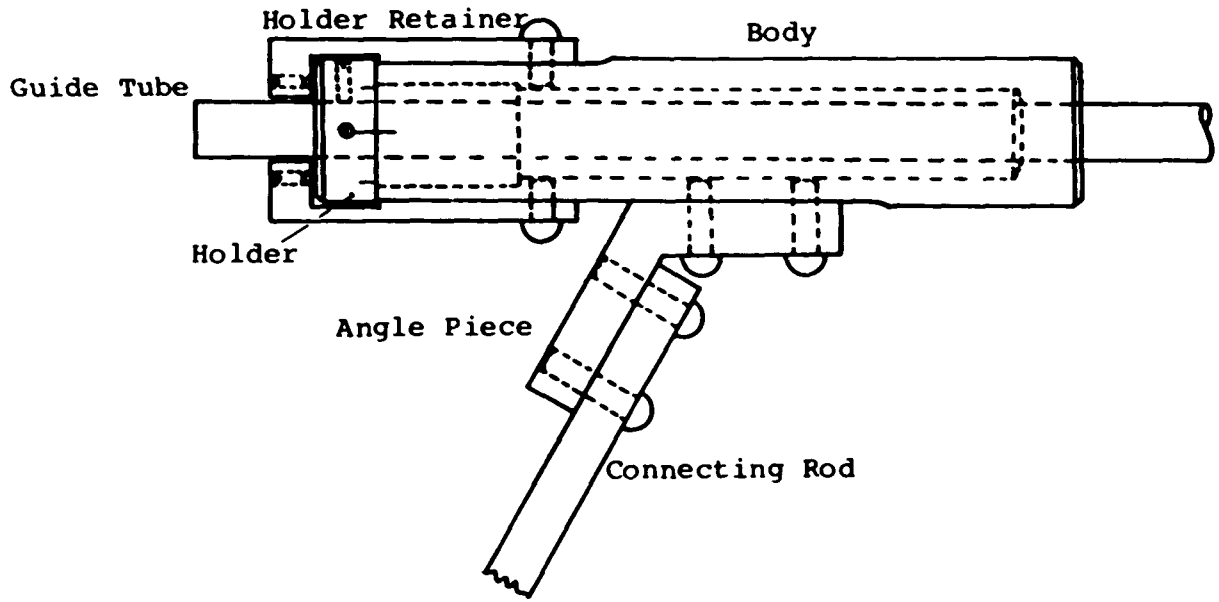

Fig. 3.6 Second Rotary Device (Rotary Device 2)

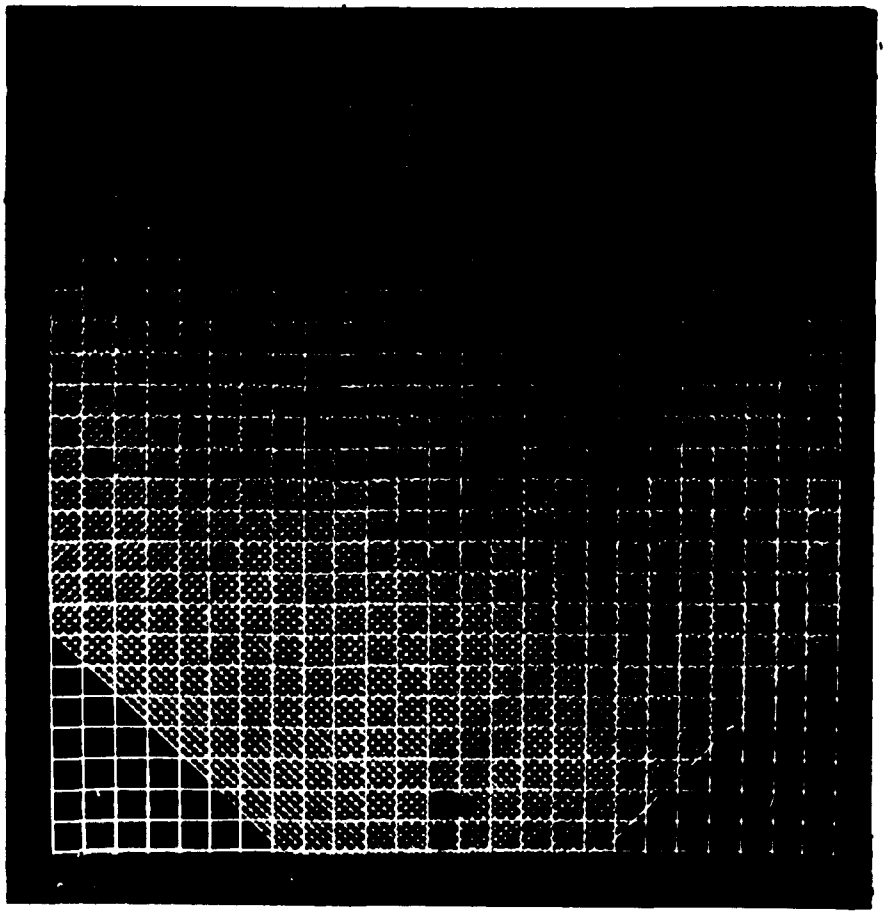

Fig. 3.7 Photograph of Turbulence Generating Grids

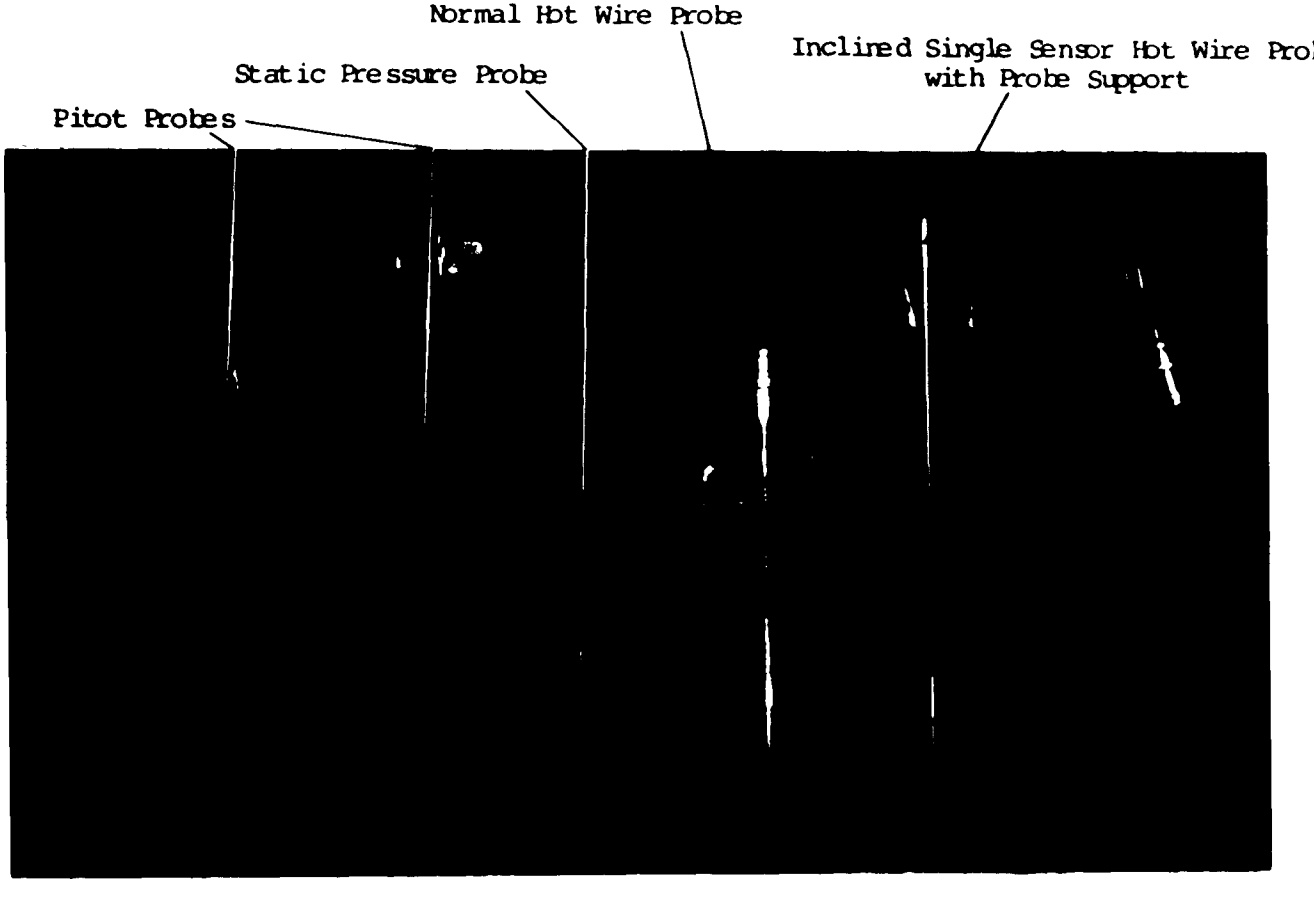

Fig. 3.8 Photograph of Probes

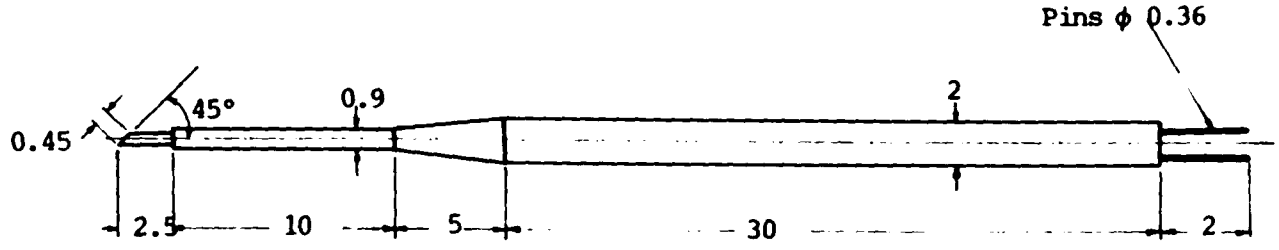

All dimensions are in mm.

Fig. 3.9 Sketch of the Inclined Single Sensor Hot Wire Probe

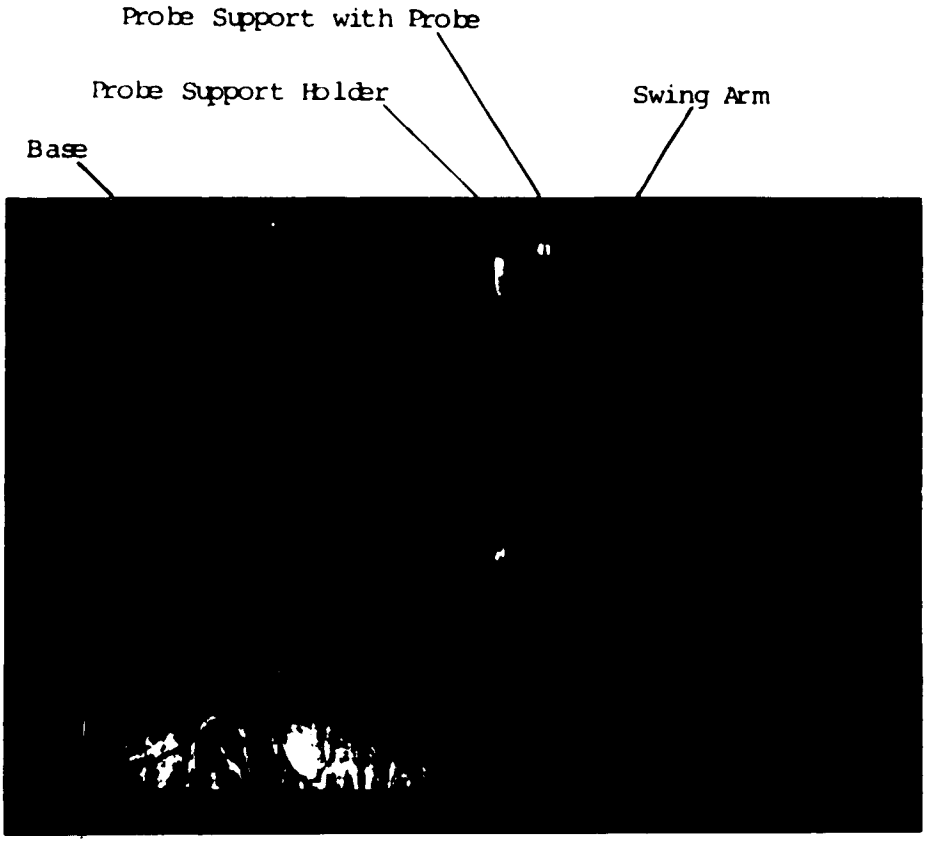

Fig. 3.10 Photograph of Directional Sensitivity Calibration Device

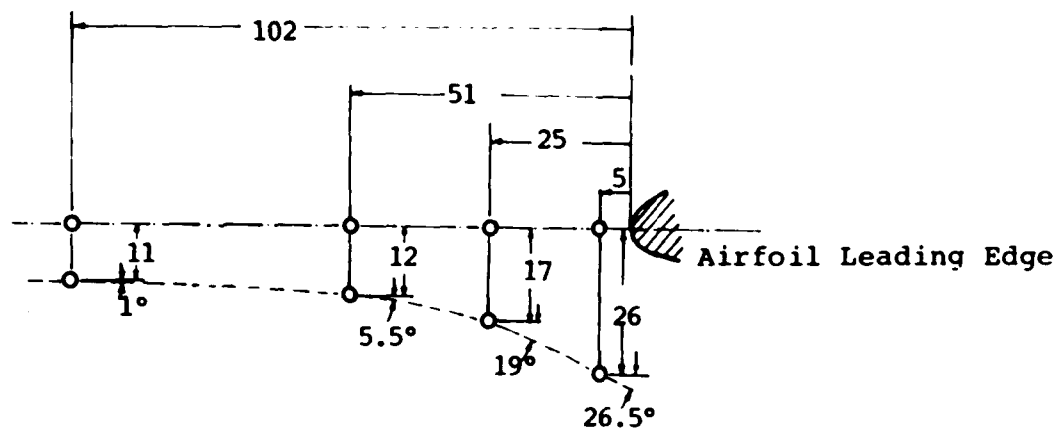

All dimensions are in mm.

Fig. 3.11 Measurement Stations for Upstream Flow

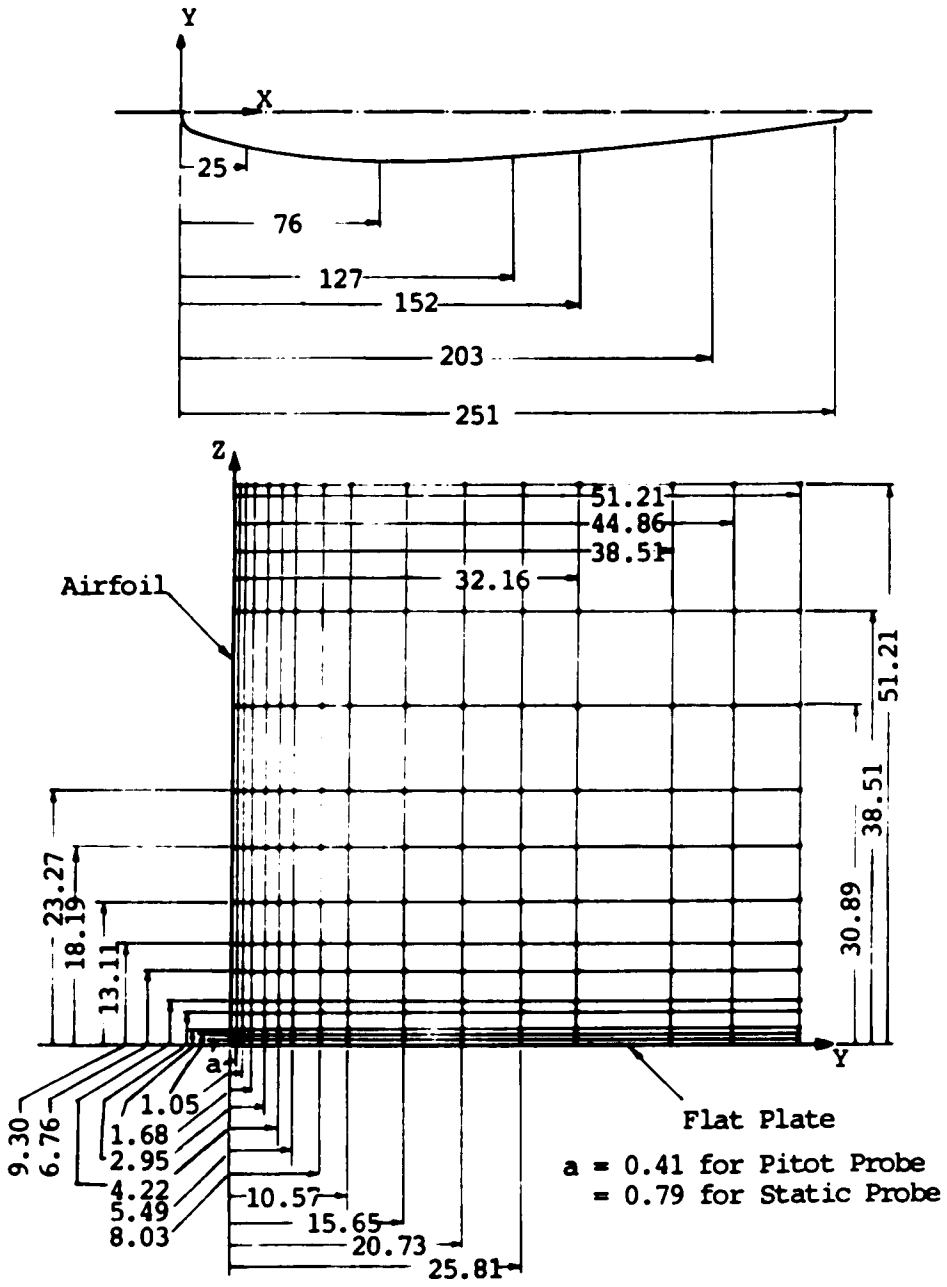

All dimensions are in mm.

Fig. 3.12 Schematic of the Measurment Stations in the Corner and the Grid Points

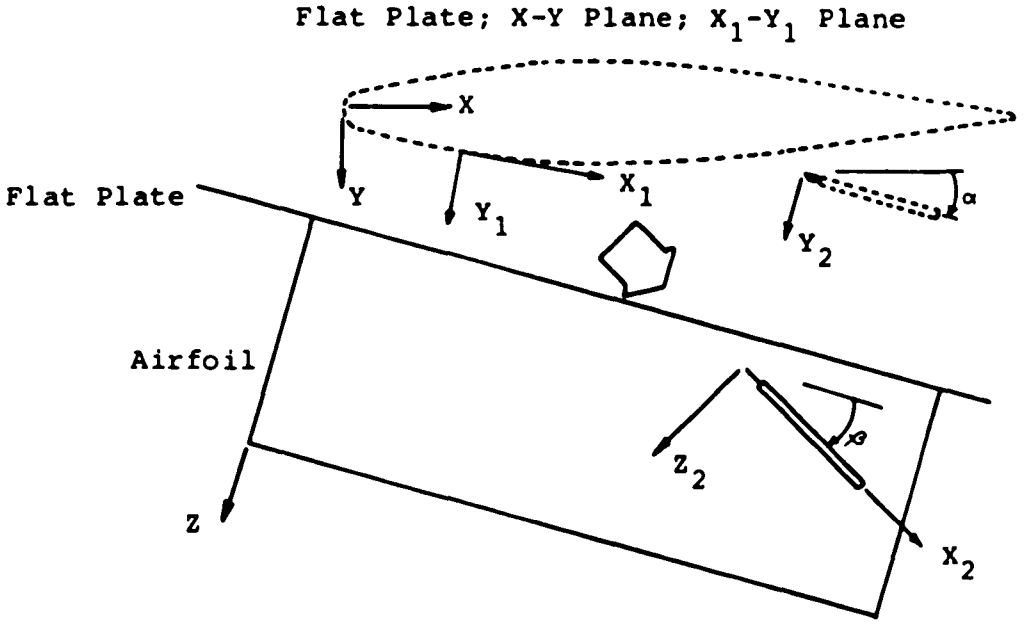

(a) View of the model and the probe

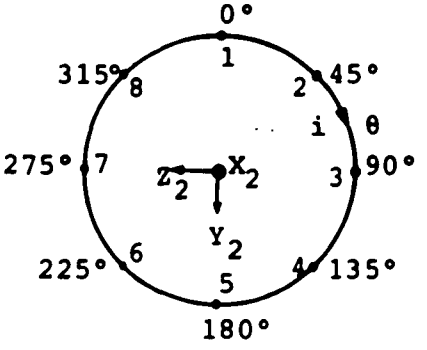

Points indicate the position of the longer prong

(b) View of the probe looking along the arrow

Fig. 3.13 Schematic of Probe Orientation

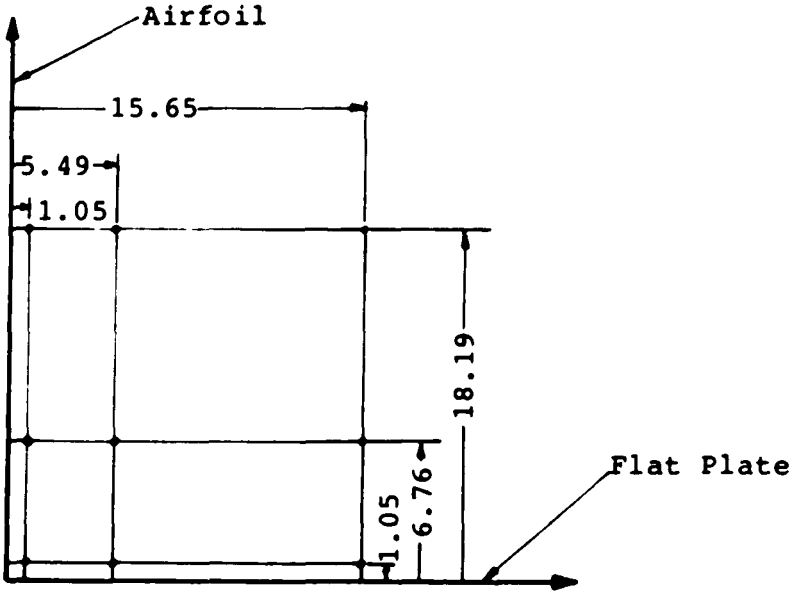

All dimensions are in mm.

Fig. 3.14 Schematic of the Grid Points for Spectra Measurement

CHAPTER IV

RESULTS AND DISCUSSION ON FLOW UPSTREAM OF THE CORNER AND MEAN QUANTITIES IN THE CORNER

The results of the initial boundary layer survey, the flow visualization, the upstream conditions, the static pressure and the total pressure measurements in the corner and the measurements of the mean velocity components in the corner with the inclined single sensor hot wire are presented and analyzed in this chapter.

4.1 Initial Condition

The flat plate had a blunt leading edge (semi - circular with 19 mm diameter) and the initial 70 mm length of the plate was roughened by glueing a strip of sand paper. Apart from this, turbulence generating grids were used to create free stream turbulence at the level of 1% to obtain thick boundary layer and avoid flow separation on the surface of the airfoil, which otherwise would have prevailed. It was also important to make sure that the boundary layer has attained equilibrium before entering the blade endwall corner.

The results of the boundary layer survey at 620 mm downstream of the flat plate leading edge (X=0, where the leading edge of the airfoil starts), in the absence of the

airfoil, are shown in Figs. 4.1 and 4.2. The velocity profiles were measured at the free stream velocity of 27.3 m/s and the maximum variation was kept within 1.5% from run to run. The boundary layer thickness δ_f was assumed to be the value of Z above the flat plate, where $\bar{U}/\bar{U}_\infty = 0.995$. The average value of δ_f was found to be 29 mm with maximum variation of 2% for different probes at different transverse positions (Y). In Figs. 4.1 and 4.2 the values Z and $\bar{U}$ were non - dimensonalized with δ_f and $\bar{U}_\infty$, respectively, for each case. For each kind of probe the variations of the velocity profiles were found to be less than 1% of the average value of the mean velocity. However, a maximum variation of 2% from the average value was observed when profiles measured by pitot tube and the hot wire probes were compared. In Fig. 4.2, slightly higher turbulence intensity was observed near the edge of the boundary layer, while at the point nearest to the flat plate surface the turbulence intensity was found to be about 2% less than the accepted value for turbulent boundary layers on smooth flat plate at zero pressure gradient. The higher value of turbulence intensity near the edge was due to the free stream turbulence introducted by the grid placed upstream of the flat plate.

For each of the velocity profiles, the displacement thickness (δ^*) and the momentum thickness (θ) were calculated

and the value of the shape factor (H) found. The average value of the shape factor was found to be 1.33 and the maximum variation was within 2%. For each of the velocity profiles, Reynolds numbr based on momentum thickness (Re_θ) was calculated and the friction velocity (U*) was found from Prandtl - Schlichting law. The average value of Re_θ was 4.64 x 10^3 with a maximum variation of less than 1% and the average value of friction velocity was 1.09 m/s with a maximum variation less than 2%. The parameters $\bar{U}/U^*$ and ZU^*/ν for the different velocity profiles were calculated using U* for each velocity profile.

The plots of $\bar{U}/U^*$ against ZU^*/ν for the measured points are shown in Fig. 4.3. The velocity profile measured with the pitot tube closely follow the log law $\bar{U}/U^* = A \log_{10} (ZU^*/\nu) + B$ with widely accepted values of the constants A = 5.75 and B = 5.5. However, the profiles measured with the two hot wire probes did not show good agreement with the above. From the self similarity, even in the case of the profiles measured by the hot wire it is evident that the equilibrium was achieved by the boundary layer at the time of its entry into the blade endwall corner.

4.2 Flow Visualization

A general view of the flow pattern on the surface of the test model is shown in Fig. 4.4. The airfoil was then removed from the flat plate and the flat plate was photographed from the top and the airfoil was photographed from the side. The photographic results are presented in Figs. 4.5 and 4.6, respectively.

The pattern of the flow streamlines on the flat plate surface (Fig. 4.5) reveals the formation of a saddle point of separation on the flat plate, 9 mm upstream of the airfoil leading edge. Two saddle points of separation, mentioned by Hsing and Teng [29] were not observed in this case due to the difference in the leading edge shape and flow velocity as pointed out by Siverding [62]. Two separation lines originate from this point and go around each side of the airfoil. The perpendicular distance from the airfoil surface to the separation line at first increases to a maximum, of about 13 mm and then starts decreasing to a minimum of about 6.5 mm at an axial distance of 204 mm from the leading edge. The perpendicular distance starts increasing again and becomes 9.5 mm at an axial distance of 250 mm downstream of the leading edge. The results are summarized in Table 4.1. Inside the horseshoe vortex and near the leading edge, the surface streamlines on the flat plate indicate a reverse flow. Up to about 76 mm downstream of the leading edge, the surface streamlines inside the horseshoe vortex are either outward (away from the corner) or parallel to the corner. In the

forward portion and nearer to the corner they are outward. Near the separation line in the later part of 76 mm, the streamlines are parallel. Afterwards, the streamlines move towards the corner. This trend of inward flow is more pronounced for the surface streamlines nearer to the airfoil. From about 150 mm downstream of the leading edge, the streasmlines become parallel and gradually start to move away from the corner in the outward direction.

The surface streamlines on the airfoil are less spectacular. The streamline starting near the leading edge, about 20 mm above the flat plate has a slight inclination, about 1°, towards the flat plate. As it proceeds downstream, the inclination reduces. At about 100 mm downstream of the leading edge the surface streamline becomes parallel to the flat plate. The streamline then gradually moves away from the surface. At about 150 mm downstream of the leading edge it makes about 2° angle with the flat plate surface and points away from it. In the vicinity of the flat plate, all along the corner the streamlines point in the direction away from the flat plate. About 2 mm above the flat plate surface, the angles made by the surface streamlines on the airfoil are summarized in Table 4.1.

Surface streamline flow visualization on the airfoil showed only discrete points in the vicinity of the corner. However, surface oil film flow visualization gave a continuous

pattern of streaks in this region. Photographs of these patterns on the airfoil are shown in Fig. 4.7 and Fig. 4.8. From these streaks it is evident that the streamlines will be similar to those obtained in the surface streamline method even in the close vicinity of the corner. The streaks clearly show that the flow is always outward on the airfoil in the vicinity of the corner.

On the flat plate in the vicinity of the corner, ahead of the leading edge, between the leading edge and the saddle point of separation, the flow reverses. Near the leading edge the flow is outward then it turns inward towards the corner and finally, from about 30 mm upstream of the trailing edge the flow is slightly outwards. This flow pattern is in agreement with the surface stream lines and confirms that the surface streamline method did not miss any of the important features of the flow over the surface forming the corner.

The pattern of streamlines on the flat plate and the airfoil can be correlated to the components of mean velocity variation and the total pressure and the static pressure profiles in the corner region. Conclusions drawn regarding the development of the vortices in the corner region, based on the surface streamlines and the profiles mentioned above, are discussed in the following sections.

4.3 Upstream Flow Condition

Variation of the pressure ($P_s - P_a$) as a fraction of the undisturbed dynamic pressure ($P_{o\infty} - P_a$) is presented in Fig. 4.9. Static pressure increases as the flow approaches the blade along the stagnation streamline. Along a streamline starting at 102 mm upstream of the leading edge and 11 mm away from the stagnation streamline the static pressure initially increases but when the streamline bends away from the airfoil, the static pressure drops. The behavior is similar to that near an elliptical body. Normal to the flat plate, there is no appreciable variation of static pressure, up to a distance of approximately 25 mm upstream. On the stagnation plane near the leading edge the static pressure increases with increasing distance from the flat plate. The behavior is opposite for the streamline away from the stagnation line. The pressure reduces away from the flat plate. Outside the boundary layer there is no appreciable pressure variation at any of the measuring stations.

The variation of pressure near the leading edge in the vicinity of the flat plate can be explained in terms of horseshoe vortex blockage effect and its induced velocity. The flow at X = -5 mm and Y = 26 mm is more complex and a simple approach to explain the behavior of flow pattern at this point based on two dimensional flow is not adequate.

Fig. 4.10 shows the variation of mean velocity profile normal to the flat plate at various stations along the stagnation plane. Fig. 4.11 shows the variation of the mean velocity profiles along the streamline starting at 102 mm upstream of the leading edge and 11 mm away from stagnation streamline. The flow decelerates along the stagnation streamline. Along the streamline away from the stagnation streamline the flow initially decelerates then starts to accelerate. The behavior is similar to that of flow near a blunt leading edge. There is no appreciable change in the boundary layer thickness δ_f in the 97 mm distance where measurements were made.

The variations of turbulence intensity in the streamline direction along the two streamlines are shown in Fig. 4.12 and Fig. 4.13, respectively. Along the stagnation streamline the turbulence intensity near the wall slowly reduces and away from the wall and outside the boundary layer the turbulence intensity reduces but at a much slower rate. Along the streamline starting at 102 mm upstream of the leading edge and 11 mm away from the stagnation streamline the free stream turbulence intensity remains fairly constant. Inside the boundary layer the turbulence intensity reduces as the flow accelerates.

The turbulence spectra taken at 5 stations, 1.3 mm above the flat plate were analyzed and they are presented in

Fig. 4.14 in wave number domain (κ). A large portion of the spectra follow $\kappa^{-5/3}$ slope, but at small wave numbers, $\kappa^{-2/3}$ is more appropriate relation for all the spectra analyzed. In the range of wave number (κ) from 1.5 x 10^3 1/m to about 5.5 x 10^3 1/m, the turbulence is in the inertial subrange where $\kappa^{-5/3}$ relation is satisfied. Below this wave number range (κ < 1.5 x 10^3 1/m) the spectrum did not follow any universal relation. But the flow at all the grid points investigated, followed $\kappa^{-2/3}$ slope, indicating that they belong to the same flow geometry.

4.4 Static and Total Pressure Variation in the Corner

The static and the total pressure variations at six axial stations X/C = 0.1, 0.3, 0.5, 0.6, 0.8 and 0.985 are presented in this section.

4.4.1 Static Pressure Variation

Static pressure variation at the six axial stations are shown in Fig. 4.15 to Fig. 4.26. At each axial station variation of static pressure parallel to the flat plate (variable Y) at different heights above the flat plate (constant Z) are plotted in Fig. 4.15 to Fig. 4.20. In Fig. 4.21 to Fig. 4.26, variation of static pressure in a direction parallel to the airfoil surface (variable Z) at different

distance from the airfoil (constant Y) are presented.

In the forward part of the airfoil, away from the corner region the static pressure decreases towards the airfoil surface. This variation is typical of an accelerating flow over a curved surface (Fig. 4.15 to Fig. 4.17). The transverse gradient of static pressure away from the airfoil surface gradually increases upto the axial position where the airfoil has maximum thickness. In the rear part of the airfoil (Fig. 4.18 to Fig. 4.20) the trend reverses and the pressure has a negative gradient away from the airfoil surface at the axial station nearest to the trailing edge. At stations downstream of the maximum thickness section, the flow near the airfoil surface decelerates and pressure recovery takes place, ultimately ending up with a positive pressure coefficient, $C_p=(P_s- P_a)/(P_{o\infty}- P_a)$, and a negative transverse gradient of pressure in the direction away from the airfoil surface. In the corner region and in the forward part of the airfoil the trend is opposed by the horseshoe vortex, this slightly increases the static pressure near the corner. In Fig. 4.16, away from the corner the pressure coefficient falls below -0.30 but in the vicinity of the corner the minimum value of pressure coefficient encountered is -0.28.

Away from the corner and normal to the flat plate (Fig. 4.21 to Fig. 4.26) the static pressure does not change significantly. However, near the corner in the forward part

of the airfoil the static pressure profiles show a gradual increase towards the flat plate, most probably due to the action of the horseshoe vortex. In the downstream stations, due to the weakening of the horseshoe vortex no significant variation of static pressure in the corner region is observed. For example, in Fig.4.20, the value of pressure coefficient for the curve Y = 0.79 mm, is -0.10 at Z = 50 mm but this value increases to -0.05 at Z = 0.79 mm.

4.4.2 Total Pressure Variation

Fig. 4.27 to Fig. 4.32 show the total pressure variation parallel to the flat plate (variable Y) at different heights above the flat plate (constant Z) at the six axial stations. In general, at a constant height above the flat plate and near the flat plate, in the direction away from the airfoil the total pressure sharply increases to a peak (indicated by the arrow on Fig. 4.27) within a short distance from the airfoil. The total pressure then gradually reduces to attain a constant value away from the airfoil surface. Near the leading edge of the airfoil (X = 25.4 mm) the distance from the airfoil at which the profile attains the constant value is of the order of the incoming boundary layer thickness δ_f (~30mm). As the height from the flat plate surface increases, the peak pressure as well as the constant pressure values increase. However, the values of constant total pressure increase at a faster rate than the peak total

pressure values. For the traverse outside the flat plate boundary layer the pressure distribution in this portion is flat giving a total pressure profile similar to that of a boundary layer over a curved surface. The positions of the peaks first move away and then move towards the airfoil surface as the heights above the flat plate increase.

The distances of the peaks from the airfoil surface increase as the axial distance of the stations increase. At X/C = 0.8, in the profile measured close to the flat plate surface, a depression (indicated by the arrow mark on Fig. 4.31) appears on the positive gradient part of the profile. This depression is more prominent at the next axial station. At the axial distance X/C = 0.985, the depression on the total pressure profile is evident even on the profile at Z = 1.04 mm. The values of the peaks and the constant total pressures of the profiles and also the positions of the peaks at three axial distances, namely X/C = 0.3, 0.8 and 0.985, are compiled in Table 4.2. From the table it is apparent that the maximum difference in the value of the peaks and constant pressures $(P_{op}-P_{oc})/(P_{o\infty}- P_a)$ are 0.355, 0.190 and 0.150 at the axial positions X/C = 0.3, 0.8 and 0.985, respectively and they occur on the profiles at Z = 0.41 mm, 2.95 mm and 4.22 mm, respectively. The reduction in this value of pressure difference with increasing X/C indicates diffusion of the horseshoe vortex resulting from the combined effect of turbulence and deceleration of the flow.

Variations of total pressure parallel to the airfoil surface (variable Z) at different distances from the airfoil surface (constant Y) at the six axial stations in the corner region are shown in Fig. 4.33 to Fig. 4.38. The most prominent feature of these total pressure profiles are the appearance of a peak (maximum, M) followed by a deep valley (minimum, m) on the profiles near the airfoil surface. The minimum point is followed by a profile resembling a boundary layer profile. With increasing axial distance (X/C), the steepness of pressure variation decreases for all the profiles. The distances from the flat plate surface to the maximum and minimum points also gradually decrease with increasing axial distance (X/C). Away from the airfoil surface (with increasing Y), the differences between the maximum and minimum values decrease and ultimately, away from the corner region, the total pressure profiles approach that of the boundary layer profiles over a flat plate. The difference between the maximum and the minimum total pressures, $(P_{oM} - P_{om})/(P_{o\infty} - P_a)$, on the profiles nearest to the airfoil surface (Y = 0.41 mm) at the axial distances X/C = 0.3, 0.8 and 0.985 are 0.14, 0.02 and 0.01, respectively. The variation of the distances of peak (Y_p) and depression (Y_d) from the airfoil surfaces with the axial distance, for the profiles nearest to the flat plate (Z = 0.41 mm), as well as the variation of the distances of maximum (Z_M) and the minimum

(Z_m) total pressure points from the flat plate surface with the axial distance, for the profiles nearest to the airfoil surface (Y = 0.41 mm) are shown in Fig. 4.39. For both the cases the variation is steeper on the downstream side of the maximum thickness section of the airfoil.

4.5 Mean Velocity Profiles

The variations of the streamwise component ($\bar{U}_1$) of the mean velocity parallel to the flat plate (variable Y) at different heights above the flat plate (constant Z) for the five axial stations, X/C = 0.3, 0.5, 0.6, 0.8 and 0.985 are shown in Fig. 4.40 to Fig. 4.44. The general shape of these profiles closely follow the total pressure profiles at the same locations. The streamwise component of mean velocity plotted against Z at constant Y also showed resemblance with the shape of the corresponding total pressure profiles. The positions of the peaks in the streamwise velocity profiles are in good agreement with those in the total pressure profiles at corresponding heights above the flat plate at same axial locations.

The variations of transverse component of mean velocity ($\bar{V}_1$) at the five axial stations are shown in Fig. 4.45 to Fig. 4.49 and that of spanwise component of mean velocity ($\bar{W}_1$) are shown in Fig 4.50 to Fig. 4.54. These

graphs are also plotted for traverses parallel to the flat plate surface (variable Y) at different heights (constant Z) above the flat plate. For the traverse very close to the flat plate, at X/C = 0.3 and Z = 1.04 mm, $\bar{V}_1/\bar{U}_\infty$ starts with a value of -0.01, and increases to a value of 0.075 at Y = 10 mm and then gradually reduces to zero (Fig. 4.45). On the other hand, for the same traverse, $\bar{W}_1/\bar{U}_\infty$ starts with a value of about 0.15, reduces to about -0.05 at Y = 5 mm, and then asymptotically increases to about 0.10 (Fig. 4.50). This general shape continues upto a height of Z = 6.76 mm for both $\bar{V}_1/\bar{U}_\infty$ and $\bar{W}_1/\bar{U}_\infty$. At Z = 9.3 mm, $\bar{V}_1/\bar{U}_\infty$ remains almost a constant at a negligibly small value (~0) but $\bar{W}_1/\bar{U}_\infty$ starts with a value of about -0.05 and asymptotically increases to 0.01. Above this height (Z = 9.3 mm), $\bar{V}_1/\bar{U}_\infty$ starts with a small positive value (~0.01) and asymptotically reduces to a small negative value (-0.04). At the same location, $\bar{W}_1/\bar{U}_\infty$ starts with a value of about 0.05 and asymptotically reduces to a slightly smaller positive value. At downstream stations (Figs. 4.44 and 4.48) near the flat plate, $\bar{V}_1/\bar{U}_\infty$ starts with a small value (-0.01 to +0.02) then gradually increases to a peak value (~0.075) and then asymptotically attains a slightly smaller value. Away from the flat plate, the asymptotic reduction is not observed, instead the value slightly increases. At these stations (Figs. 4.53 and 4.54), the profiles of $\bar{W}_1/\bar{U}_\infty$ near the flat plate are similar to those of

$\overline{V}_1/\overline{U}_\infty$. Slightly away from the flat plate (Z = 4.22 mm to Z = 9.3 mm) the values decrease slightly and then asymptotically increase to a slightly higher value. Above Z = 9.3 mm, the profiles of $\overline{W}_1/\overline{U}_\infty$ again take the general shape of the profiles of $\overline{W}_1/\overline{U}_\infty$ at the same heights as described before.

4.6 Bernoulli Surfaces

To obtain a physical picture of the flow field in the blade endwall corner region it is helpful to observe the evolution of the Bernoulli surfaces. These are the surfaces on which the total pressure is constant. In the flow over curved surfaces the Bernoulli surfaces provide a physical understanding more accurate than the isovels. The Bernoulli surfaces were developed from the corresponding total pressure profiles shown in Fig. 4.27 to Fig. 4.38. The surfaces obtained at three axial locations, namely X/C = 0.3, 0.8 and 0.985 are presented in Figs. 4.55, 4.56 and 4.57 respectively.

At X/C = 0.3, in the immediate vicinity of the corner, the Bernoulli surface for $(P_o - P_a)/(P_{o\infty} - P_a)$ = 0.4 (Fig. 4.55) has an outward bulge which is the characteristic shape for a laminar corner flow. Away from this region, in the Y direction, the surfaces sharply move towards the flat plate and then gradually move away from it. In the Z direction, they first move away then gradually move towards

the airfoil. At X/C = 0.8 and 0.985, the shape of the Bernoulli surfacs, away from the immediate vicinity of the corner, are similar to that of Fig. 4.55. However, in the immediate vicinity of the corner, the characteristic bulge of the laminar corner flow no longer exists. Instead there is a hint of bending towards the corner which is a characteristic of a turbulent corner flow. Away from the corner, the spacing between the Bernoulli surfaces parallel to the airfoil rapidly increases as the flow proceeds downstream. The rate of increase of the spacing between the Bernoulli surfaces parallel to the flat plate is much slower.

The distortion of the total pressure profiles and the Bernoulli surfaces at X/C = 0.3 are believed to be caused by the combined action of vortices shown in Fig. 4.58. The largest of these vortices is the horseshoe vortex generated by the distortion of the vortex sheet of the incoming boundary layer. This distortion is due to the presence of the thick airfoil leading edge. In the first octant (X, Y and Z all positive) this streamwise component vorticity points towards the downstream direction (positive X). Away from the corner region, the boundary layer formed on the airfoil gives rise to a vortex sheet with the vector pointing towards negative Z direction. However, in the corner region the vortex is distorted to produce a streamwise component pointing in the upstream direction (negative X). This vortex is enclosed between the walls forming the corner and the horseshoe vortex.

The vortex in the corner (hereafter referred to as the corner vortex) and the horseshoe vortex rotate in opposite directions. On the flat plate, the limiting streamlines move away from the corner due to the influence of the horseshoe vortex and move towards the corner due to the influence of the corner vortex. This is verified by the flow visualization traces. The surface streamlines on the flat plate, between the airfoil and the position of the peak of the total pressure profile nearest to the flat plate, lean slightly towards the corner. If the shape of the corner vortex is a slightly distorted form of circular cylinder, the height (Z_m) at which the minimum occurs in the total pressure profile nearest to the airfoil surface, and the distance (Y_p) at which the peak occurs on the total pressure profile nearest to the flat plate should be roughly equal. This was the case near the leading edge (Fig. 4.39). The corner vortex was also observed by Gorsky et al. [21]; however, it could not have been the secondary flow of the second kind, as reported by them, since it was present even near the leading edge of the airfoil where characteristic bulge of the laminar corner flow was observed.

As the flow proceeds downstream, the stress induced secondary flow is generated. In a simple corner it would have appeared as a pair of contra-rotating vortices. In the present case the vortex with its vector pointing upstream merges with the corner vortex. The system of vortices formed in this manner is shown in Fig. 4.59. The appearance of the

secondary vortex of the second kind does not alter the general shape of the total pressure profiles in the Z direction. At X/C = 0.8 and 0.985, total pressure profiles nearest to the flat plate show a depression on the protion of the profile where the gradient is positive thus indicating a pair of vortices of the second kind. The secondary vortex does not alter the total pressure profiles in the Z direction because the vortex has the same direction as the corner vortex and merges with it.

Magnified plots (Figs. 4.60 and 4.61) of the total pressure profiles in the vicinity of the corner at Z = 0.41 mm and at Y = 0.41 mm at six axial stations reveal further information pertinent to the corner vortex and the stress induced vortices. In both the figures, the profiles flatten out up to the axial distance of X/C = 0.6. It is thought that this trend is due to diffusion of the horseshoe vortex and the corner vortex by the action of the Reynolds stresses and pressure gradient. At X/C = 0.8 and 0.985 the trend is reversed; the total pressure profiles become fuller. Near a wall the total pressure may increase in the downstream only if the high momentum fluid from other parts of the flow field is advected towards the wall. In these figures, it is evident that the profiles in both the directions are energized near the wall. Therefore, it is proposed that a pair of contra-rotating vortices advect high momentum fluid (from regions away from the corner) along the corner bisector

towards the corner. The profiles parallel to the flat plate (Z = 0.41 mm) also show a depression appearing on the profiles. The peak values in the profiles at Z = 0.41 mm monotonically decrease along the axial direction. However, in the case of profiles at Y = 0.41 mm, the maximum value decreases up to X/C = 0.6. At the last two stations (X/C = 0.8 and 0.985) the maximum value of total pressure near the airfoil surface starts increasing. This indicates that the corner vortex which created the maximum values in the total pressure profiles are being strengthened by the new phenomena, namely the appearance of the stress induced vortices.

The changes in the positions of the peaks in the total pressure profiles along Y and minima in the total pressure profiles along Z are a measure of the distortion of the vortices. These are presented graphically in Fig. 4.39 as a function for X. The variation in the rate of change of these distances with respect to X, in the front and the rear part of the airfoil can be explained from the fact that the accelerating flow reduces the size of streamwise vortices and the decelerating flow increases it. Therefore, the rate of change of the position of maxima and minima with X is slower in the front part of the corner, compared with the rear part of the corner. Position of maxima (Z_M) and minima (Z_m) as well as the position of the peak (Y_p) are plotted against the boundary layer thickness on the airfoil (δ_a) in Fig. 4.62.

The boundary layer thickness is determined from the total pressure profiles, 51.21 mm above the flat plate (outside the corner region), and is assumed to be where $(P_o - P_a)/(P_{o\infty} - P_a)$ is 0.99 (equivalent to $\bar{U}/\bar{U}_\infty = 0.995$ for flat plate). The correlations are very good as seen from the low scatter about the straight lines. Since the position of maxima, minima and peaks relate to the size of the corner vortex, it is evident that the corner vortex scales the boundary layer thickness on the airfoil outside the corner region (δ_a).

A plot of the secondary veloctiy vectors obtained from the measurements at the axial location X/C = 0.30 is shown in Fig. 4.63. The secondary velocity vectors were able to show the horseshoe vortex which is counterclockwise looking downstream, but was unable to show the corner vortex and the secondary vortex of the second kind. It is due to the fact that enough measurements could not be taken very close to the solid surfaces. Moreover, the secondary velocity due to the vortex of the second kind is very small and difficult to measure with any degree of accuracy. It is also noted that a small error in the determination of the angles α and β will show a large shift in the apparent location of the center of the vortex; thus, no attempt was made to determine the variation of the position of the center of vortex. The existence of the horseshoe vortex and the corner vortex can be seen from the variation of the spanwise velocity component

($\overline{W}_1$) and the variation of the transverse velocity component ($\overline{V}_1$). Although the shapes of the velocity profiles bear out the existence of the vortices as stated, the direction of these velocity components at some stations do not. The anomaly is due to the accuracy involved in the estimation of the angle of the probe. The uncertainty in measurement of the angles was about 2° which introduces an uncertainty of the order of 0.03 $\overline{U}_1$. But the value of $\overline{V}_1$ and $\overline{W}_1$ are one order of magnitude smaller than $\overline{U}_1$. Thus, high fixed error warrants that the shape of the profiles instead of the magnitude should be given more importance. Since the stress induced secondary flow is one order of magnitude smaller than the skew induced secondary flow it is beyond the accuracy of the instruments to detect any hint of the stress induced vortex from the measurement of the secondary flow. The indication of the presence of these vortices can be felt only from the distortion of total pressure profiles and the distortion of the streamwise mean velocity profiles.

Table 4.1 Data from Surface Streamline Flow Visualization and Total Pressure Profiles

Axial distance X mm	25	51	76	102	127	152	178	203	229	251
Normal distance of the separation line from the airfoil	12	13	13	12	10	7.5	7	6.5	7.5	9.5
Streamline angle on the airfoil at Z = 2 mm	3°	-	-	5°	7°	8°	7°	4°	7°	-
Boundary layer thickness on the airfoil away from the corner δ_a	0.5	-	1.5	-	2.5	4.0	-	6.5	-	10.5
For curve at Z = 0.41 mm										
Peak Y_p mm	2	-	3.7	-	4.5	5.5	-	7.5	-	9.5
Depression Y_d mm	-	-	-	-	-	-	-	2	-	3
For curve at Y = 0.41 mm										
Maxima Z_M mm	1	-	1	-	1.5	2	-	3	-	4
Minima Z_m mm	2.2	-	2.7	-	3.5	4	-	5.5	-	6.5

Table 4.2 Comparison of Data from Total Pressure Profiles

X/C	Z mm ⇨ / ⇩ Quantity	0.41	1.05	1.68	2.95	4.22	6.76	9.30	13.11	18.19	23.27	30.89
0.30	Y_p	3.75	4.50	4.25	3.75	3.00	2.50	2.25	2.00	1.70	1.70	1.70
	$(P_{op}-P_a)/(P_{ooo}-P_a)$	0.665	0.72	0.735	0.76	0.79	0.835	0.875	0.92	0.96	0.98	0.98
	$(P_{oc}-P_a)/(P_{ooo}-P_a)$	0.32	0.44	0.50	0.57	0.62	0.69	0.74	0.82	0.90	0.95	0.98
0.80	Y_p	7.25	7.50	7.50	7.25	7.00	6.50	5.50	5.50	5.50	5.50	5.50
	$(P_{op}-P_a)/(P_{ooo}-P_a)$	0.325	0.43	0.535	0.69	0.75	0.79	0.83	0.89	0.94	0.975	0.98
	$(P_{oc}-P_a)/(P_{ooo}-P_a)$	0.25	0.33	0.40	0.50	0.58	0.67	0.72	0.79	0.88	0.94	0.98
0.985	Y_p	9.50	9.50	8.75	8.00	8.00	8.00	8.00	8.00	8.00	8.00	8.00
	$(P_{op}-P_a)/(P_{ooo}-P_a)$	0.325	0.41	0.48	0.61	0.70	0.78	0.825	0.875	0.94	0.97	0.98
	$(P_{oc}-P_a)/(P_{ooo}-P_a)$	0.25	0.34	0.40	0.48	0.55	0.65	0.71	0.79	0.88	0.95	0.98

(See Fig. 4.3 for legend)

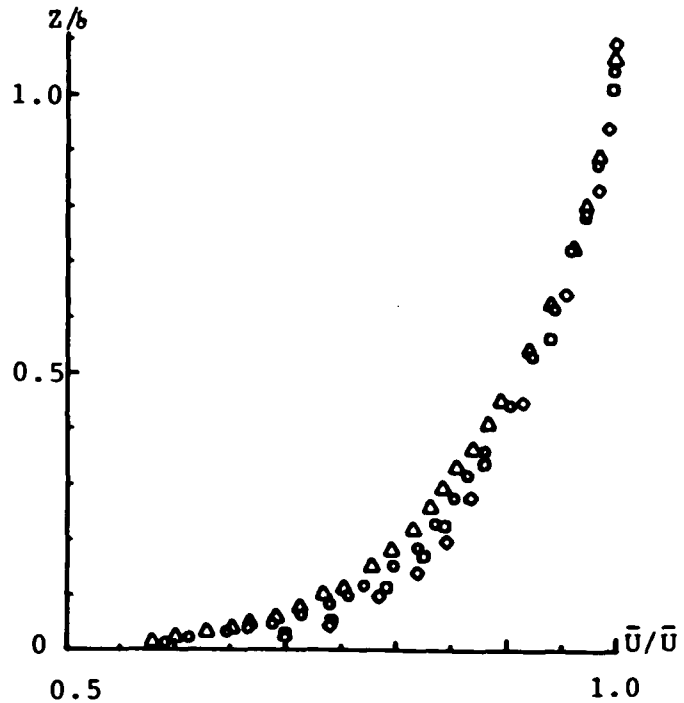

Fig. 4.1 Mean Velocity Profile Without the Airfoil

(See Fig. 4.3 for legend)

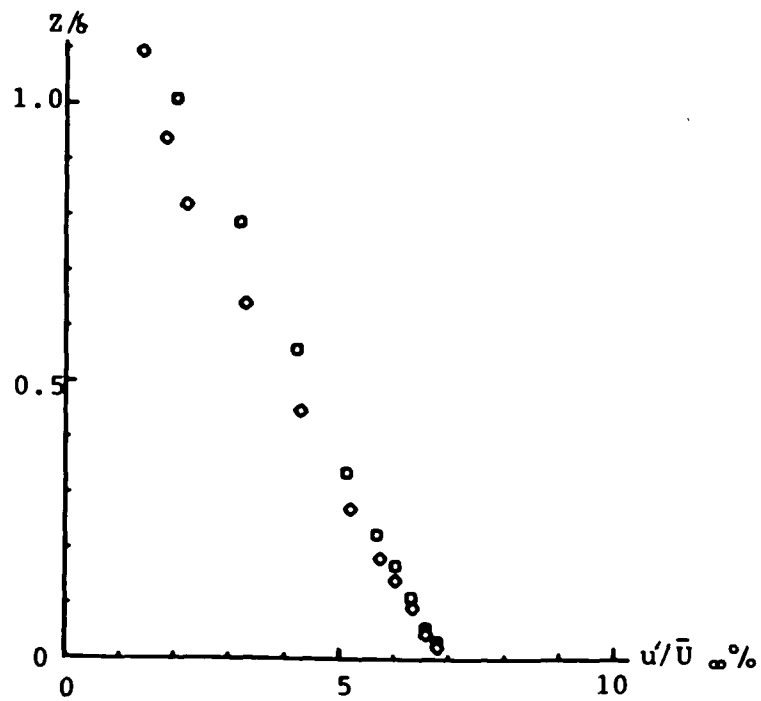

Fig. 4.2 Turbulence Intensity Variation Without the Airfoil

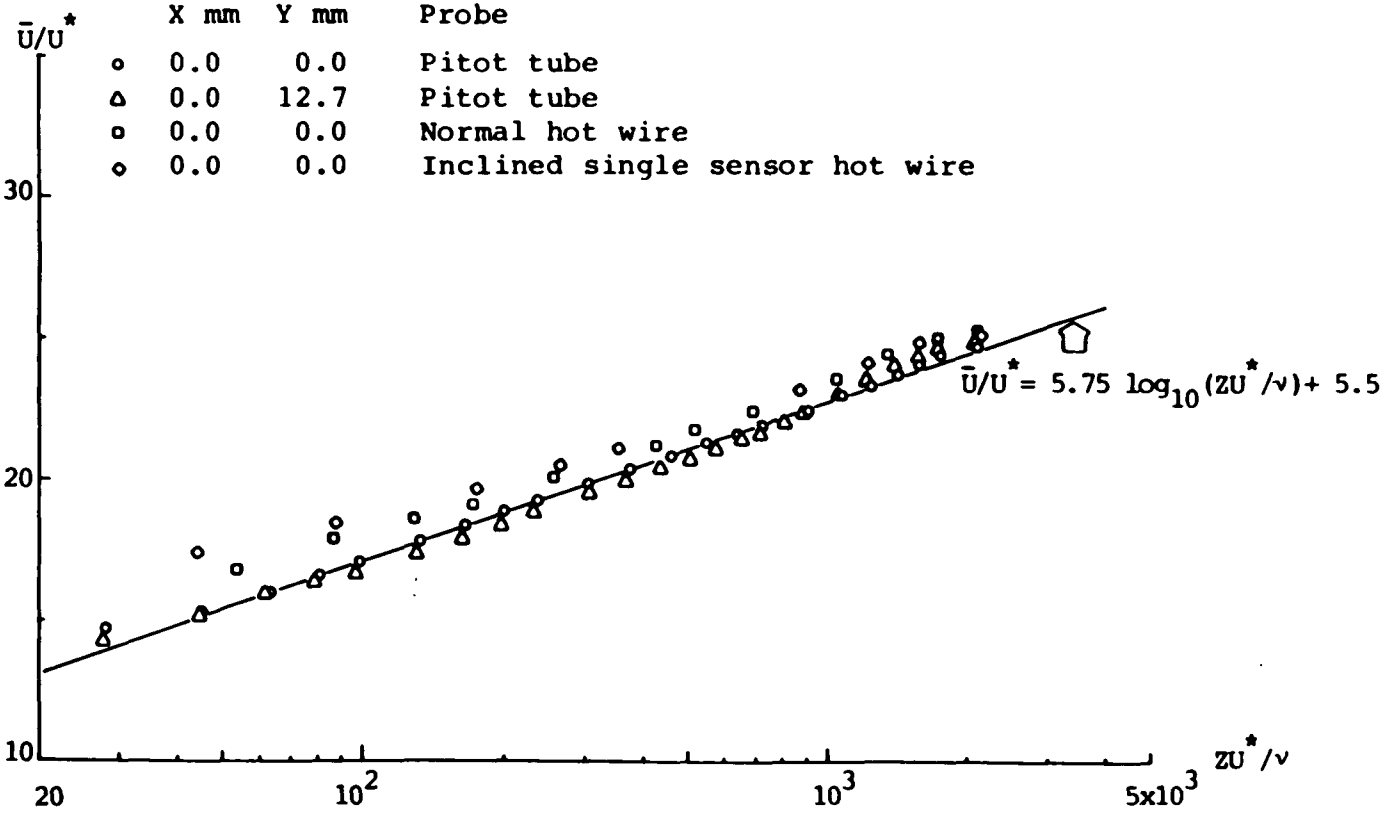

Fig. 4.3 Comparison of Boundary Layer on the Flat Plate (Without the Airfoil) With Log-law Profile

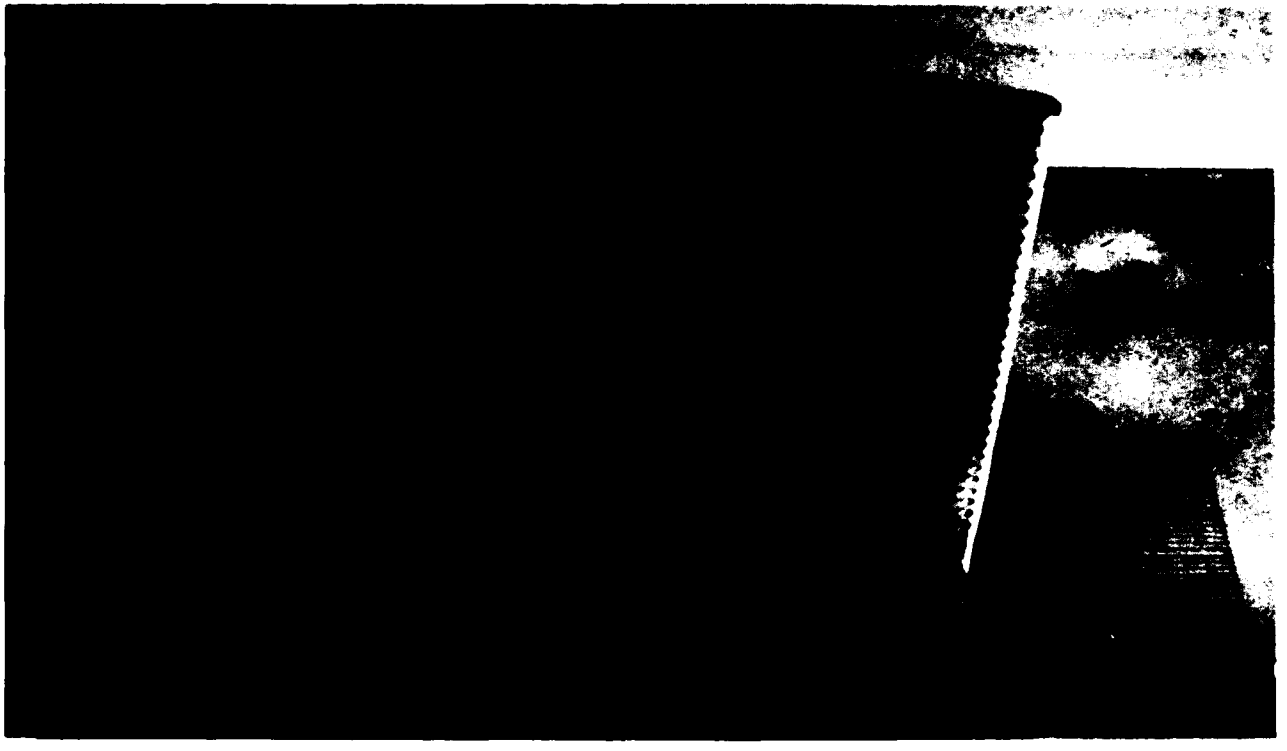

Fig. 4.4 Photograph of Surface Streamlines on the Model

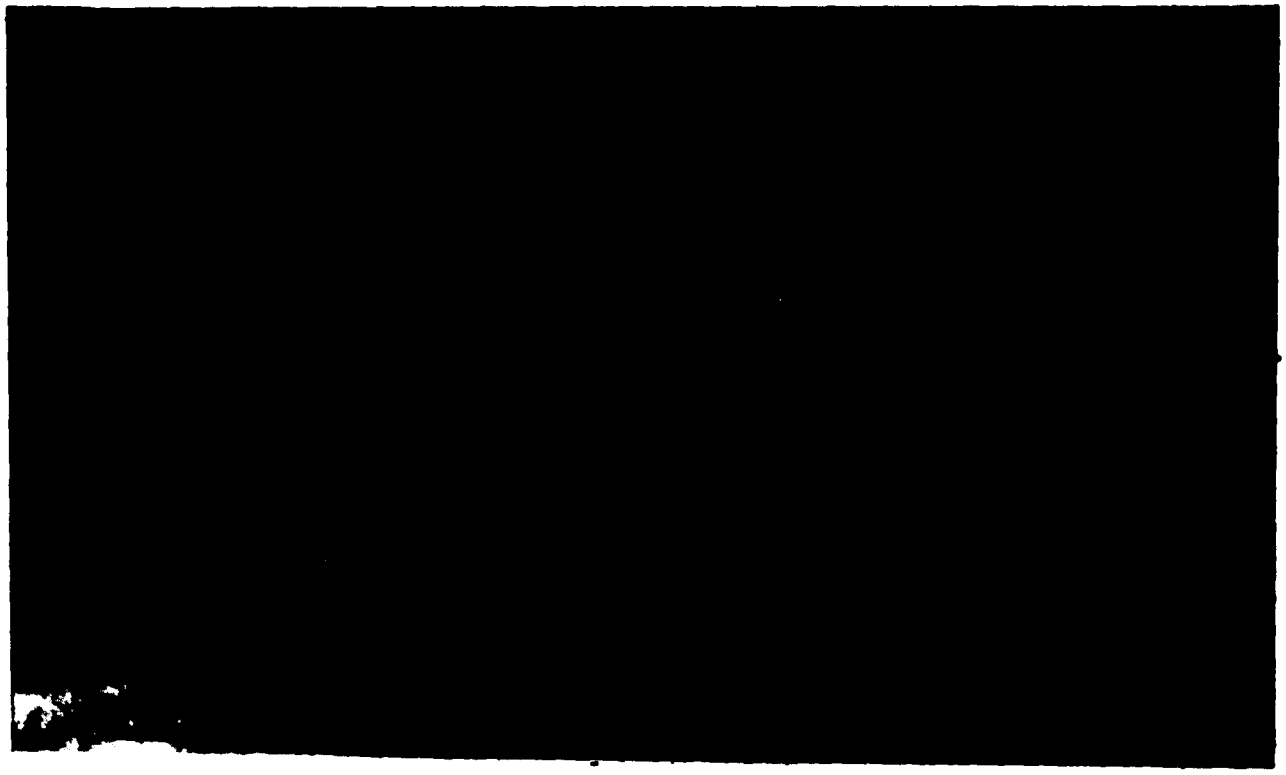

Fig. 4.5 Photograph of Surface Streamlines on the Flat Plate

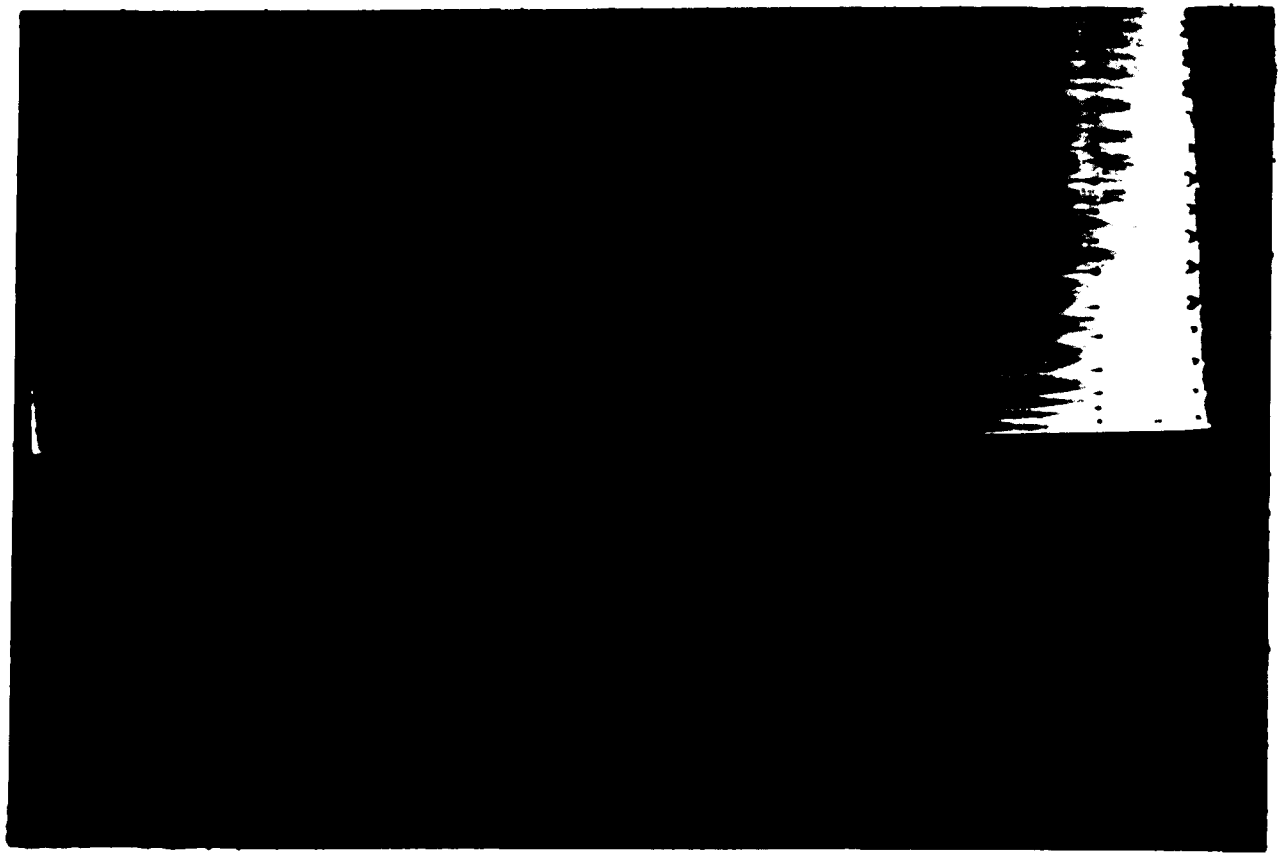

Fig. 4.6 Photograph of Surface Streamlines on the Airfoil

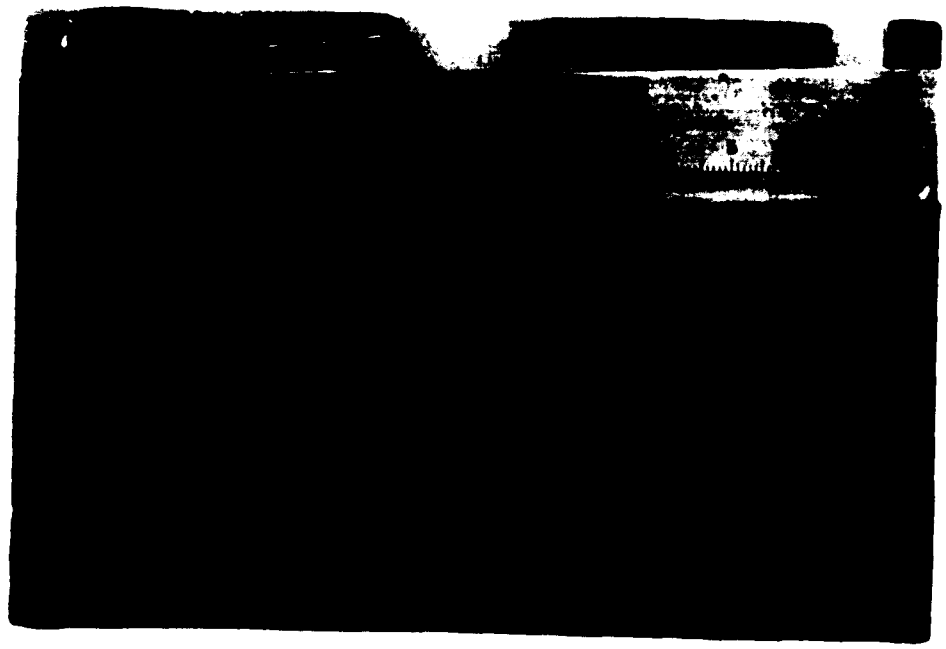

Fig. 4.7 Photograph of Surface Oilfilm Pattern on the Front Part of the Airfoil

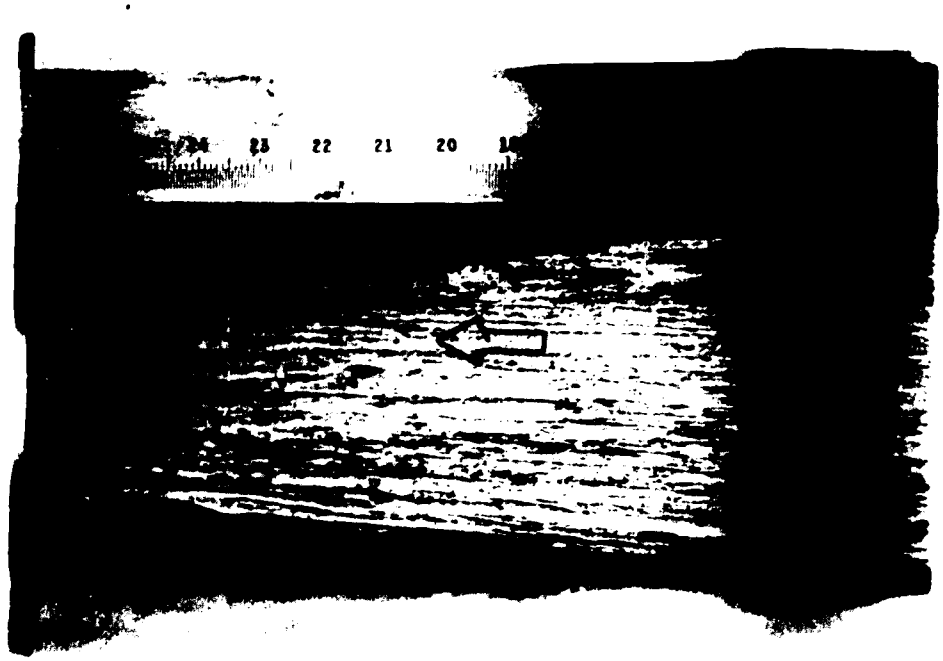

Fig. 4.8 Photograph of Surface Oilfilm Pattern on the Rear Part of the Airfoil

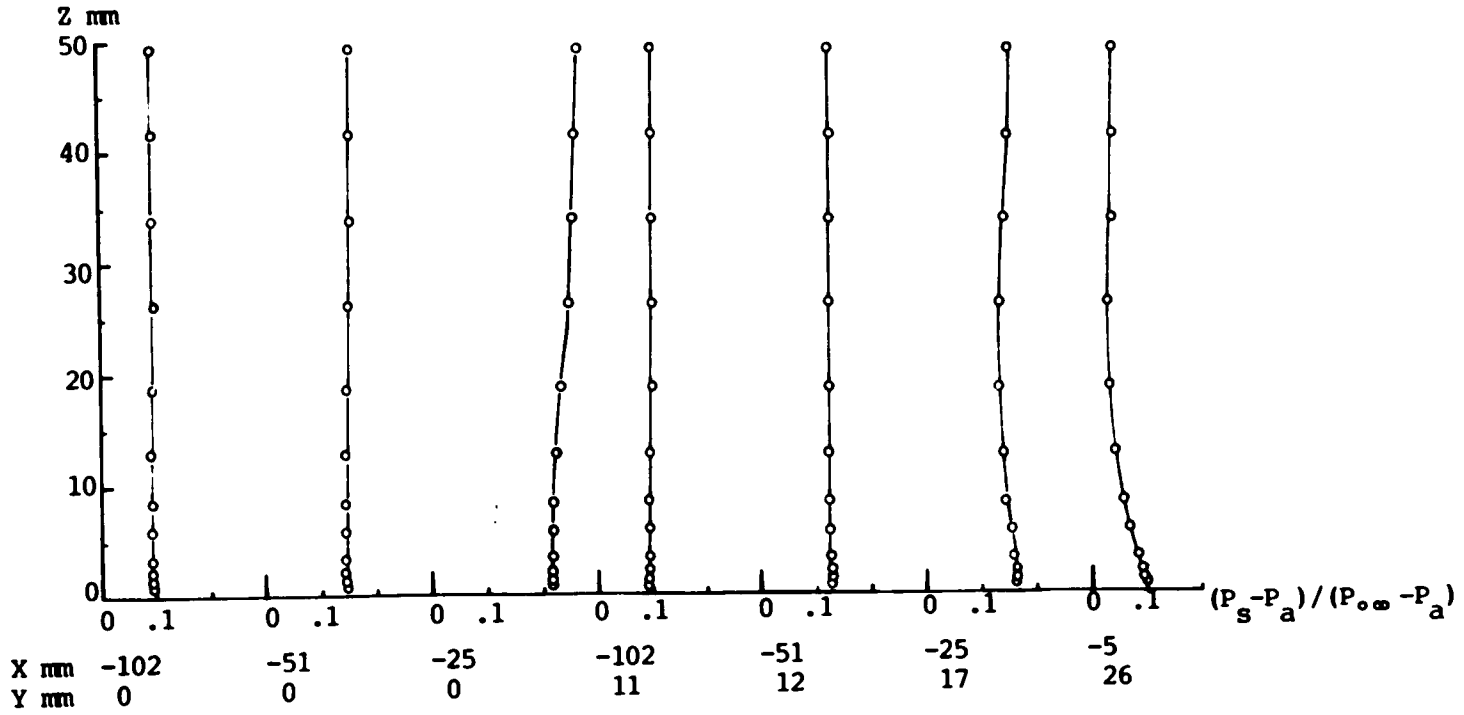

Fig. 4.9 Static Pressure Variation Upstream of the Airfoil

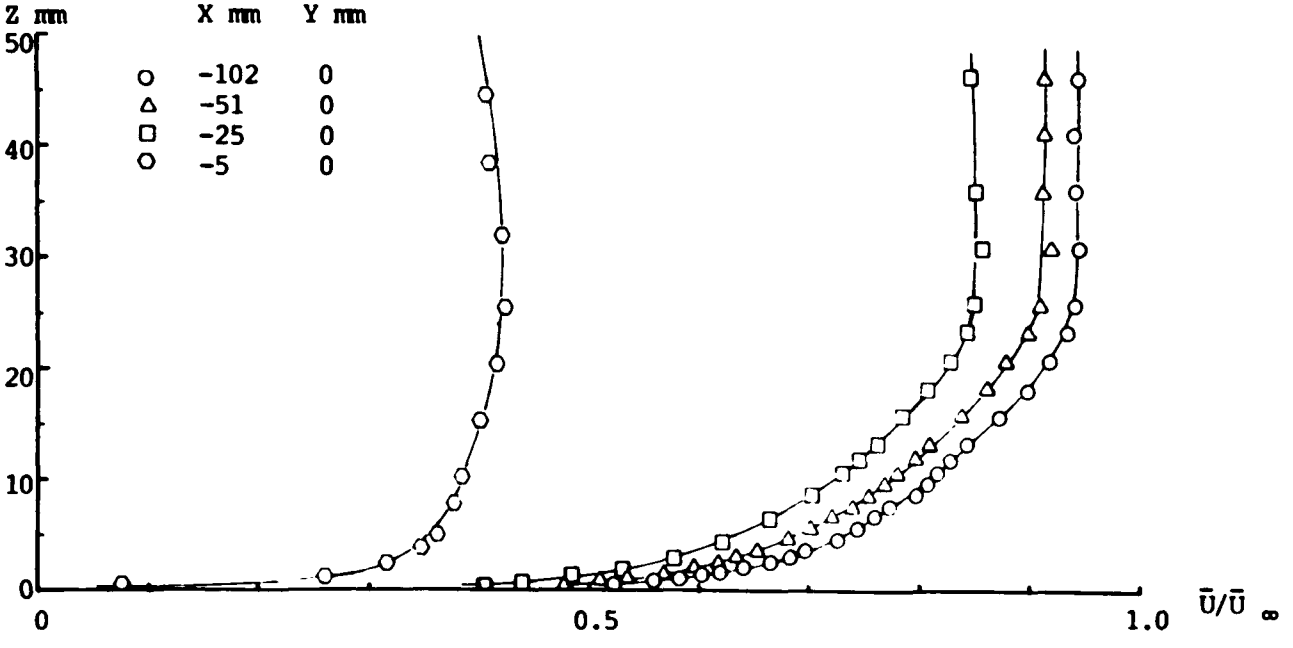

Fig. 4.10 Mean Velocity Profiles Upstream of the Airfoil

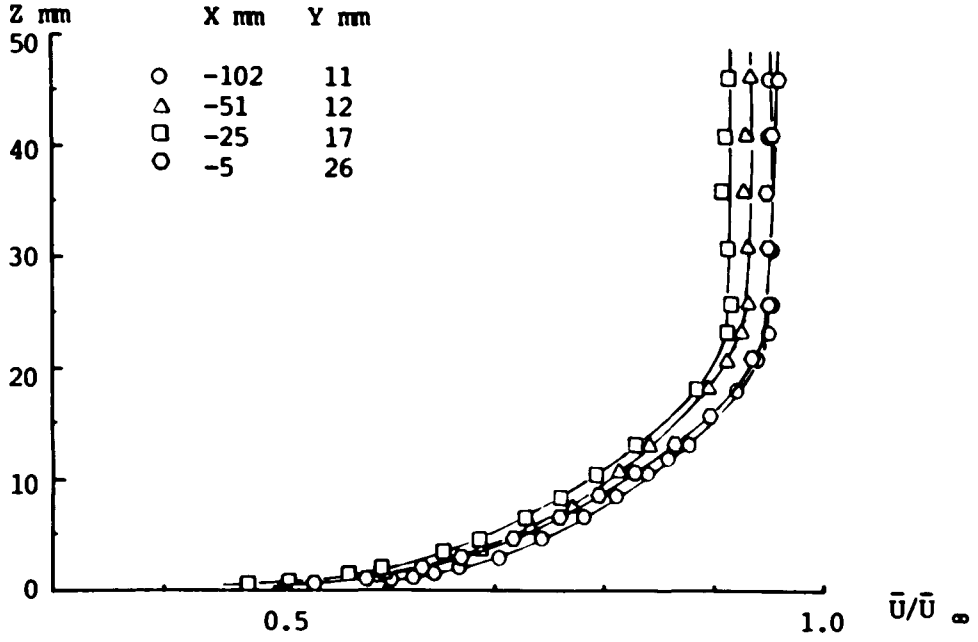

Fig. 4.11 Mean Velocity Profiles Upstream of the Airfoil

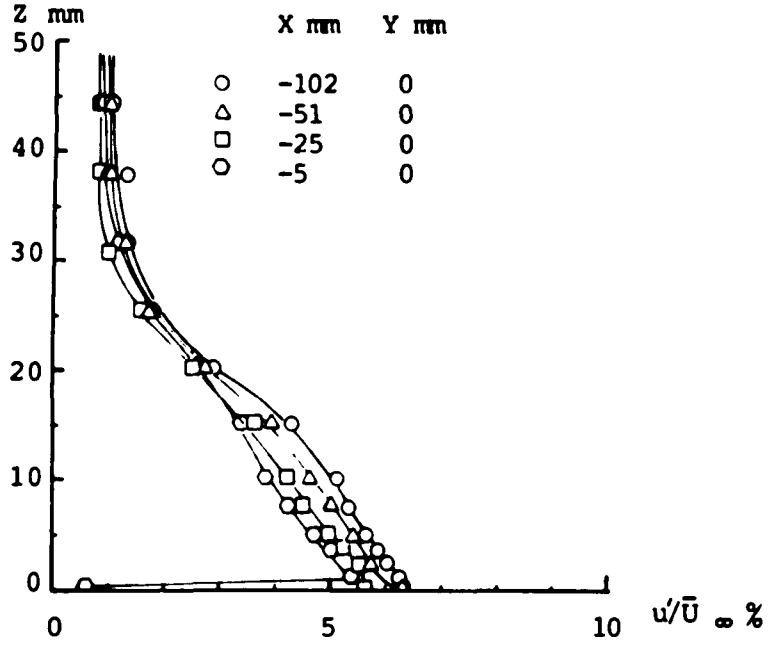

Fig. 4.12 Variation of Turbulence Intensity Upstream of the Airfoil

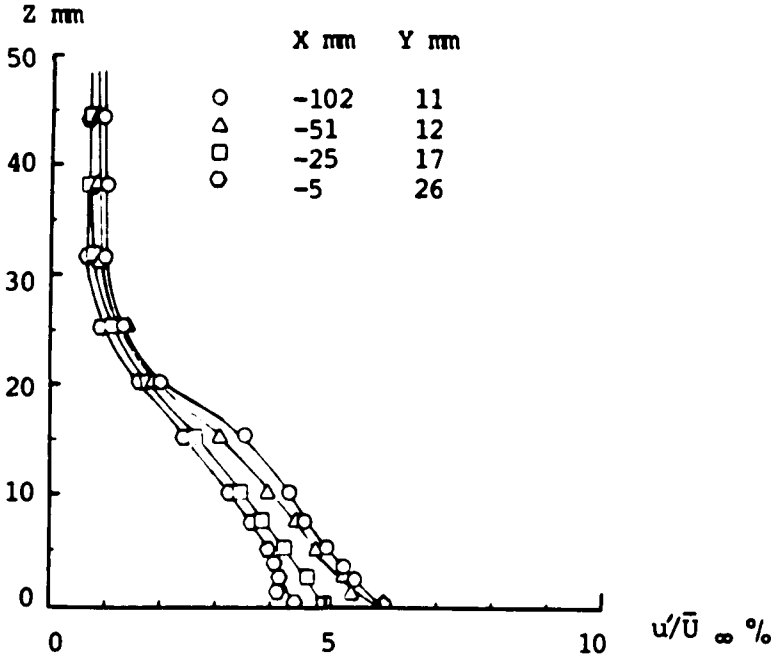

Fig. 4.13 Variation of Turbulence Intensity Upstream of the Airfoil

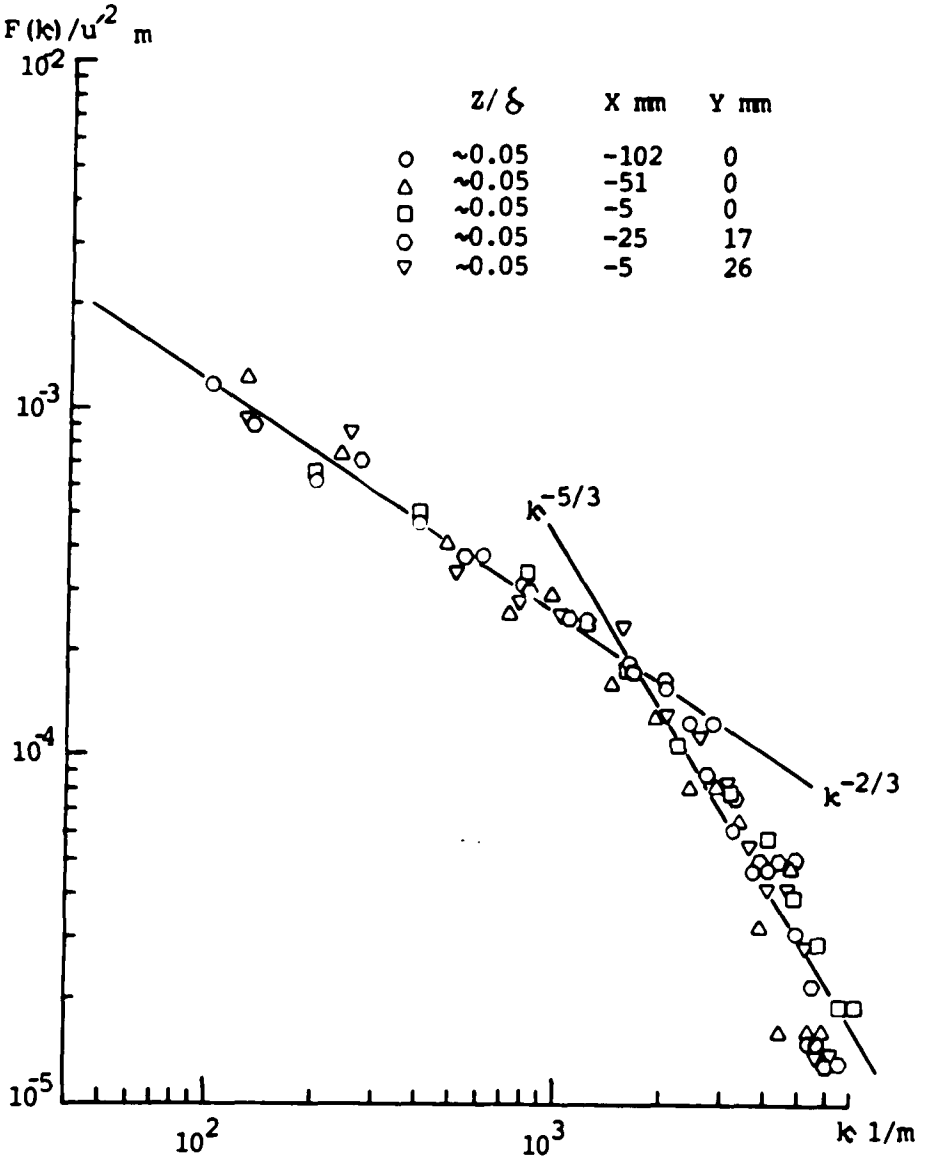

Fig. 4.14 Spectra of $\overline{u}^2$ in the Inner Region Upstream of the Airfoil

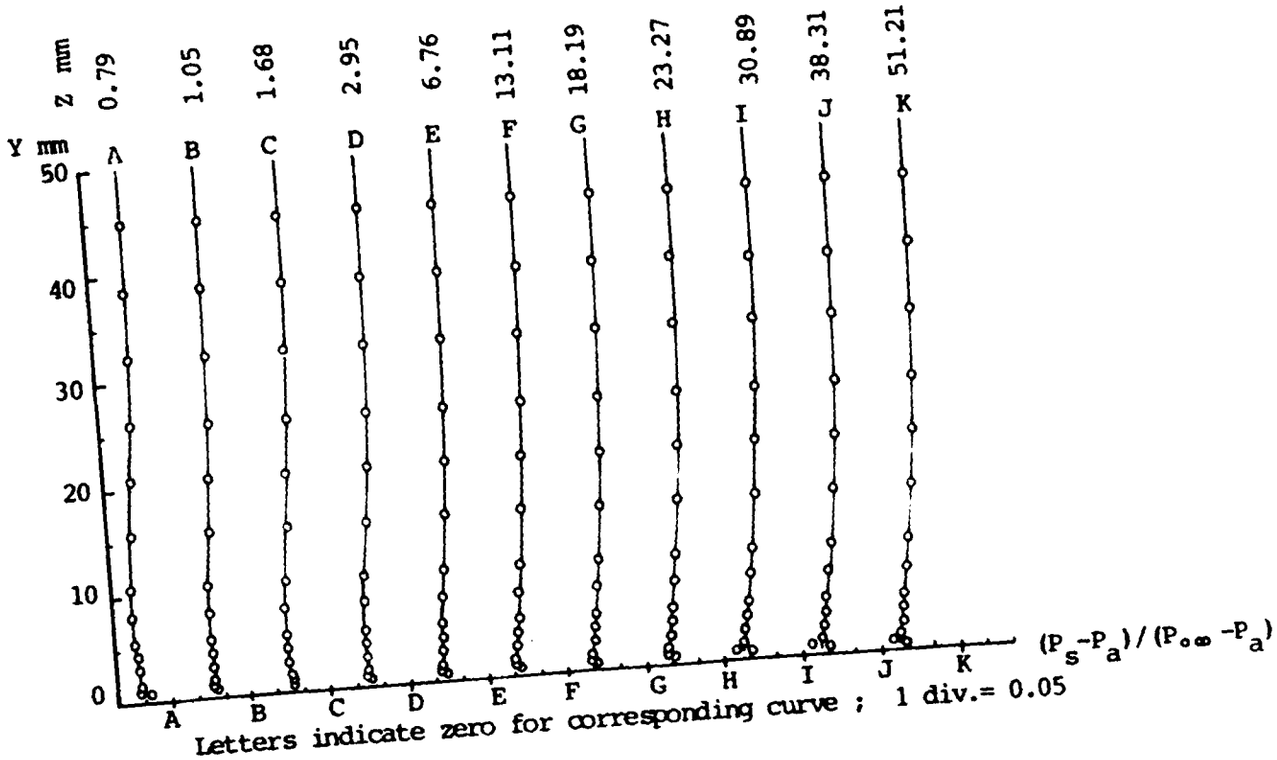

Fig. 4.15 Static Pressure Variation Parallel to the Flat Plate
X = 25 mm, X/C = 0.10

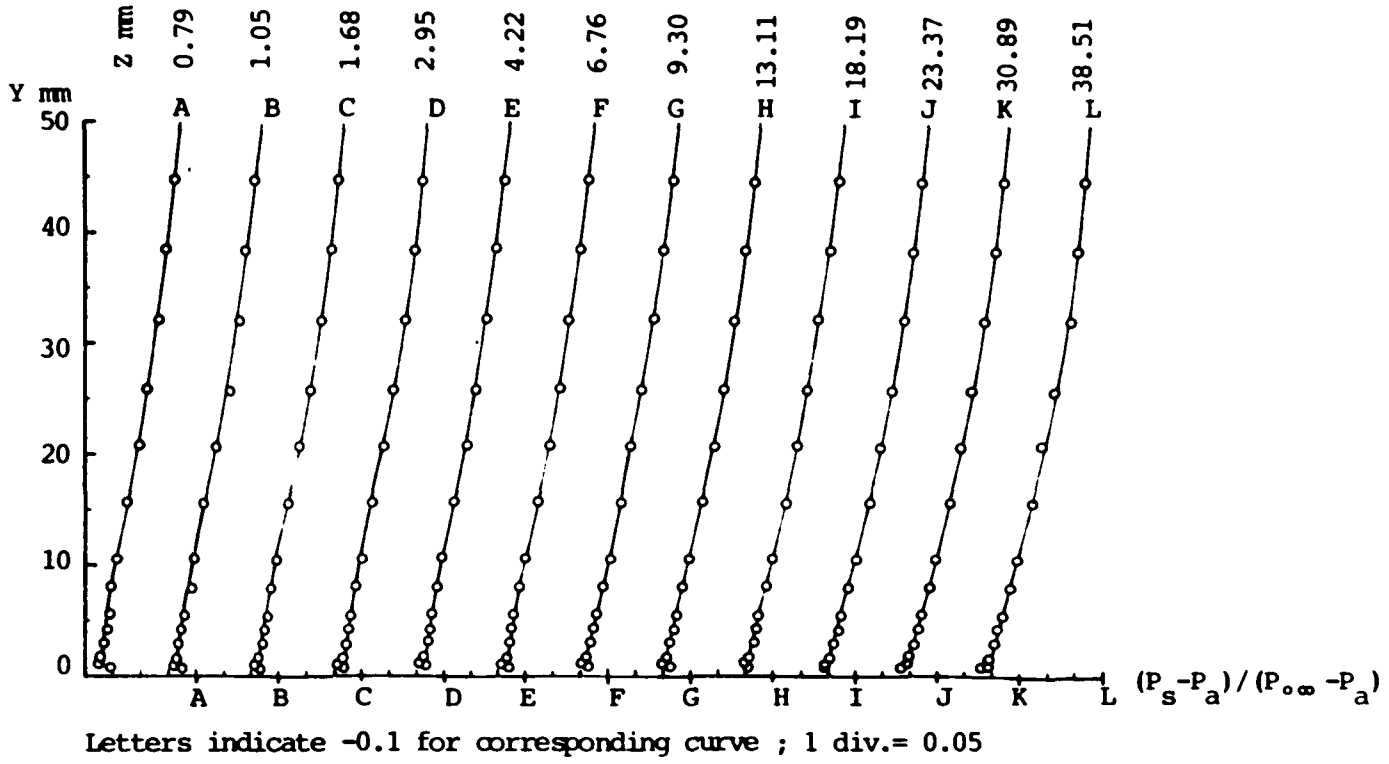

Fig. 4.16 Static Pressure Variation Parallel to the Flat Plate
X = 76 mm, X/C = 0.30

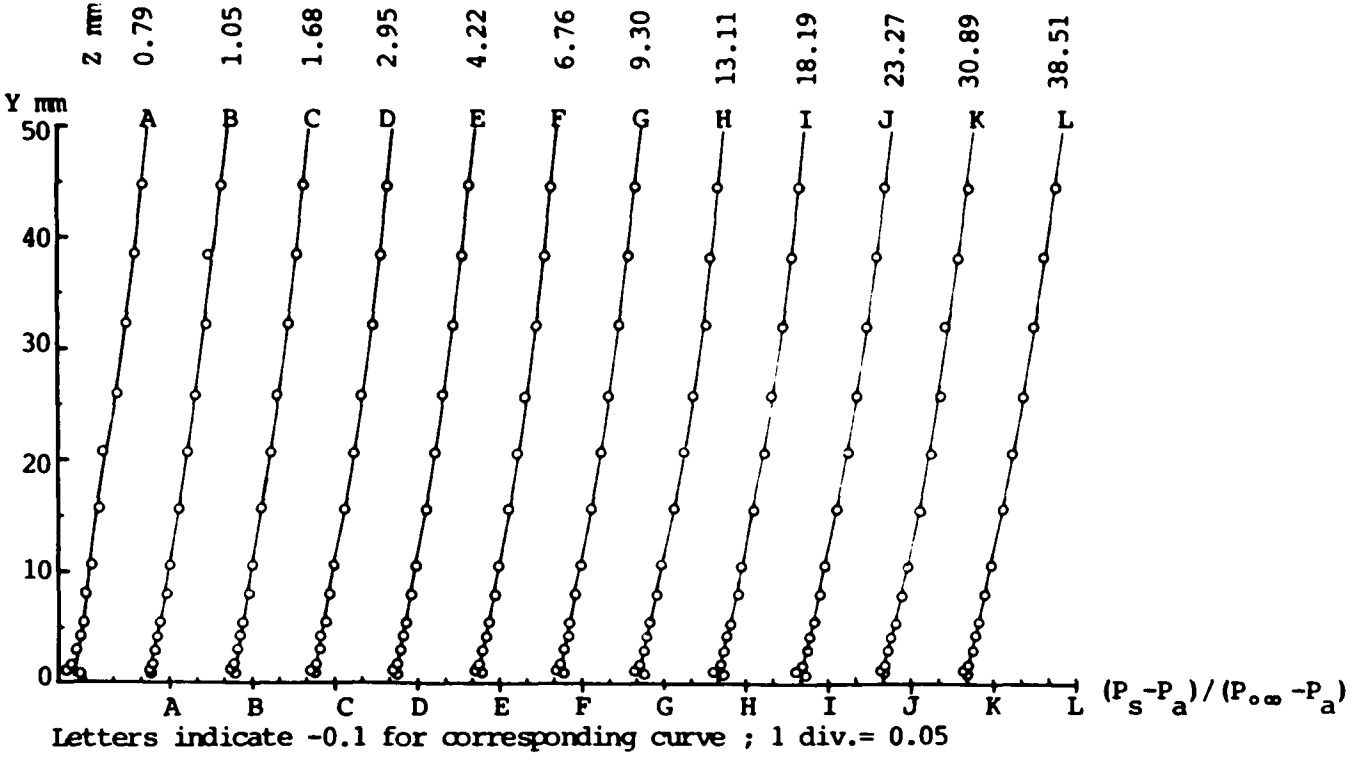

Fig. 4.17 Static Pressure Variation Parallel to the Flat Plate
X = 127 mm, X/C = 0.50

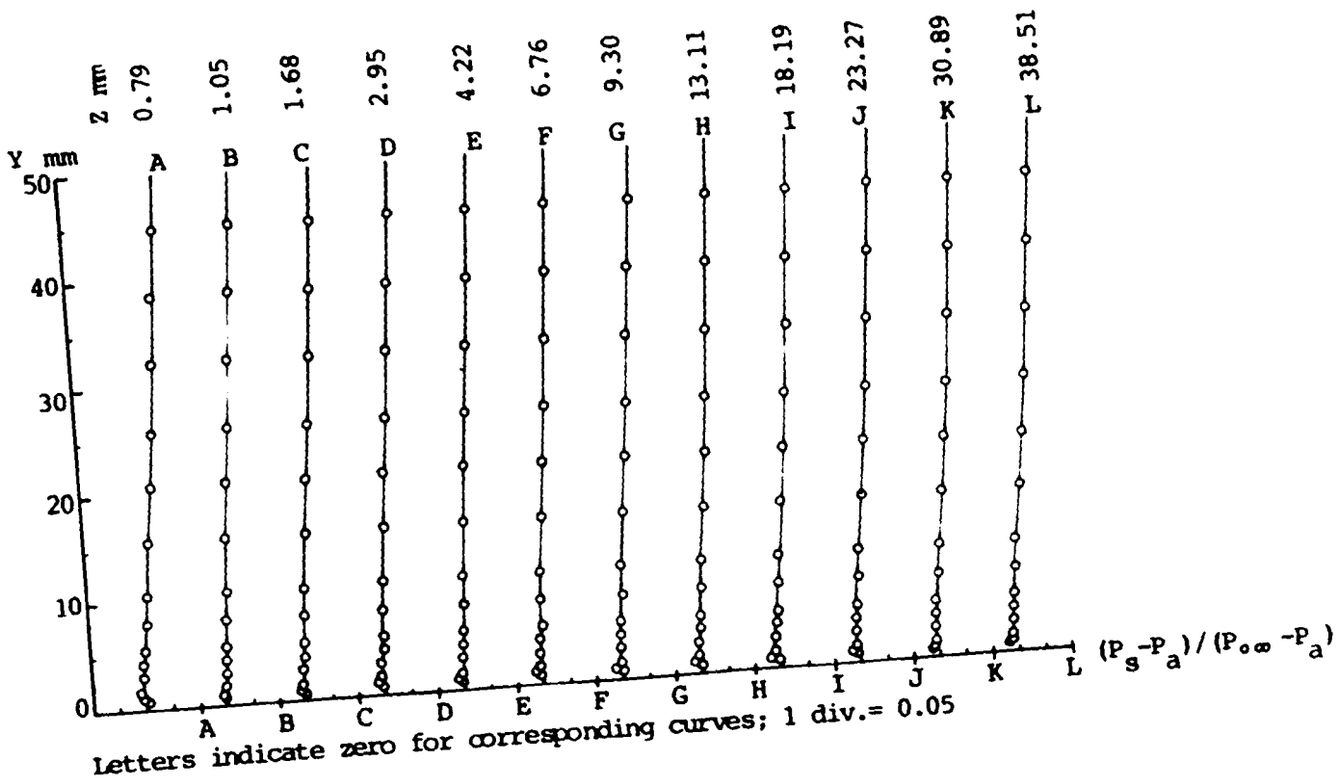

Fig. 4.18 Static Pressure Variation Parallel to the Flat Plate
X = 152 mm, X/C = 0.60

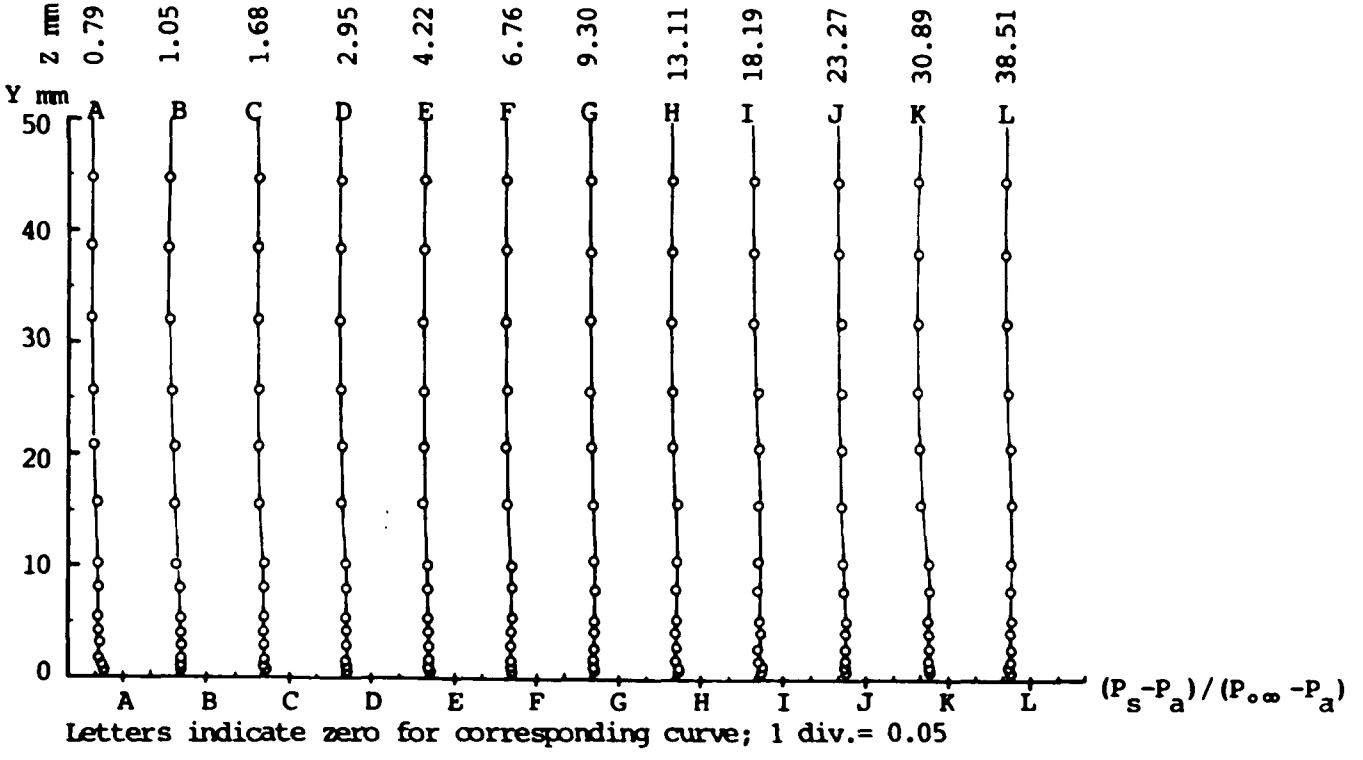

Fig. 4.19 Static Pressure Variation Parallel to the Flat Plate
X = 203 mm, X/C = 0.80

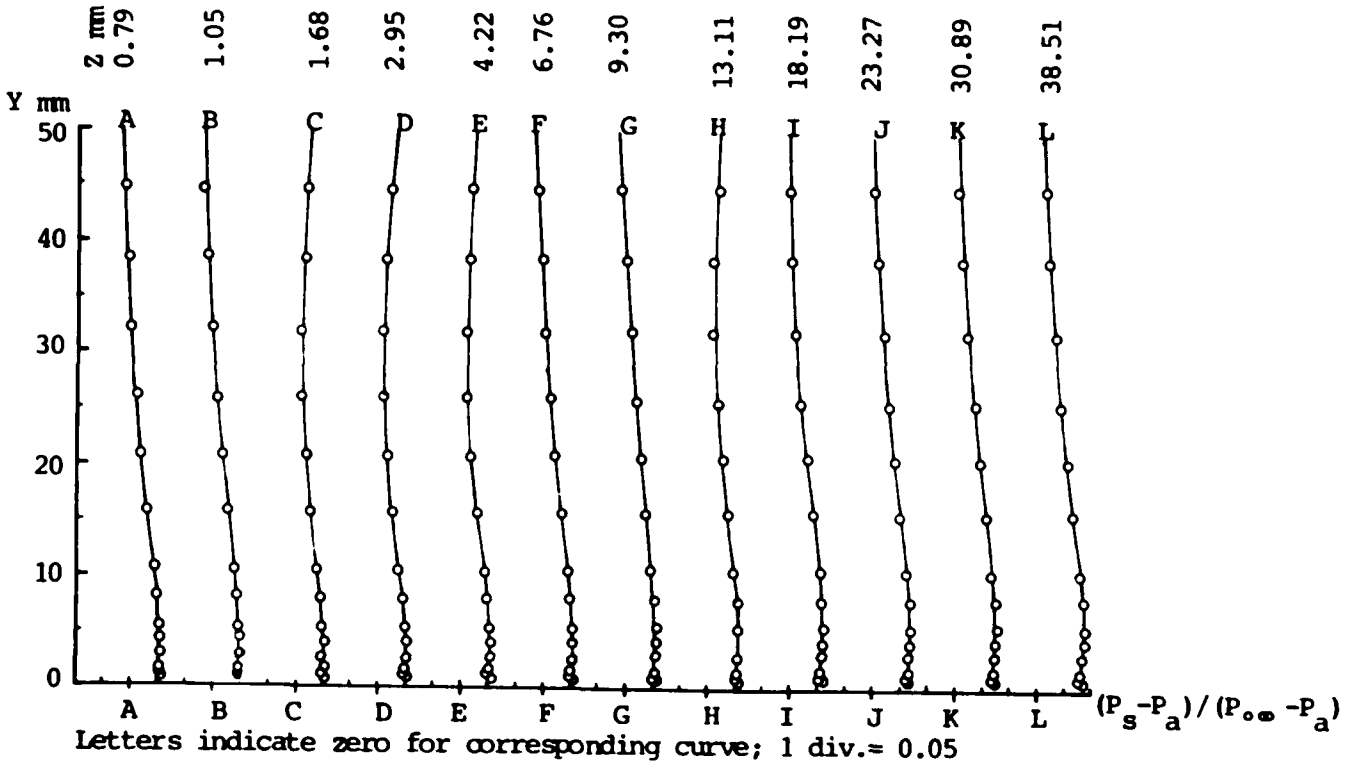

Fig. 4.20 Static Pressure Variation Parallel to the Flat Plate
X = 251 mm, X/C = 0.985

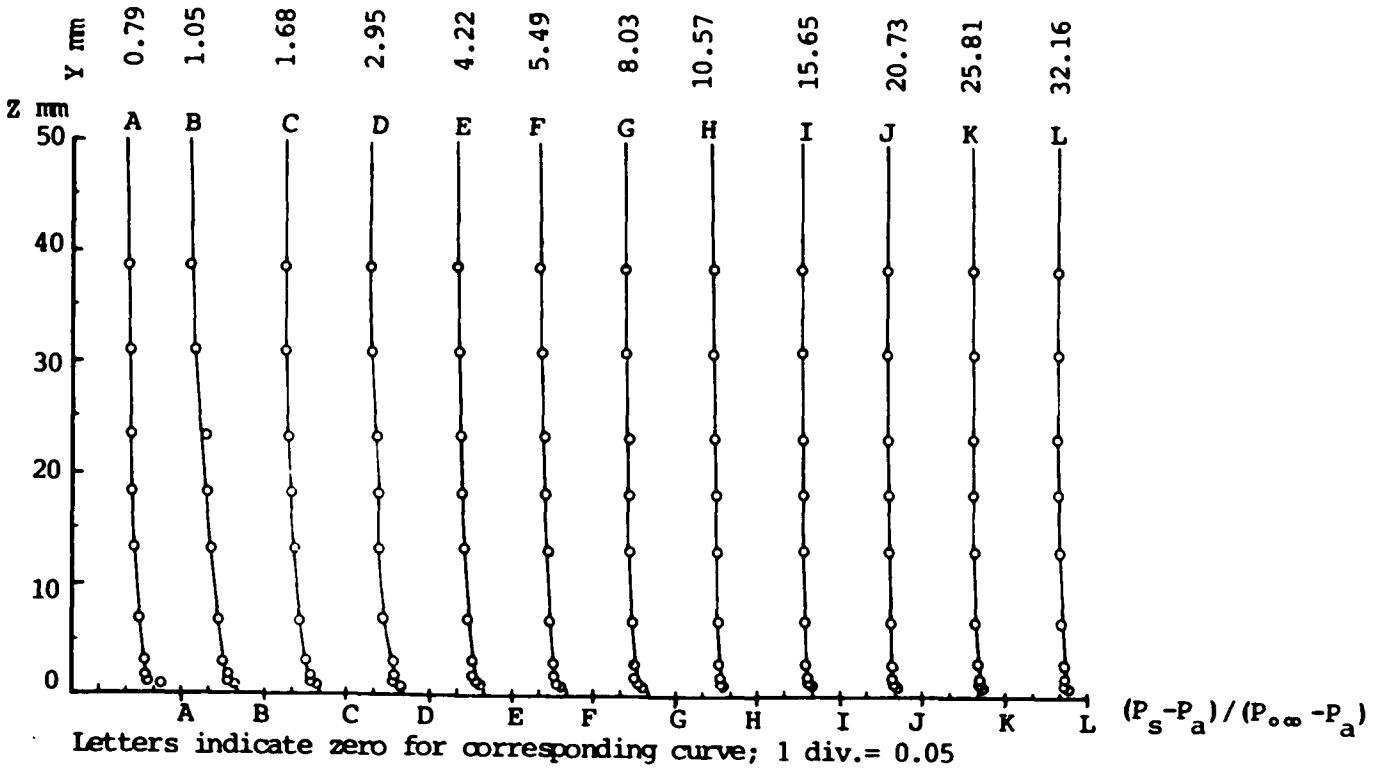

Fig. 4.21 Static Pressure Variation Parallel to the Airfoil
X = 25 mm, X/C = 0.10

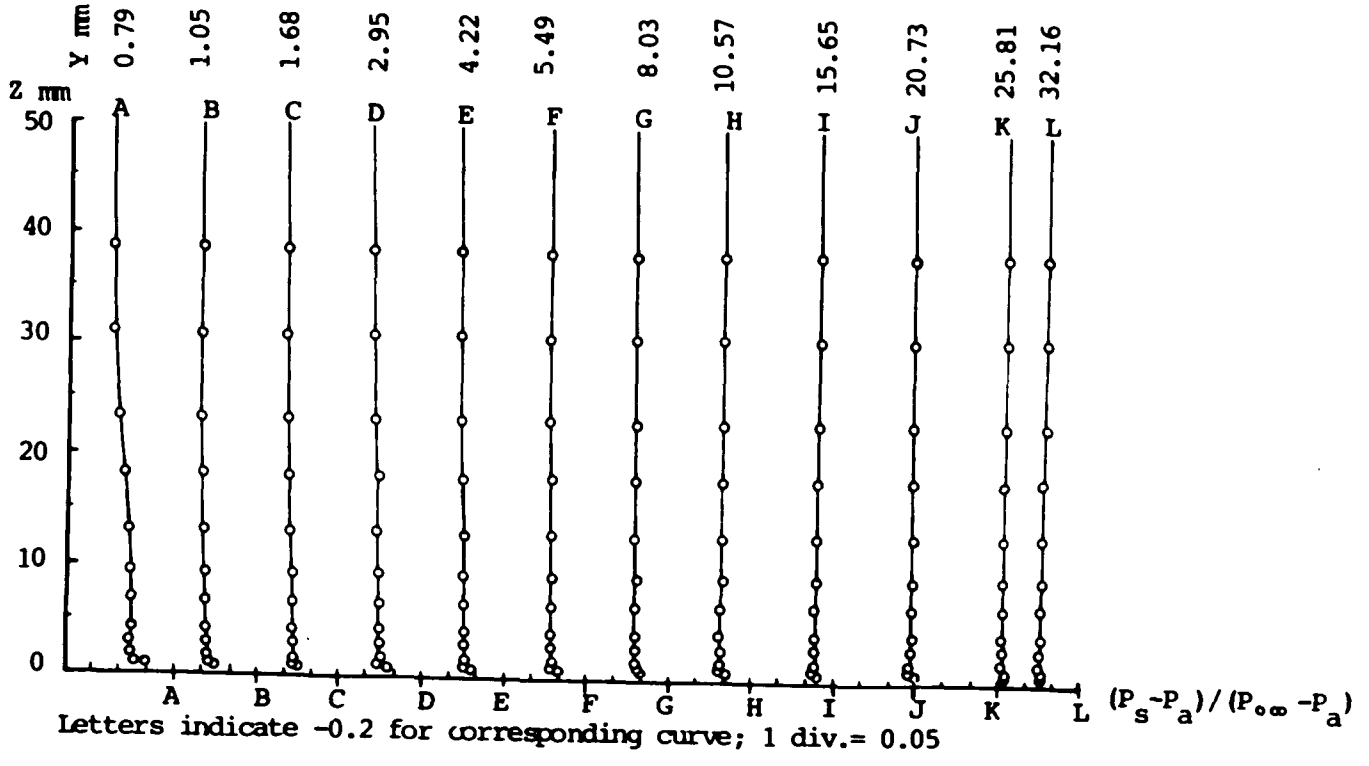

Fig. 4.22 Static Pressure Variation Parallel to the Airfoil
X = 76 mm, X/C = 0.30

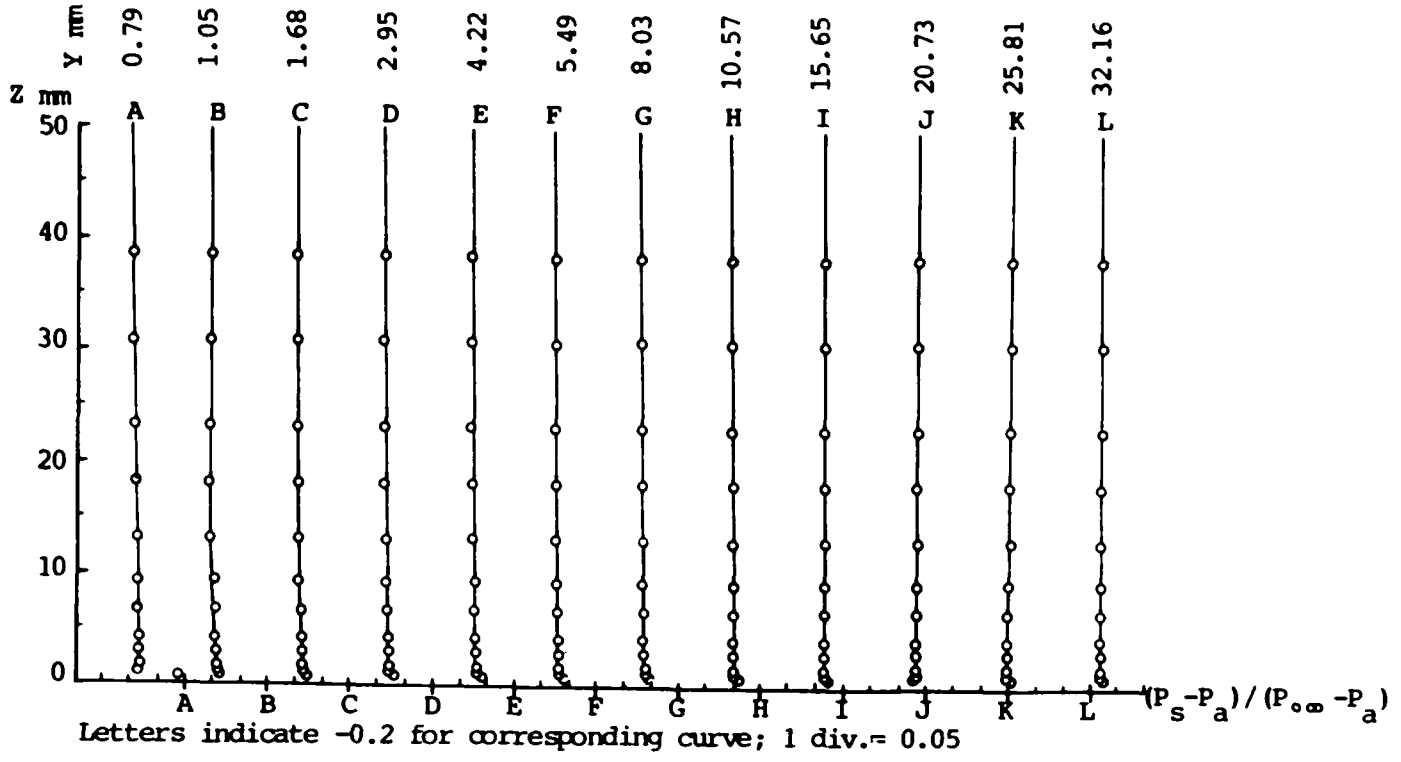

Fig. 4.23 Static Pressure Variation Parallel to the Airfoil
X = 127 mm, X/C = 0.50

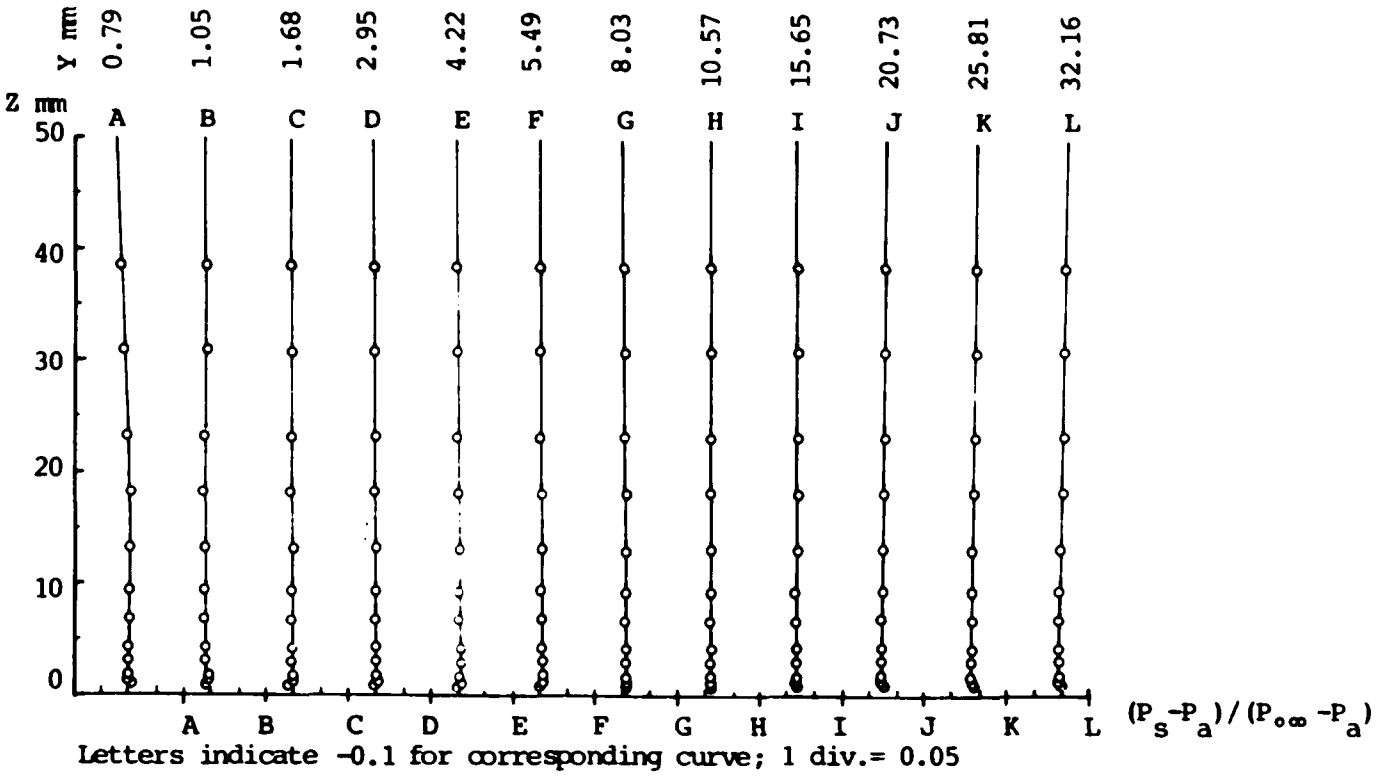

Fig. 4.24 Static Pressure Variation Parallel to the Airfoil
X = 152 mm, X/C = 0.60

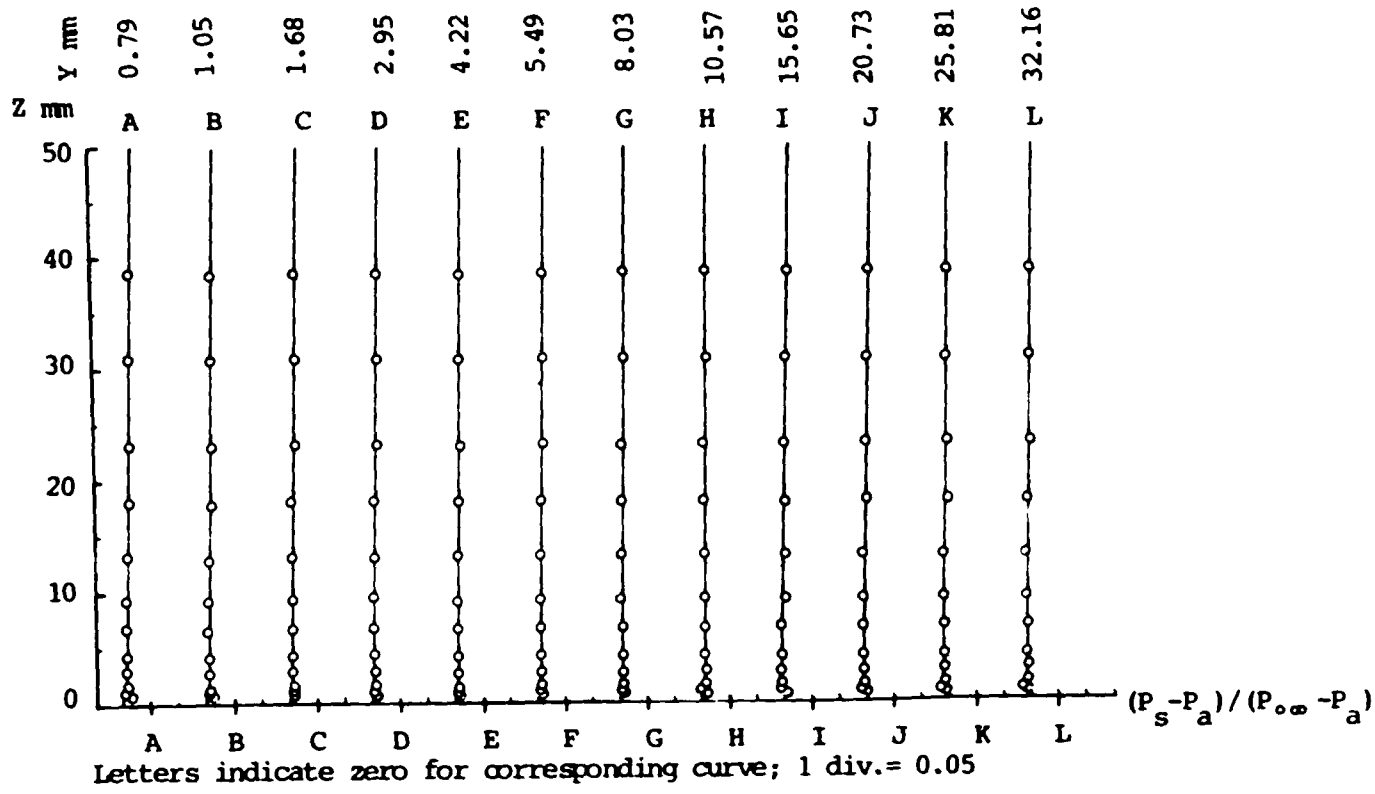

Fig. 4.25 Static Pressure Variation Parallel to the Airfoil
X = 203 mm, X/C = 0.80

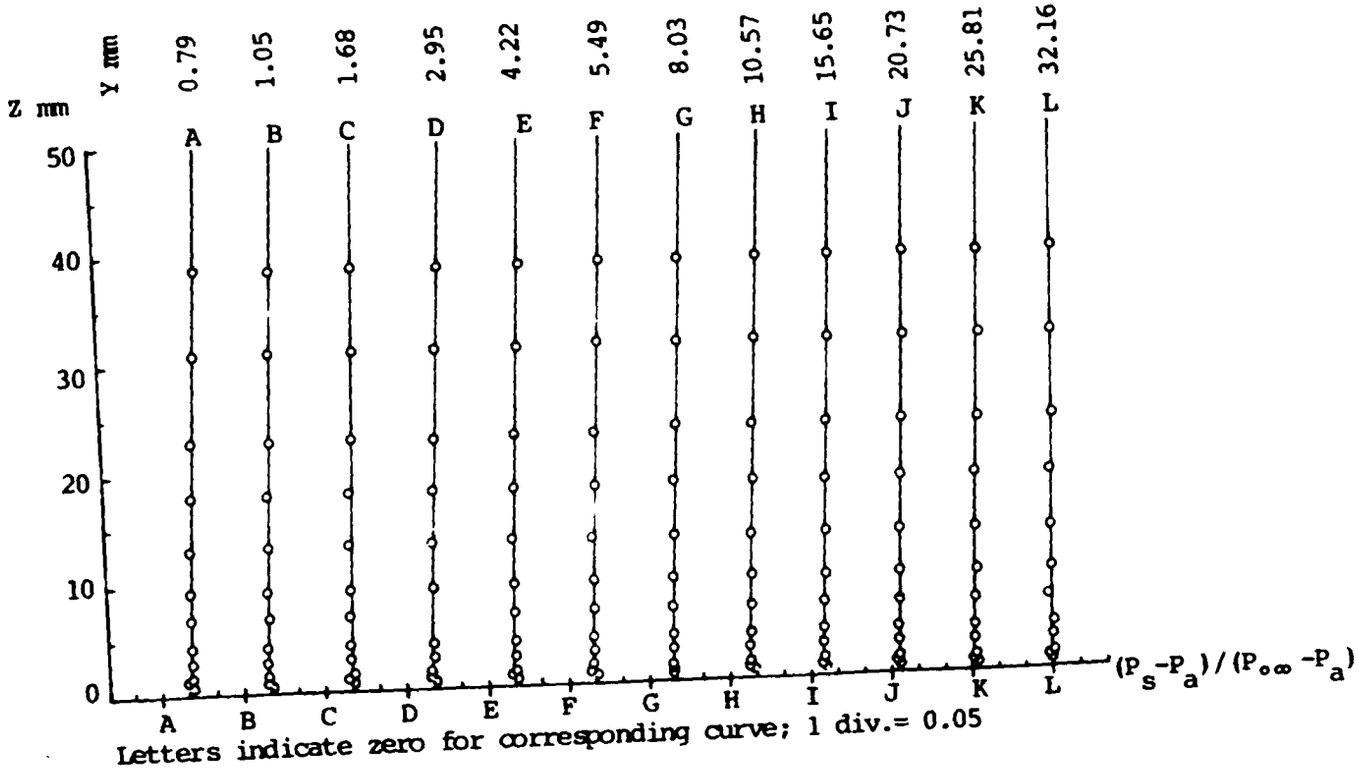

Fig. 4.26 Static Pressure Variation Parallel to the Airfoil
X = 251 mm, X/C = 0.985

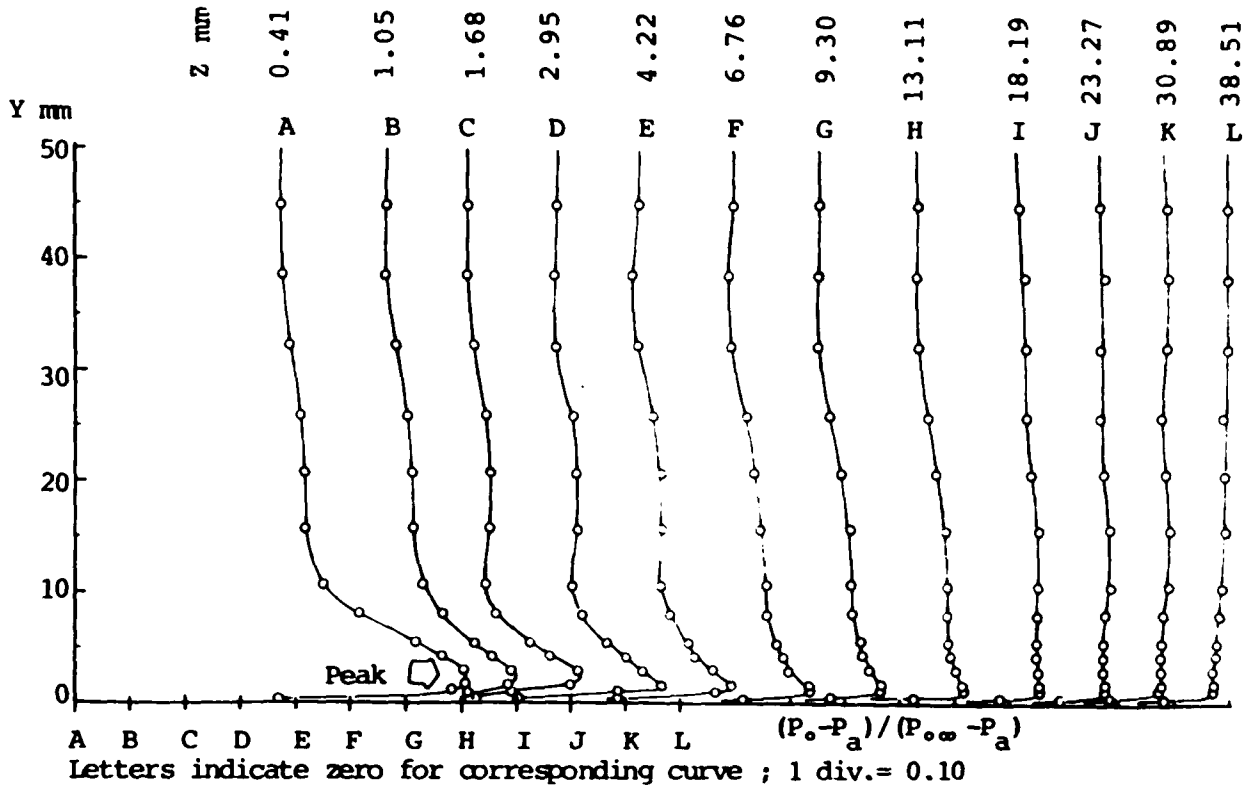

Fig. 4.27 Total Pressure Variation Parallel to the Flat Plate
X = 25 mm, X/C = 0.10

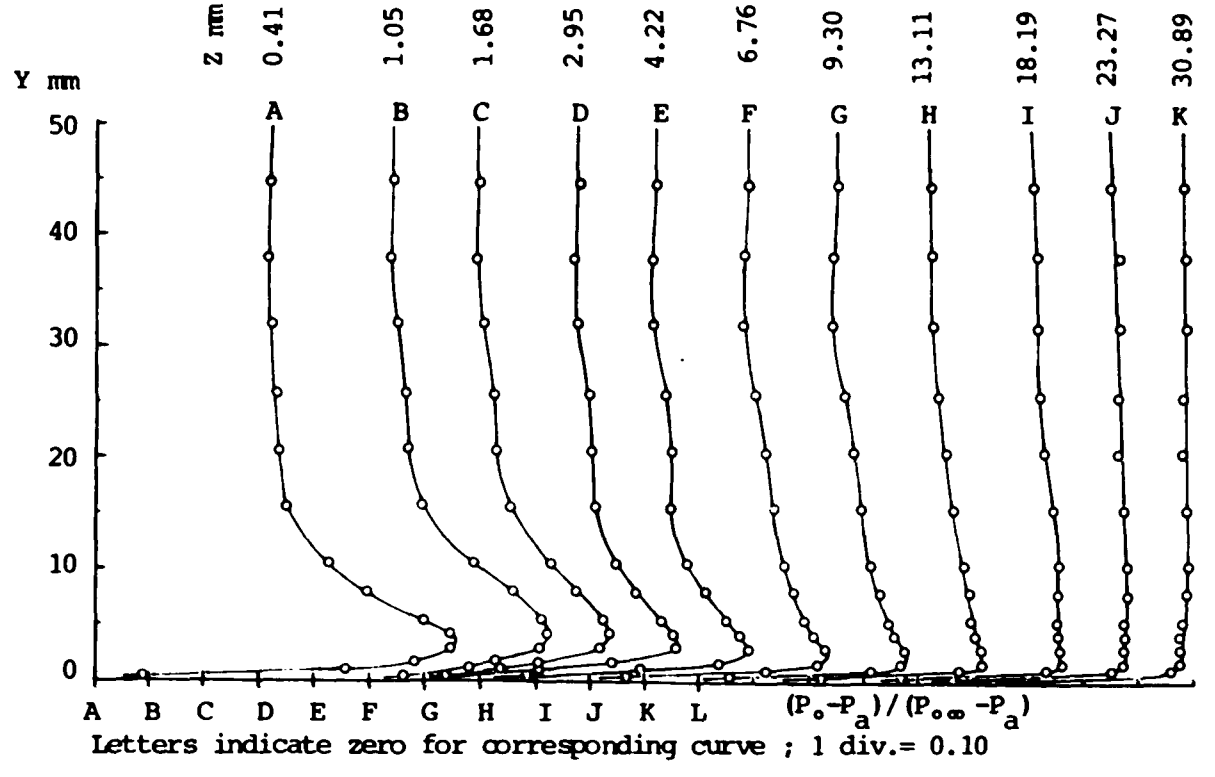

Fig. 4.28 Total Pressure Variation Parallel to the Flat Plate
X = 76 mm, X/C = 0.30

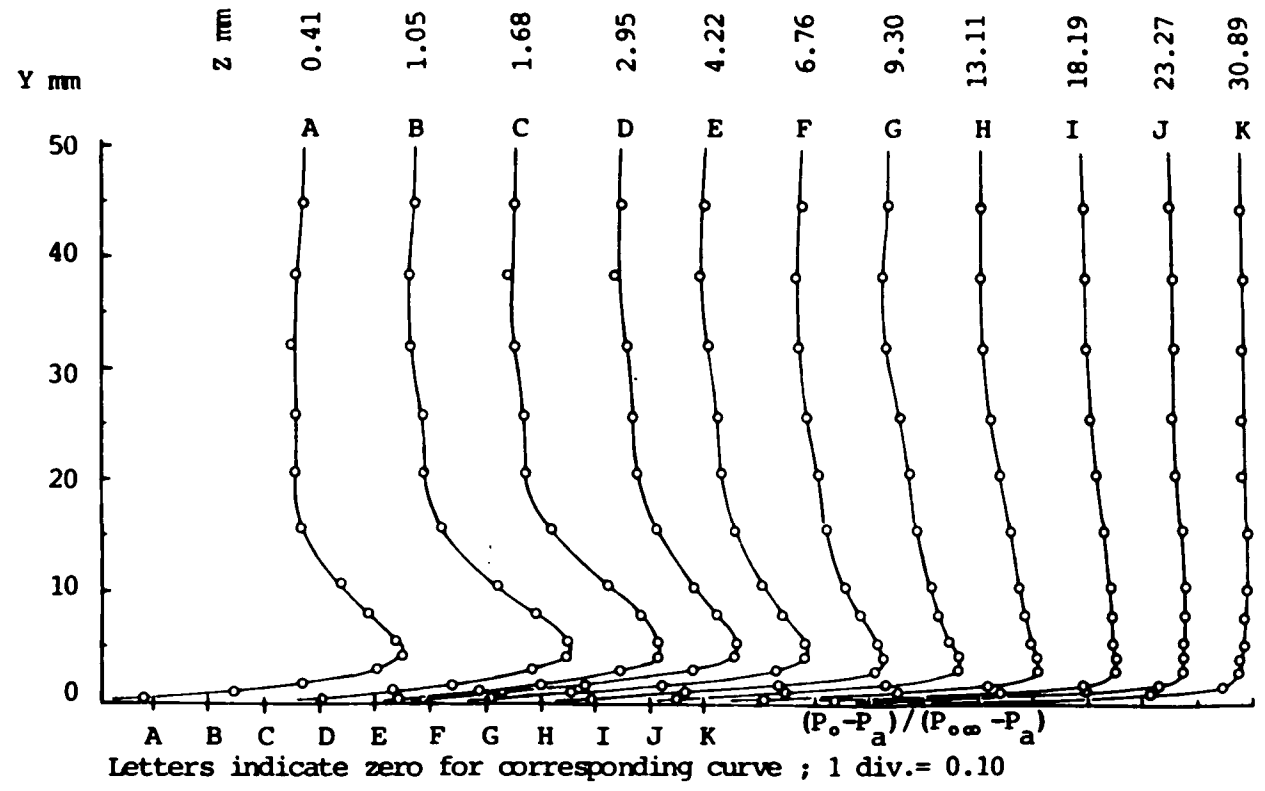

Fig. 4.29 Total Pressure Variation Parallel to the Flat Plate
X = 127 mm, X/C = 0.50

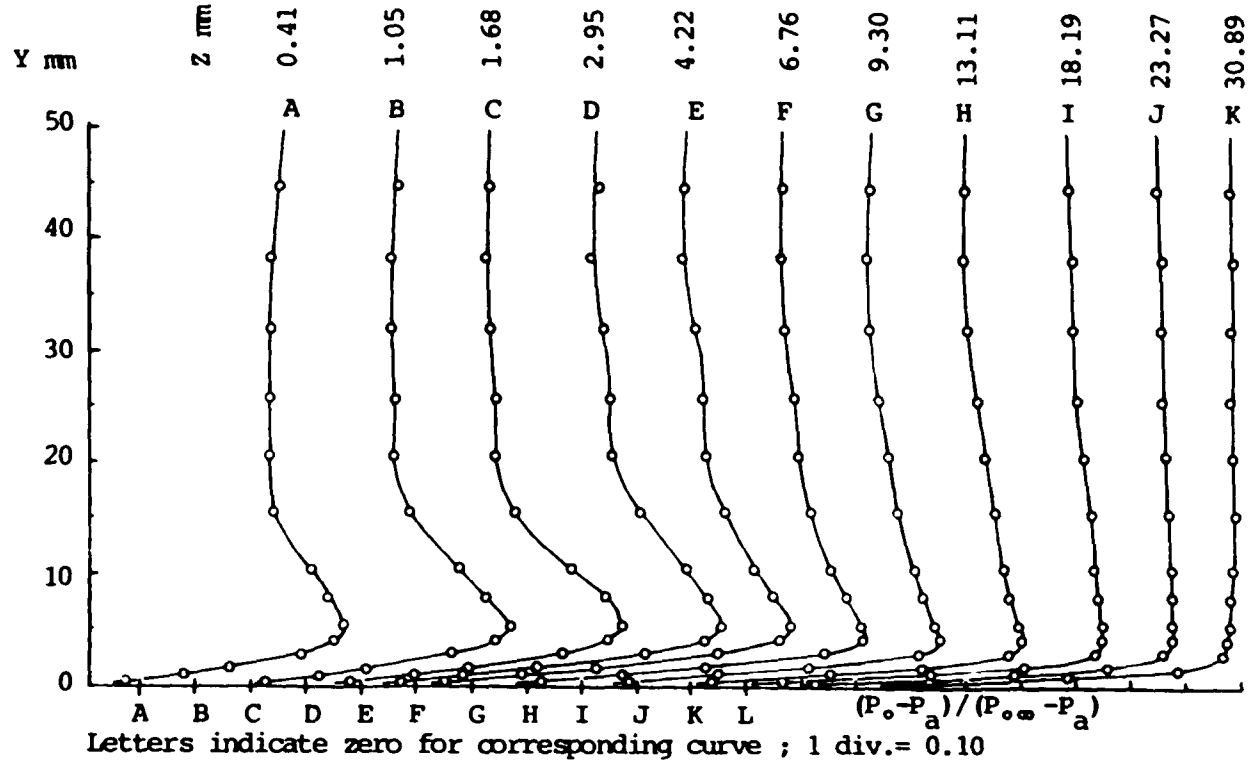

Fig. 4.30 Total Pressure Variation Parallel to the Flat Plate
X = 152 mm, X/C = 0.60

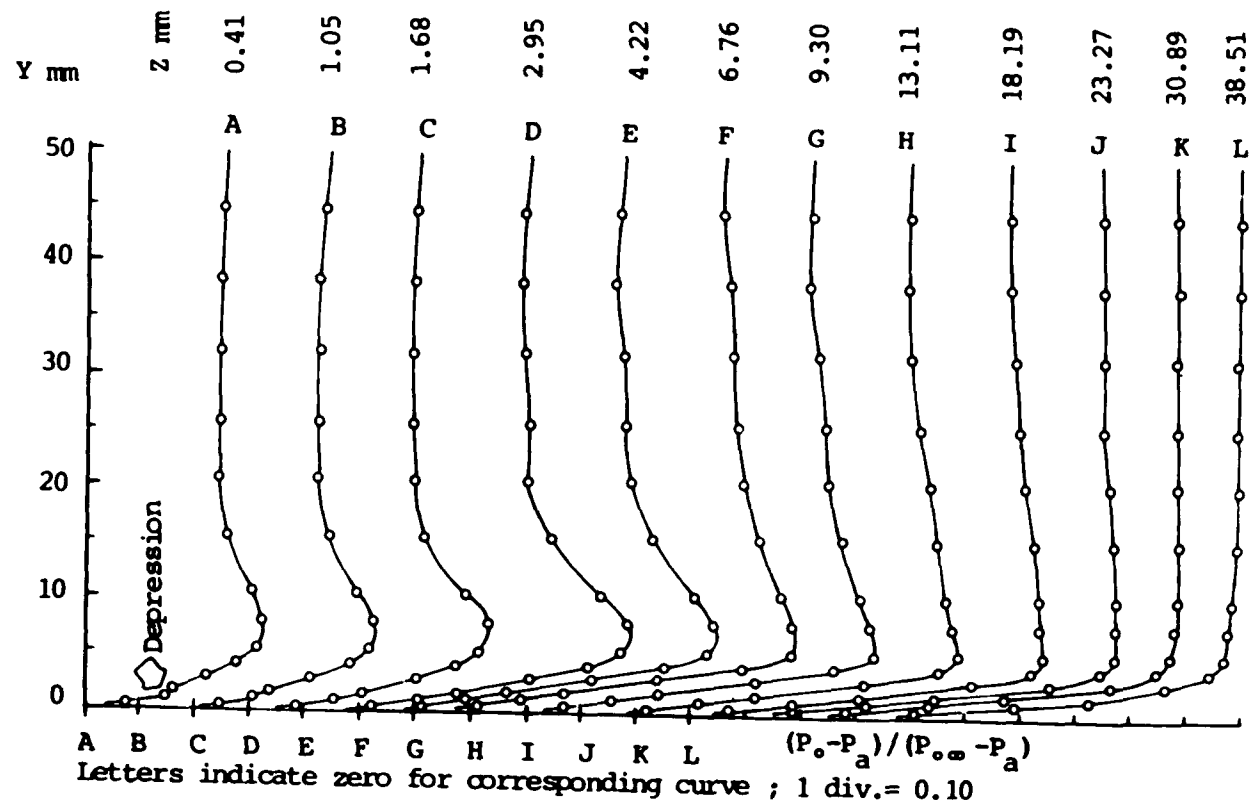

Fig. 4.31 Total Pressure Variation Parallel to the Flat Plate
X = 203 mm, X/C = 0.80

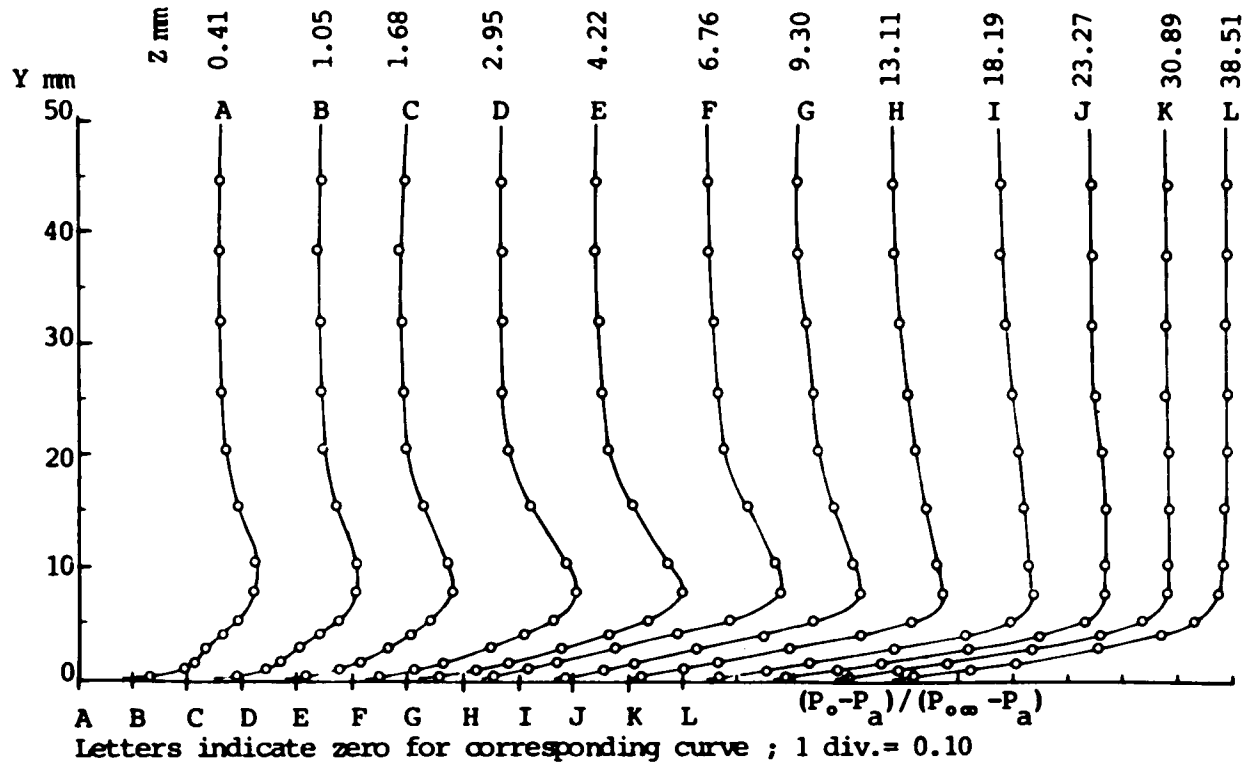

Fig. 4.32 Total Pressure Variation Parallel to the Flat Plate
X = 251 mm, X/C = 0.985

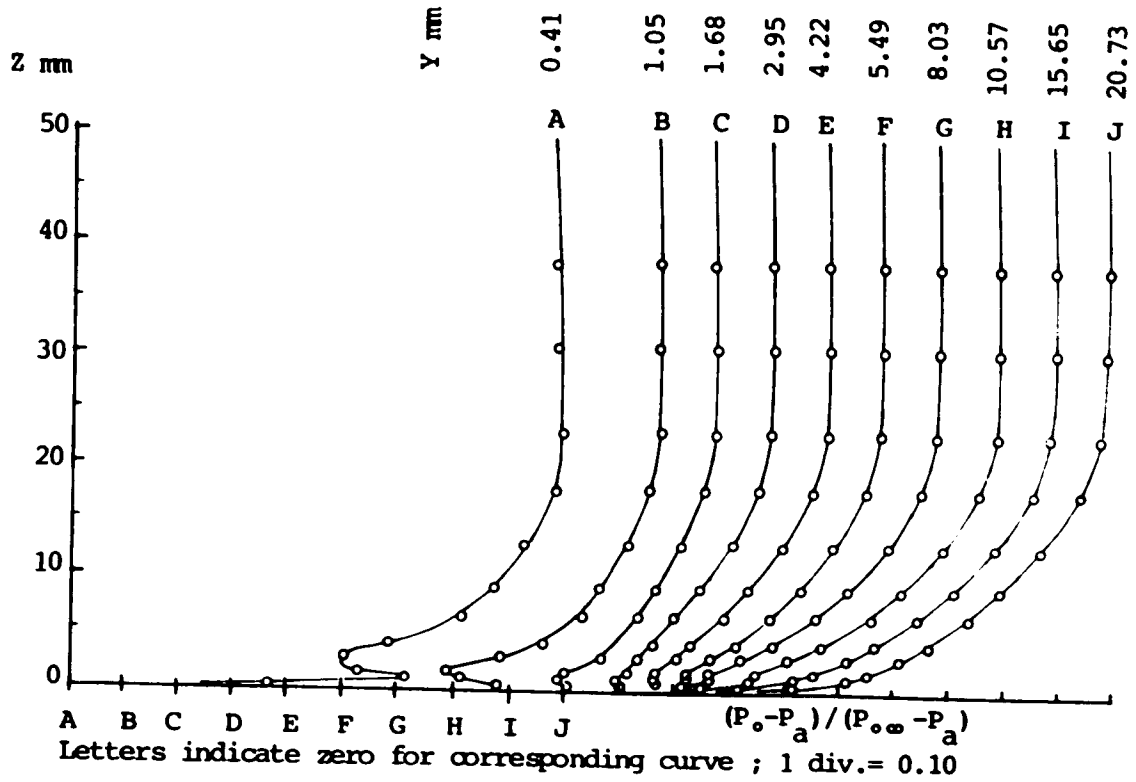

Fig. 4.33 Total Pressure Variation Parallel to the Airfoil
X = 25 mm, X/C = 0.10

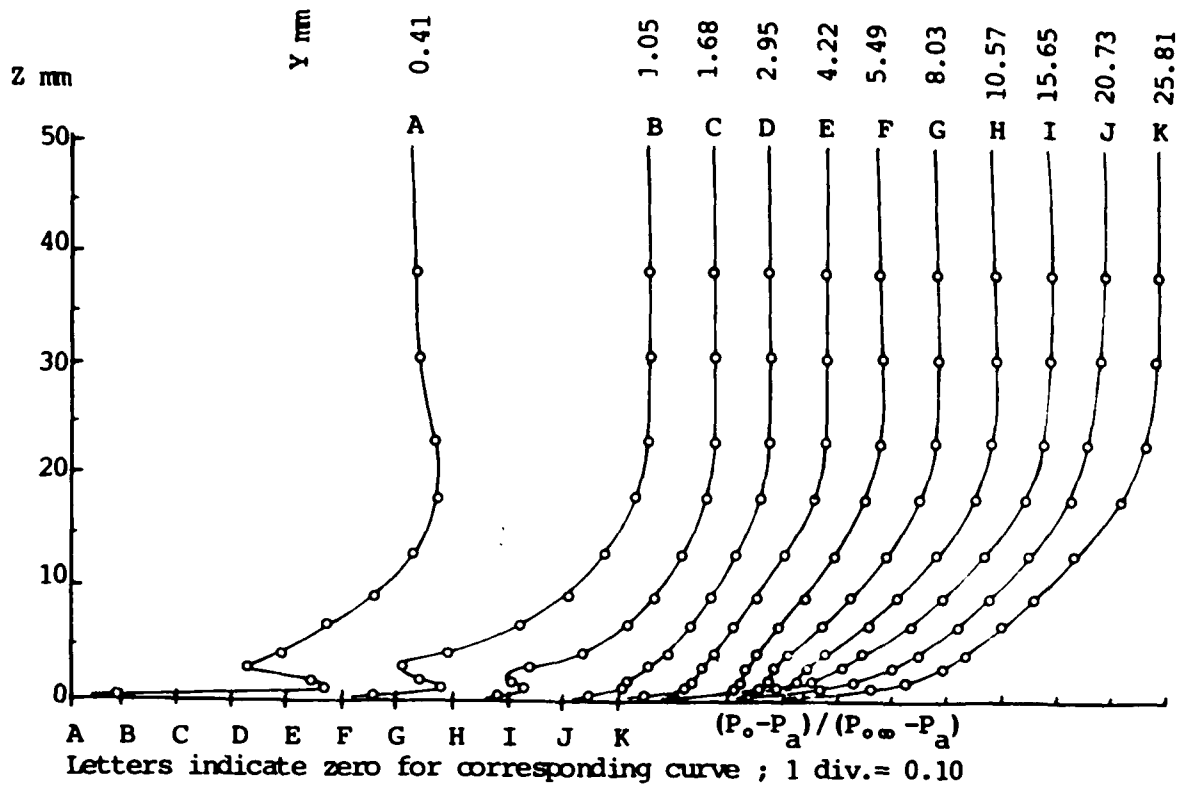

Fig. 4.34 Total Pressure Variation Parallel to the Airfoil
X = 76 mm, X/C = 0.30

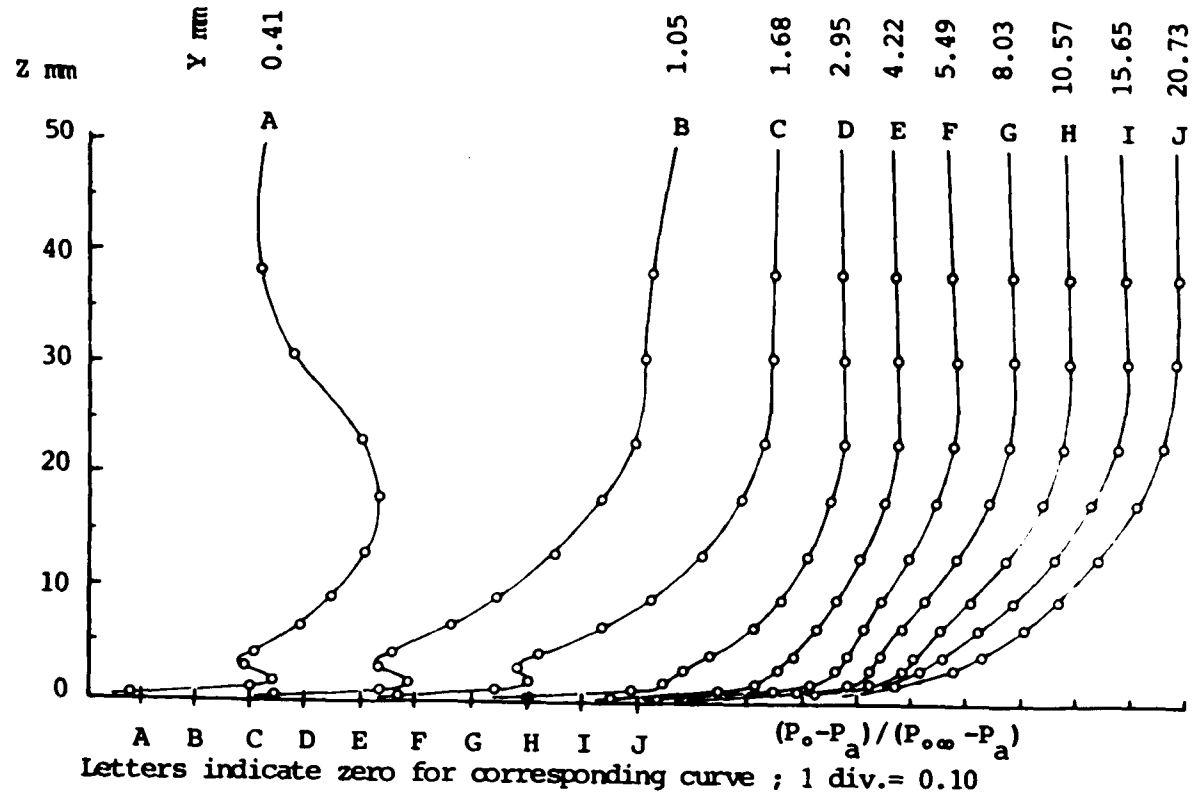

Fig. 4.35 Total Pressure Variation Parallel to the Airfoil
X = 127 mm, X/C = 0.50

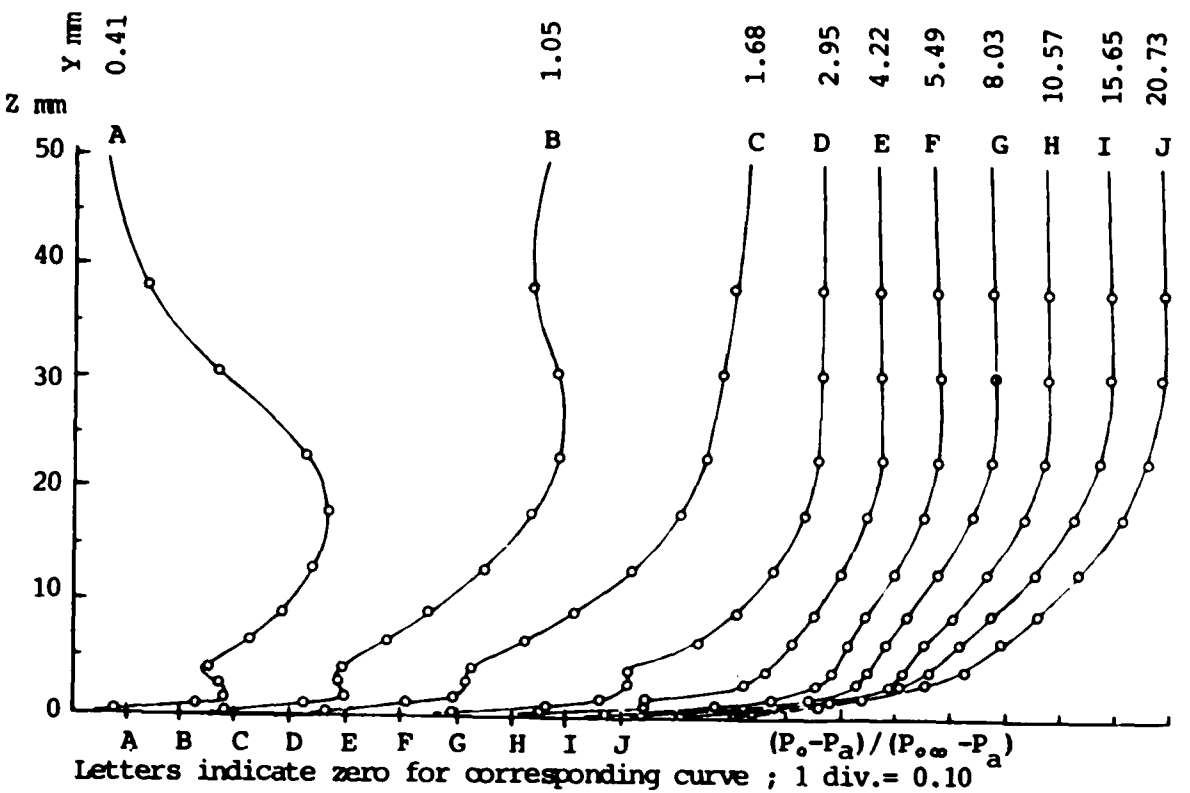

Fig. 4.36 Total Pressure Variation Parallel to the Airfoil
X = 152 mm, X/C = 0.60

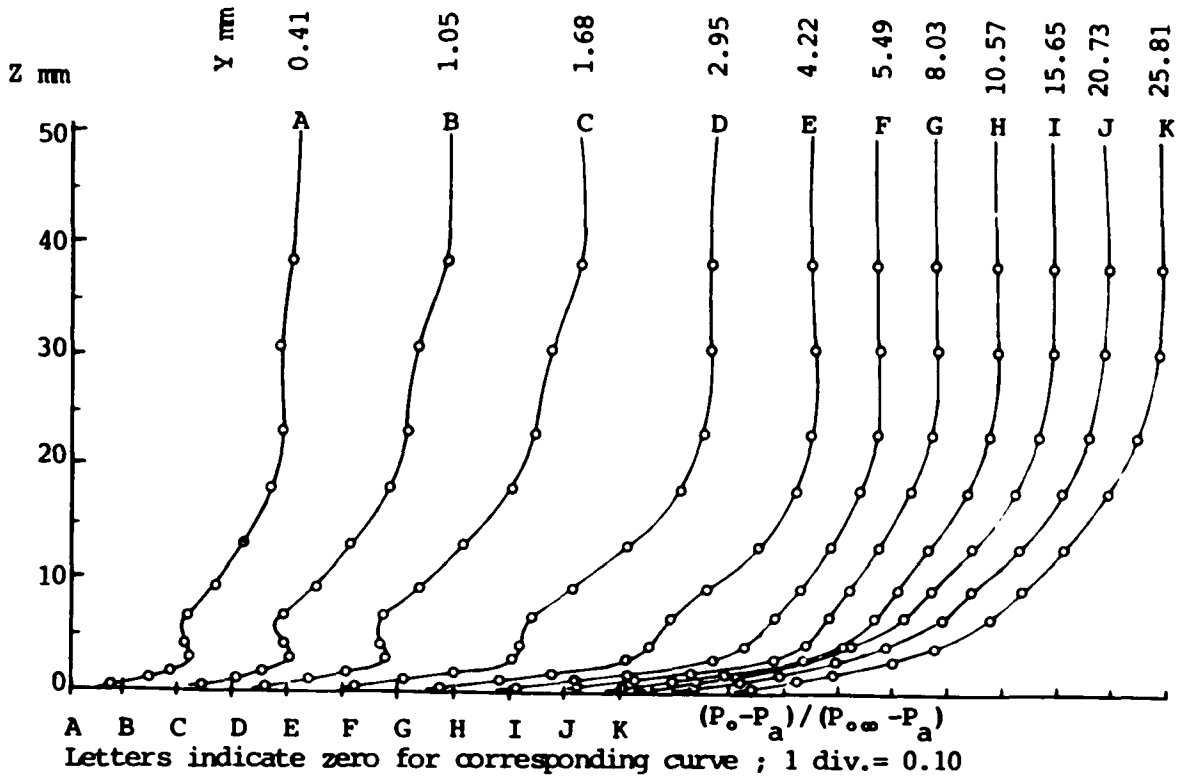

Fig. 4.37 Total Pressure Variation Parallel to the Airfoil
X = 203, X/C = 0.80

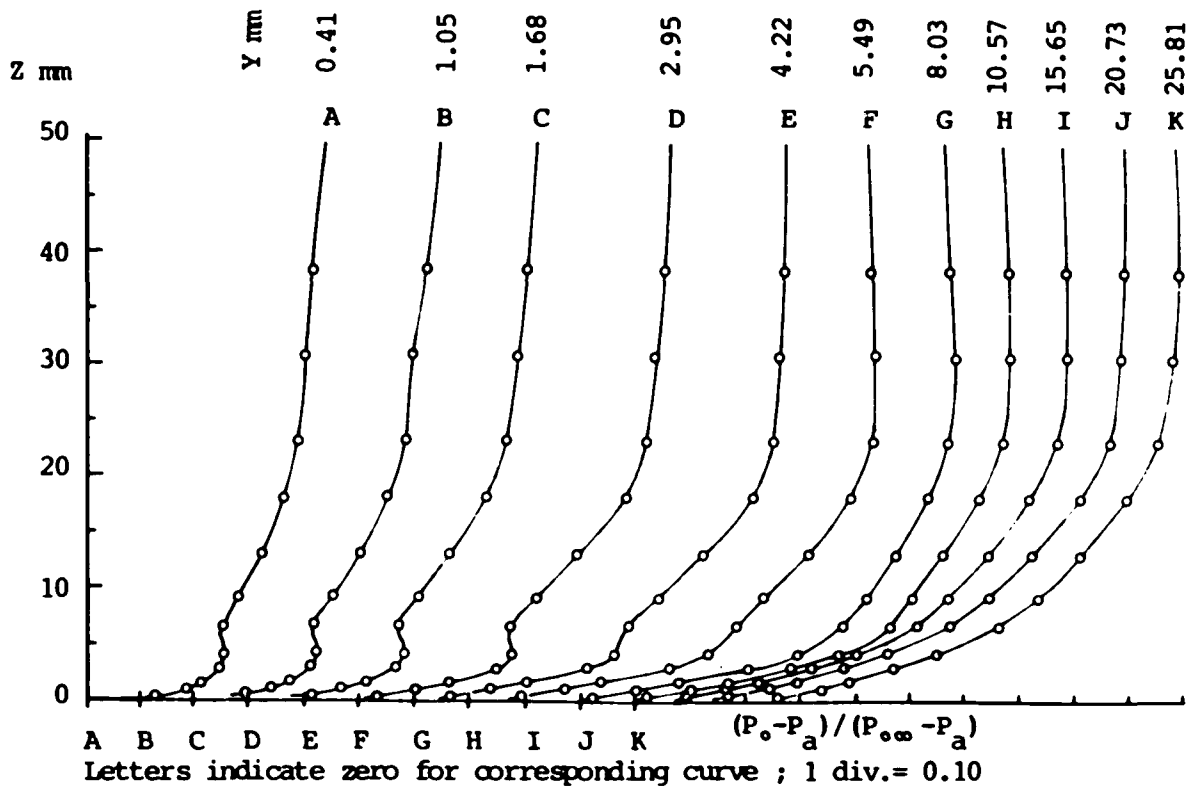

Fig. 4.38 Total Pressure Variation Parallel to the Airfoil
X = 251 mm; X/C = 0.985

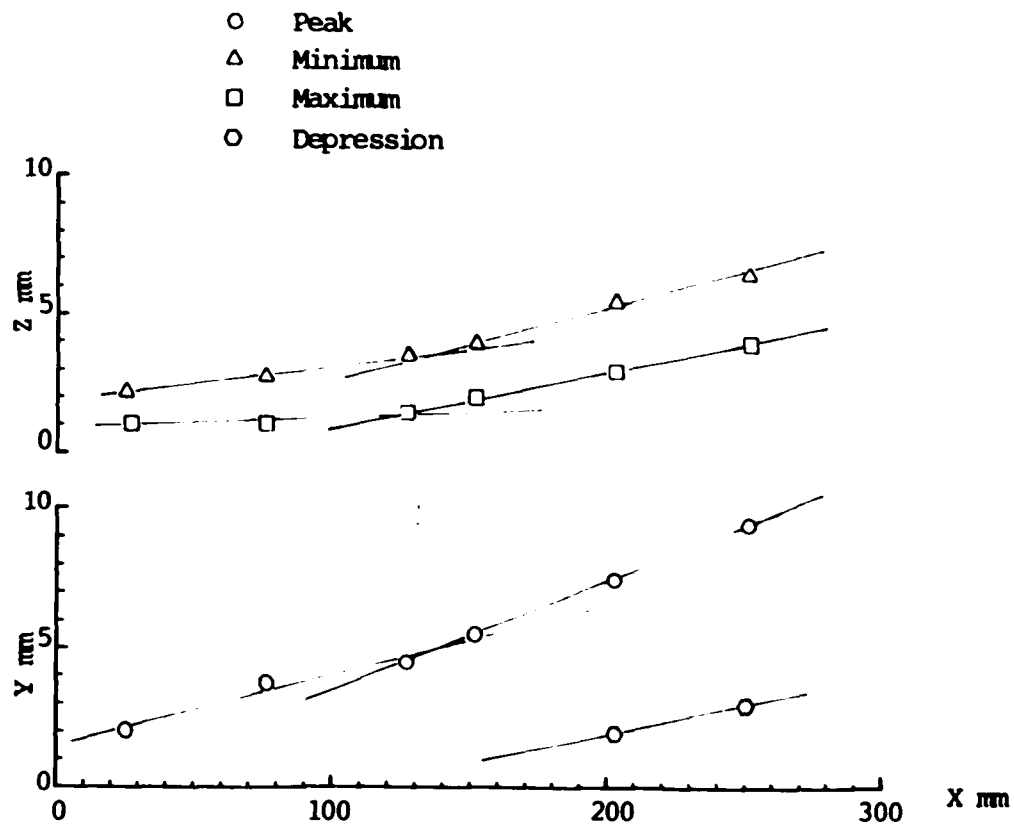

Fig. 4.39 Variation of Positions of Peak, Depression, Maximum and Minimum Points on the Curves Closest to the Surfaces (Y=0.41mm, Z=0.41mm)

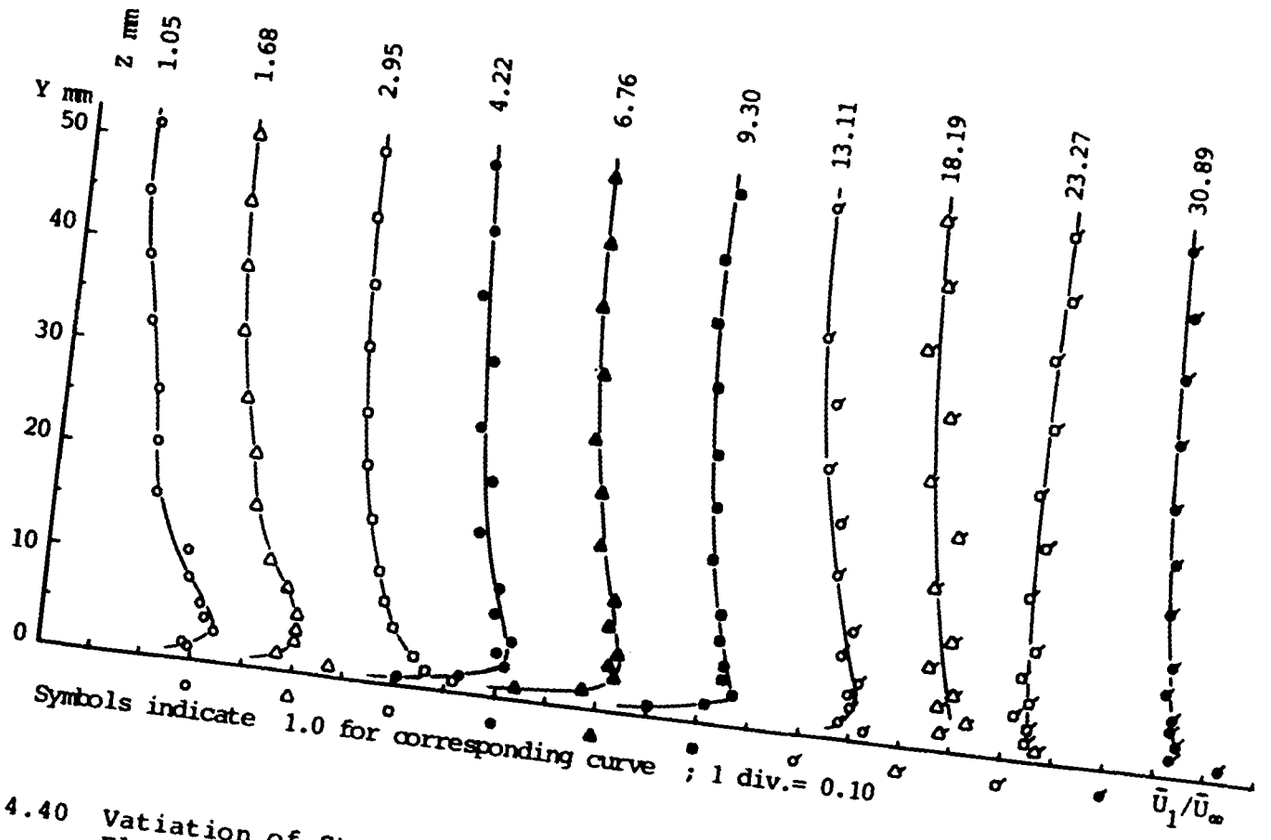

Fig. 4.40 Vatiation of Streamwise Component of Mean Velocity Parallel to the Flat Plate, X = 76 mm, X/C = 0.30

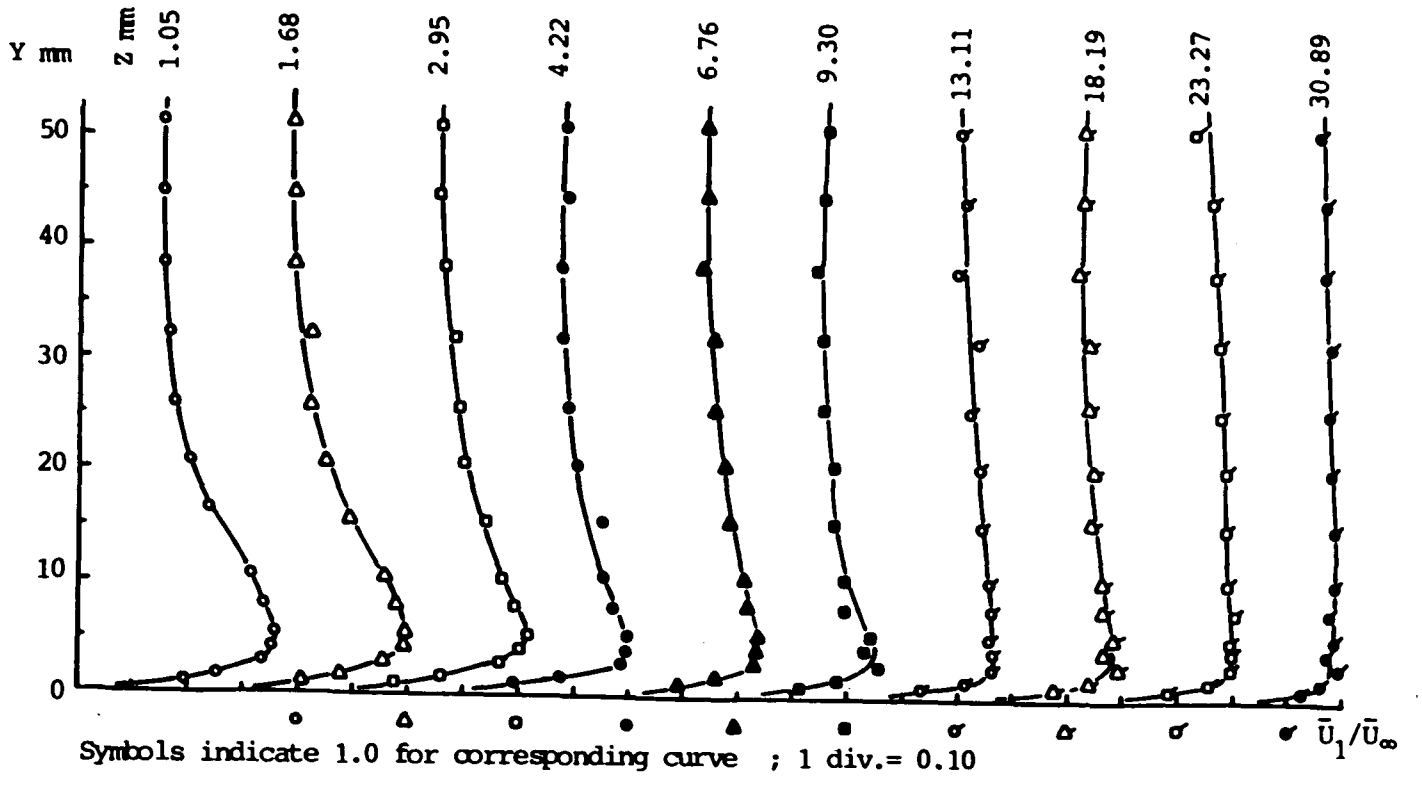

Fig. 4.41 Variation of Streamwise Component of Mean Velocity Parallel to the Flat Plate , X = 127 mm, X/C = 0.50

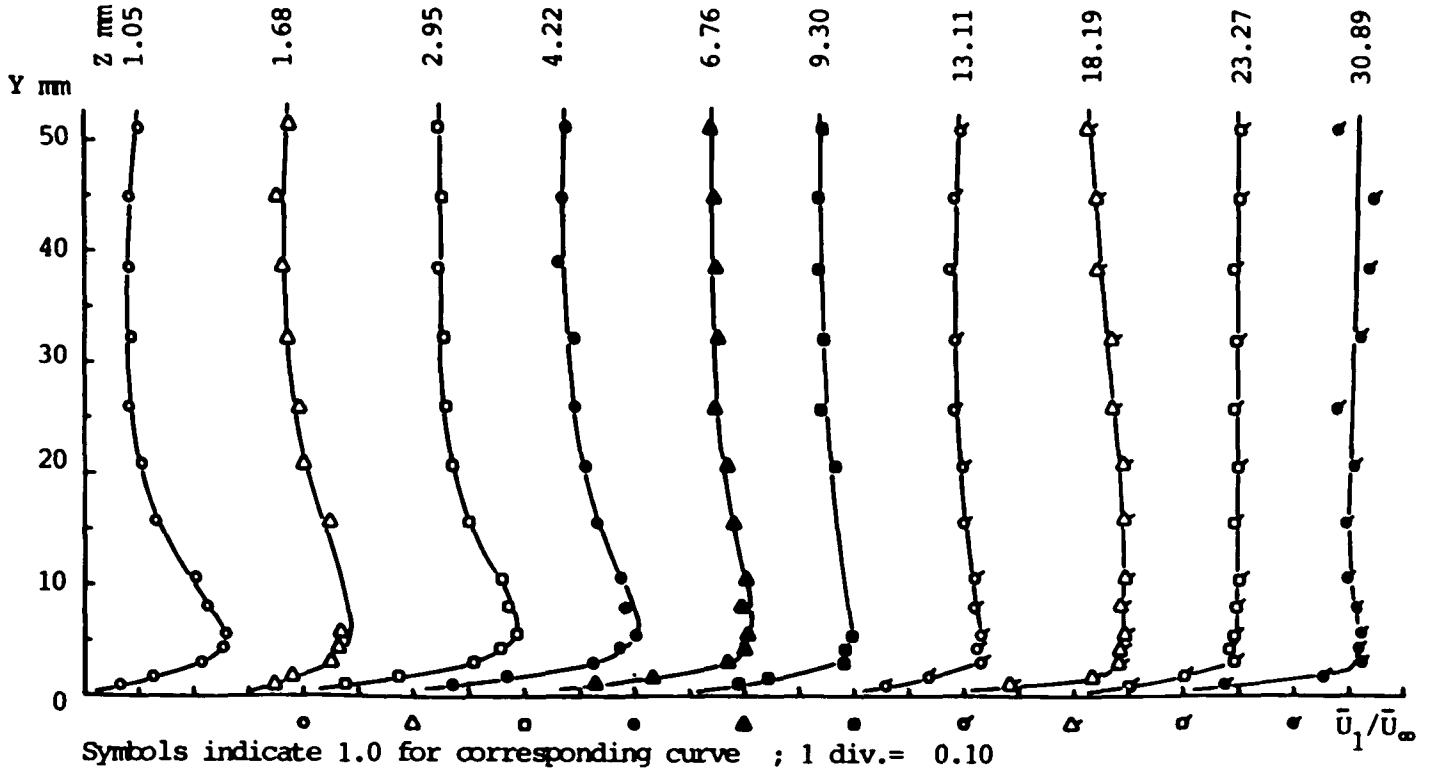

Fig. 4.42 Variation of Streamwise Component of Mean Velocity Parallel to the Flat Plate , X = 152 mm , X/C = 0.60

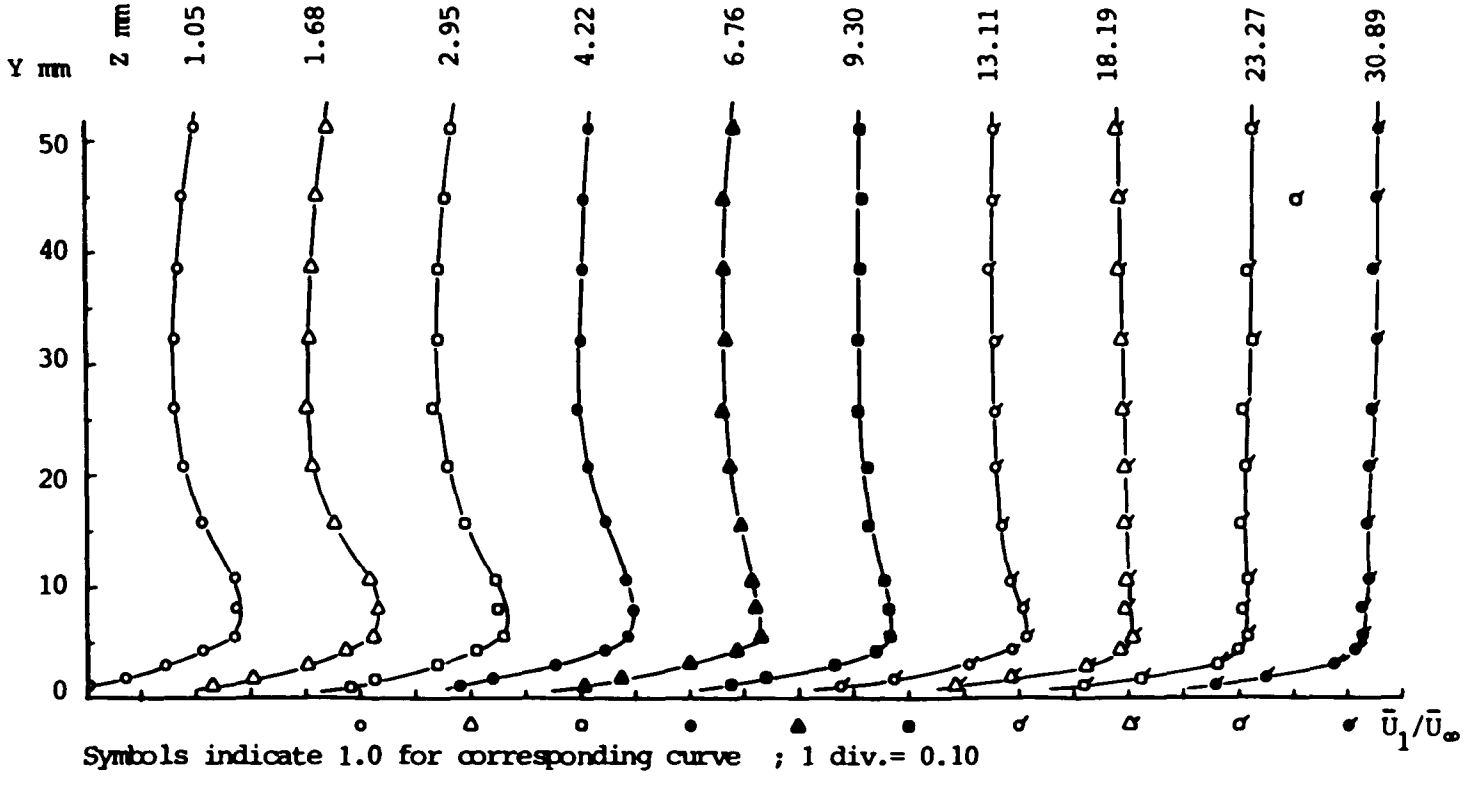

Fig. 4.43 Variation of Streamwise Component of Mean Velocity Parallel to the Flat Plate , X = 203 mm , X/C = 0.80

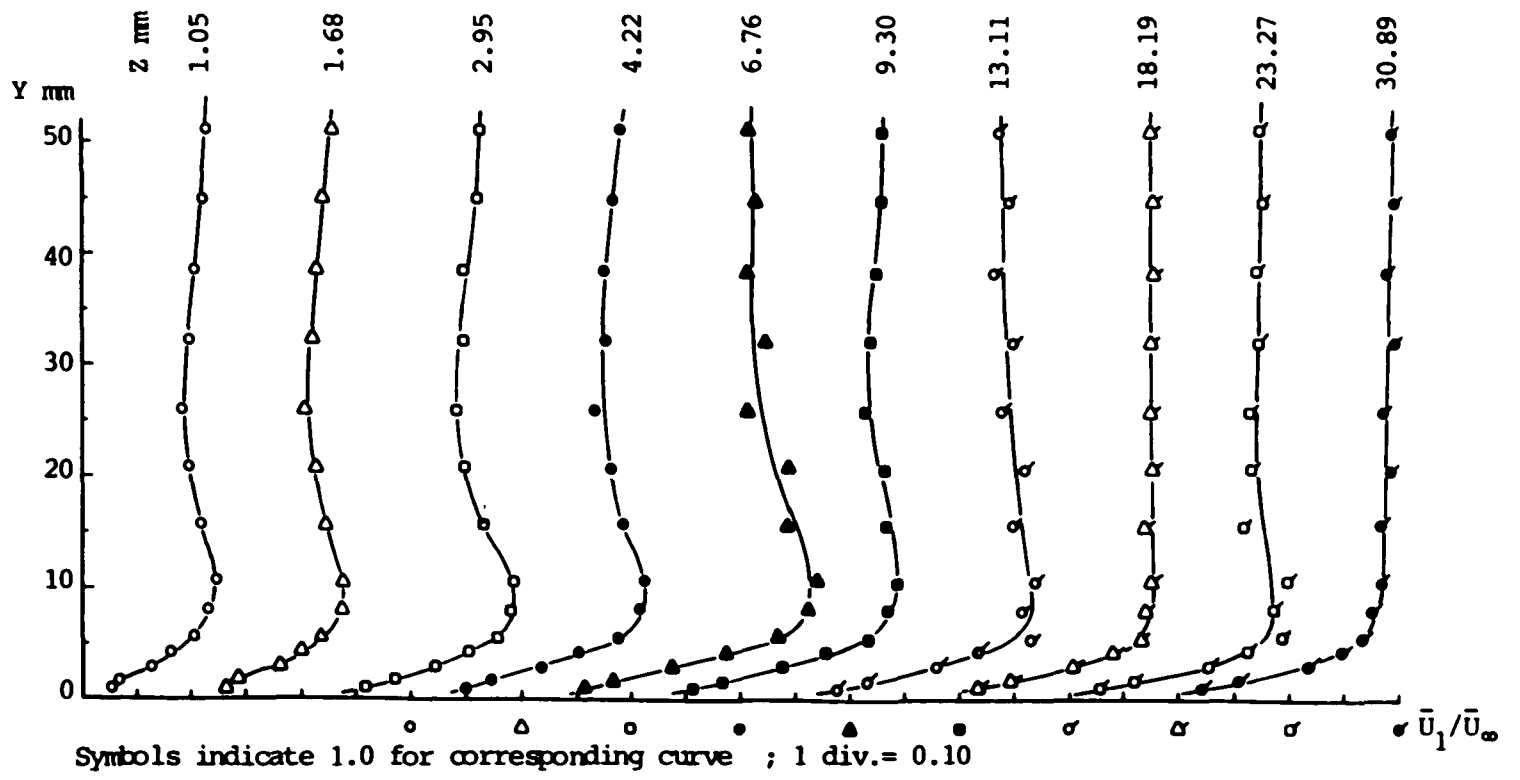

Fig. 4.44 Variation of Streamwise Component of Mean Velocity Parallel to the Flat Plate , X = 251 mm , X/C = 0.985

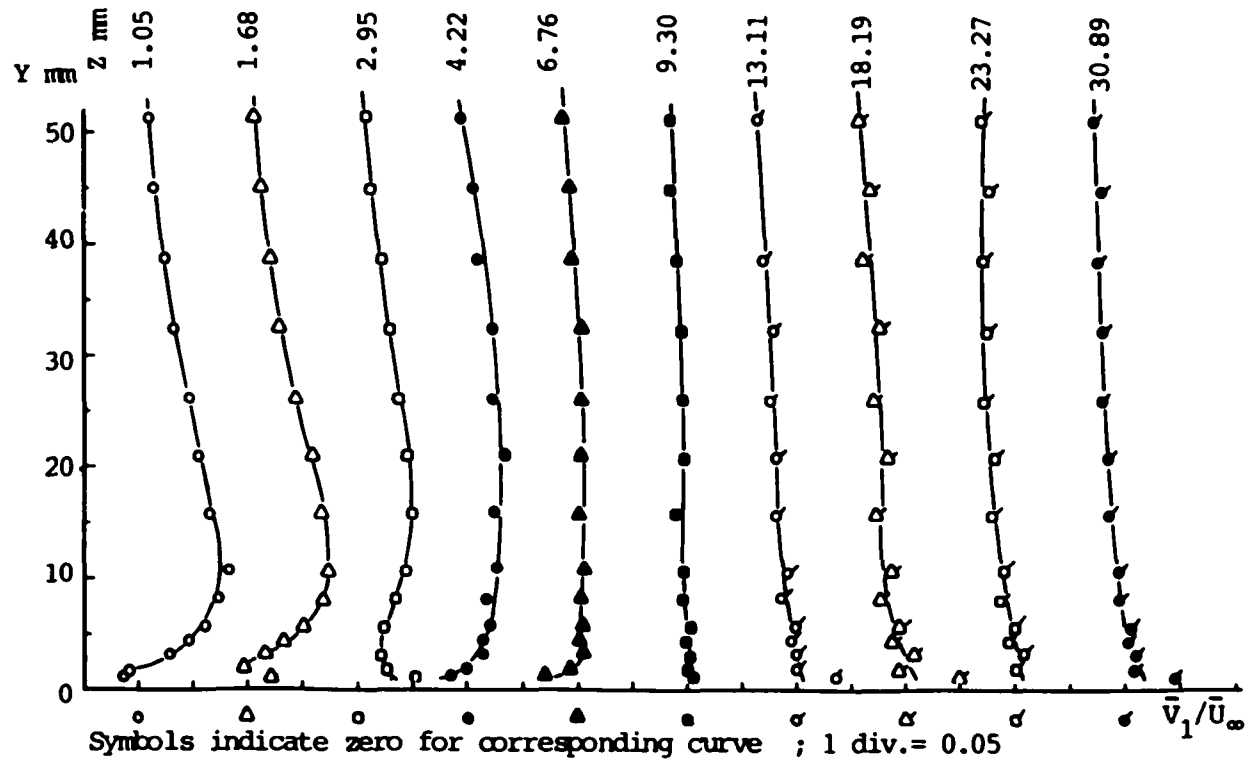

Fig. 4.45 Variation of Transverse Component of Mean Velocity Parallel to the Flat Plate , X = 76 mm , X/C = 0.30

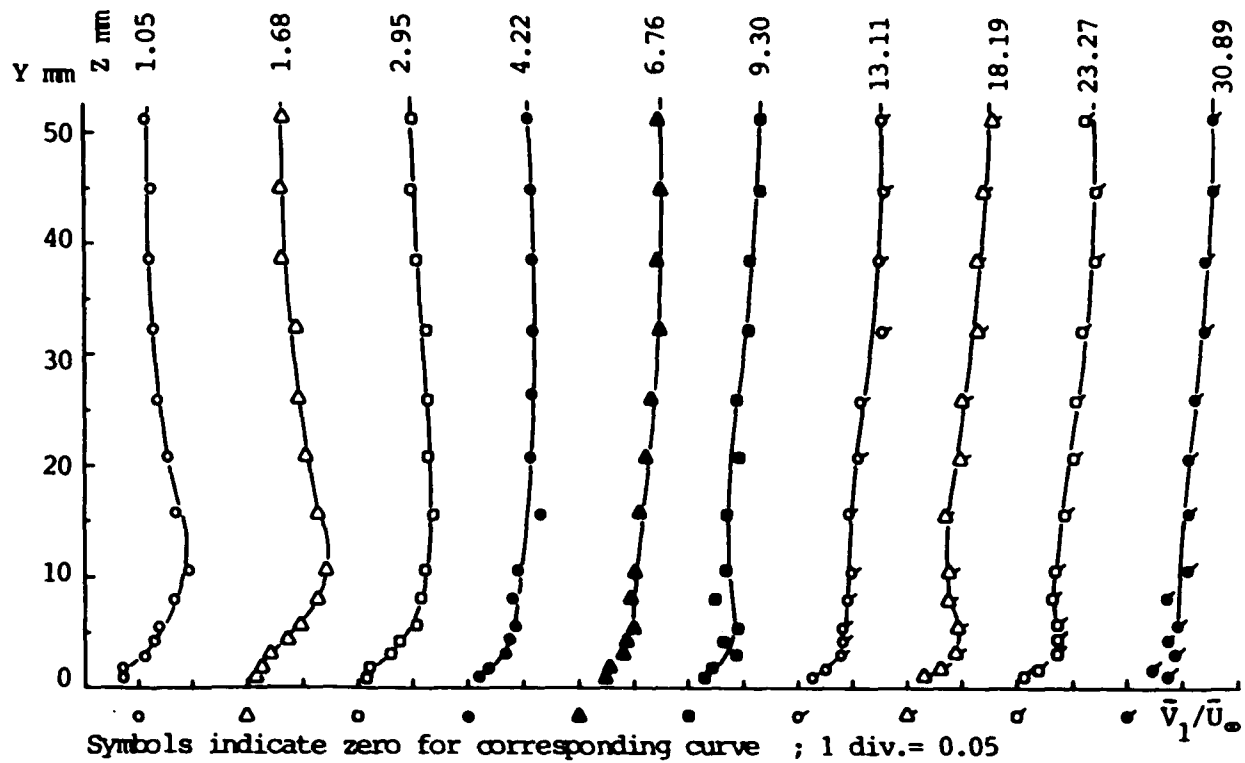

Fig. 4.46 Variation of Transverse Component of Mean Velocity Parallel to the Flat Plate , X = 127 mm , X/C = 0.50

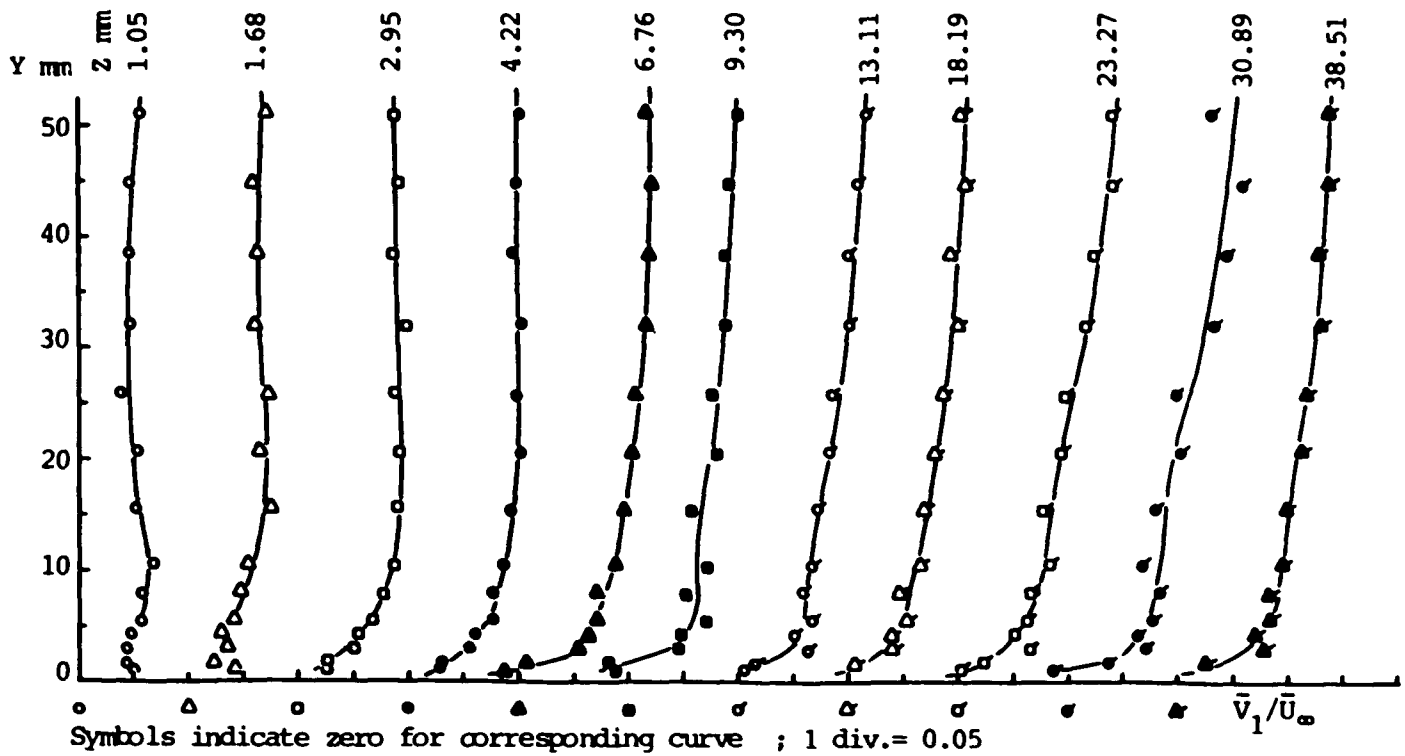

Fig. 4.47 Variation of Transverse Component of Mean Velocity Parallel to the Flat Plate , X = 152 mm , X/C = 0.60

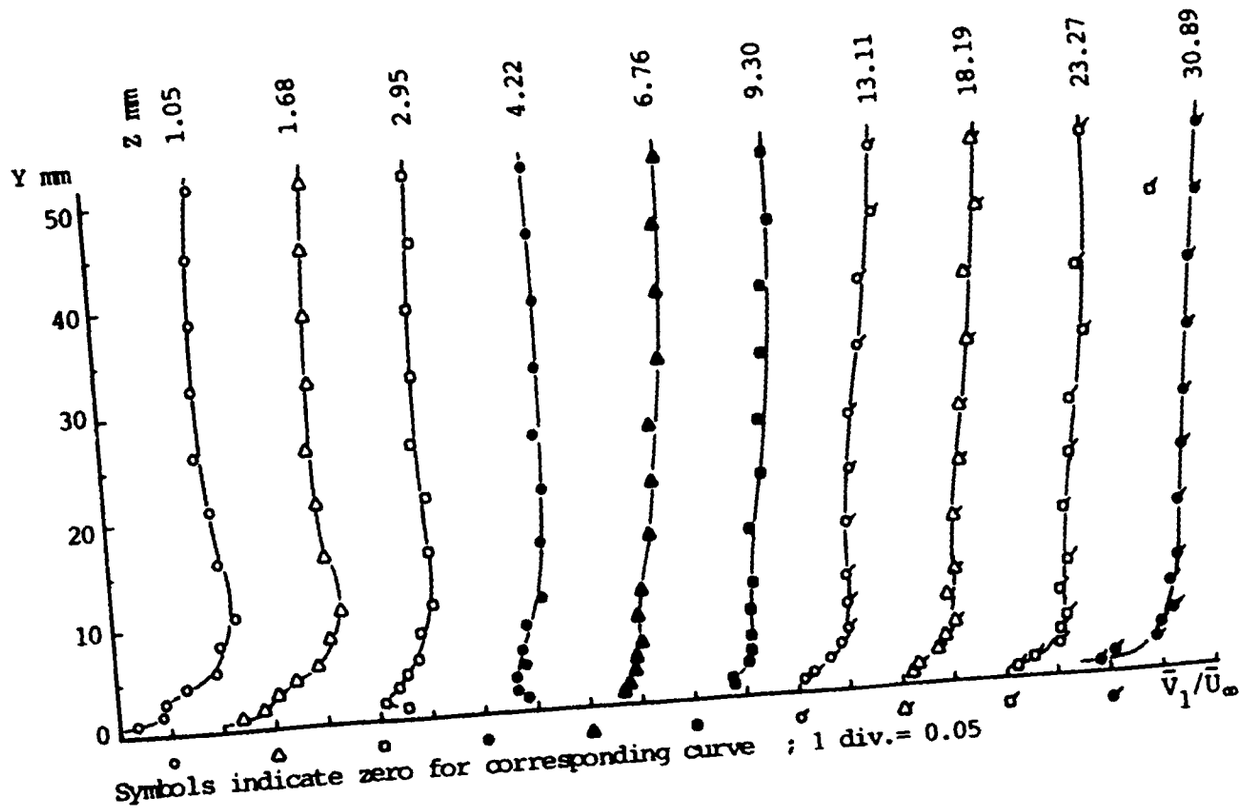

Fig. 4.48 Variation of Transverse Component of Mean Velocity Parallel to the Flat Plate , X = 203 mm , X/C = 0.80

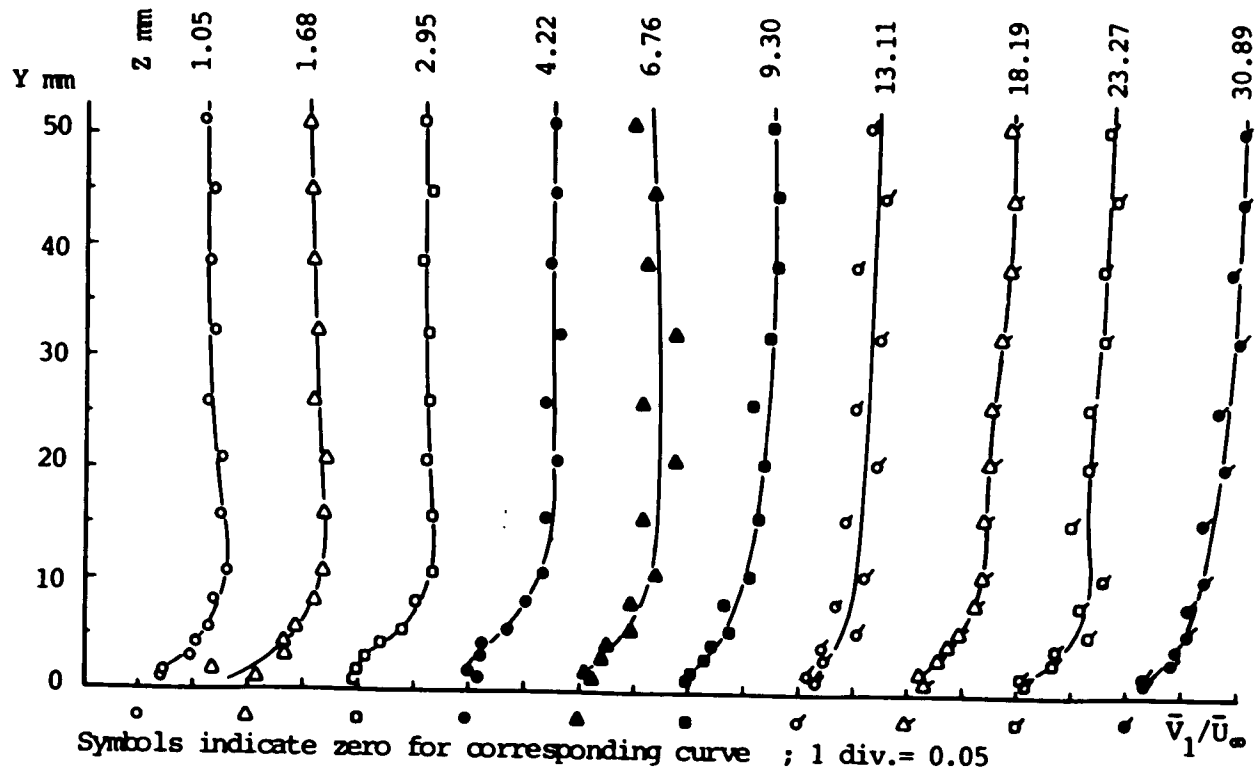

Fig. 4.49 Variation of Transverse Component of Mean Velocity Parallel to the Flat Plate , X = 251 mm , X/C = 0.985

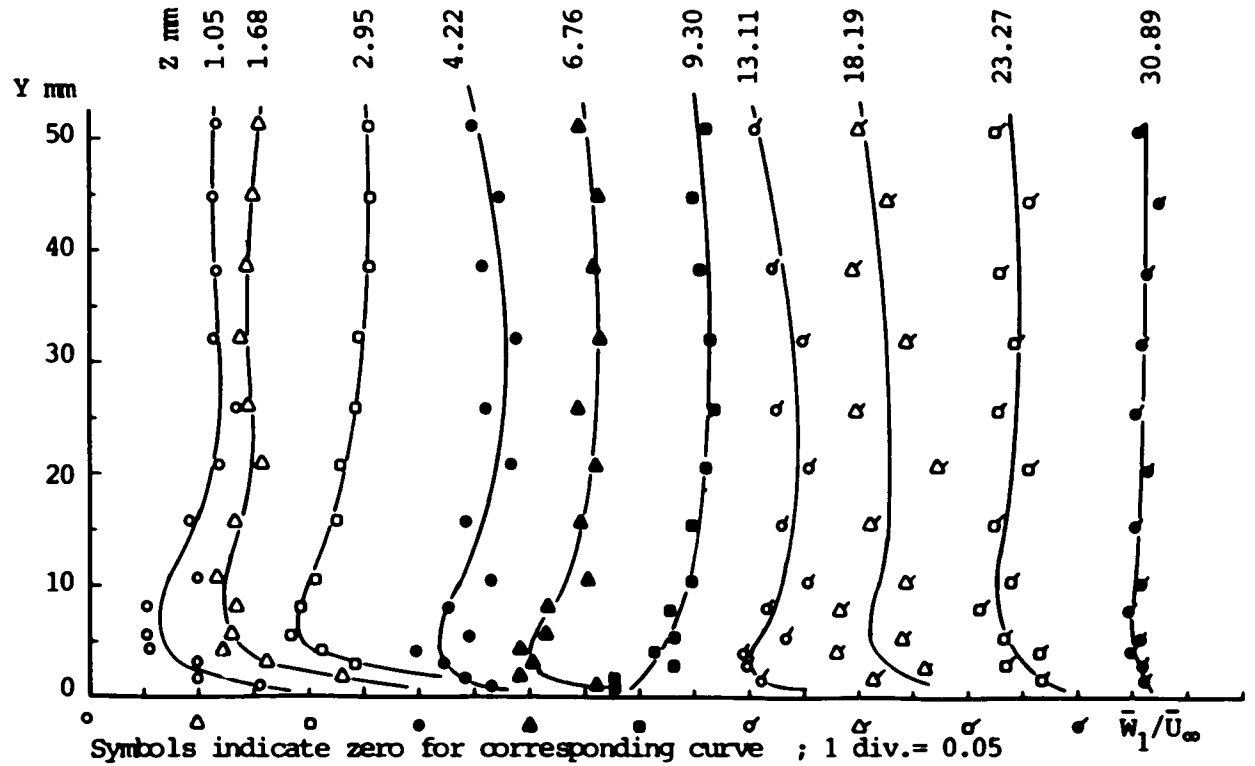

Fig. 4.50 Variation of Spanwise Component of Mean Velocity Parallel to the Flat Plate , X = 76 mm , X/C = 0.30

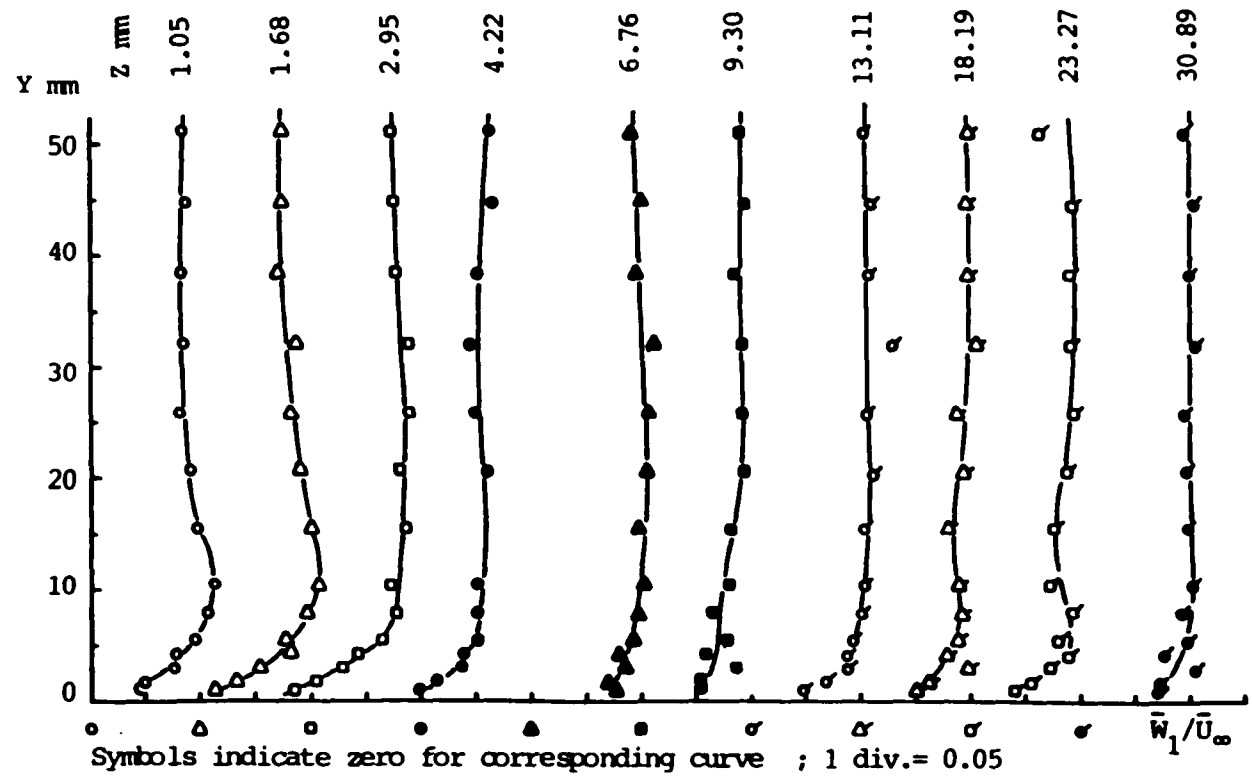

Fig. 4.51 Variation of Spanwise Component of Mean Velocity Parallel to the Flat Plate , X = 127 mm , X/C = 0.50

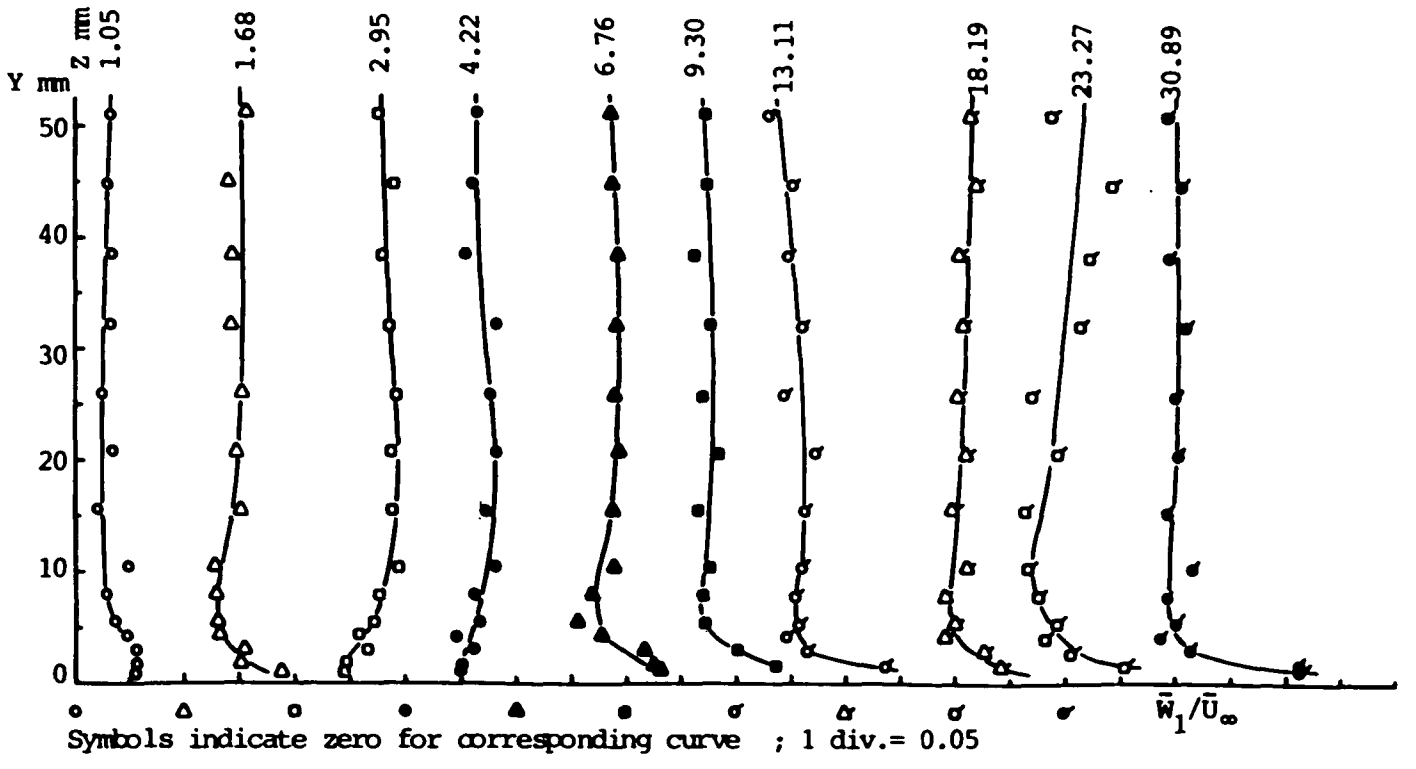

Fig. 4.52 Variation of Spanwise Component of Mean Velocity Parallel to the Flat Plate , X = 152 mm , X/C = 0.60

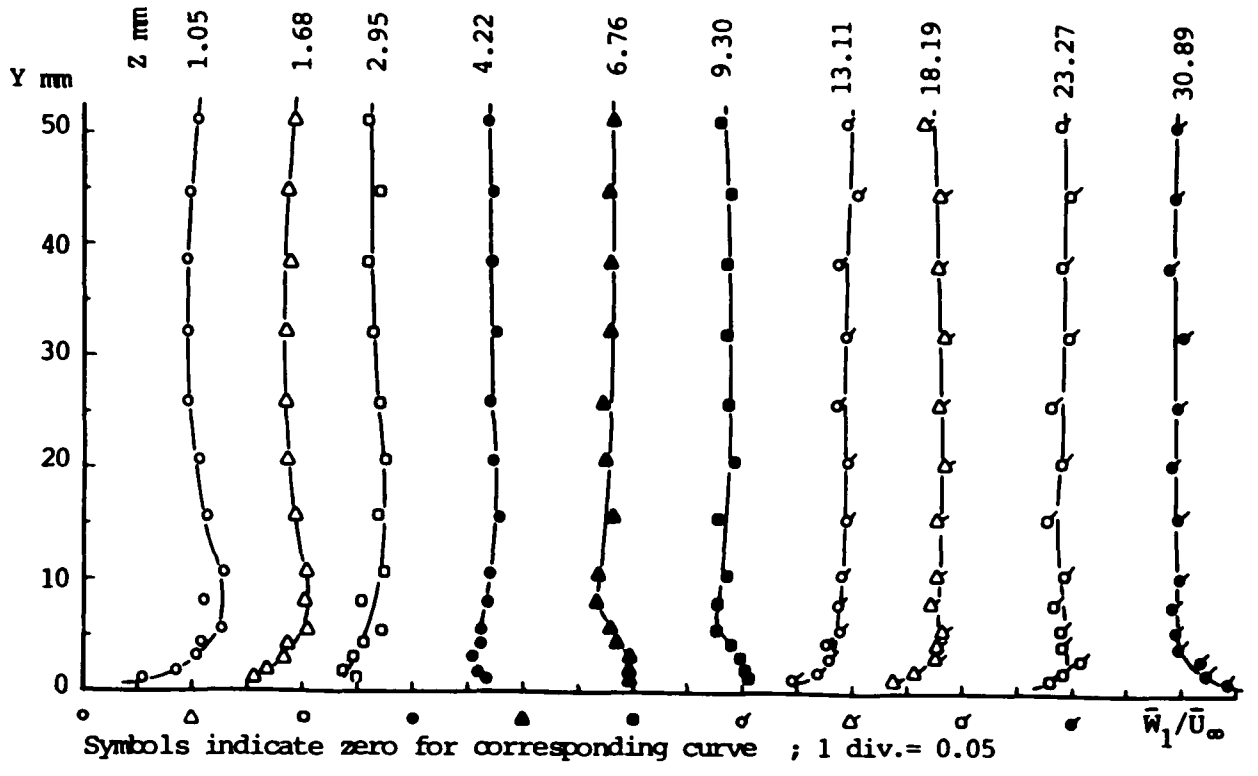

Fig. 4.53 Variation of Spanwise Component of Mean Velocity Parallel to the Flat Plate , X = 203 mm , X/C = 0.80

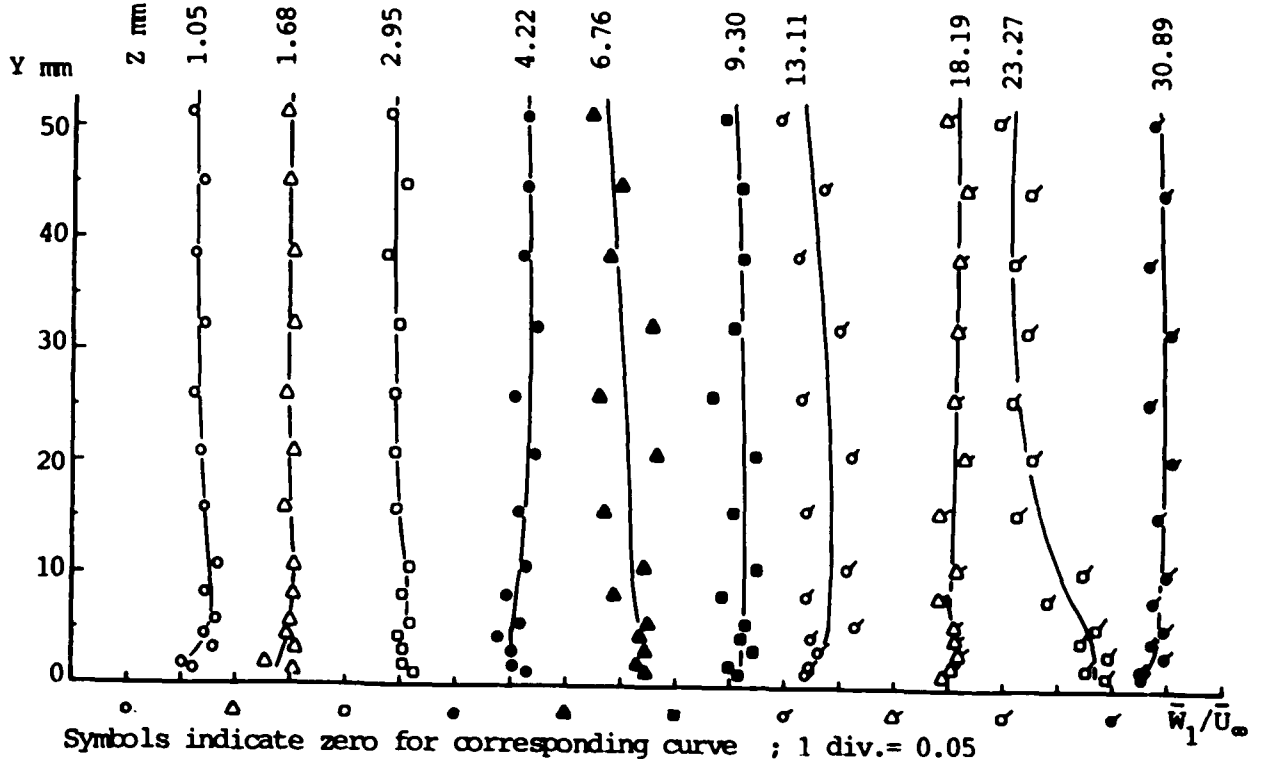

Fig. 4.54 Variation of Spanwise Component of Mean Velocity Parallel to the Flat Plate , X = 251 mm , X/C = 0.985

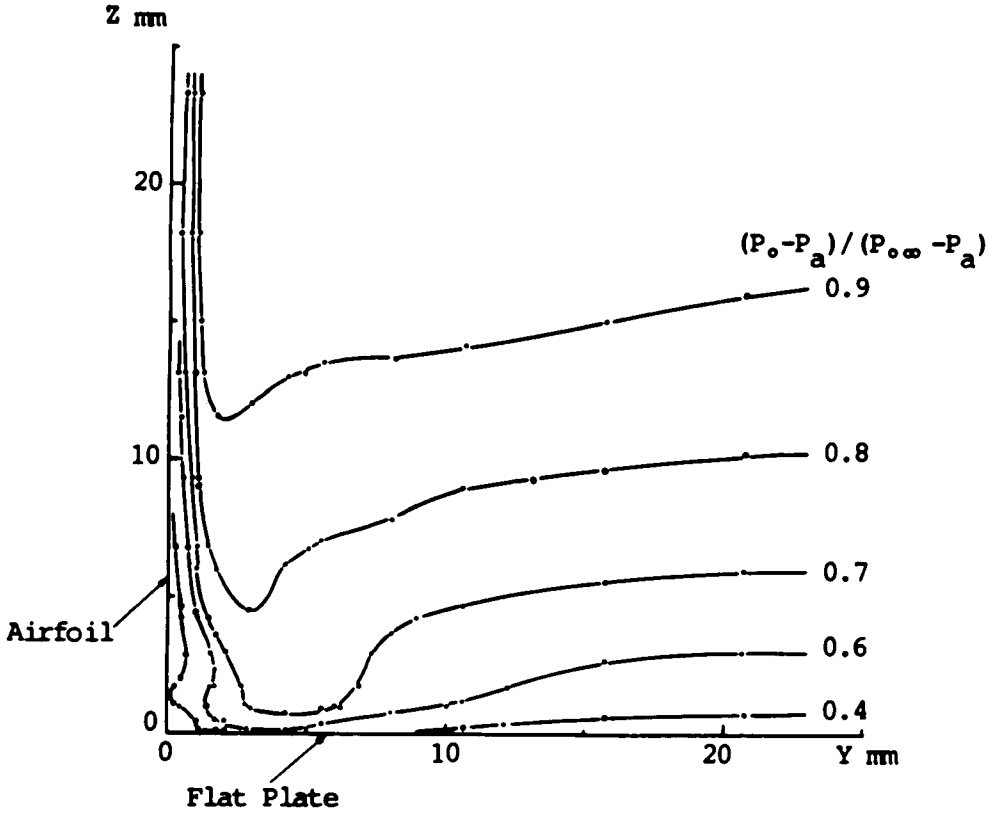

Fig. 4.55 Bernoulli Surfaces in the Corner
X = 76 mm , X/C = 0.30

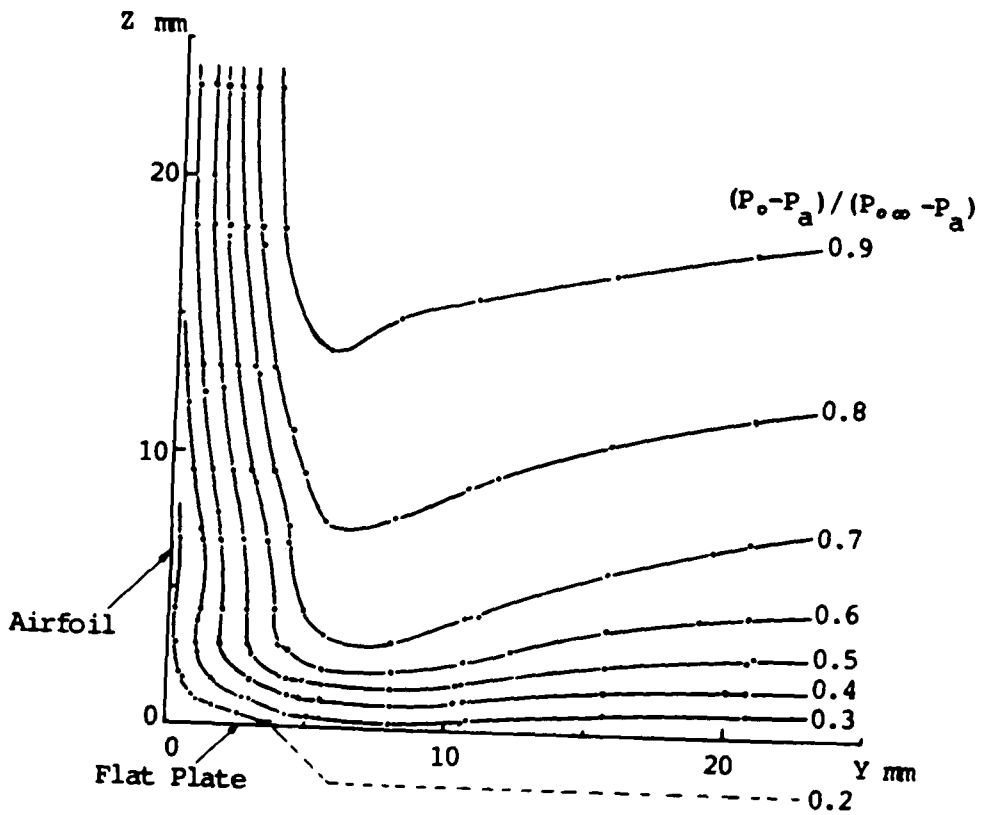

Fig. 4.56 Bernoulli Surfaces in the Corner
X = 203 mm , X/C = 0.80

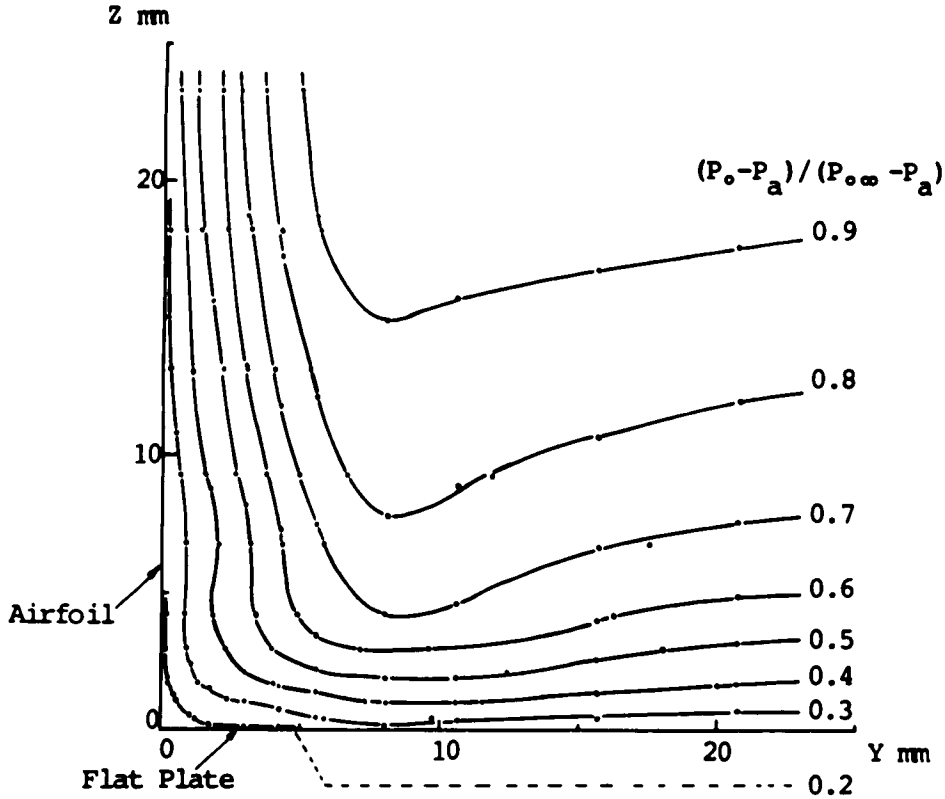

Fig. 4.57 Bernoulli Surfaces in the Corner
X = 251 mm , X/C = 0.985

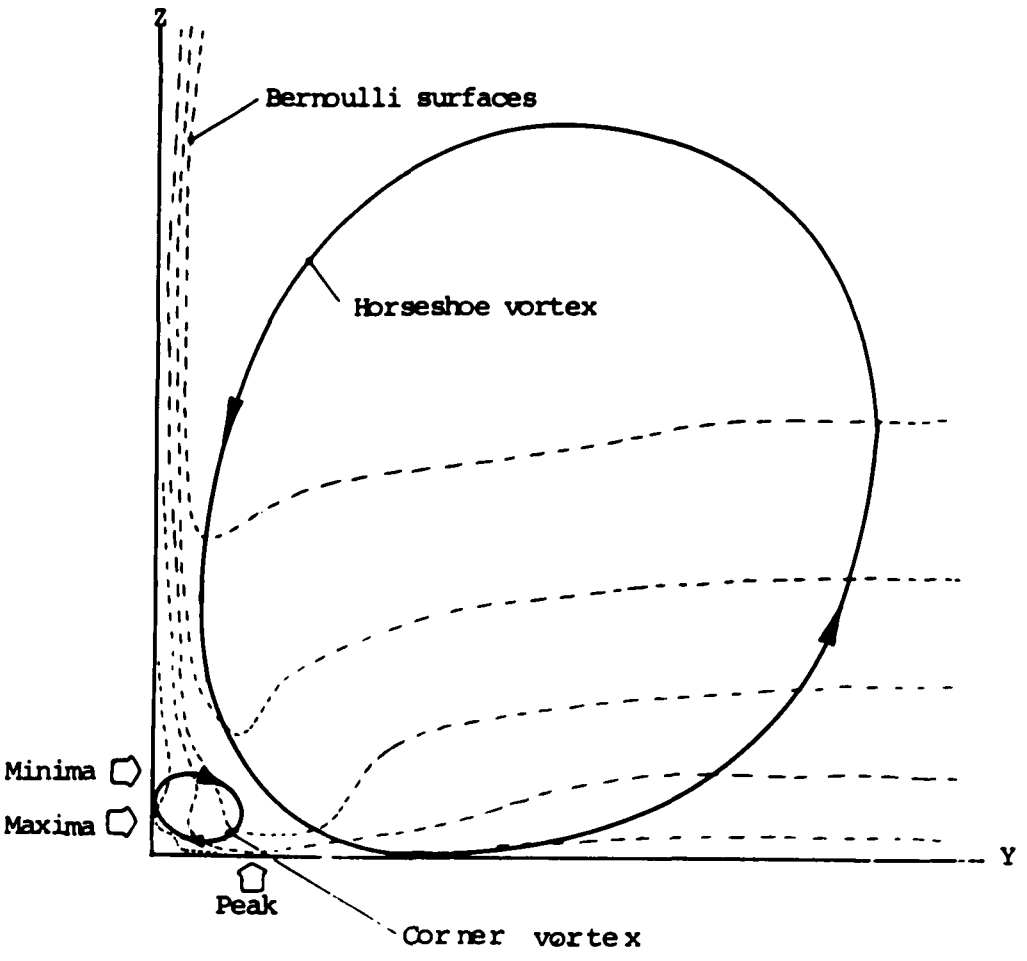

Fig. 4.58 Vortex System Leading to the Distortion of the Bernoulli Surfaces in the Forward Part of the Corner

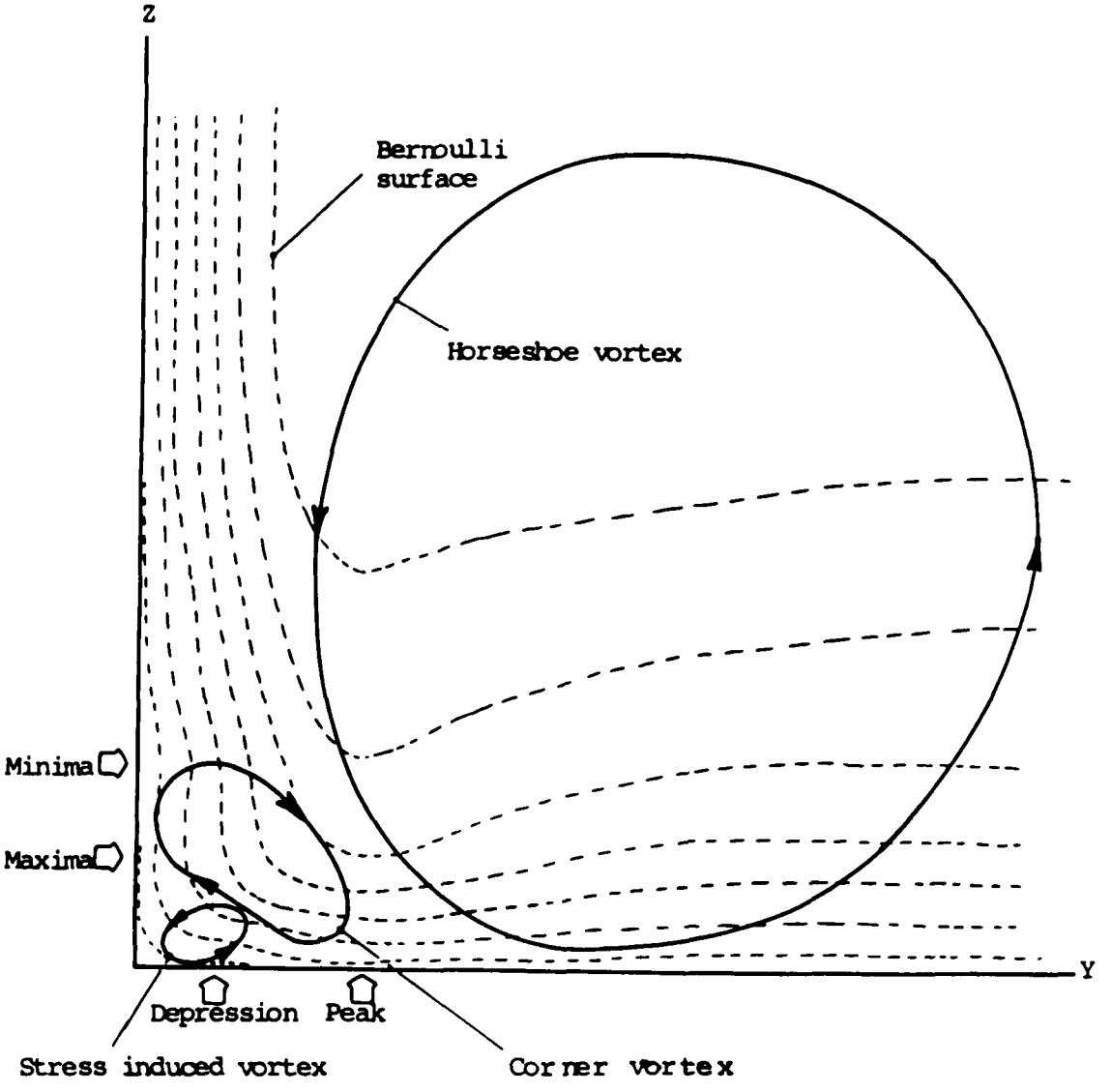

Fig. 4.59 Vortex System Leading to the Distortion of the Bernoulli Surfaces in the Rear Part of the Corner

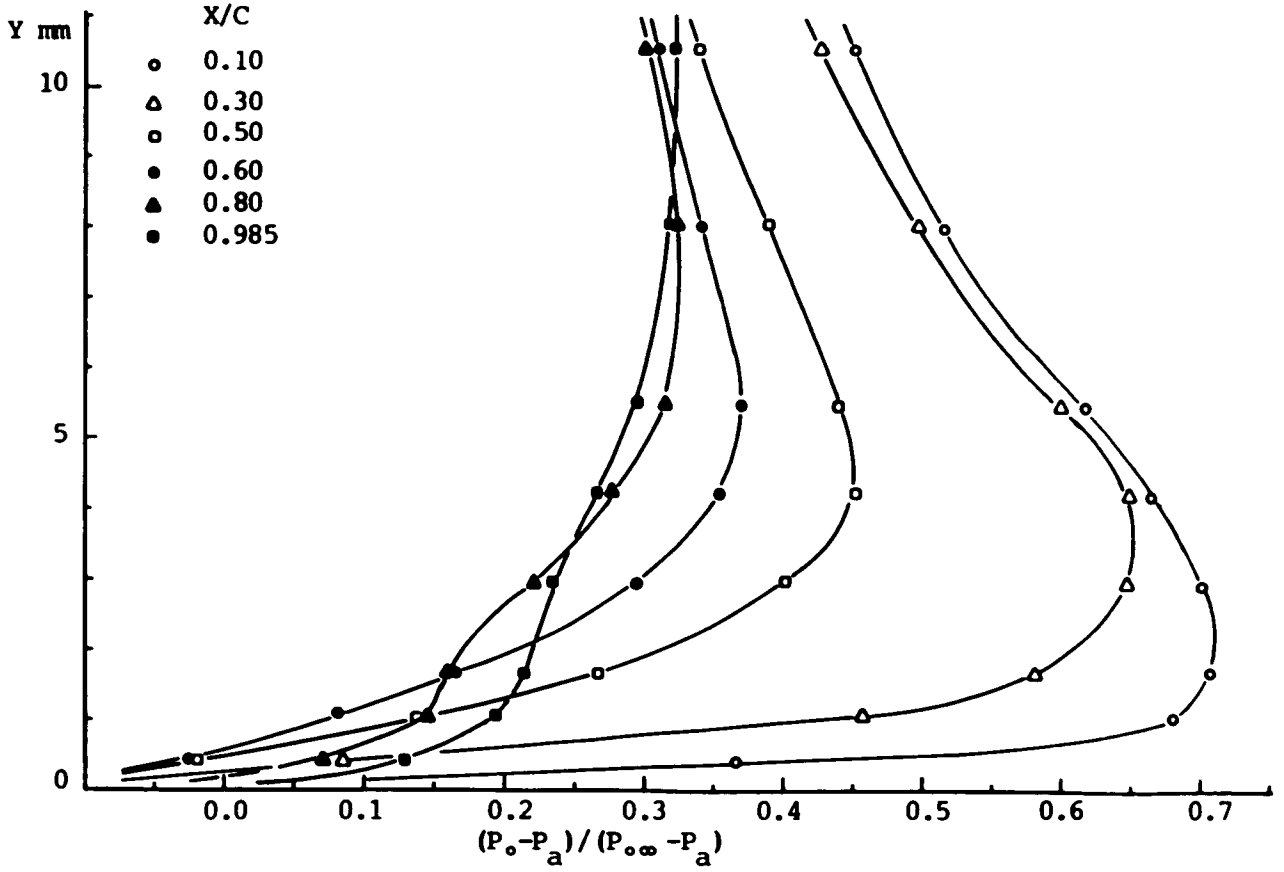

Fig. 4.60 Development of Total Pressure Profiles Closest to the Flat Plate (Z = 0.41 mm) in the Corner

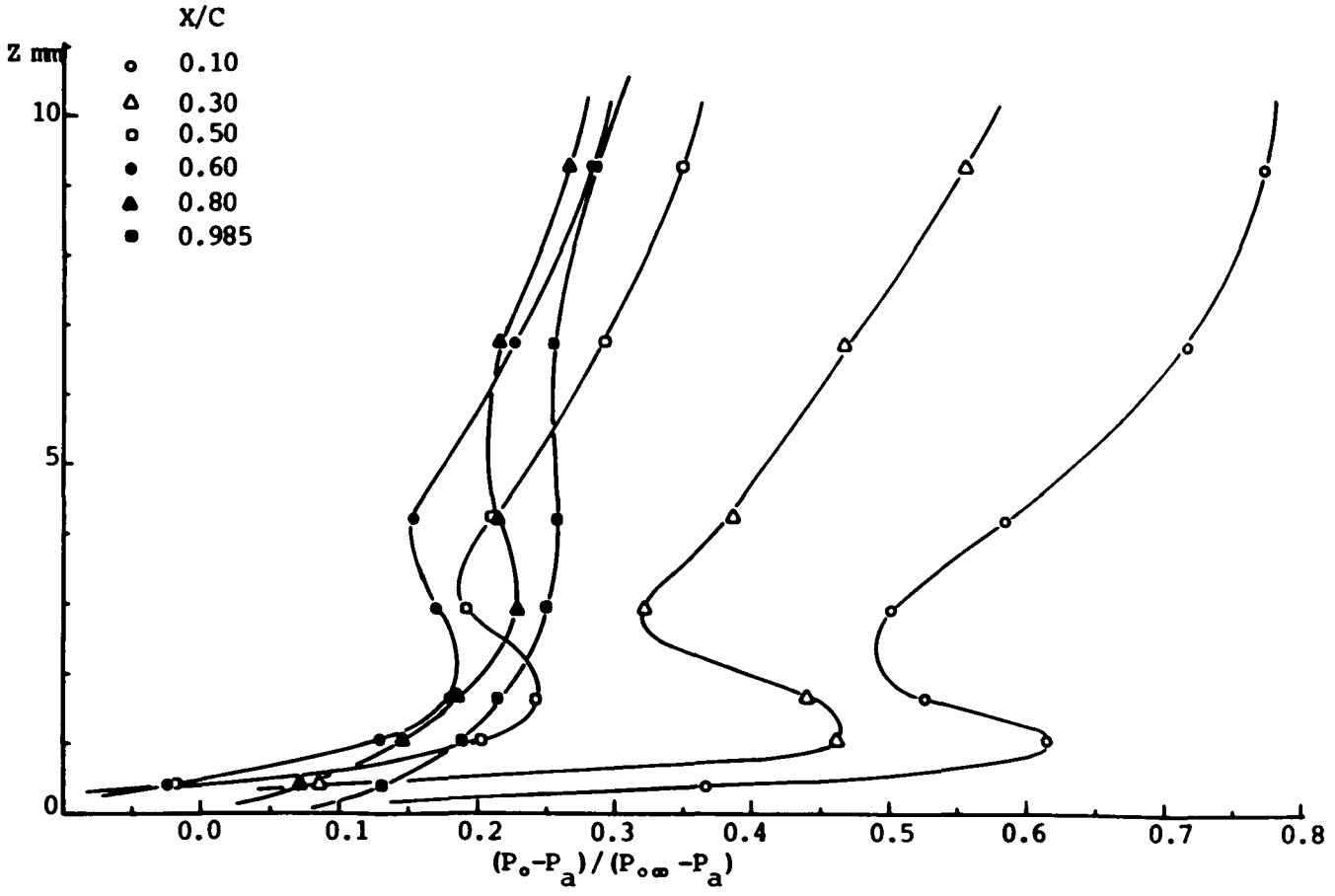

Fig. 4.61 Development of Total Pressure Profiles Closest to the Airfoil (Y = 0.41 mm) in the Corner

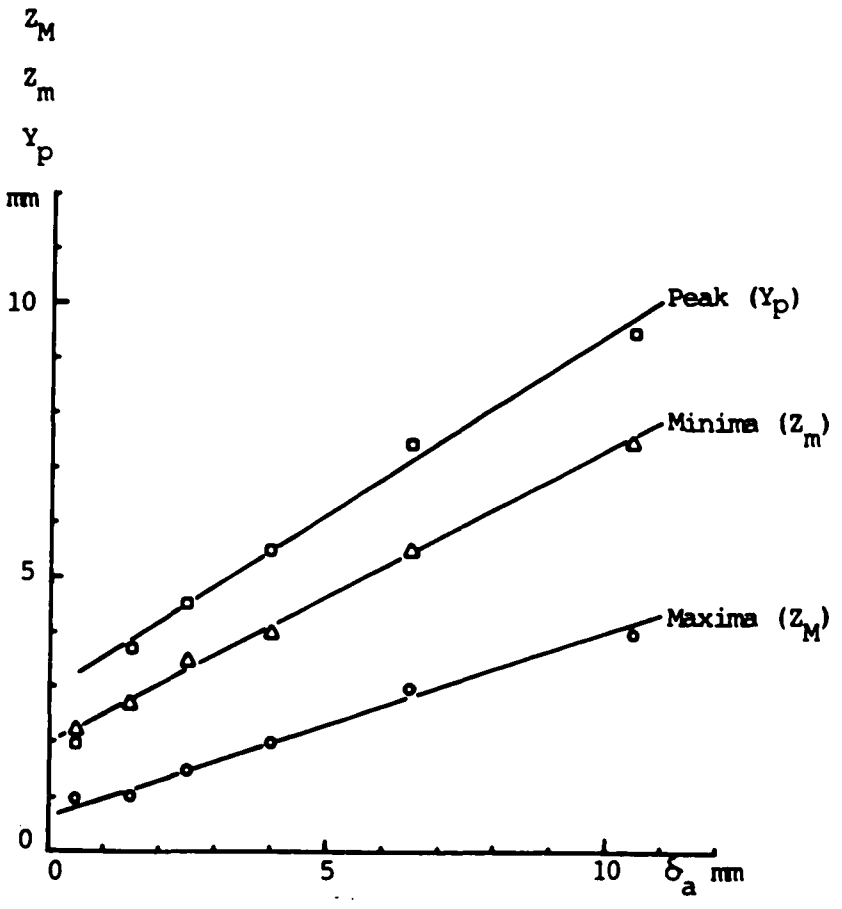

Fig. 4.62 Correlation Between Phenomena Related to the Corner Vortex and the Boundary Layer Thickness on the Airfoil Away from the Corner

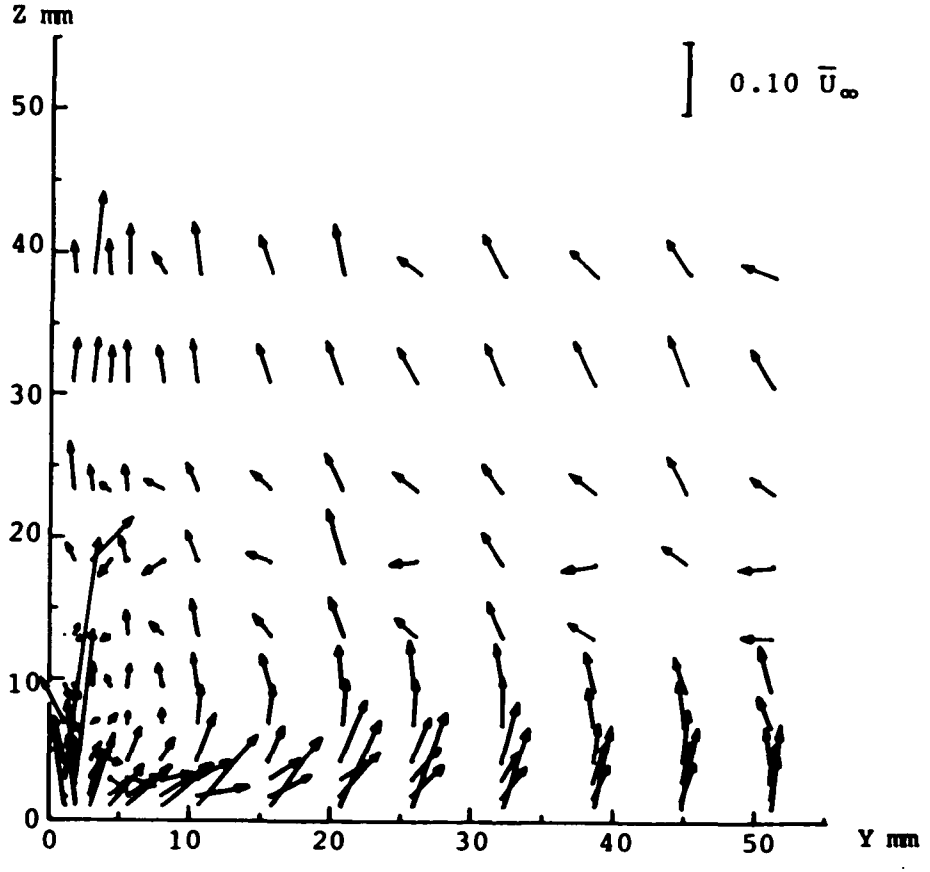

Fig. 4.63 Secondary Flow Vectors at X = 76 mm, X/C = 0.30

CHAPTER V

RESULTS AND DISCUSSION ON TURBULENCE QUANTITIES

The turbulence intensities and the Reynolds stresses measured with the inclined single sensor hot wire probe at the grid points shown in Fig. 3.12, and the results of the spectral analyses at the grid points shown in Fig. 3.14, are presented in this chapter. The turbulence intensities are normalized with the undisturbed free stream velocity calculated from the reference Kiel probe measurements at the time the particular readings were taken. The Reynolds stresses are normalized with the undisturbed free stream dynamic pressure obtained from the same reference Kiel probe measurements. These quantities are derived in the model frame of reference and plotted along the coordinates of the test section, where distances Y and Z are measured from the surface of the airfoil and the surface of the flat plate, respectively.

5.1 Turbulence Intensities

The variation of the streamwise turbulence intensity (u_1') parallel to the airfoil (variable Y) at various heights above the flat plate are presented in Figs.5.1 to 5.5. Away from the corner the variation of the streamwise turbulence intensity with Y is similar at all axial locations. These

curves are near the edge of the boundary layer of the flat plate. At all the axial stations the peak value of the streamwise turbulence intensity for each curve was found at the point of measurement nearest to the airfoil surface (Y = 1.05 mm). From this point the intensity rapidly decreases to a small value (of the order of free stream turbulence) within a short distance from the airfoil (of the order of δ_a), and remains fairly constant at that value. Up to the axial distance X/C = 0.5, the peak value observed near the surface increases to about 10% and then remains fairly constant at that value. This type of variation of streamwise turbulence intensity is characteristic of boundary layer over a convex surface.

Well inside the boundary layer of the flat plate, but not too near the flat plate ($Z > 0.3\ \delta_f$) the profiles show a trend different from the profiles near the edge of the flat plate boundary layer. After rapid fall to a small value, the streamwise turbulence intensity gradually increases with Y and then levels off to a constant value. The constant value attained by individual curve increases as the height above the flat plate (Z) reduces. For the curves close to the flat plate ($Z < 0.3\ \delta_f$), after rapid decrease of the streamwise turbulence intensity to a small value, it gradually increases to attain another maximum value and then slightly reduces to a

constant value away from the corner. For the curves nearest to the flat plate (Z = 1.05 mm), at various axial stations the constant values range between 7% and 9% as it was expected from the variation of u_1' due to acceleration and deceleration of flow.

The lowest measured value in the corner region was found to occur around the point where the streamwise component of the mean velocity and the total pressure profiles parallel to the flat plate have the peak values. This phenomenon can be explained from the fact that the streamwise turbulence intensity reduces towards the outer edge of the boundary layer and the total pressure increases. Since the horseshoe vortex advect the fluid from the edge of the flat plate boundary layer towards the flat plate near the corner, the peak in the total pressure and the minimum value in the streamwise turbulence intensity appear at the same point. At this point the production of turbulence energy (q^2) is also very small because $\partial\bar{U}_1/\partial Y_1 \simeq 0$.

The shape of the curves near the flat plate at the last axial station (Fig. 5.5, X/C = 0.985) can be explained from the fact that very near the corner the stress induced vortex pair increases the mixing of the fluid. At this station the size of the stress induced vortex is about 3 mm. Thus, the curves up to a height of 3 mm are affected by the

stress induced vortex. The effect of the stress induced vortex at the section X/C = 0.80 is not observed because the vortex is not large enough to bring about any noticeable change in the streamwise turbulence intensity at the traverse heights.

Figs. 5.6 to 5.10 show the variation of the transverse turbulence intensity v_1' parallel to the flat plate (variable Y) at constant heights above the flat plate surface (constant Z) at five axial stations. The curves on the extreme right of the figures represent the variation of v_1' near the edge of the boundary layer of the flat plate. At all the stations the peak values of v_1' were found close to the airfoil surface. The value of v_1' rapidly decreases from this peak value to the free stream value within a short distance from the airfoil surface. Along the axial direction of the wind tunnel, the peak values on these curves increase upto X/C = 0.60, thereafter, the peak values reduce in a manner similar to the streamwise turbulence intensity variation.

The variation of v_1' with Y nearer to the flat plate also show a trend similar to that of the streamwise turbulence intensity variation. For v_1' distribution not too near to the flat plate, the peak values of v_1' occurs near the airfoil surface. From the peak value, the transverse turbulence

intensity reduces rapidly to a small value and then gradually increases and attains a constant value. Similar to the distribution of the streamwise turbulence intensity u_1', the constant values attained by the transverse turbulence intensity v_1' also increase near the flat plate, because of large values of $\partial\bar{v}_1/\partial z_1$ near the flat plate.

Very close to the flat plate the variation of the transverse turbulence intensity shows different trend at the stations upstream compared with the stations downstream of the maximum thickness section of the airfoil. In the forward part of the airfoil (Figs. 5.6 and 5.7), the peak value of v_1' occurs very near the airfoil surface. Then, it rapidly drops to a low value followed by a gradual increase to a maximum value. After attaining the maximum value, the value of v_1' slightly reduces and levels off to a constant value. At the downstream stations (Figs. 5.8, 5.9 and 5.10), the peak in the values of the transverse turbulence intensity v_1' occurs away from the airfoil surface, followed by a gradual decrease in the value of v_1' and then leveling off to a constant value.

The variation of the spanwise turbulence intensity w_1' parallel to the flat plate (variable Y) at various heights above the flat plate (constant Z) at five axial stations are shown in Figs. 5.11 to 5.15. The curves at the extreme right

of the figures, correspond to the edge of the boundary layer of the flat plate. The maximum value of the spanwise turbulence intensity appears very close to the airfoil surface. Away from the airfoil surface the values rapidly decrease to the free stream value. The variation of the peak values of w_1' with streamwise direction is similar to that of u_1' and v_1'; that is, the peak value initially increases up to axial station X/C = 0.50 and then gradually reduces downstream of this station.

In general, the rest of the curves of spanwise turbulence intensity variation show a trend similar to that of the transverse turbulence intensity variation. For curves not too close to the flat, plate but well within the boundary layer of the flat plate (2 mm < Z < 10 mm) the peak values of w_1' occur near the airfoil surface. In the case of the curves nearer to the flat plate, the peaks in w_1' appear slightly away from the airfoil surface. The peak is followed by a rapid decrease in the value of w_1' to a lower value which slightly increases to reach a maximum and then does not change significantly in case of the curves slightly away from the flat plate surface. For curves close to the flat plate surface (Z = 1.05 mm) the maximum value of w_1', in most cases seem to occur at a distance from the airfoil surface.

Near the edge of the boundary layer of the flat plate (Z > 20 mm) the ratio of the maximum values of the spanwise and the streamwise turbulence intensities $w_1'_M/u_1'_M$ at the forward part of the airfoil (X/C = 0.30) start with an average value of 1.2. As the flow proceeds downstram it gradually reduces and near the trailing edge it becomes nearly 0.6. The ratio of maximum values of the transverse and the streamwise turbulence intensities $v_1'_M/u_1'_M$, on the other hand, start with a value of 0.6 at the forward part of the airfoil. As the flow proceeds downstream the ratio gradually increases to about 1.1 at X/C = 0.60 and thereafter it starts decreasing and becomes approximately 0.6 near the trailing edge.

For the curves close to the flat plate (Z = 1.05 mm) the variation of the ratios of the constant values of u_1' and v_1', away from the corner is as follows: the ratio $v_1'_C/u_1'_C$ at X/C = 0.3 starts with a value of 0.6, which gradually inceases to about 0.9 at X/C = 0.5, and then falls back to approximately 0.5 at X/C = 0.985. The ratio $w_1'_C/u_1'_C$, starts with about 0.7 at X/C = 0.3 and gradually reduces to 0.5 at X/C = 0.985.

For the same curves (Z = 1.05 mm), at the points where u_1' becomes minimum, the ratios v_1'/u_1' and w_1'/u_1' vary

in the following manner: the ratio v_1'/u_1' at X/C = 0.3 is 0.75, which reduces to about 0.5 at X/C = 0.5 and at the downstream stations gradually increases back to 0.75. The value of w_1'/u_1' at X/C = 0.3 is 0.65 and reduces to approximately 0.5 at X/C = 0.5. The value of w_1'/u_1' then sharply increases to about 0.9 at X/C = 0.6 and drops to 0.5 as the flow proceeds downstream.

In the close vicinity of the corner, where the peak values of u_1' occur on the curves close to the flat plate (Z = 1.05 mm), the variation of the ratios v_1'/u_1' and w_1'/u_1' in the flow direction are as follows: the ratio v_1'/u_1' starts with a value of approximately 0.4 near the leading edge, which gradually increases to 0.76 at X/C = 0.6 and drops to 0.5 near the trailing edge. The value of w_1'/u_1' also varies in a manner similar to the value of v_1'/u_1'. The ratio w_1'/u_1' starts with a value of 0.3 near the leading edge, increases to approximately 0.7 at X/C = 0.6 and then gradually reduces to about 0.5 near the trailing edge.

The variation in turbulence intensities close to the corner reduces as the flow proceeds along the corner. For example, the ratio of the peak intensity and the minimum intensity for the curves close to the flat plate (Z = 1.05 mm)

vary in the following way: the ratio $u_1'_M/u_1'_m$ at X/C =0.3 is 1.54 and reduces to 1.12 at X/C =0.8, the value of $v_1'_M/v_1'_m$ reduces from 2.54 to 1.58 between the same two stations and $w_1'_M/w_1'_m$ changes from 3.35 to 2.00.

In the vicinity of the corner the turbulent kinetic energy q^2 was found to be of the order of 2% of the mean kinetic energy of the undisturbed flow $\bar{U}_\infty^2/2$. Along the corner bisector, away from the corner, initially the value drops rapidly and then gradually levels off. For example, at X/C = 0.8, nearest to the corner (Y = 1.05 mm, Z = 1.05 mm) q^2 was found to be 1.8% of $\bar{U}_\infty^2/2$, along the corner bisector, 3 mm away from the corner it reduces to 0.8% and at a distance 6 mm from the corner the value becomes 0.6%. The change beyond this point is less rapid and falls to 0.4% at 12 mm away from the corner along the corner bisector.

5.2 Reynolds Stress Variation

The variation of the cross correlation of fluctuating velocities ($\overline{u_1v_1}$, $\overline{u_1w_1}$ and $\overline{v_1w_1}$) at grid points parallel to the flat plate are presented in Figs 5.16 to 5.30. These quantities are normalized by the square of the undisturbed free stream mean velocity ($\bar{U}_\infty^2$). This, in effect, gives half the value of Reynolds stresses normalized

by undisturbed free stream dynamic pressure in the negative sense.

The distribution of $\overline{u_1 v_1}/\bar{U}_\infty^2$ at the axial measuring stations at grid points parallel to the flat plate (variable Y) at different heights above the flat plate (constant Z) are shown in Figs. 5.16 to 5.20. In the vicinity of the corner these curves start with a negative value. The profiles have a positive gradient in the Y direction up to the distance where the value of $\overline{u_1 v_1}/\bar{U}_\infty^2$ is maximum and positive. The quantity $\overline{u_1 v_1}/\bar{U}_\infty^2$ then gradually reduces and becomes nearly zero far away from the airfoil surface. The trend of variation of $\overline{u_1 v_1}/\bar{U}_\infty^2$ can be explained with the help of the effect of the horseshoe vortex on the mean velocity gradient. The fluid transported by the horseshoe vortex from the outer part of the boundary layer has large streamwise mean velocity but small velocity fluctuations. This produces a large positive gradient of streamwise component of mean velocity in the Y direction up to a short distance away from the airfoil surface. After reaching a peak, the velocity gradually reduces producing a negative gradient in Y direction then leveling off to give zero gradient of velocity in Y direction. From the surface of the airfoil up to the distance where the peak in the mean velocity profile occurs, the shear stress is positive, thus $\overline{u_1 v_1}/\bar{U}_\infty^2$ will have negative value. The crossover from the negative value to the positive value occurs

approximately at the same distance from the airfoil surface where the peak in the mean streamwise velocity component appears. Beyond the peak in the mean streamwise velocity the value of $\overline{u_1 v_1}/\bar{U}_\infty^2$ remains positive, attains a maximum value and then starts reducing and becomes very small outside the corner regions where the mean freestream velocity becomes constant. In slender shear layers the transverse components of the mean velocity are an order of magnitude smaller than the streamwise component. Thus, the streamwise gradients of the transverse components of mean velocity are also small and do not contribute significantly to the shear stress. As the flow proceeds along the corner, $\overline{u_1 v_1}/\bar{U}_\infty^2$ takes a slightly larger negative value and the maximum positive value reduces towards the trailing edge. This trend of variation is consistent with the mean velocity variation. In some of the plots, the quantity $\overline{u_1 v_1}/\bar{U}_\infty^2$ nearest to the airfoil corner was found positive. It may be explained from the fact that the measurements could not be taken very close to the surface and there is some amount of error as shown in Appendix C. These positive values could also be due to presence of energy reversal regions due to asymmetry in bodies forming corner.

Variation of $\overline{u_1 w_1}/\bar{U}_\infty^2$ parallel to the flat plate (variable Y) at various heights above the flat plate (constant Z) are shown in Figs. 5.21 to 5.25. In the forward part of the airfoil, the variation of $\overline{u_1 w_1}/\bar{U}_\infty^2$ is more rapid than at

the last two axial stations. This behavior is consistent with the behavior of the mean velocity components. The spanwise gradient of the streamwise mean velocity becomes smaller as the flow proceed downstream along the corner. The changes that occur at different heights above the flat plate surface are not strange as it appears at the first glance. It is to be taken into consideration that the major contributor to the shear stress on the X-Z plane are the terms associated with the spanwise and transverse gradients of the streamwise mean velocity component ($\overline{v_1 w_1}\ \partial\bar{U}_1/\partial Y_1$ and $\overline{w_1^2}\ \partial\bar{U}_1/\partial Z_1$).

Figs. 5.26 to 5.30 illustrate the variation of the quantity $\overline{v_1 w_1}/\bar{U}_\infty^2$, parallel to the flat plate surface (variable Y) and at different heights above the flat plate (constant Z). The difference in the second order derivatives of the term $\overline{v_1 w_1}$ with respect to the transverse (Y) and spanwise (Z) directions lead to the production of streamwise vorticity component. The value of $\overline{v_1 w_1}$ was found to be of the same order of magnitude as the other two Reynolds stress components. At all the stations in the corner region the variation of $\overline{u_1 w_1}/\bar{U}_\infty^2$ was observed to be quite significant indicating that the contribution to the production of the streamwise component of vorticity by this component of Reynolds stress is significant.

In the corner region the peak values of $\overline{u_1v_1}$ and $\overline{u_1w_1}$ appear close to the corner. The ratios of the maximum magnitudes of these two stress terms ($\overline{u_1w_1}_M/\overline{u_1v_1}_m$) for the corresponding curves vary between 0.5 and 2.0. Towards the trailing edge, the maximum values $\overline{u_1v_1}_M$ and $\overline{u_1w_1}_M$ appear roughly at the same location. However, near the leading edge, such a trend was not always observed. No such similarities were observed for the profiles of $\overline{v_1w_1}/\bar{U}_\infty^2$ with the profiles of other two stress terms. The ratio of magnitudes $\overline{u_1w_1}_M/\overline{u_1v_1}_M$ for the maximum values of the stresses for the curves mentioned above, were also found to vary between 0.5 and 2.0.

The ratio $(|\overline{u_1v_1}|+|\overline{u_1w_1}|+|\overline{v_1w_1}|)/(u_1'^2+ v_1'^2+ w_1'^2)$ at the axial station X/C = 0.8 showed a variation between 0.5 and 0.15. The variation of the quantity along the corner bisector was found to be very gradual and stable compared to those parallel to the airfoil and parallel to the flat surfaces.

From the measurements presented in the present and the previous chapter, calculations were carried out to examine the magnitudes of the different terms in the streamwise vorticity equation. At axial station X/C = 0.8, these calculations reveal that the various terms in the equation

differ by an order of magnitude. The quantities $(\bar{\Omega}_x \partial\bar{U}/\partial X)$, $(\partial^2/\partial Y^2 - \partial^2/\partial Z^2)(-\overline{vw})$ and $(\partial^2/\partial Y \partial Z)(\overline{v^2} - \overline{w^2})$ are of the same order of magnitude in the vicinity of the corner at this station. But the quantities $(\bar{\Omega}_z \partial\bar{U}/\partial Z)$ and $(\bar{\Omega}_y \partial\bar{U}/\partial Y)$ are one order of magnitude larger at the same locations but possess opposite sign. Therefore, the sum of these two quantities in some regions gives values of the same order of magnitude as the other three terms mentioned above. This was the case very close to the corner at X/C = 0.8. The calculations carried out with measured variations of mean and turbulence quantities indicate that the variation of streamwise vorticity close to the corner was also affected by the Reynolds stress terms in the streamwise vorticity equation leading to the appearance of streamwise vorticity due to turbulence and thus the secondary flow of the second kind. Near the leading edge, on the other hand, $(\bar{\Omega}_x \partial\bar{U}/\partial X)$, $(\bar{\Omega}_y \partial\bar{U}/\partial Y)$ and $(\bar{\Omega}_z \partial\bar{U}/\partial Z)$ are of same order of magnitude and the rest of the terms are negligible leading only to skew induced secondary flow.

5.3 Turbulence Spectra in the Corner

The results of spectral analyses at three axial locations, namely at X/C =0.1, 0.5 and 0.985 are shown in Figs. 5.31 to 5.40. The curves in the figures show the results of the measurements taken nearest to the solid surfaces. Figs. 5.31 to 5.35 are plotted in the wave number

domain in the form $F(\kappa)/u_1'^2$ against κ. Figs. 5.36 to 5.40 show plots of the same spectra, $\omega\Phi(\omega)/u_1'^2$ against ω, on semi-log papers. These plots show relative contribution of each frequency range towards the turbulence kinetic energy.

Fig.5.31 shows the spectra at Y = 1.05 mm and Z = 1.05 mm at the three axial locations. From this figure it is evident that the power spectra can be divided into three distinct regions with different slopes. In the region $\kappa < 1.5 \times 10^3$ 1/m all the three spectra have -1/3 slope, showing that the eddies in this range of wave numbers scale alike. In the range 1.5×10^3 1/m $< \kappa < 4 \times 10^3$ 1/m all the three spectra have -1 slope. In the wave number range above this value, $\kappa > 4 \times 10^3$ 1/m all the three spectra follow a line with slope -7/3.

The spectra at Y = 5.49 mm and Z = 1.05 mm at axial locations X/C = 0.1, 0.5 and 0.985 are shown in Fig. 5.32. In the wave number range $\kappa < 1 \times 10^3$ 1/m, all the three spectra have -1/2 slope. For the wave number range 1×10^3 1/m $< \kappa <$ 4×10^3 1/m, the spectra at X/C = 0.1 and 0.5 have -1 slope and in the range $\kappa > 4 \times 10^3$ 1/m the slopes are -4. However, the spectrum at X/C = 0.985, has -1 slope in a very narrow range of wave number 1×10^3 1/m $< \kappa < 2 \times 10^3$ 1/m, above the

wave number $\kappa > 2 \times 10^3$ 1/m the slope is -5/3.

Fig. 5.33 shows the spectra at Y = 15.65 mm and Z = 1.05 mm at the three axial stations. In this case also the spectra can be divided into three distinct parts. The first part of the spectra has -1/2 slope and for this part the wave number $\kappa < 1.5 \times 10^3$ 1/m. The next region is 1.5×10^3 1/m < $\kappa < 5 \times 10^3$ 1/m; in this range of wave numbers the slope of the spectra is -5/3. In the highest wave number range $\kappa > 5 \times 10^3$ 1/m the slope of the spectra is approximately -4.

At Y = 1.05 mm and Z =6.76 mm the spectra are more diverse as seen in Fig. 5.34. In the wave number range $\kappa < 1.5 \times 10^3$ 1/m the spectra at X/C = 0.1 and 0.985 have -1 slope but the spectrum at X/C = 0.5 has -1/2 slope. In the wave number range $\kappa > 2 \times 10^3$ 1/m, the spectrum at X/C = 0.1 follows a slope of -2 but the spectra at X/C = 0.5 and 0.985 have a slope approximately -4/3.

Fig 5.35 indicates that the structure of turbulence at X/C = 0.1 and Y = 1.05 mm and Z = 18.19 mm is similar to the structure of turbulence present ahead of the airfoil and in the close vicinity of the surface of the flat plate. However, in this case the size of the eddies are slightly larger. At X/C = 0.1, the spectrum has a slope of -2/3 up to

the wave number $\kappa = 10^3$ 1/m, for the wave number range $\kappa > 10^3$ 1/m the spectrum has a slope of -5/3. In the next downstream station X/C = 0.5, up to the wave number $\kappa = 0.5 \times 10^3$ 1/m the slope of the spectrum is -2/3. In the wave number range 0.5×10^3 1/m $< \kappa < 1 \times 10^3$ 1/m the slope is zero and after the wave number exceeds a value of 2×10^3 1/m i.e., $\kappa > 2 \times 10^3$ 1/m, the slope becomes -5/3. In the last station of measurement X/C = 0.985, the slope of the spectrum is -2/3 in the range $\kappa < 1.5 \times 10^3$ 1/m. In the range of wave number 2×10^3 1/m $< \kappa < 5 \times 10^3$ 1/m the slope is approximately -5/3 and thereafter ($\kappa > 5 \times 10^3$ 1/m) the slope becomes -4.

Fig. 5.36 shows the contributions of eddies of different sizes to $u_1'^2$ at Y = 1.05 mm and Z = 1.05 mm at the three axial stations. The curves for X/C = 0.1 and 0.5 do not show any significant variation of contribution by eddies of same frequency at these two stations. At X/C = 0.985, it is evident that the energy associated with the eddies in the frequency range $\omega < 3 \times 10^4$ rad./s. contains approximately 30% more energy than the spectra in the two upstream stations. And in effect, the same amount of energy is reduced from the frequency range $\omega > 3 \times 10^4$ rad./s. It is also important to note that this cross over point ($\omega \simeq 3 \times 10^4$ rad./s.) approximately coincides with the value of wave number ($\kappa =$

1.5 x 10^3 1/m) where the spectra in the wave number domain change its slope from -1/3 to -1.

Fig. 5.37 shows the variation of contribution by different frequency eddies at Y = 5.49 mm and Z = 1.05 mm at the three stations. The behavior of these curves are similar to those in Fig. 5.36. However, in this case the largest contributors to energy are the eddies of frequency ω = 8 x 10^4 rad./s. (as shown by the peaks) instead of the eddies of frequency ω = 5 x 10^4 rad./s. for the points nearest to the corner (Fig. 5.36). Also, the contribution by the same frequency eddies are different (specially in the high frequency range) at X/C = 0.1 and 0.5.

The spectra at Y = 15.65 mm and Z = 1.05 mm have slightly different contributions by the same frequency eddies at the three measuring stations, as seen in Fig. 5.38. For the station at X/C = 0.5 the contribution by the eddies in the mid range of frequencies show lower contribution to energy, compared to the other two spectra. Apart from this the variation in contribution is not as diverse as in the other figures.

The difference in contribution by the eddies of same frequency is quite large from station to station Y = 1.05 mm and Z = 6.76 mm as seen in Fig. 5.39. Out of the three spectra analyzed, the spectrum at X/C = 0.5 has the maximum

difference, whereas the spectra at X/C = 0.1 and 0.985 are closer to each other. The difference is caused by the curvature of the airfoil which affects the turbulence structure more severely than the secondary flow due to the horseshoe vortex because these grid points are very close to the airfoil surface. The contribution by the high frequency ($\omega > 3 \times 10^4$ rad./s.) eddies at X/C = 0.5 is higher compared to the contribution by the high frequency ($\omega > 3 \times 10^4$ rad./s.) eddies at X/C = 0.1 and 0.985, as seen in Fig. 5.39. The stretching of the eddies, due to the acceleration of the flow is responsible for this shift in contribution of energy by the eddies of different frequencies. This effect is partially reduced by deceleration of the flow, thus reducing the difference between the curves at X/C = 0.1 and X/C = 0.985.

The effect of curvature is more severe at Y = 1.05 mm and Z = 18.19 mm (Fig. 5.40). The contribution by the eddies of lower frequencies ($\omega < 2.5 \times 10^4$ rad./s.) reduces to approximately half for the spectrum at X/C = 0.5 as compared to the spectrum at X/C = 0.1. Slight recovery is observed in the spectrum at X/C = 0.985, however the recovery is not as much as was observed in Fig. 5.39; the effect can be attributed to the severity of the secondary flow due to the horseshoe vortex which is more severe nearer to the corner.

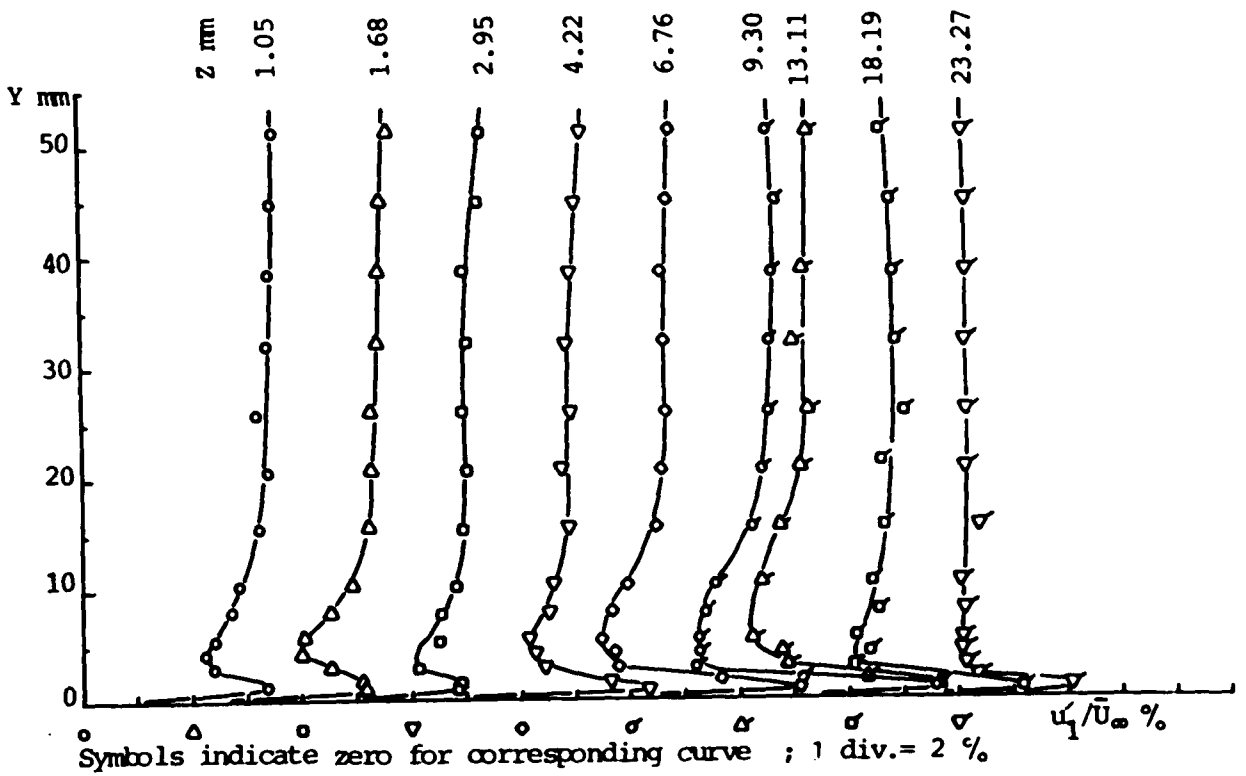

Fig. 5.1 Variation of Streamwise Turbulence Intensity Parallel to the Flat Plate , X = 76 mm , X/C = 0.30

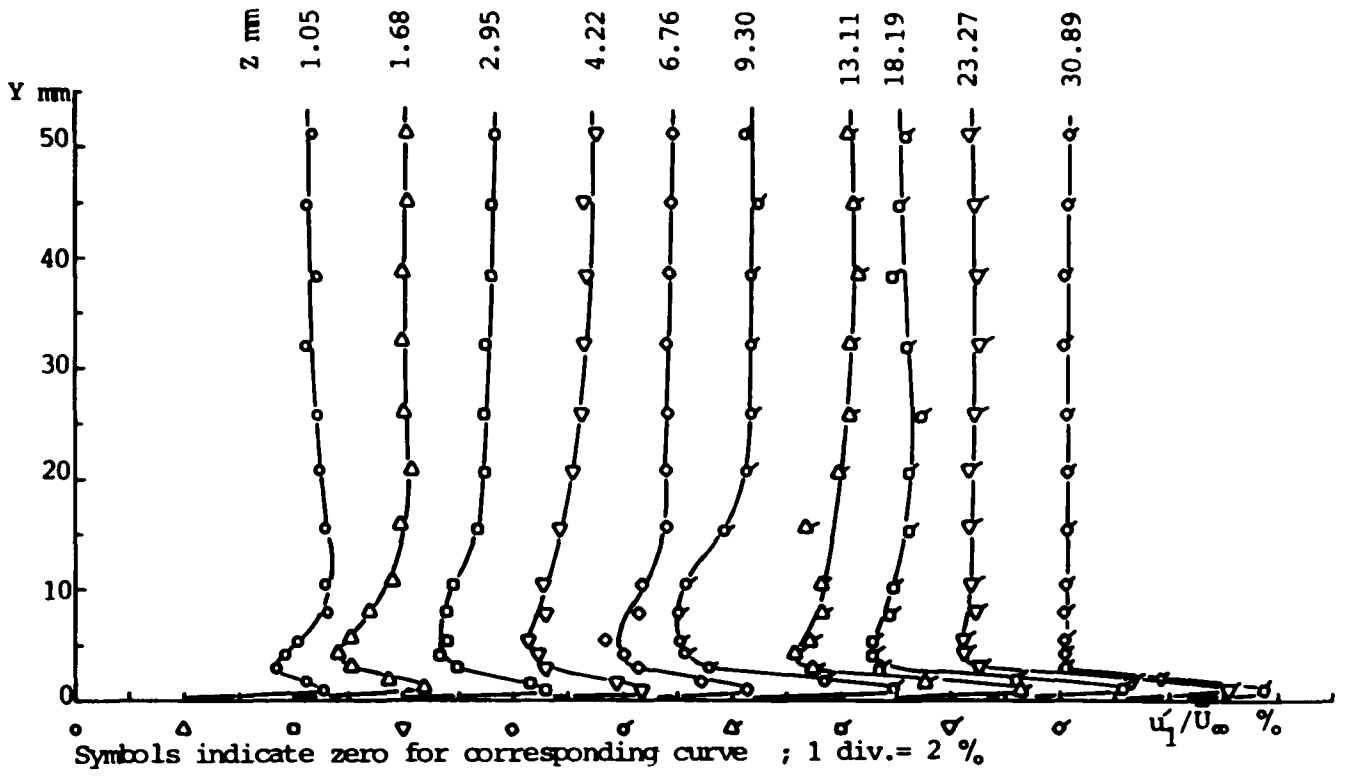

Fig. 5.2 Variation of Streamwise Turbulence Intensity Parallel to the Flat Plate , X = 127 mm , X/C = 0.50

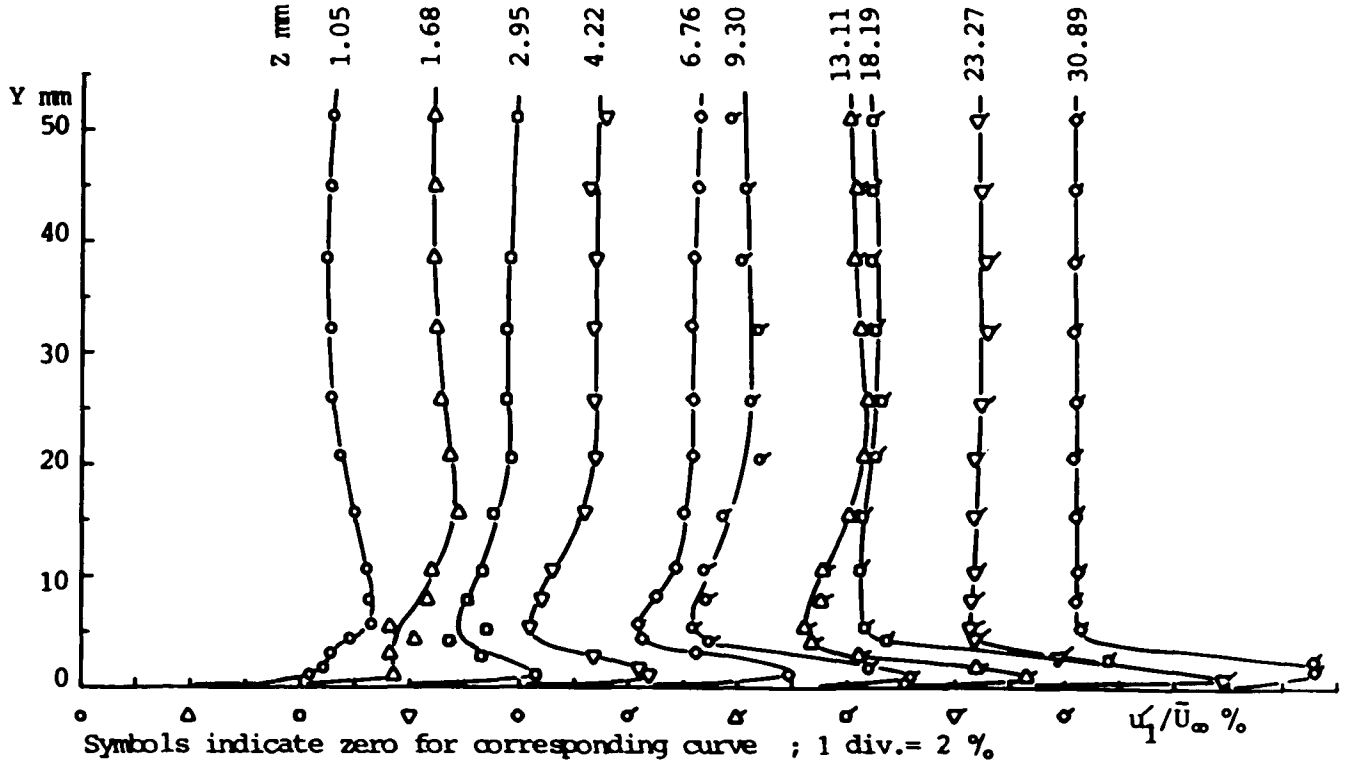

Fig. 5.3 Variation of Streamwise Turbulence Intensity Parallel to the Flat Plate , X = 152 mm , X/C = 0.60

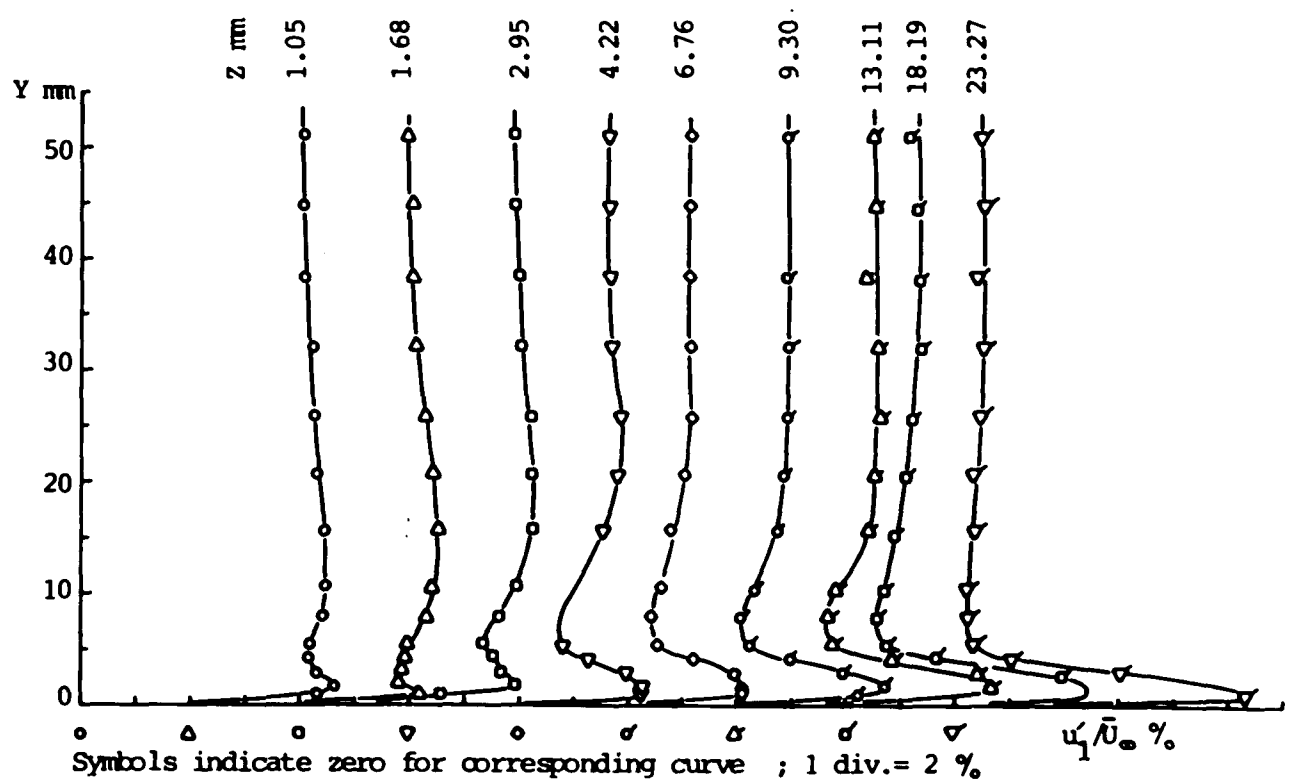

Fig. 5.4 Variation of Streamwise Turbulence Intensity Parallel to the Flat Plate , X = 203 mm , X/C = 0.80

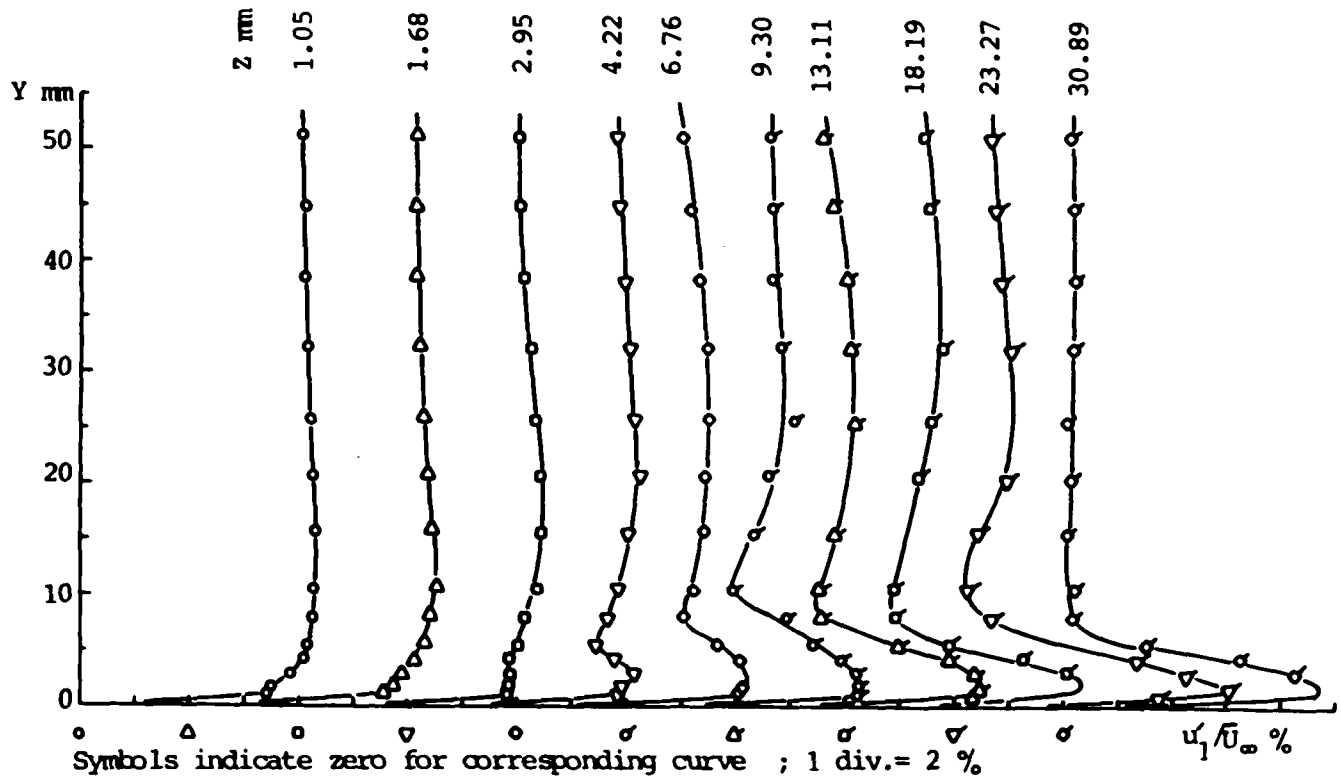

Fig. 5.5 Variation of Streamwise Turbulent Intensity Parallel to the Flat Plate , X = 251 mm , X/C = 0.985

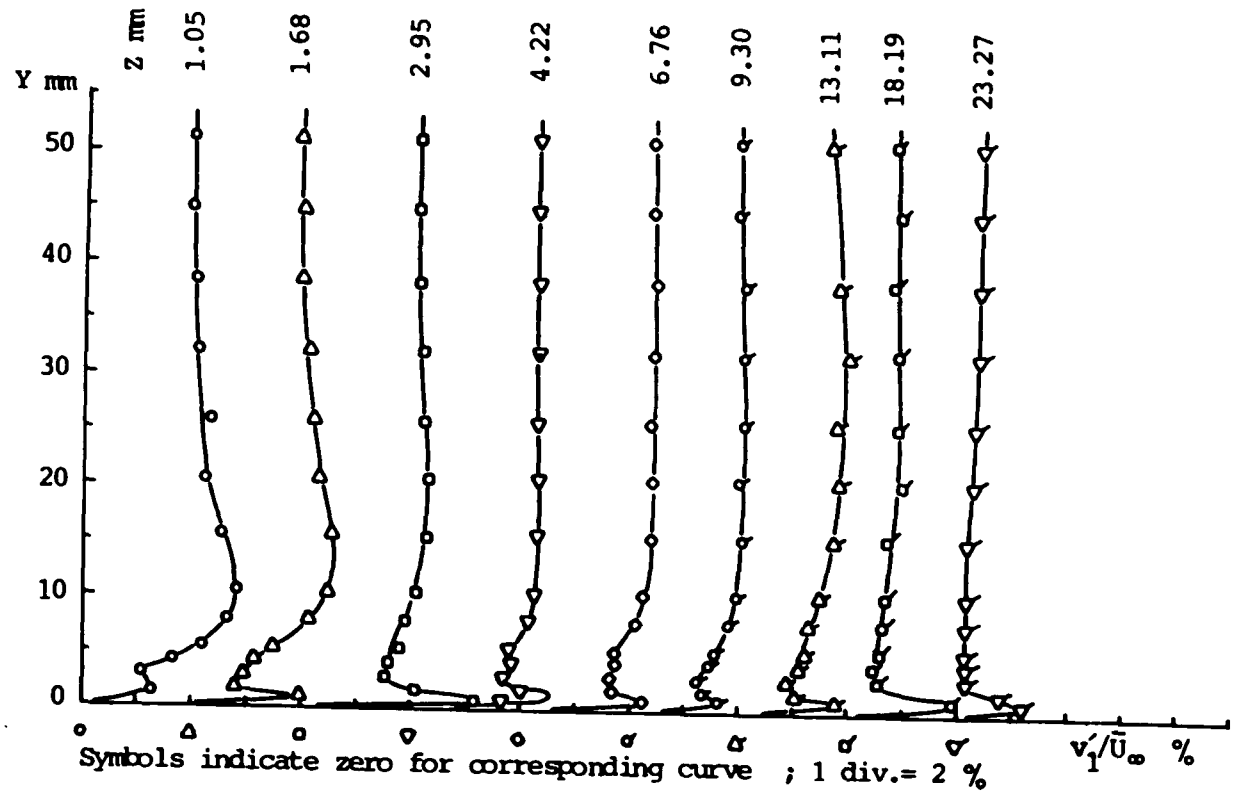

Fig. 5.6 Variation of Transverse Turbulence Intensity Parallel to the Flat Plate , X = 76 mm , X/C = 0.30

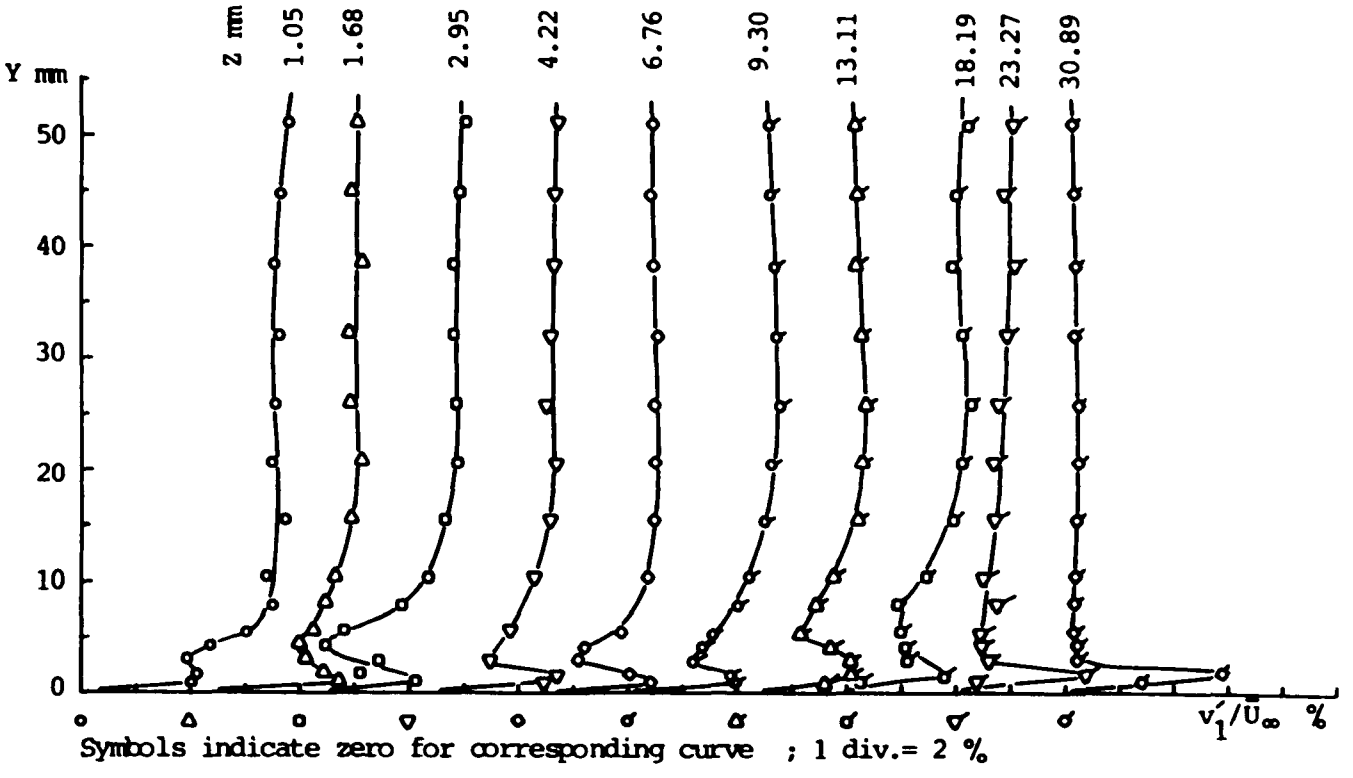

Fig. 5.7 Variation of Transverse Turbulence Intensity Parallel to the Flat Plate , X = 127 mm , X/C = 0.50

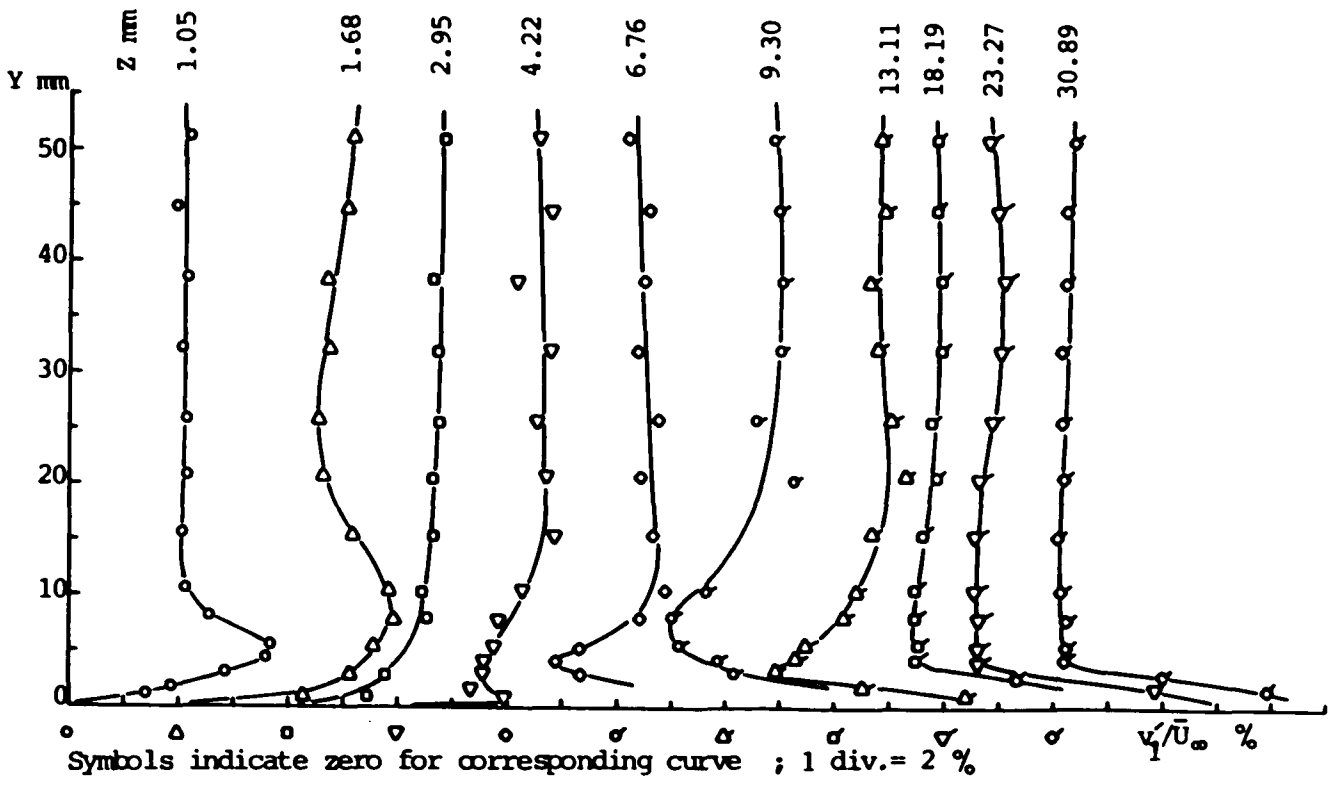

Fig. 5.8 Variation of Transverse Turbulence Intensity Parallel to the Flat Plate , X = 152 mm , X/C = 0.60

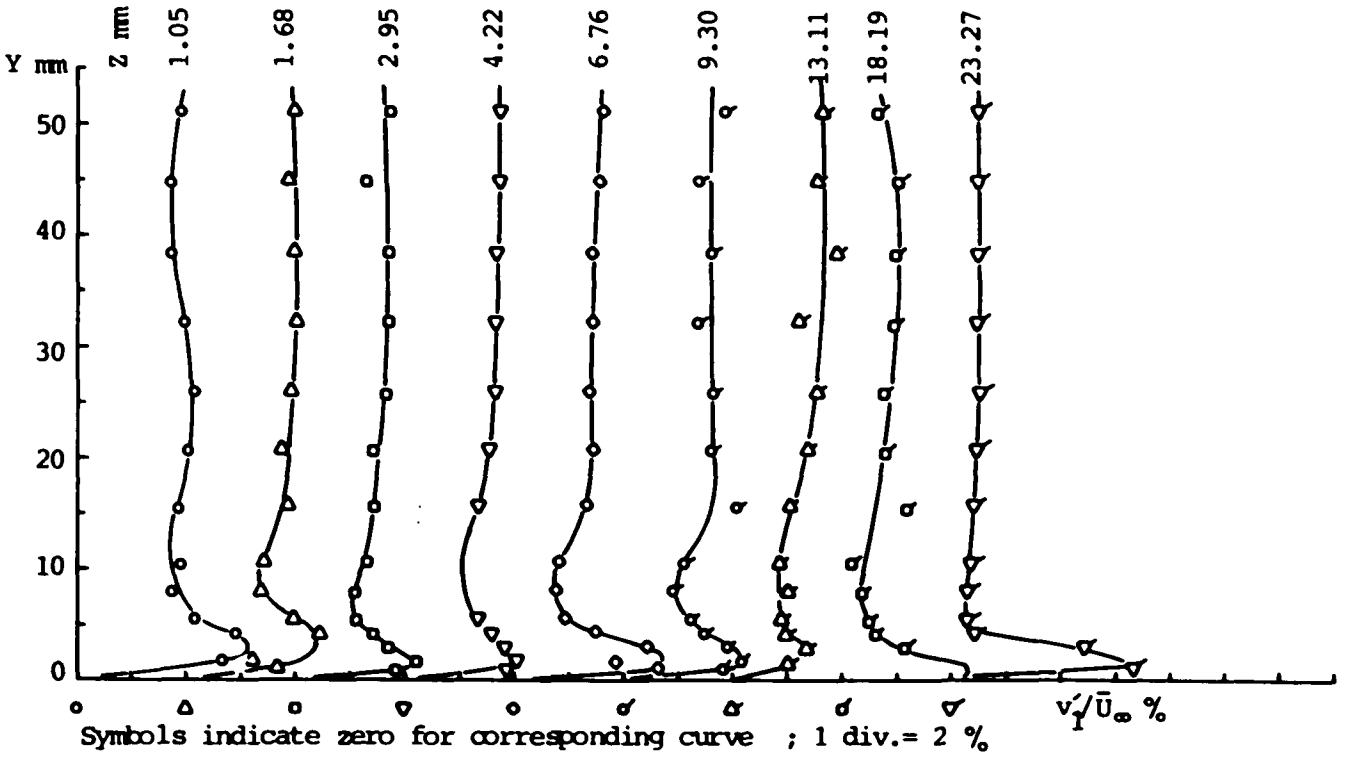

Fig. 5.9 Variation of Transverse Turbulence Intensity Parallel to the Flat Plate , X = 203 mm , X/C = 0.80

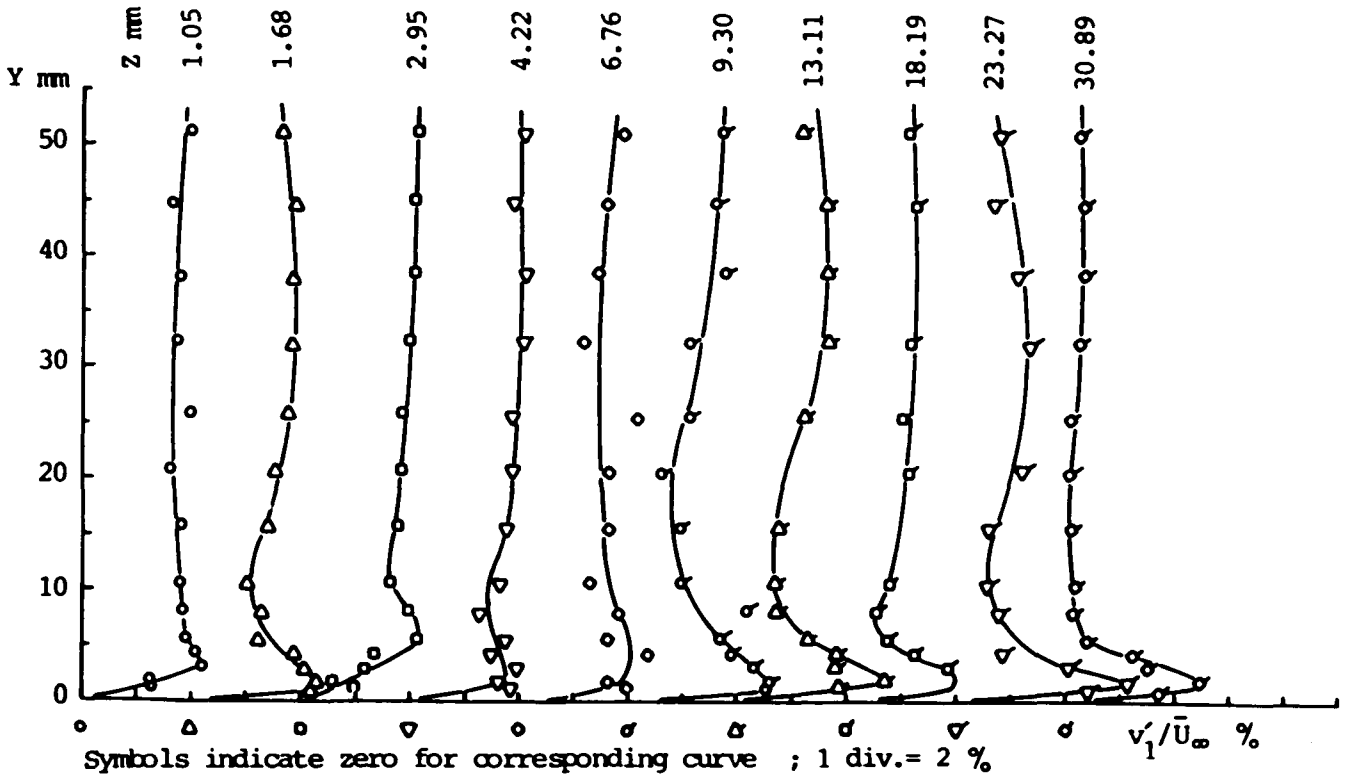

Fig. 5.10 Variation of Transverse Turbulence Intensity Parallel to the Flat Plate , X = 251 mm , X/C = 0.985

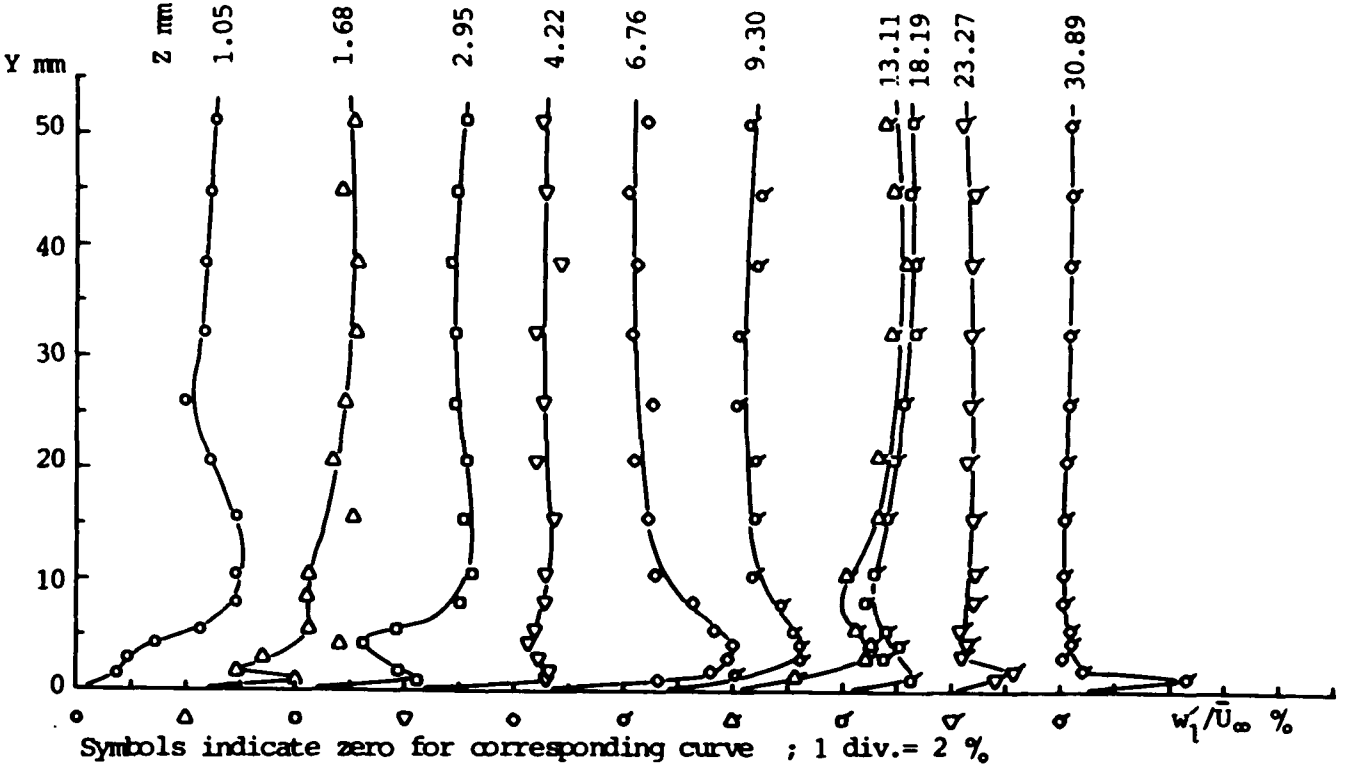

Fig. 5.11 Variation of Spanwise Turbulence Intensity Parallel to the Flat Plate , X = 76 mm , X/C = 0.30

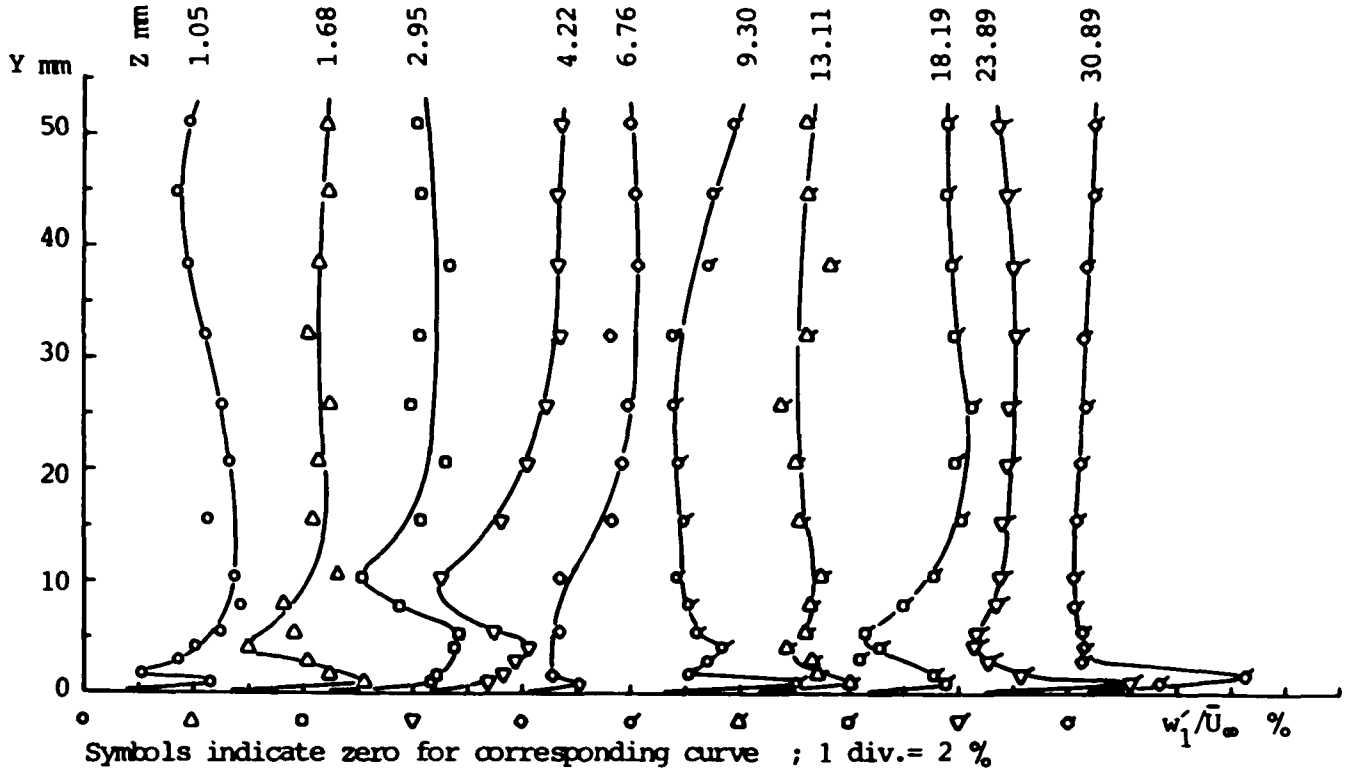

Fig. 5.12 Variation of Spanwise Turbulence Intensity Parallel to the Flat Plate , X = 127 mm , X/C = 0.50

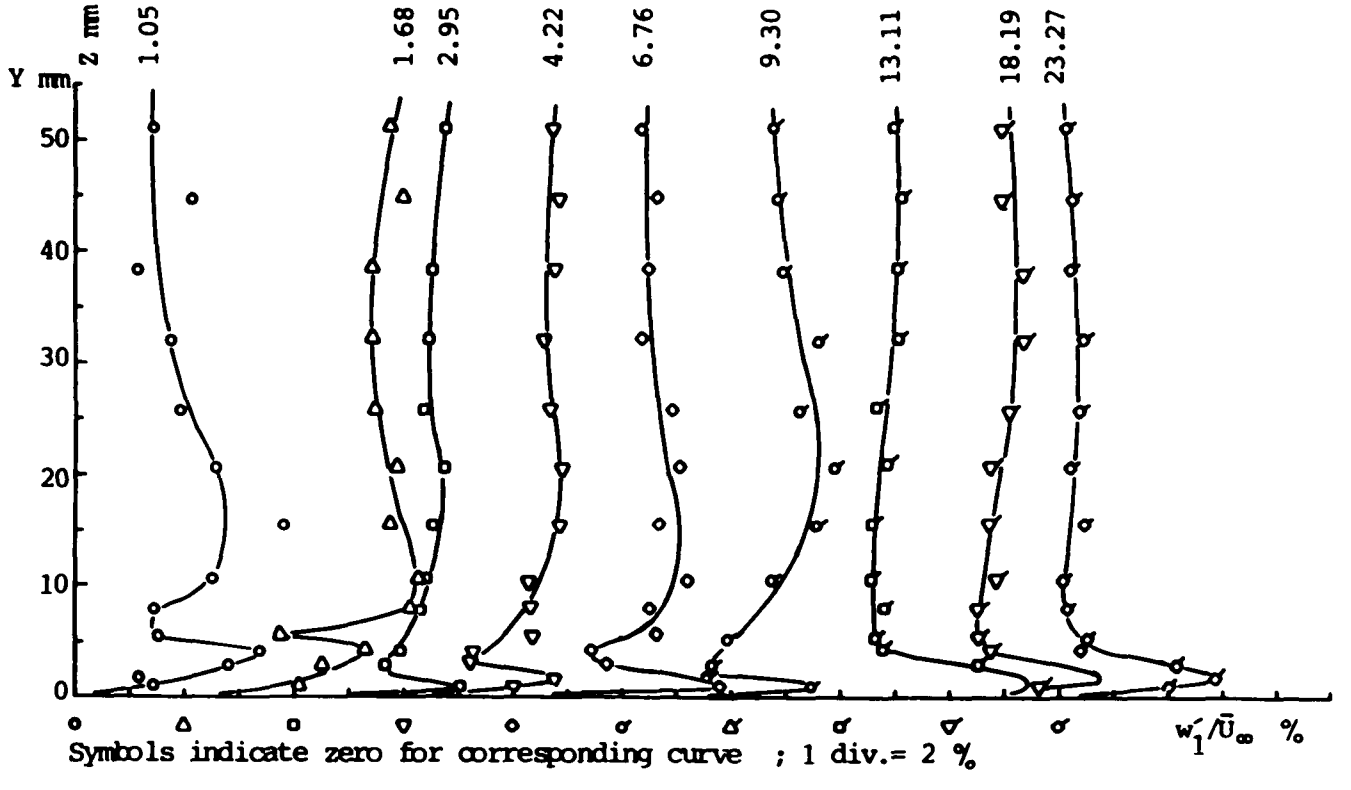

Fig. 5.13 Variation of Spanwise Turbulence Intensity Parallel to the Flat Plate , X = 152 mm , X/C = 0.60

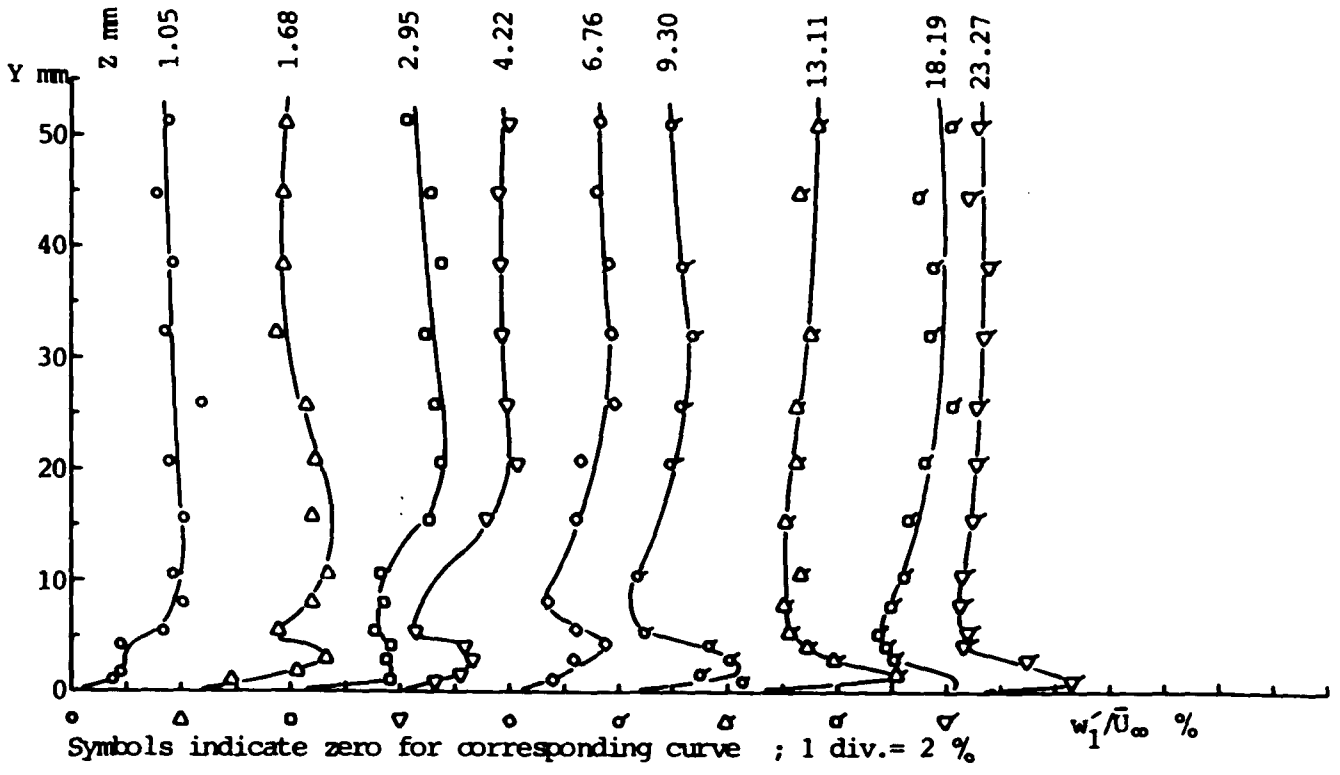

Fig. 5.14 Variation of Spanwise Turbulence Intensity Parallel to the Flat Plate , X = 203 mm , X/C = 0.80

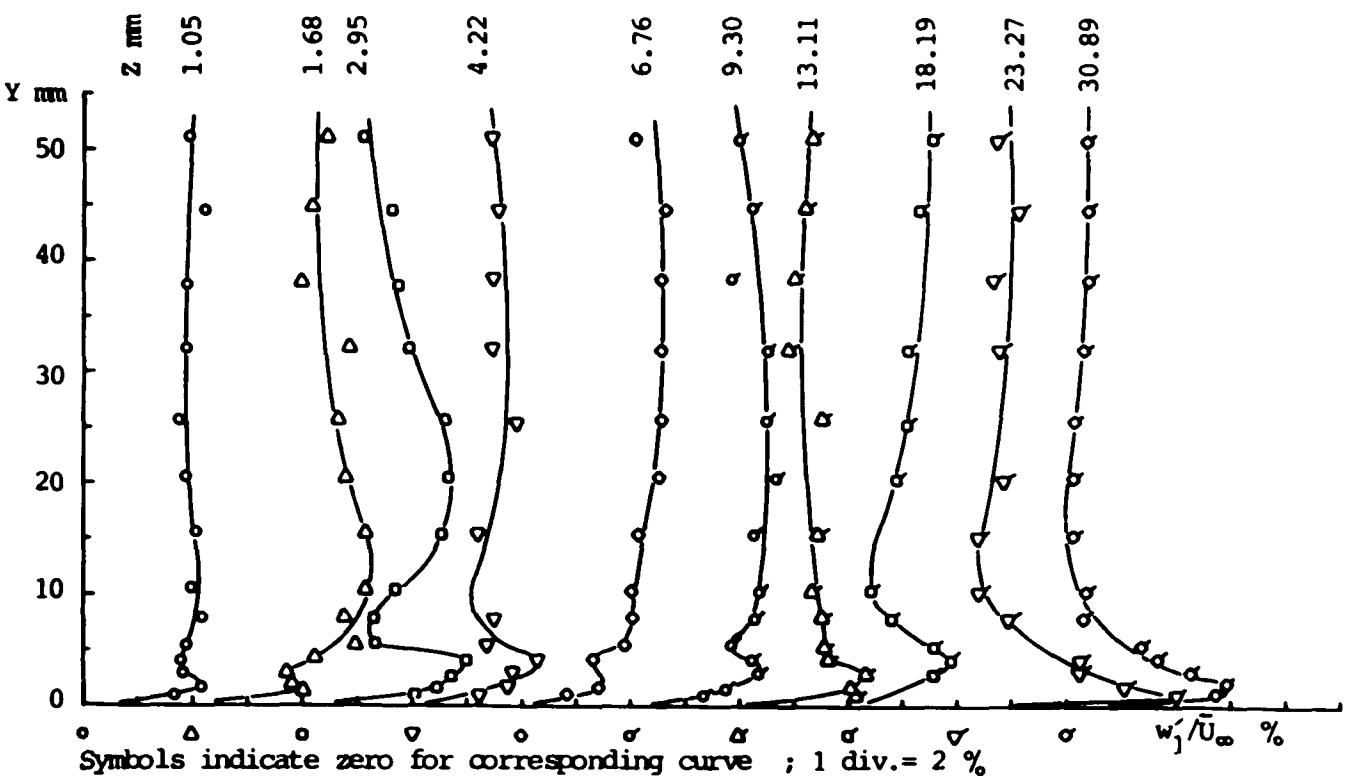

Fig. 5.15 Variation of Spanwise Turbulence Intensity Parallel to the Flat Plate , X = 251 mm , X/C = 0.985

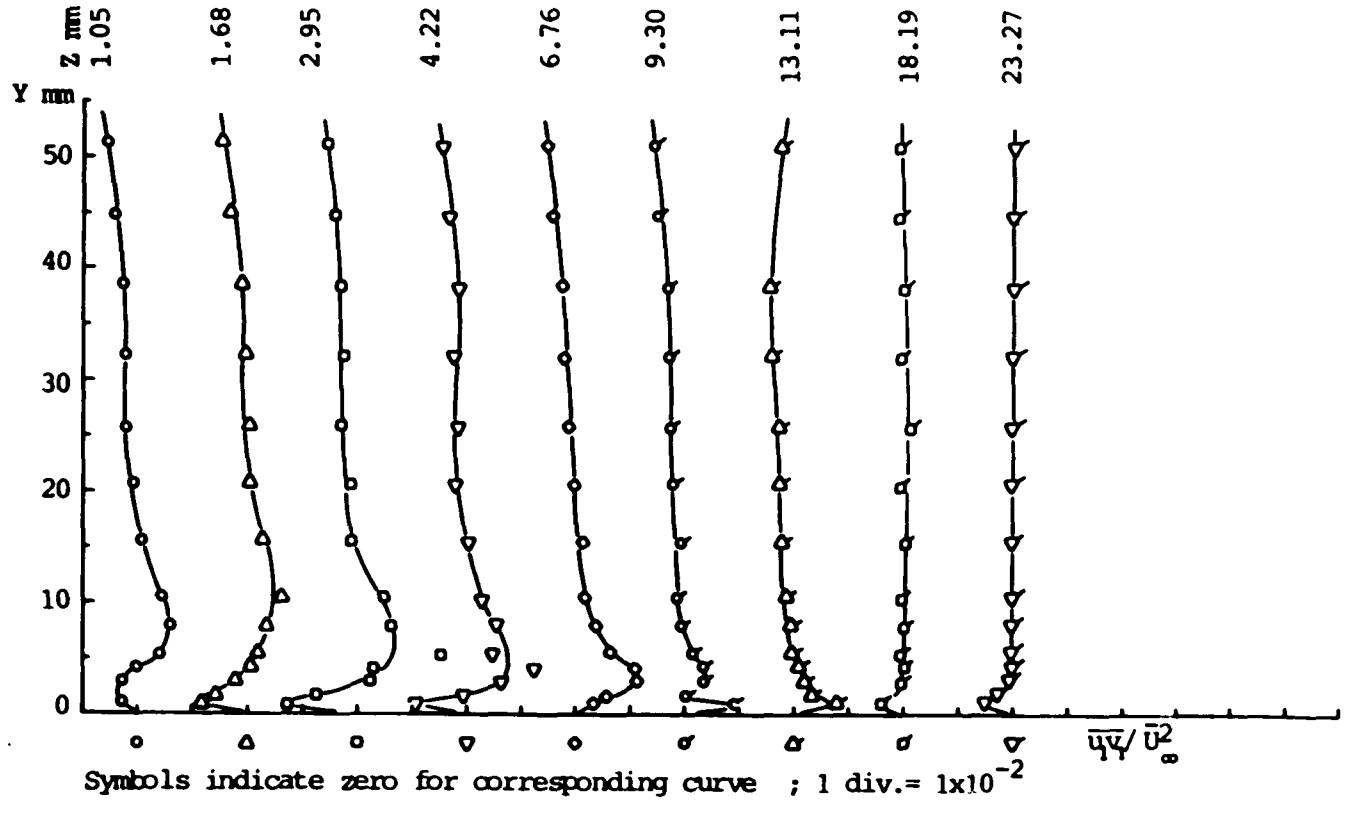

Fig. 5.16 Variation of $\overline{uv}/\bar{U}_\infty^2$ Parallel to the Flat Plate
X = 76 mm, X/C = 0.30

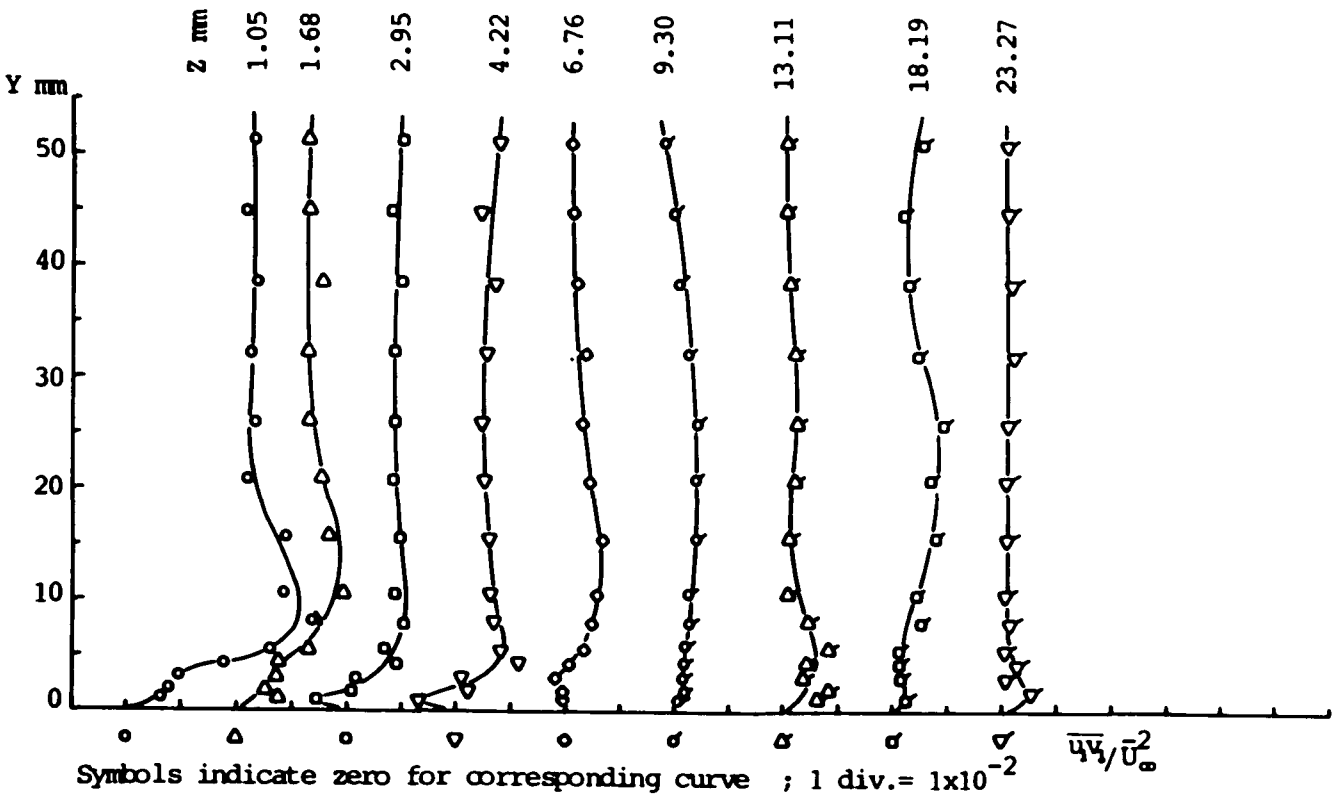

Fig. 5.17 Variation of $\overline{uv}/\bar{U}_\infty^2$ Parallel to the Flat Plate
X = 127 mm , X/C = 0.50

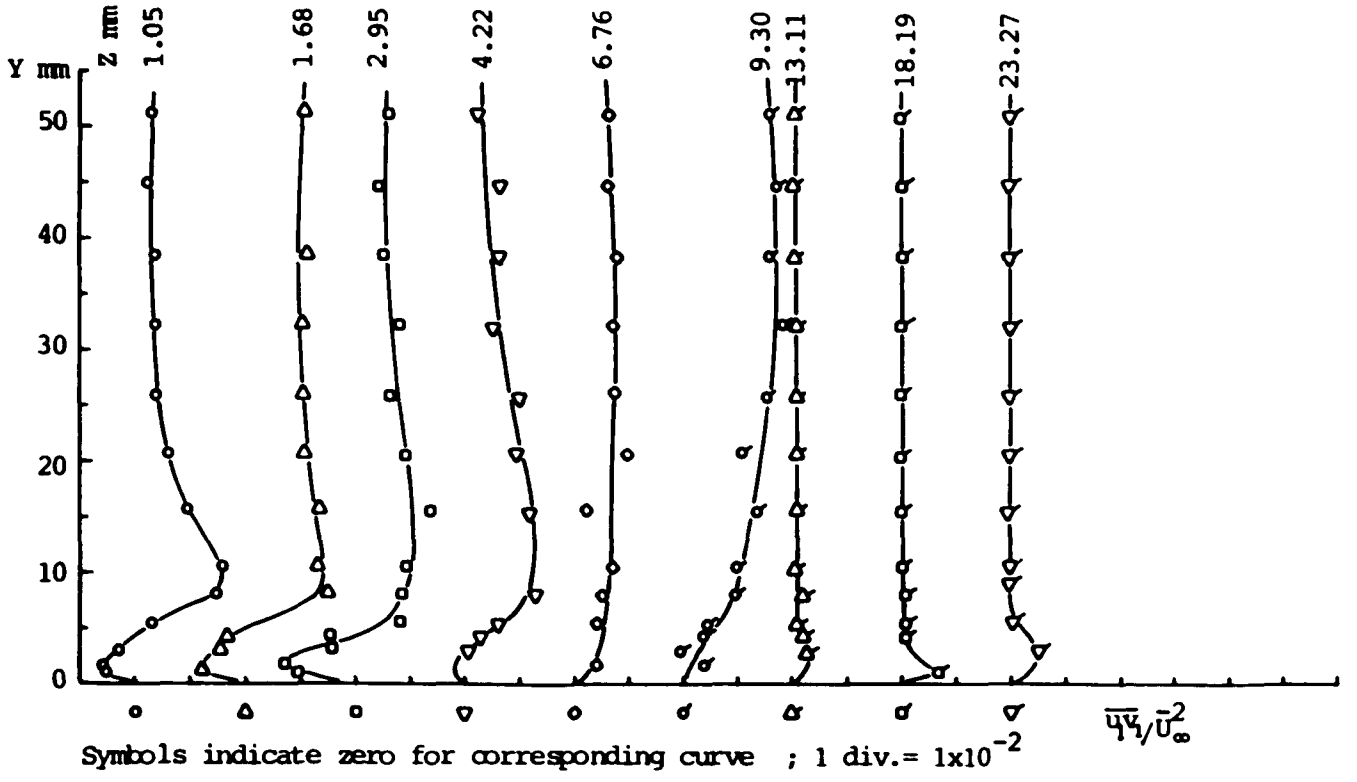

Fig. 5.18 Variation of $\overline{u_1u_1}/\tilde{U}_\infty^2$ Parallel to the Flate Plate
X = 152 mm , X/C = 0.60

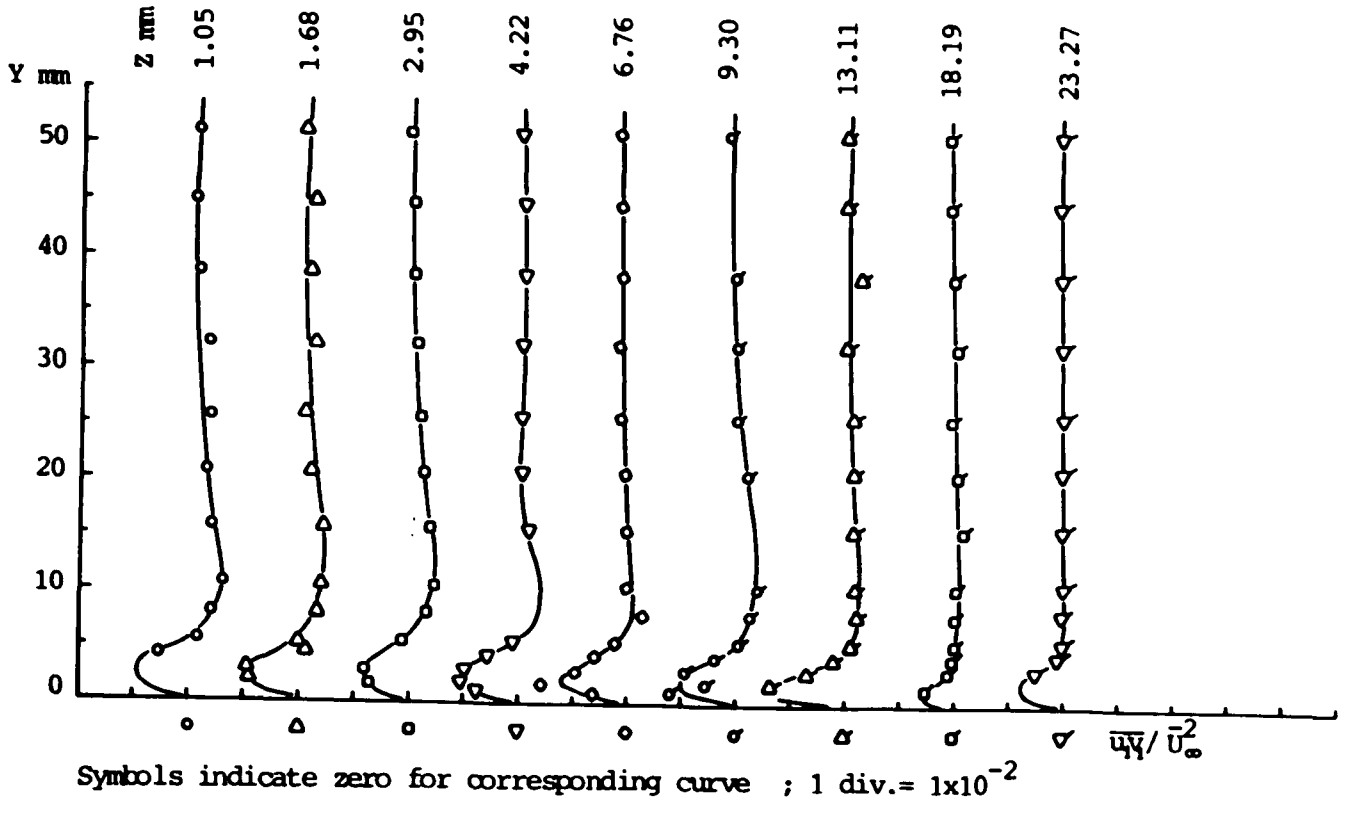

Fig. 5.19 Variation of $\overline{uv}/\bar{U}_\infty^2$ Parallel to the Flat Plate
X = 205 mm , X/C = 0.80

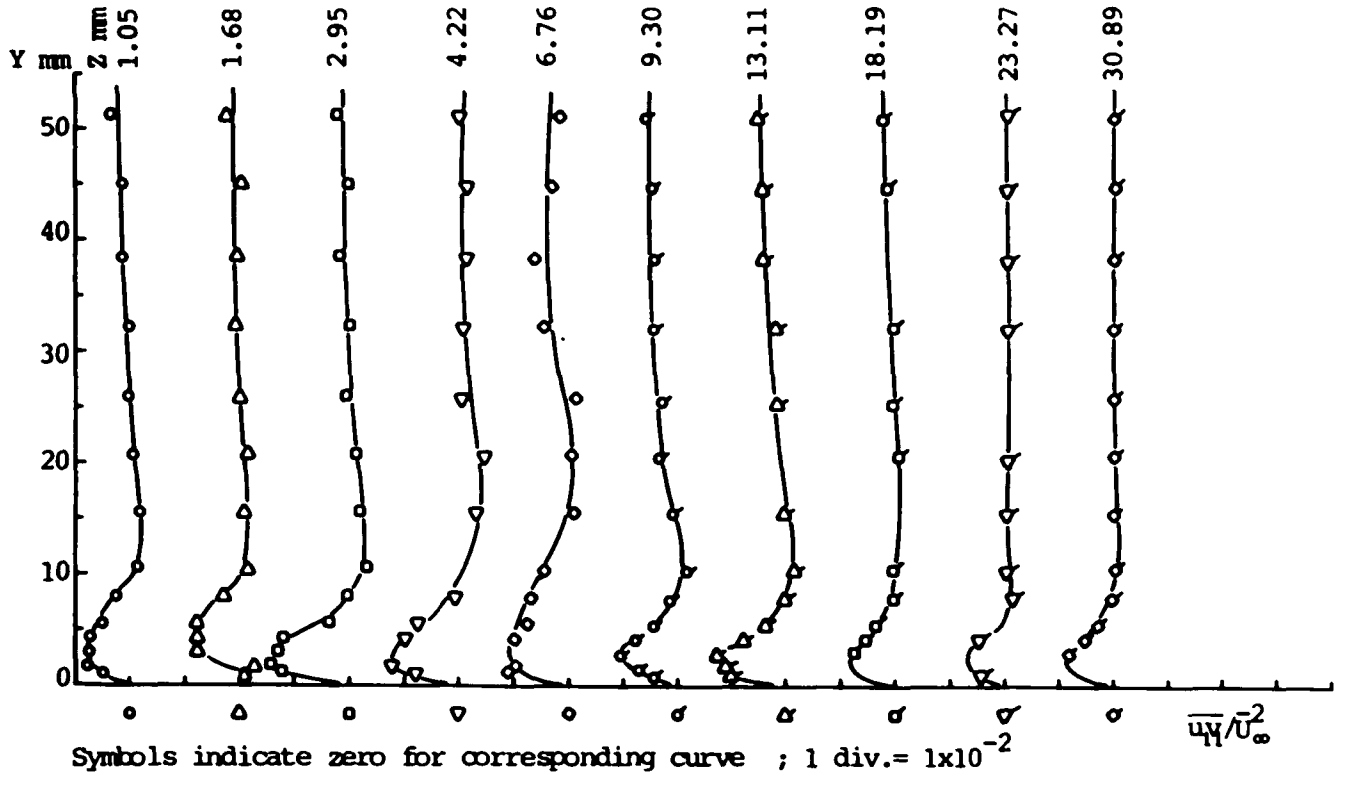

Fig. 5.20 Variation of $\overline{uv}/\bar{U}_\infty^2$ Parallel to the Flat Plate
X = 251 mm , X/C = 0.985

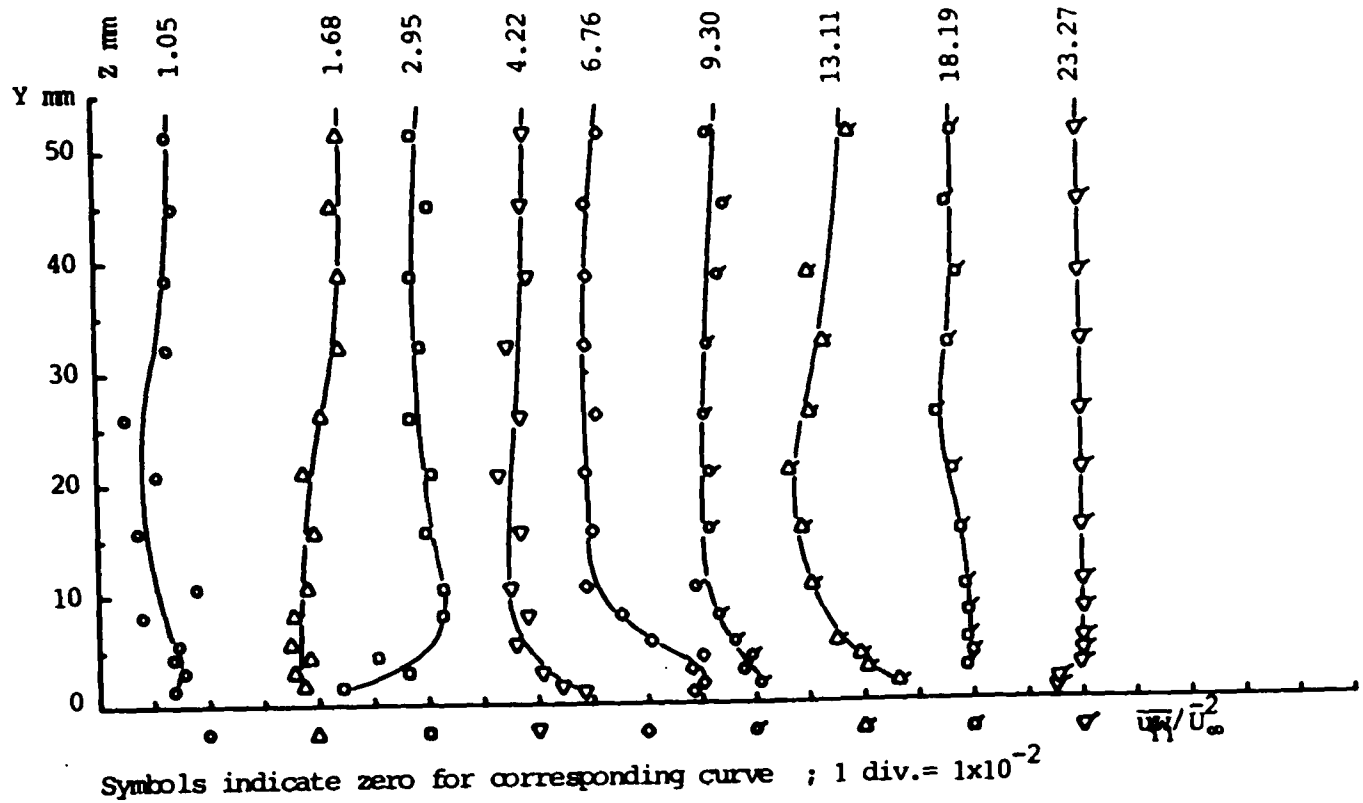

Fig. 5.21 Variation of $\overline{uv}/\bar{U}_\infty^2$ Parallel to the Flat Plate
X = 76 mm , X/C = 0.30

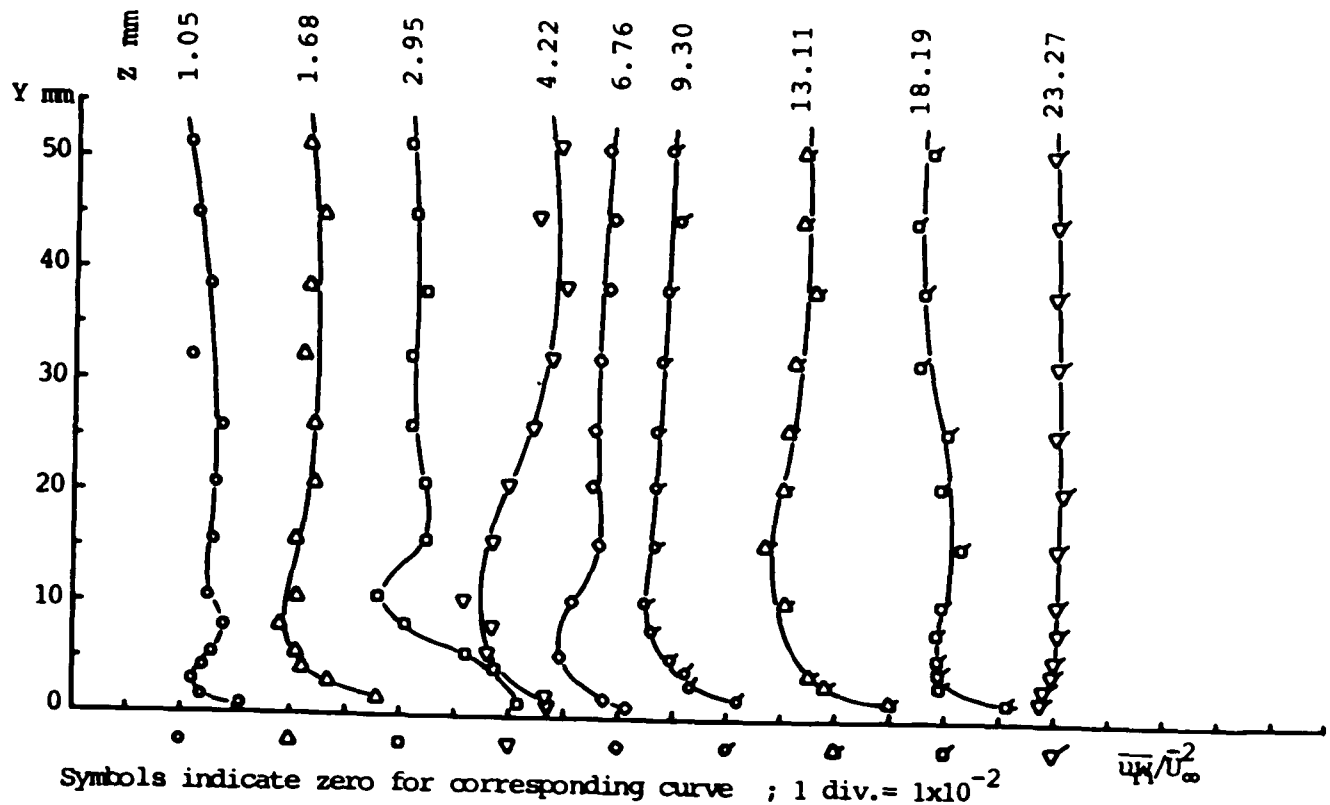

Fig. 5.22 Variation of $\overline{uw}/\bar{U}_\infty^2$ Parallel to the Flat Plate
X = 127 mm , X/C = 0.50

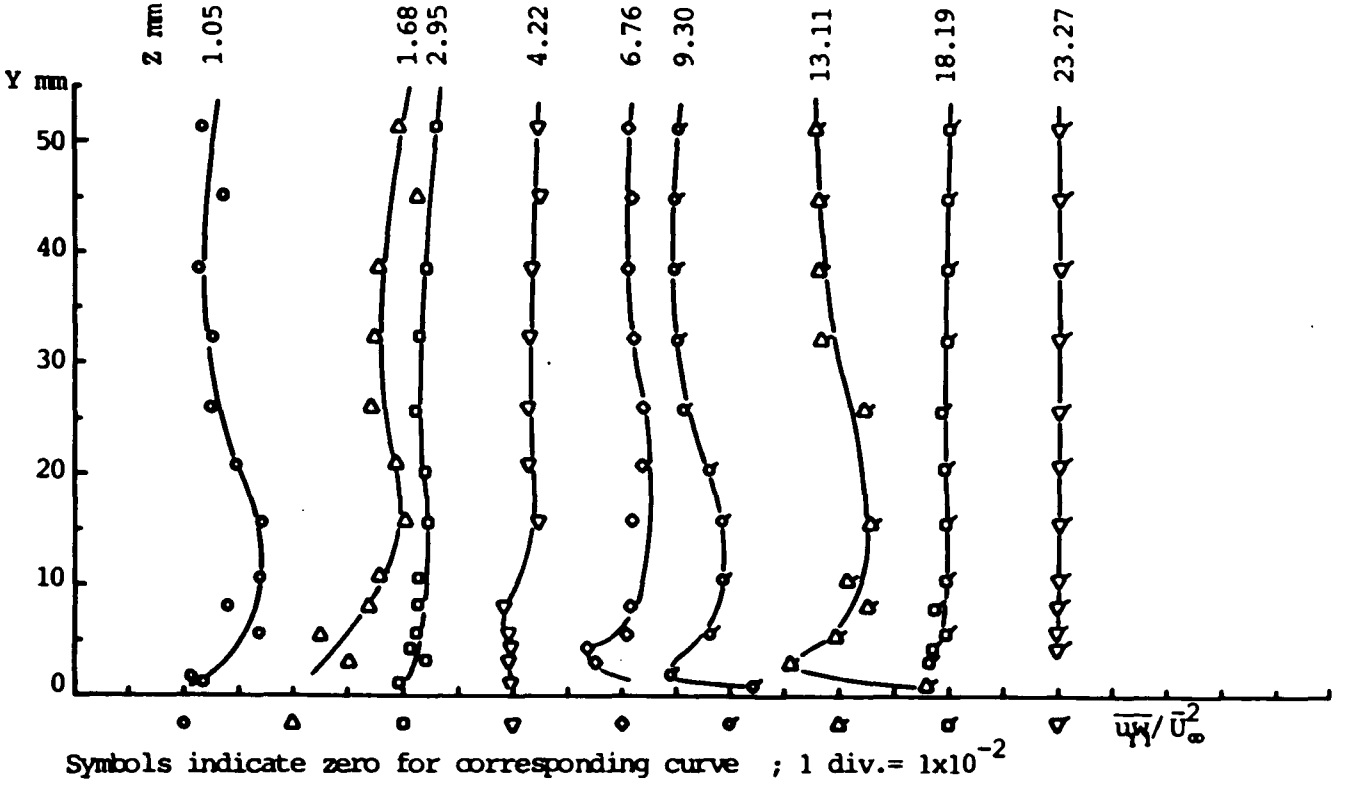

Fig. 5.23 Variation of $\overline{uw}/\bar{U}_\infty^2$ Parallel to the Flat Plate
X = 152 mm , X/C = 0.60

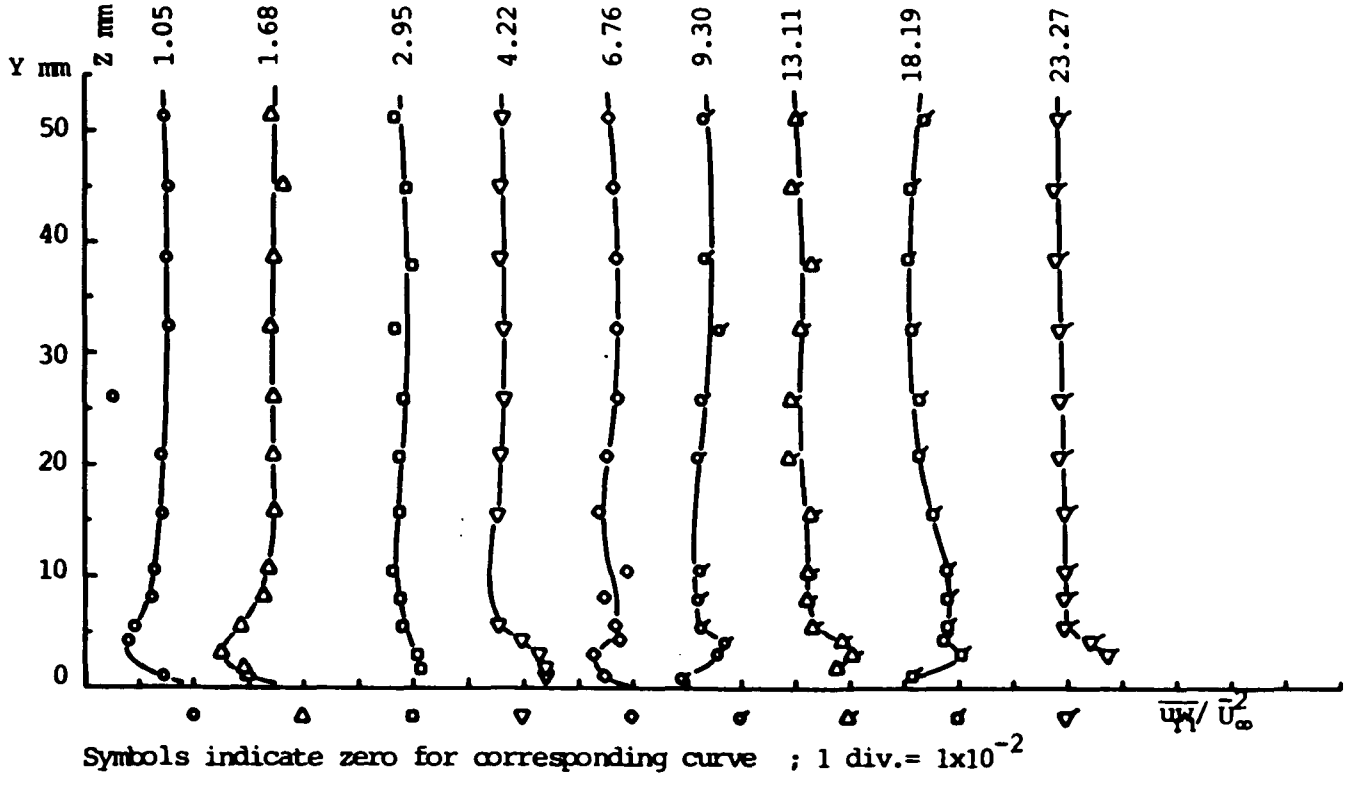

Fig. 5.24 Variation of $\overline{uv}/\bar{U}_\infty^2$ Parallel to the Flat Plate
X = 203 mm , X/C = 0.80

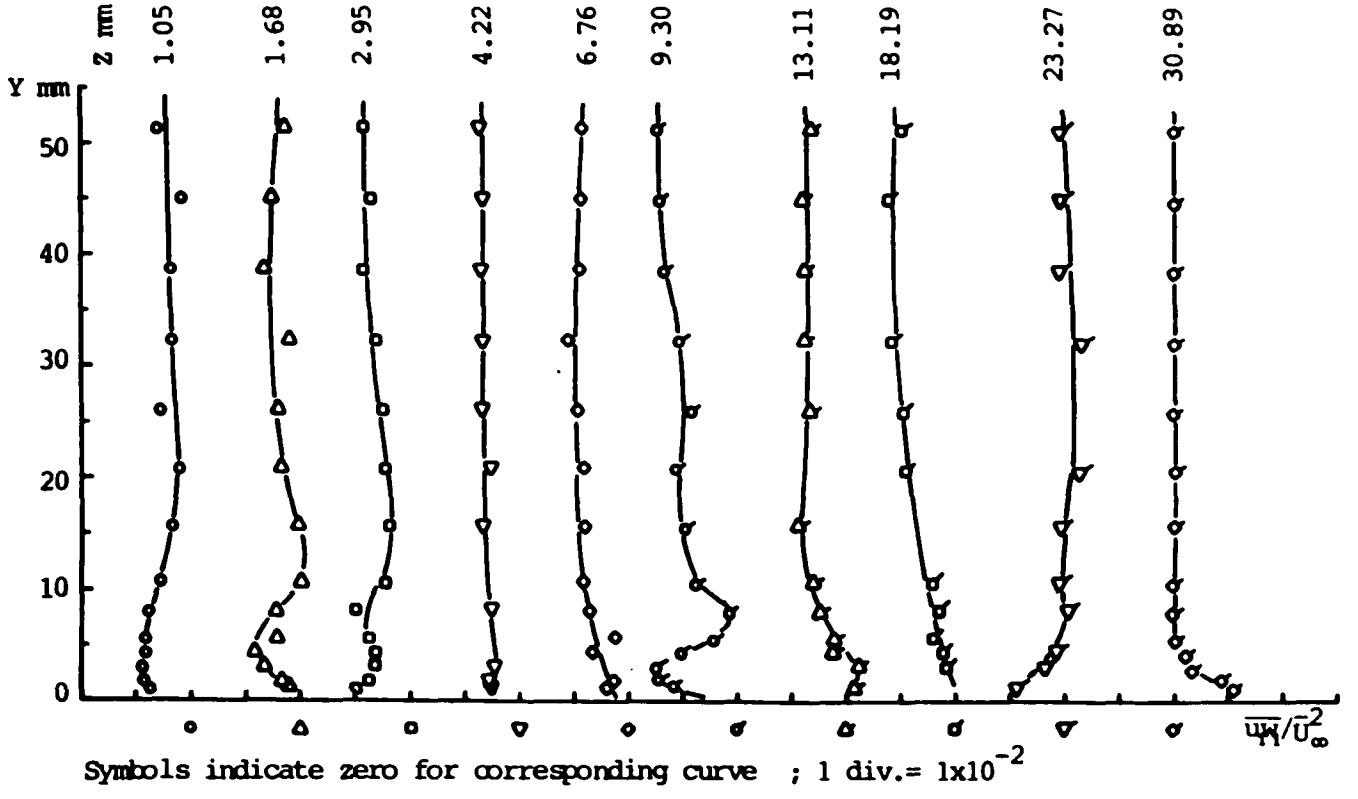

Fig. 5.25 Variation of $\overline{uw}/\bar{U}_\infty^2$ Parallel to the Flat Plate
X = 251 mm , X/C = 0.985

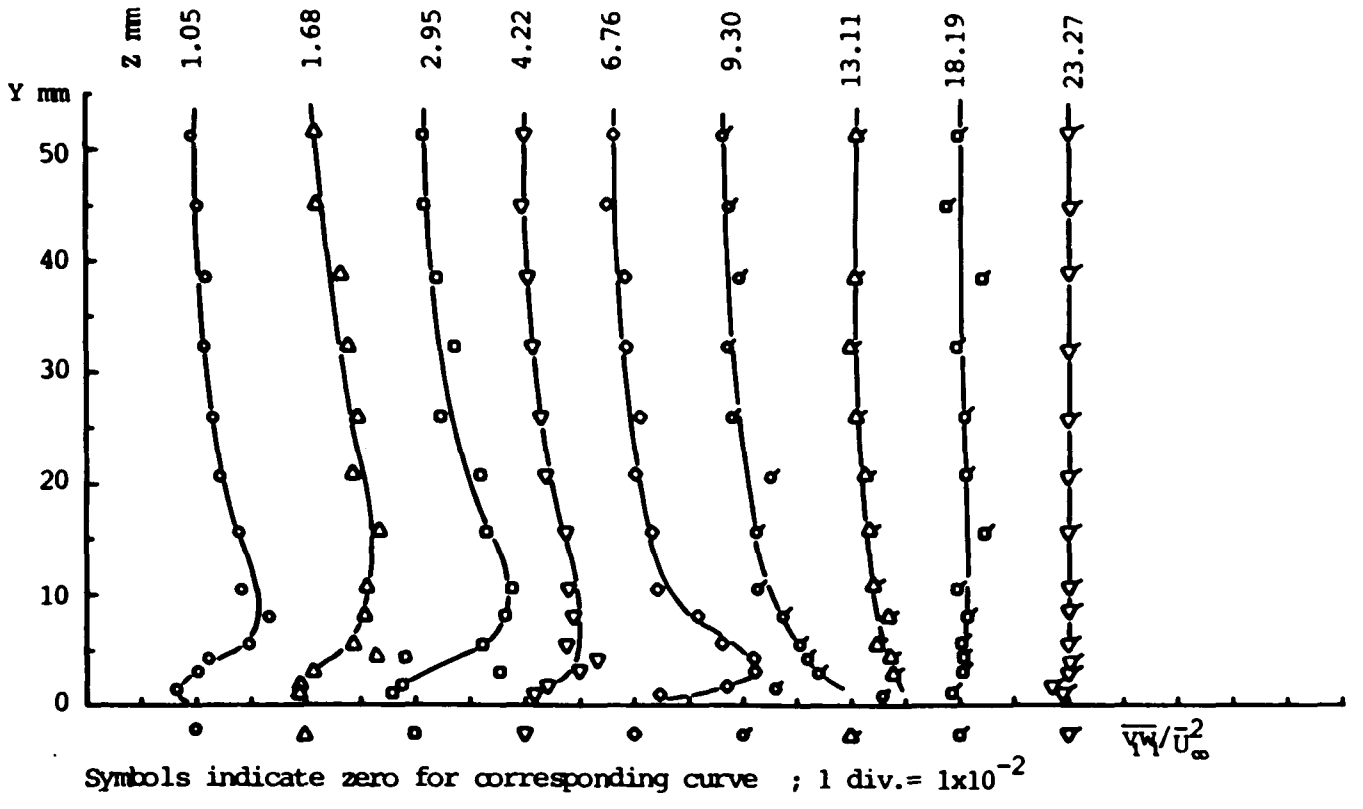

Fig. 5.26 Variation of $\overline{vw}/\bar{U}_\infty^2$ Parallel to the Flat Plate
X = 76 mm , X/C = 0.30

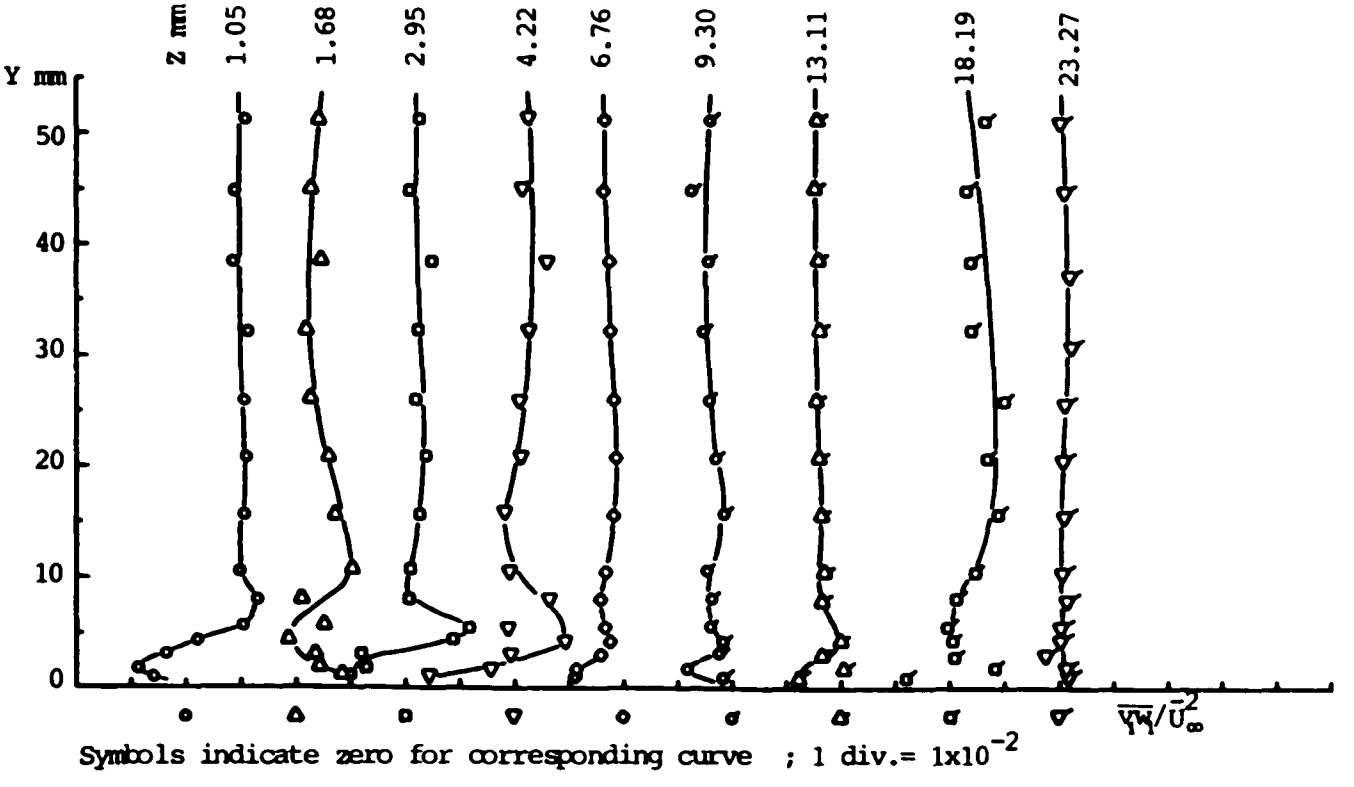

Fig. 5.27 Variation of $\overline{vw}/\bar{U}_\infty^2$ Parallel to the Flat Plate
X = 127 mm , X/C = 0.50

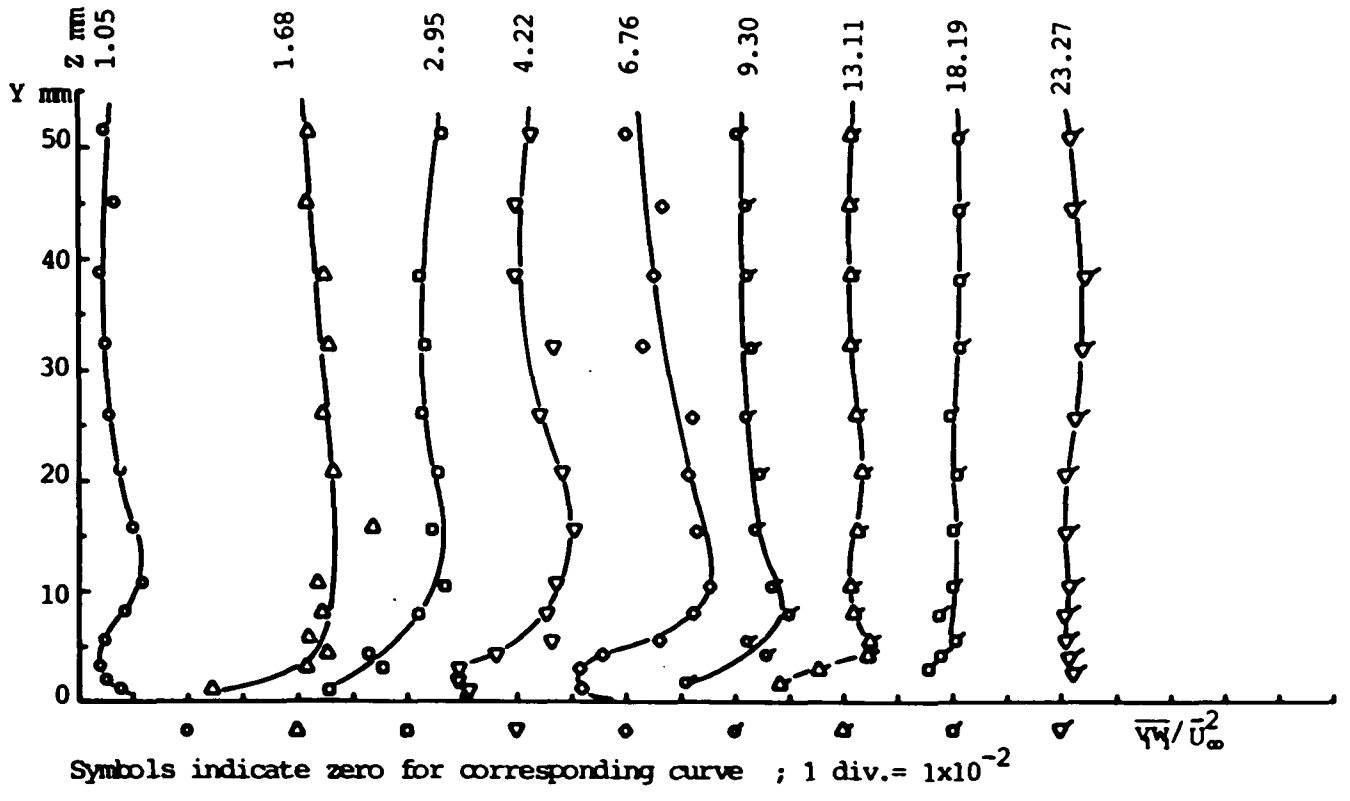

Fig. 5.28 Variation of $\overline{vw}/\bar{U}_\infty^2$ Parallel to the Flat Plate
X = 152 mm , X/C = 0.60

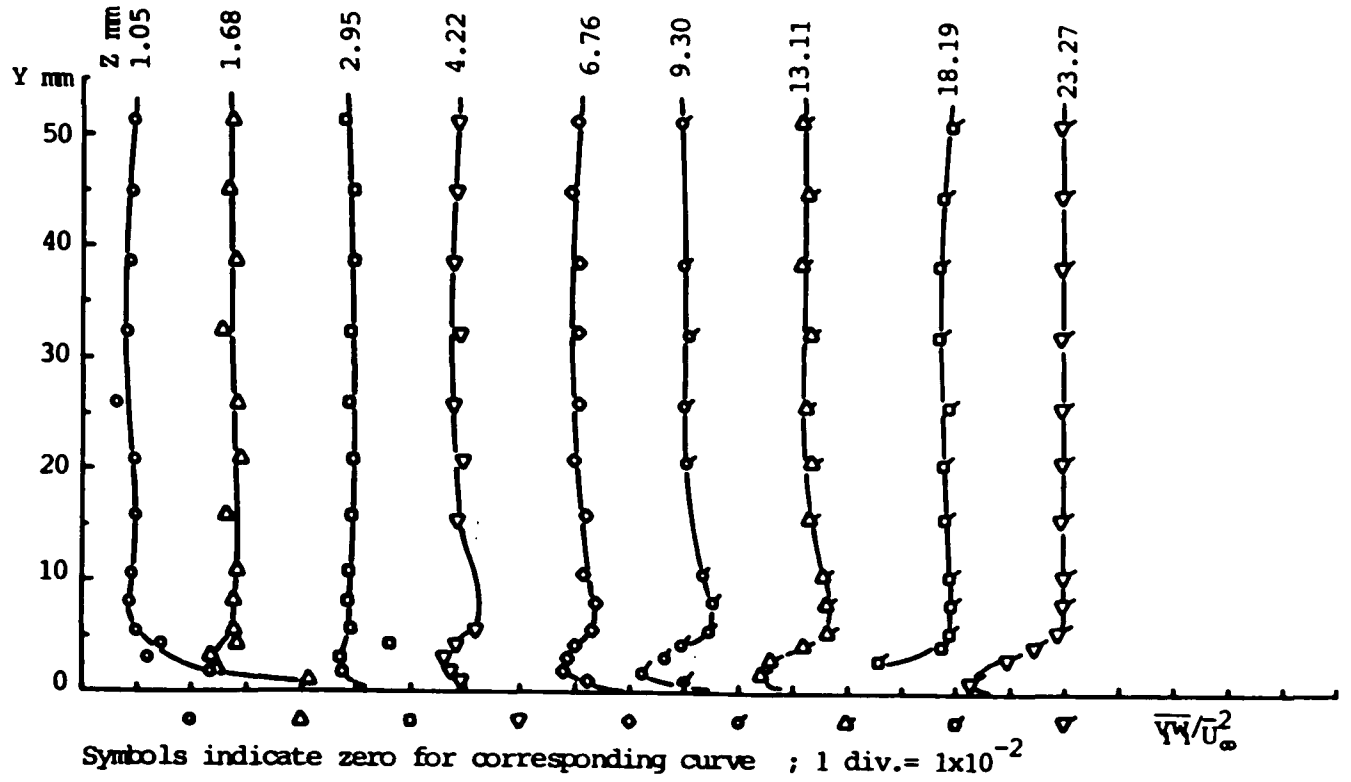

Fig. 5.29 Variation of $\overline{vw}/\bar{U}_\infty^2$ Parallel to the Flat Plate
X = 203 mm , X/C = 0.80

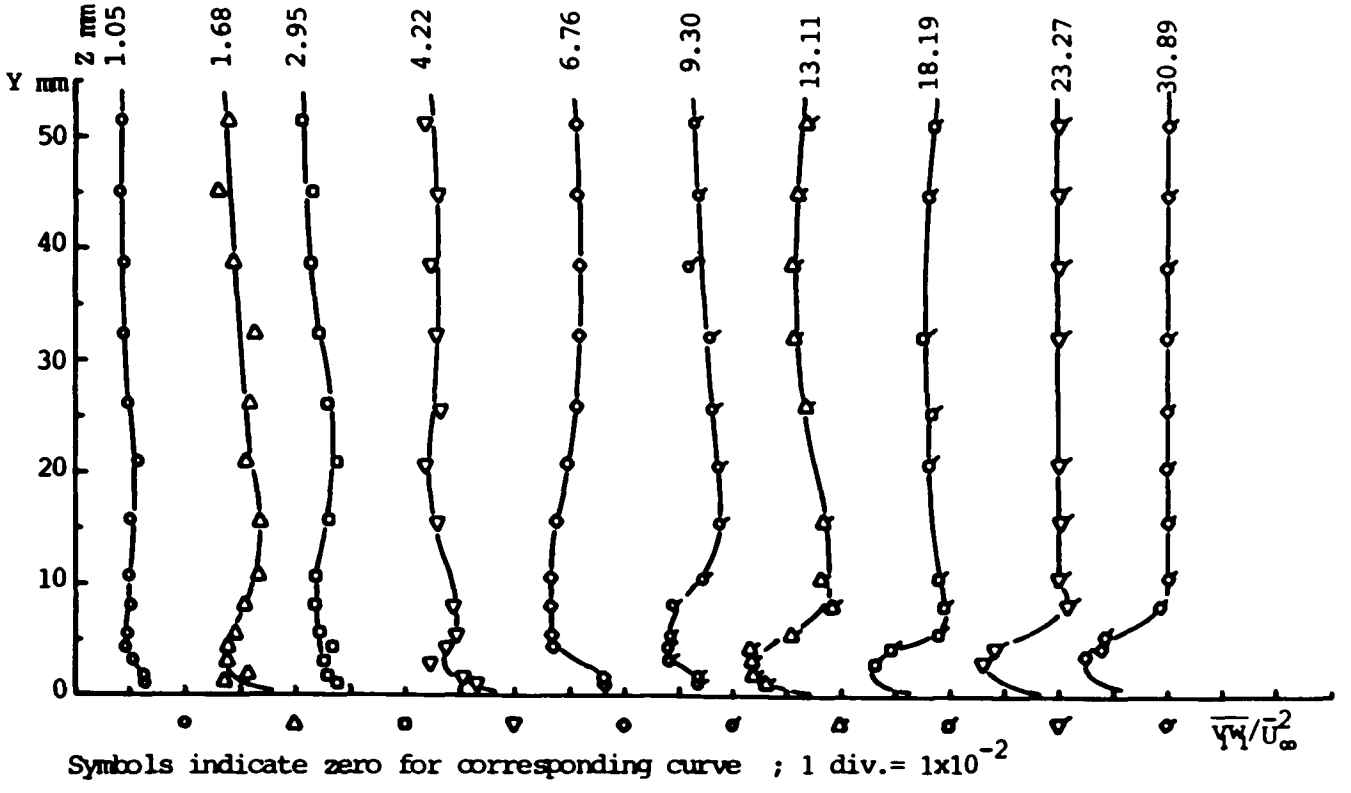

Fig. 5.30 Variation of $\overline{vw}/\bar{U}_\infty^2$ Parallel to the Flat Plate
X = 251 mm , X/C = 0.985

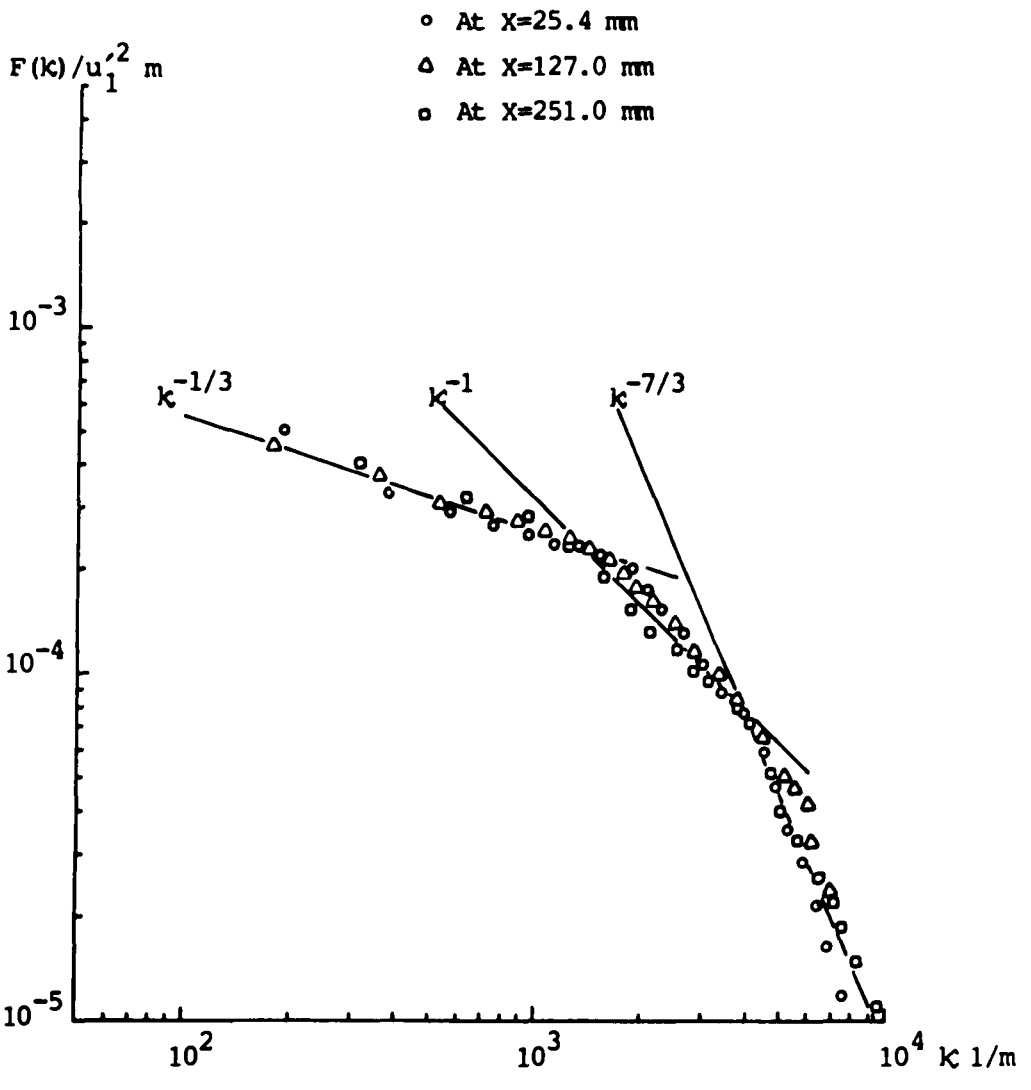

Fig. 5.31 Evolution of Power Spectra Along the Corner
Y = 1.05 mm , Z = 1.05 mm

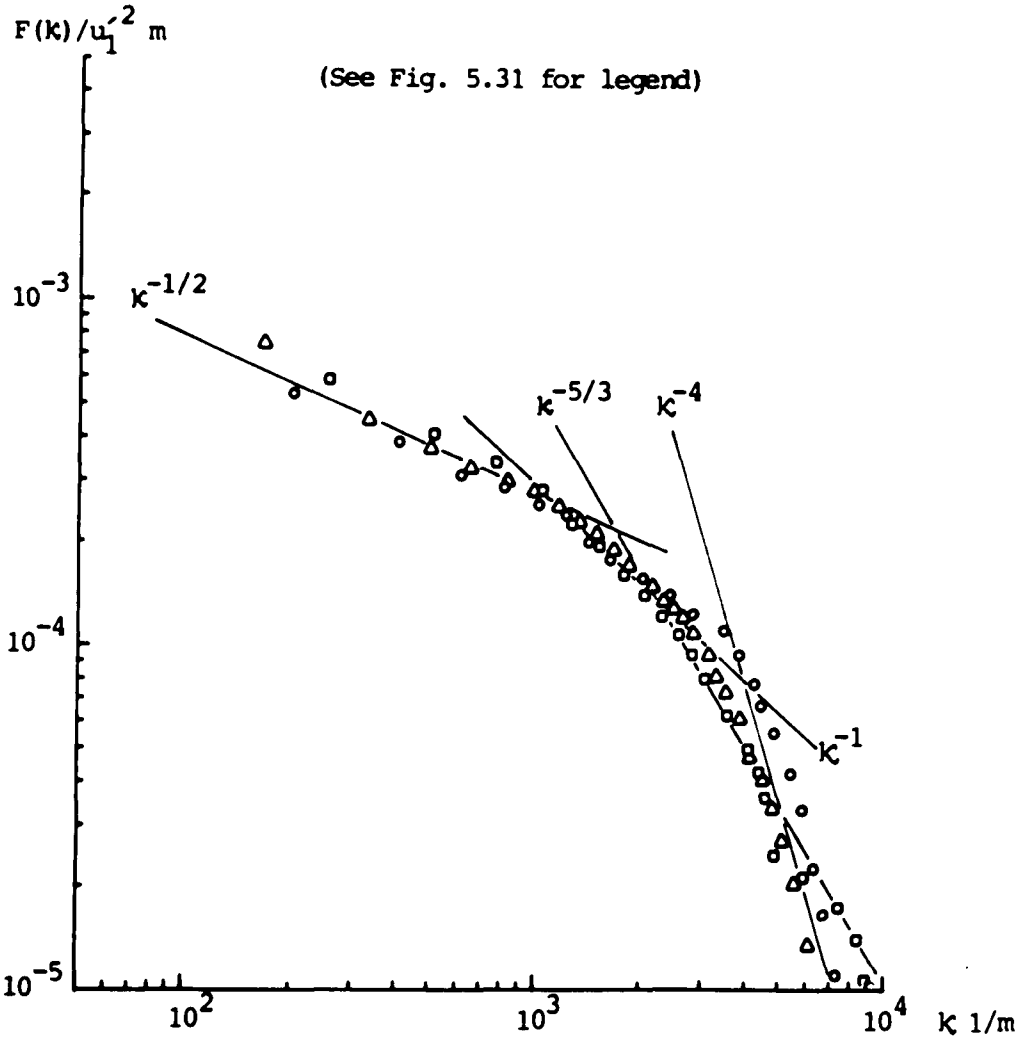

Fig. 5.32 Evolution of Power Spectra Along the Corner
Y = 5.49 mm , Z = 1.05 mm

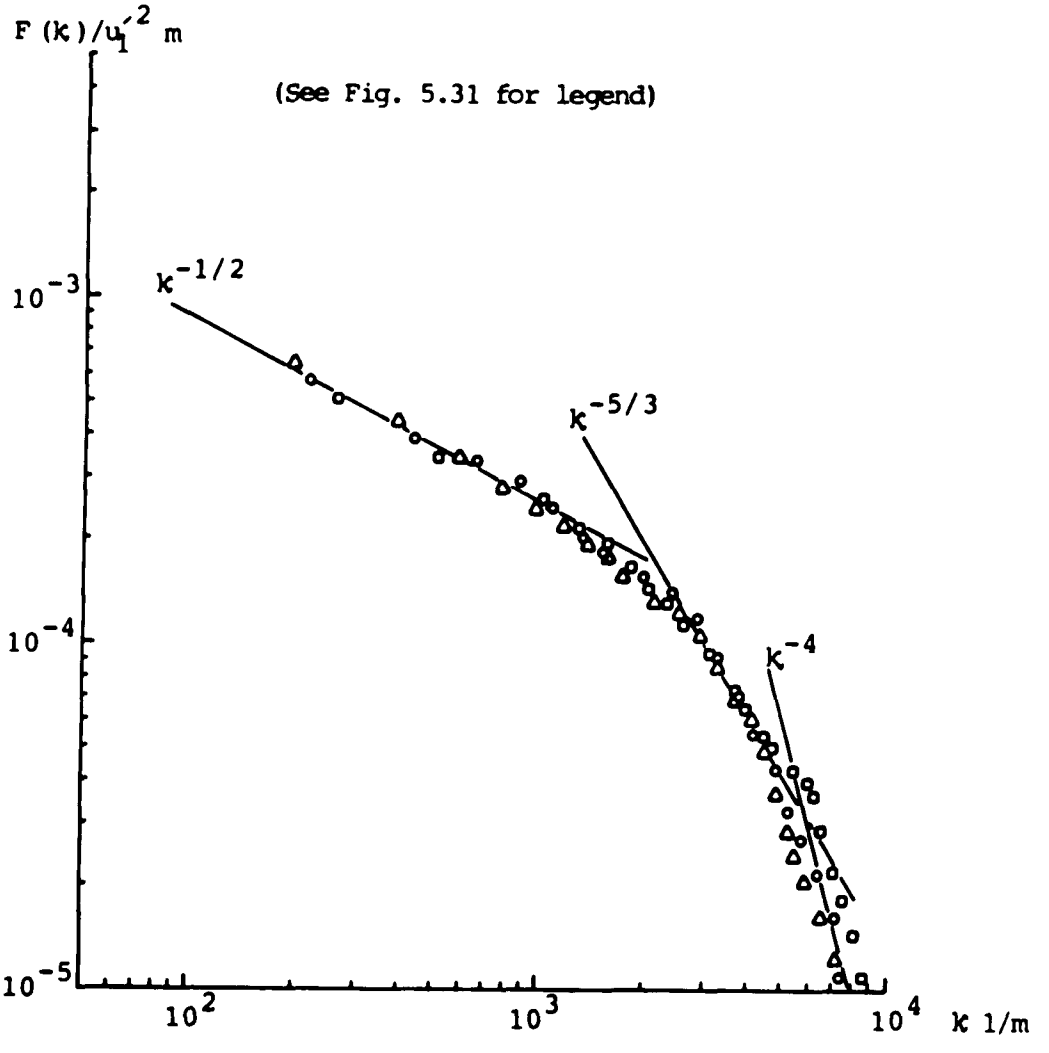

Fig. 5.33 Evolution of Power Spectra Along the Corner
Y = 15.65 mm , Z = 1.05 mm

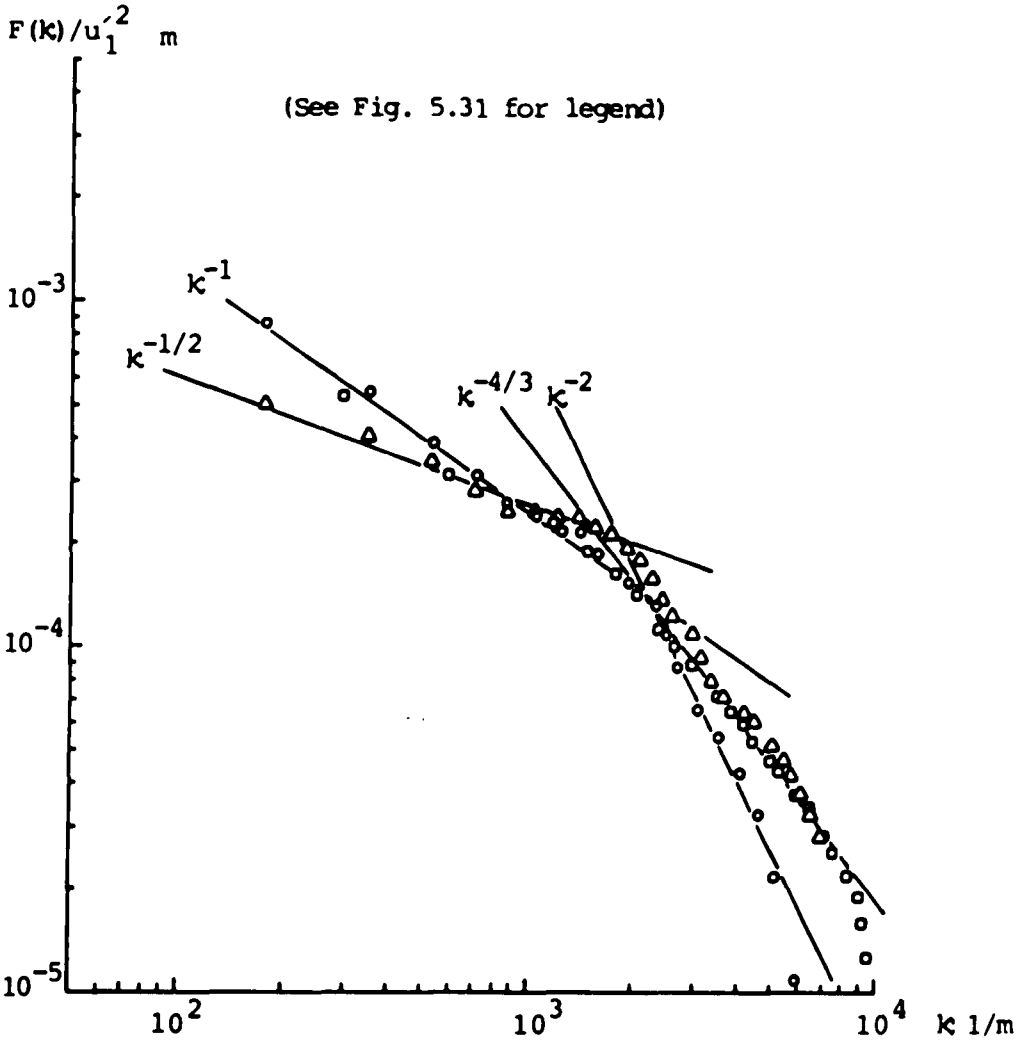

Fig. 5.34 Evolution of Power Spectra Along the Corner
Y = 1.05 mm , Z = 6.76 mm

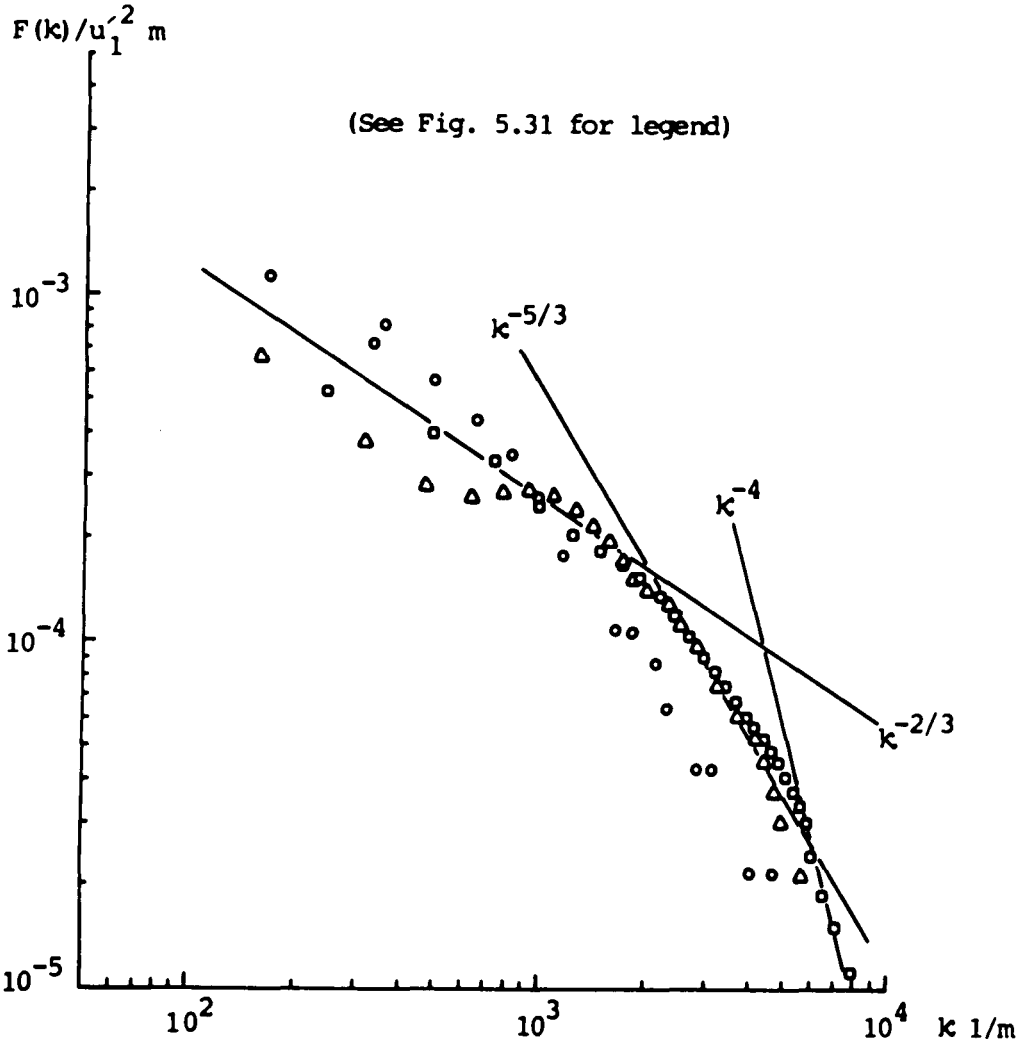

Fig. 5.35 Evolution of Power Spectra Along the Corner
Y = 1.05 mm , Z = 18.19 mm

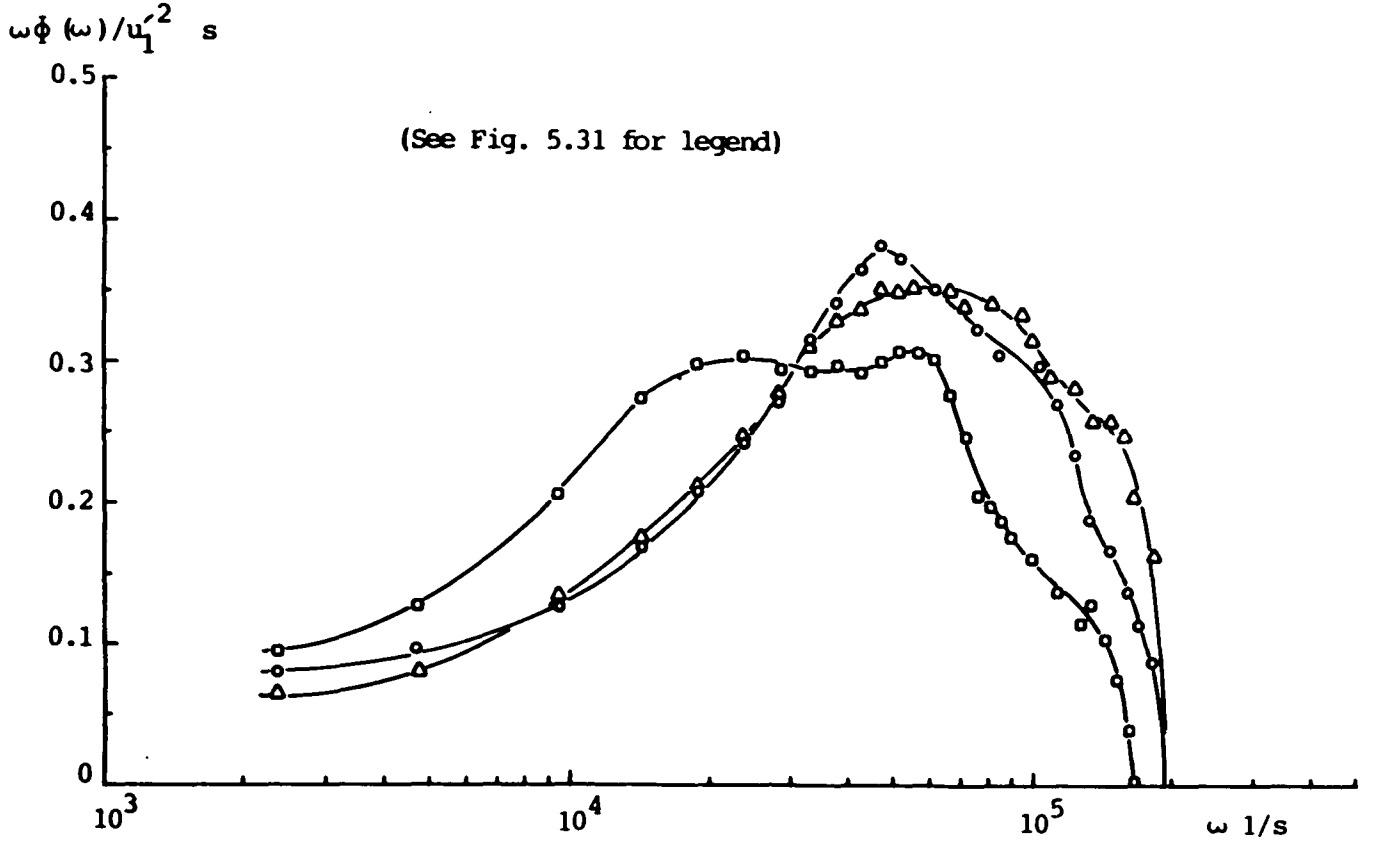

Fig. 5.36 Relative Contribution to $u_1'^2$ by Eddies of Various Frequencies
Y = 1.05 mm , Z = 1.05 mm

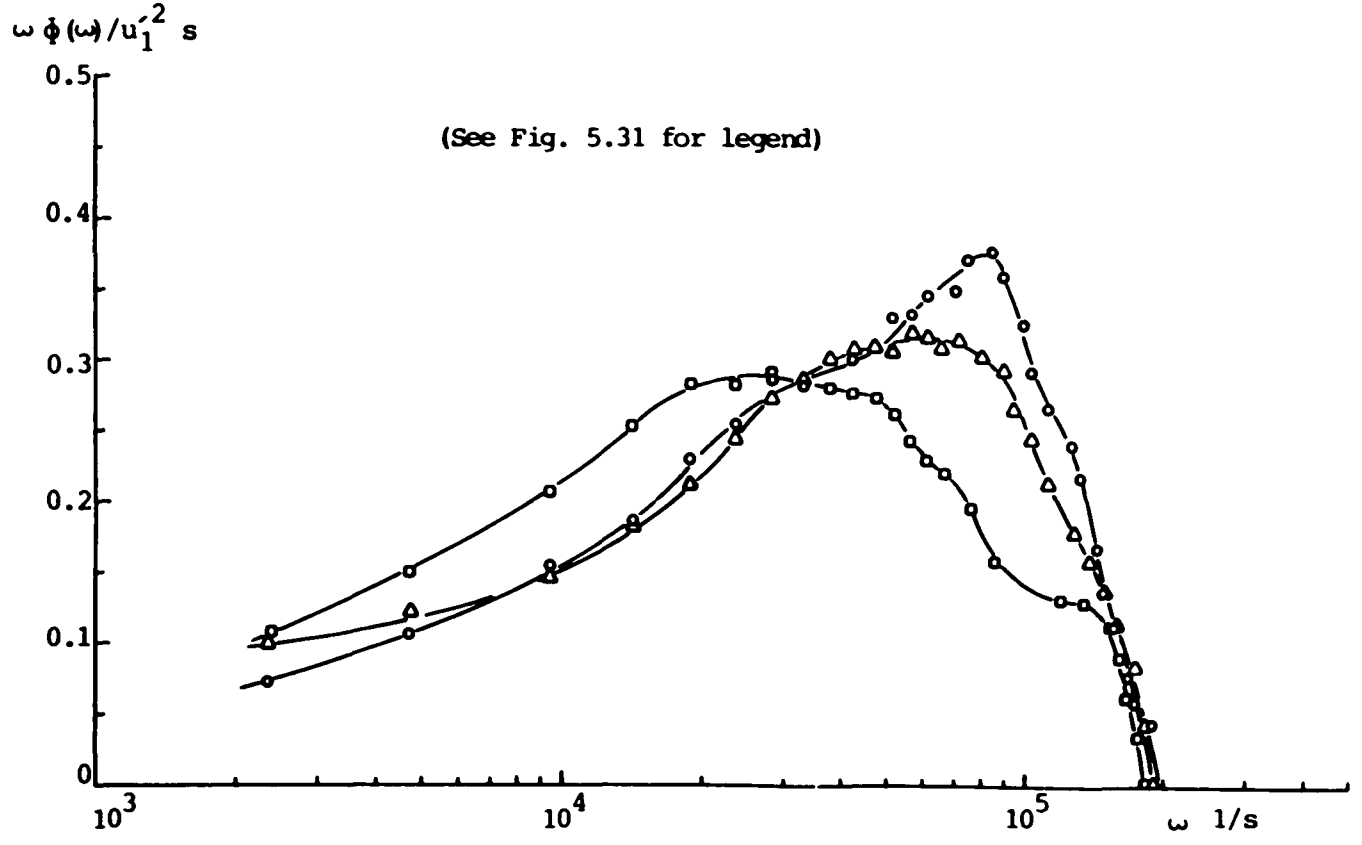

(See Fig. 5.31 for legend)

Fig. 5.37 Relative Contribution to $u_1'^2$ by Eddies of Various Frequencies
Y = 5.49 mm , Z = 1.05 mm

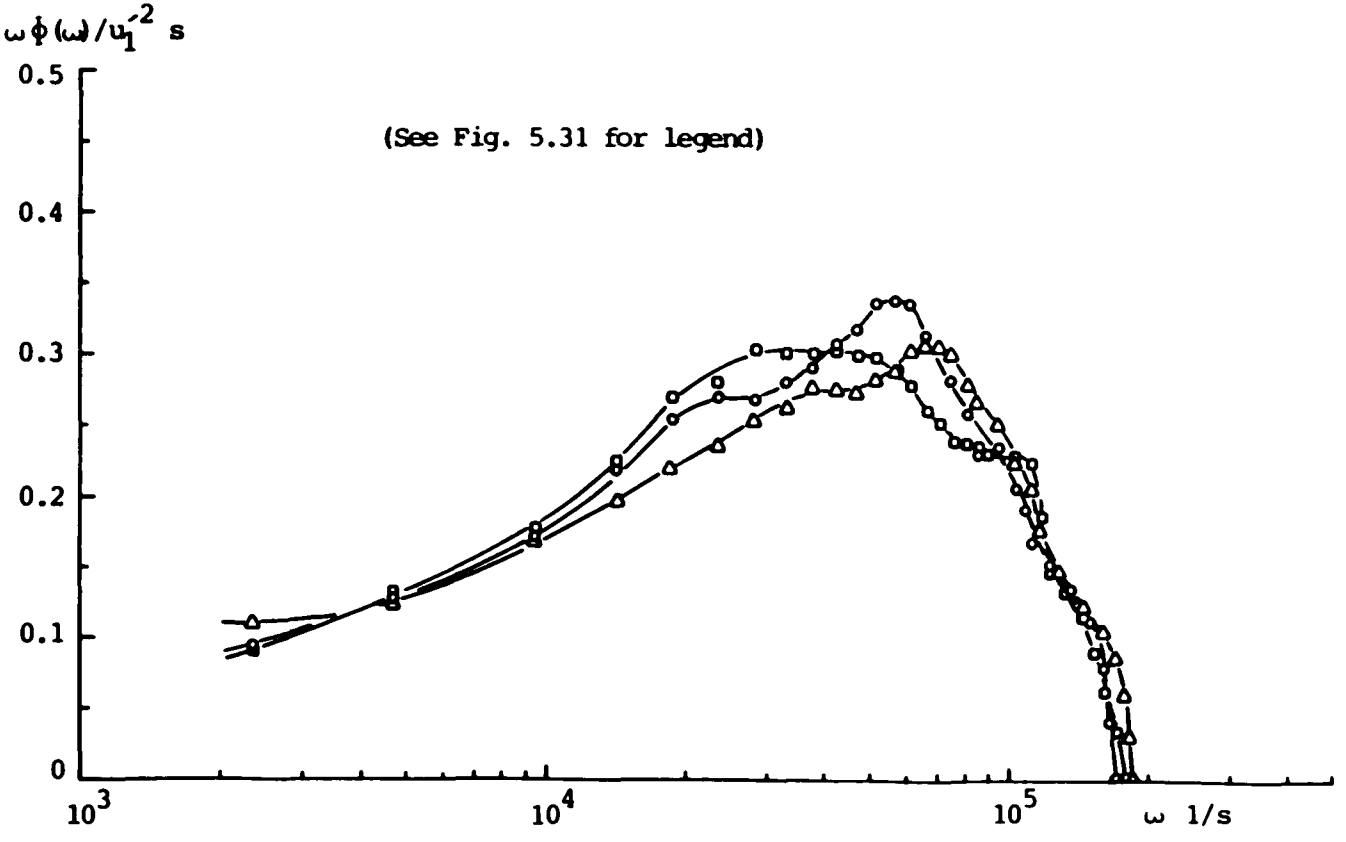

Fig. 5.38 Relative Contribution to $u_1'^2$ by Eddies of Various Frequencies
Y = 15.65 mm , Z = 1.05 mm

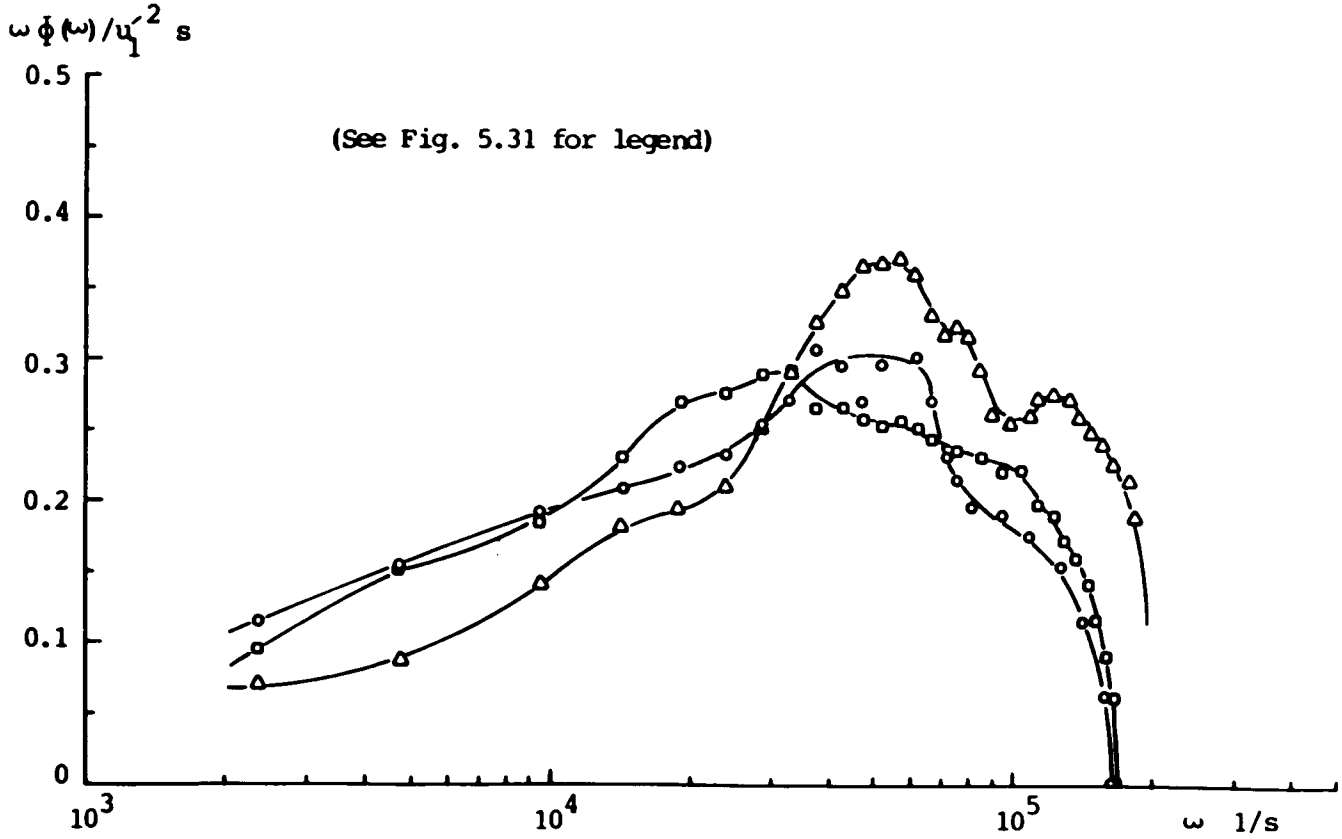

Fig. 5.39 Relative Contribution to $u_1'^2$ by Eddies of Various Frequencies
Y = 1.05 mm , Z = 6.76 mm

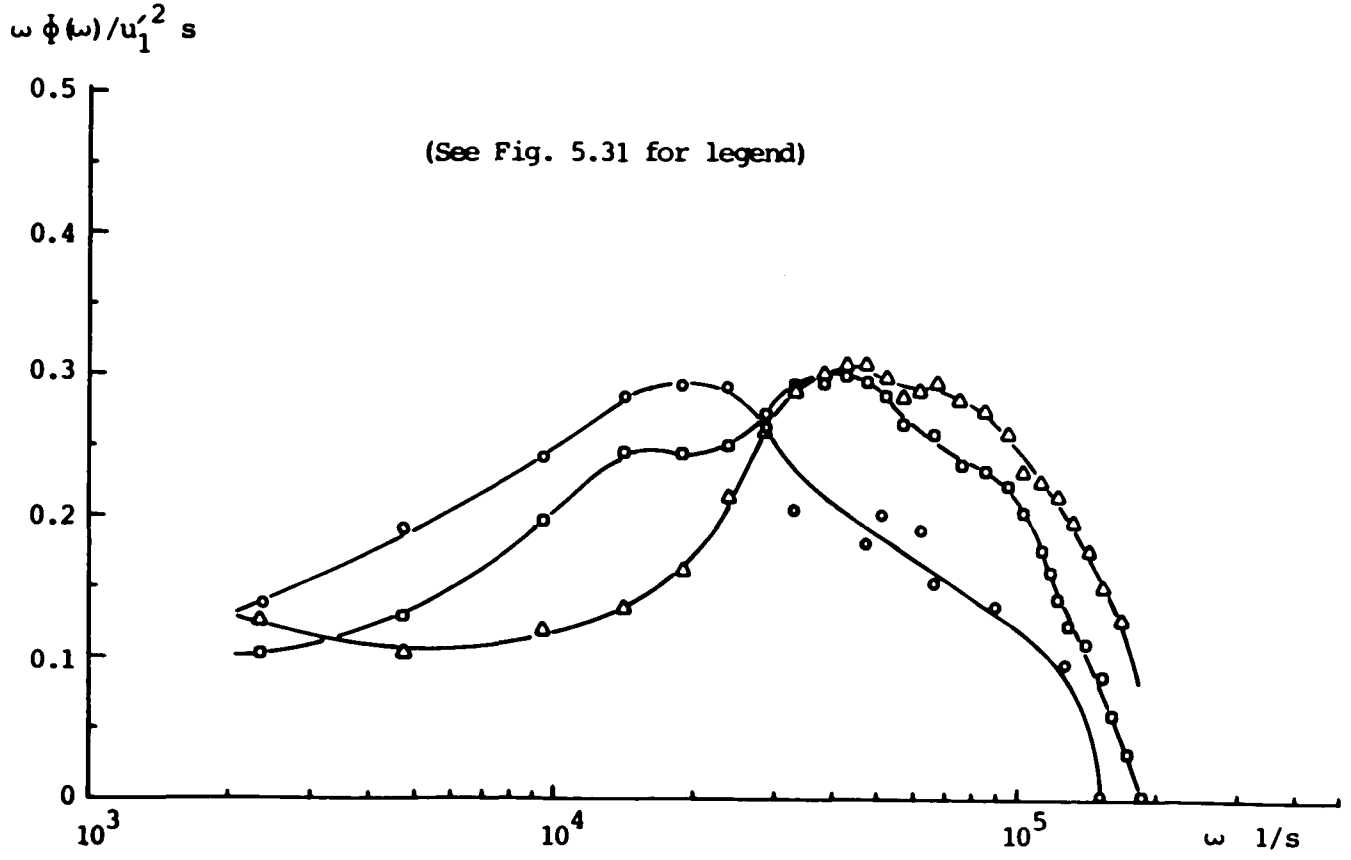

(See Fig. 5.31 for legend)

Fig. 5.40 Relative Contribution to $u_1'^2$ by Eddies of Various Frequencies
Y = 1.05 mm , Z = 18.19 mm

CHAPTER VI

CONCLUSIONS

The following conclusions were drawn from a careful analysis of the experimental results presented in this thesis:

(i) A horseshoe shaped vortex forms around the airfoil, in the corner region, when boundary layer of the flat plate flows past the airfoil. Within a short distance (less than 25 mm) downstream along the corner, in the region between the solid surfaces and the horseshoe vortex, a corner vortex (Fig. 4.58) is formed. The direction of vorticity of the corner vortex is opposite to the direction of vorticity of the horseshoe vortex.

(ii) The horseshoe vortex and the corner vortex are diffused by the combined action of the velocity gradient in the streamwise direction and the Reynolds stresses. The size of the corner vortex increases at a slower rate upstream of the maximum thickness section of the airfoil (accelerating flow) compared to that downstream (decelerating flow) of the section (Fig. 4.39). The rate of change of the size of the corner vortex is strongly correlated to the rate of growth of the boundary layer on the airfoil away from the corner (Fig. 4.62).

(iii) A pair of contra-rotating vortices are generated in the region between the solid surfaces and the corner vortex downstream of the maximum thickness section. The appearance of these vortices is due to inhomogeneity and anisotropy in turbulence. The vortex next to the airfoil surface has the same direction of rotation as the corner vortex and merges with it. The other vortex, formed near the surface of the flat plate, has the direction of rotation opposite to the corner vortex. This is the only part of the stress induced vortex pair indipendently present in the flow (Fig. 4.59). The stress induced vortices advect fluid with high momentum towards the corner (Fig. 4.60 and Fig. 4.61). The stress induced vortex grows approximately at the same rate as the corner vortex (Fig. 4.39). Near the trailing edge, the size of the stress induced vortex is approximately half the size of the corner vortex.

(iv) In blade end wall corner region the turbulence quantities are strongly affected by the streamwise vortices. Advection due to secondary flows predominates the distribution of turbulent intensities. Advection by the horseshoe vortex and the corner vortex creates low streamwise turbulence intensity regions near the surface of the flat plate in the corner region (Figs. 5.1, 5.2). In these regions of low streamwise turbulence intensity, the transverse gradient of streamwise velocity is very small (Figs. 4.28, 4.29). Therefore, the production of turbulence is also negligible.

In the close vicinity of the corner, near the trailing edge of the airfoil, the growth of the stress induced vortex eliminates this low turbulence intensity region from vicinity of the flat plate surface (Fig. 5.5).

(v) The regions with low streamwise turbulence intensity coincide with the zero turbulence shear stress ($-\rho\overline{u_1 v_1} = 0$) regions. Away from the airfoil, in the corner region there is a region negative shear stress (Figs. 5.16 to 5.20). Beyond this region (in the direction away from the airfoil) the shear stress $-\rho\overline{u_1 v_1} \simeq 0$. Close to the flat plate surface, the shear stress term $-\rho\overline{u_1 w_1}$ changes more gradually in the transverse direction (Figs. 5.21 to 5.25).

(vi) In the corner region, all the three turbulent stress terms are of the same order of magnitude as the normal stress terms. Close to the corner, near the trailing edge, the turbulent production of streamwise vorticity is of the same order as the net production of streamwise vorticity by the mean shear.

(vii) Away from the corner and near the surface of the airfoil the structure of turbulence is considerably modified along the flow direction (Figs. 5.35 and 5.40). In the close vicinity of the corner, the streamwise vorticity has the

opposing effect. At points nearest to the corner the spectra at different axial locations are identical (Fig. 5.31) though the level of energy associated at different frequencies vary from station to station (Fig. 5.36).

APPENDIX A

CALIBRATION AND DATA REDUCTION FOR TRANSDUCERS AND PITOT TUBES

A.1 Calibration of Pressure Transducer

Two Validyne DP15 pressure transducers with CP15 carrier demodulators, used for pressure measurements, were calibrated against a Miriam micro-manometer before and after each series of experiments. The least count of the micro-manometer was 0.001 inch (0.0254 mm) of water. A TSI calibrator model 1125, connected to a high pressure nitrogen cylinder through a pressure regulator, as shown in Fig. A1, was used as the steady pressure source. No change in calibration could be detected for the pressure transducers after any of the experiments. Typical calibration curves for the transducers are shown in Fig. A2.

A.2 Data Reduction

A.2.1 Atmospheric Pressure

The atmospheric pressure, measured with a Fortin type barometer, is given by (mercury in brass tube construction, calibrated at 62 F),

$$P_a = W_{Hg}\, h_{to} \quad psi \tag{A1}$$

where, $W_{Hg} = 0.491154\ g/32.174 \quad lb_f/in^3$

$h_{to} = h_{tI} - C$

h_{tI} = barometer reading in inch of mercury

$C = - h_{tI}\{9.08(t - 28.63)10^{-5}\}/\{1 + 1.01 (t - 32)10^{-4}\}$

t = room temperature in F

g = acceleration due to gravity, ft/s^2

A.2.2 Density of Air

The air stream temperature (T_a in Rankine) was measured with a thermometer fixed in the test section. Density of air was calculated using ideal gas relation which reduces to,

$$\rho_a = 43.245\ P_a/T_a \quad Kg/m^3 \tag{A2}$$

A.2.3 Velocity Calculation from Pitot and Kiel Probe Measurements

The velocity from the experimental measurements were

calculated according to the following equation:

$$\bar{U} = 22.315\ (C_t/\rho_a)^{1/2}\ (V_t)^{1/2}\ \text{m/s} \qquad \text{(A3)}$$

where, C_t = transducer constant, inch of water/volt

V_t = transducer output with total and static pressure probes connected across it.

A.3 Calibration of Pitot Tubes

The pitot tubes, constructed at the Turbomachinery Laboratory of The City College, were calibrated in the calibrator and the arrangement described in section A.1 and shown in Fig. A1. The pressure measured by the pitot tubes matched with the pressure at the calibrator plenum chamber, confirming that the calibration constant for the pitot tubes were unity. The pitot tubes were also checked for yaw sensitivity. It was found that no difference in pressure readings was registered by the transducers within the range of yaw angles of $\pm$ 10°.

APPENDIX B

HOT WIRE CALIBRATION AND EQUATIONS

The block diagram of the experimental arrangement for the hot wire measurements is shown in Fig.A3. The probe was connected to a constant temperature anemometer (CTA); the output of the CTA is linearized with the linearizer in the circuit. The linearized signal was fed into a spectrum analyzer, an integrating digital voltmeter (VM 1) and a RMS meter through a channel selector. The output of the RMS meter was read from another integrating digital voltmeter (VM 2).

B.1 Determination of Tangential (k) and Normal (h) Sensitivity Coefficients and Wall Proximity Effect of the Inclined Single Sensor Hot Wire Probe

The directional sensitivity calibration device, described in Chapter III, was used to determine both the coefficients k and h for the inclined single sensor hot wire built in the Turbomachinery Laboratory of The City College. The calibration device was fixed in the place of the removed bottom wall of the wind tunnel test section. The inclined single sensor hot wire was mounted on the probe support. The probe support was clamped on the probe support holder with the plane of the prongs horizontal and the pivot axis bisecting

the hot wire sensor. The Kiel probe was inserted from the top of the test section with its axis along the pivot axis of the swing arm and the sensing head of the Kiel probe 1 cm above the hot wire sensor. The IGV of the wind tunnel blower were adjusted for the wind speed variation of 20 m/s to 30 m/s at the test section. The Kiel probe pressure and the hot wire output were recorded for different angular positions of the swing arm starting with the sensor parallel to the wind tunnel test section axis. Since the plane of the prongs was parallel to the flow direction,

$$U_n = 0 \tag{B1}$$

$$U_e^2 = U_p^2 + k^2 U_t^2 \tag{B2}$$

If δ was the angle between the wind tunnel test section axis and the sensor, then, $U_p = U \sin\delta$ and $U_n = U \cos\delta$, therefore,

$$U_e^2 = U^2(\sin^2\delta + k^2\cos^2\delta)$$

$$\text{or,} \quad k = \{(U_e/U)^2 - \sin^2\delta\}^{1/2}/\cos\delta \tag{B3}$$

A plot of (U_e/U) against δ, for different sensors is shown in

Fig. A4. The values of k were calculated from this figure and were plotted against ζ in Fig. A5. The tangential sensitivity coefficient k varies considerably with the angle ζ. However, it is not sensitive to the flow velocity (in the range encountered) nor the diameters of the sensors investigated (4μ and 5μ). In the present investigation the angle ζ was expected to vary between 15° to 75°, but an average value of k of 0.22 was considered to be satisfactory.

To determine the normal sensitivity coefficient h, the swing arm was moved to a position where ζ was 90°. At this position, the output of the hot wire and the Kiel probe were recorded for various IGV openings to change the test section air speed between 6 m/s to 30 m/s. For this case,

$$U_n = U_t = 0$$

$$U_e = U_p = S\ E_p = U$$

therefore,

$$E = U/S \qquad \text{(B4)}$$

The swing arm was then moved to a position where the probe axis became perpendicular to the test section axis. At

this position the probe support was unclamped and rotated about its axis to a position where the plane of the prongs became vertical. The probe support was clamped at that position. The output of the Kiel probe and the hot wire for various IGV openings were recorded. For this case,

$$U_p = U_t = 0$$

$$U_e = h\, U_n = S\, E_n = h\, U \qquad \text{(B5)}$$

Therefore, at any wind speed, the ratios of outputs at these two positions give the normal sensitivity coefficient h,

$$h = E_n/E_p \qquad \text{(B6)}$$

The calibration curves for E_n and E_p for one set of experiments are shown in Fig.A5. The value of h remains the same for the same hot wire at various velocities if the linearizer is adjusted properly to get a straight line passing through the origin. But the value seems to vary from build to build, even for the same diameter sensor. The value of h changed due to the variation of the amount of solder deposited on the tips of the prongs as well as the slight difference in the distance between the prongs. Therefore, the normal sensitivity coefficients were determined for each run before and after each traverse.

The effect of wall proximity was determined by finding the no flow output of the hot wire at various distances of the sensor from the surface of the model. No noticeable change was observed when the sensor was more than 0.5 mm away from the surface. Since all the measurements with the hot wires were taken more than 1 mm away from the surfaces, there was no need for wall proximity correction.

B.2 Compensation for Fouling of the Hot Wire

During the course of the investigation, it was observed that the fouling of the hot wire sensor due to the deposit of sub-micron particles could not be avoided. The rate of loss of sensitivity due to fouling was observed to be uniform if the fouling of the sensor was not too severe. Washing in acetone only partially recovered the wire from loss of sensitivity.

The inclined single sensor hot wire was calibrated before and after each experiment. The change of sensitivity during each traverse was estimated by measuring the output of the hot wire at a fixed location and orientation before and after the traverse. The hot wire was washed with acetone after every traverse. The loss of sensitivity during each traverse was equally distributed over each point of measurement. The calculation of sensitivity estimation is

explained below.

At any fixed point in the flow field, for small variation in the Reynolds number, the direction of mean velocity at each point in the flow remains fixed and remains a fixed ratio with the reference velocity (kinematically similar flow).

The velocity at a point is given by,

$$\vec{U} = \hat{i}\, U_x + \hat{j}\, U_y + \hat{k}\, U_z$$

and, $$U_1 : U_{x1} : U_{y1} : U_{z1} : U_{\infty 1} :: U_2 : U_{x2} : U_{y2} : U_{z2} : U_{\infty 2} \quad (B7)$$

where subscripts 1 and 2 signify two different reference velocities within the range of permissible variation. If the hot wire is placed at this position at a fixed orientation,

$$U_1 : U_{p1} : U_{t1} : U_{n1} : U_{\infty 1} :: U_2 : U_{p2} : U_{t2} : U_{n2} : U_{\infty 2} \quad (B8)$$

and, $$E = U_e/S = (U_p^2 + k^2 U_t^2 + h^2 U_n^2)^{1/2}/S \quad (B9)$$

For constant sensitivity,

$$E_1/U_{e1} = E_2/U_{e2} \quad (B10)$$

If the velocity is same but the sensitivities are different after a period of time,

$$E/U_e = 1/S \quad \text{and} \quad E'/U_e = 1/S' \tag{B11}$$

If the velocity also changes during this time, then,

$$E_1/U_{e1} = 1/S \quad \text{and} \quad E_2'/U_{e2} = 1/S' \tag{B12}$$

However, since U_{e1} and U_{e2} are not known, it is not possible to determine S and S'. From equation (B8):

$$U_{e1} = c\, U_{\infty 1} \quad \text{and} \quad U_{e2} = c\, U_{\infty 2}$$

therefore,

$$S/S' = (E_1/E_2')(U_{\infty 1}/U_{\infty 2}) \tag{B13}$$

At every station coordinates Y = 50.8 mm (2 inch) and Z = 50.8 mm (2 inch) were chosen as the fixed point and angular orientation $\theta_3 = 90°$ was kept as fixed orientation. S was the sensitivity of the hot wire from the calibration curve at the beginning of the experiment. The sensitivity S_1 at the beginning of any traverse, and the sensitivity S_2 at the end

of the same traverse, were calculated from equation (B13). The sensitivity during the traverse was assumed to vary linearly with time.

B.3 Coordinate Transformation in Hot Wire Response Equations

The angles involved in the relationship between the test section coordinate axes XYZ and the sensor coordinate axes TPN are related by the angles α, β, θ and ψ. α is the angle between the XZ plane and the vertical plane passing through the axis of the probe; β is the angle between the line of intersection between these two planes and the axis of the probe and ψ is the angle the sensor makes with the axis of the probe. θ is the angle between the plane of the prongs and the plane passing through the axis of the probe and normal to the vertical plane passing through the axis of the probe.

The equivalent cooling velocity is given by,

$$U_e^2 = U_p^2 + k^2U_t^2 + h^2U_n^2 \qquad \text{(B14)}$$

The relationship between U_p, U_t, U_n and U, V, W are required to evaluate U, V, and W from the hot wire output. The hot wire output and the cooling velocity are related by,

$$U_e = S(E_e - E_o) \tag{B15}$$

The following transformations are needed to arrive at the required relationship:

B.3.1 First Transformation

Rotate the XYZ coordinate system about Z axis through an angle α, as shown in Fig. A7. Designate the new coordinates as X'Y'Z' and the velocity components in the new coordinate system are,

$$\begin{aligned} U' &= U\,\mathrm{Cos}\alpha + V\,\mathrm{Sin}\alpha \\ V' &= -U\,\mathrm{Sin}\alpha + V\,\mathrm{Cos}\alpha \\ W' &= W \end{aligned} \tag{B16}$$

B.3.2 Second Transformation

Rotate the X'Y'Z' coordinate system about the axis Y' through an angle ß as shown in Fig. A7, to assume the position X", Y" and Z". The velocity components in this case are,

$$\begin{aligned} U'' &= U'\mathrm{Cos}\beta + W'\mathrm{Sin}\beta \\ &= U\,\mathrm{Cos}\alpha\,\mathrm{Cos}\beta + V\,\mathrm{Sin}\alpha\,\mathrm{Cos}\beta + W\,\mathrm{Sin}\beta \\ V'' &= V' = -U\,\mathrm{Sin}\alpha + V\,\mathrm{Cos}\alpha \\ W'' &= W'\,\mathrm{Cos}\beta + U'\,\mathrm{Sin}\beta \end{aligned} \tag{B17}$$

$$= -U \cos\alpha \sin\beta - V \sin\alpha \sin\beta + W \cos\beta$$

B.3.3 Third Transformation

Rotate the coordinate system X"Y"Z" about the axis X" through an angle θ as shown in Fig. A7 to assume the position X"', Y"' and Z"'. Then,

$$\begin{aligned}
U"' &= U" \\
&= U \cos\alpha \cos\beta + V \sin\alpha \cos\beta + W \sin\beta \\
V"' &= V" \cos\theta + W" \sin\theta \\
&= U (-\sin\alpha \cos\theta - \cos\alpha \sin\beta \sin\theta) \\
&\quad + V (\cos\alpha \cos\theta - \sin\alpha \sin\beta \sin\theta) \\
&\quad + W \cos\beta \sin\theta \qquad \text{(B18)} \\
W"' &= V" \sin\theta + W" \cos\theta \\
&= U (-\cos\alpha \sin\beta \cos\theta + \sin\alpha \sin\theta) \\
&\quad + V (-\sin\alpha \sin\beta \cos\theta - \cos\alpha \sin\theta) \\
&\quad + W \cos\beta \cos\theta
\end{aligned}$$

B.3.4 Fourth Transformation

The coordinates X"'Y"'Z"' with respect to the sensor coordinates TPN is shown in Fig. A7 and the relationship between the velocity components in these two coordinate

systems lead to,

$$
\begin{aligned}
U_t &= - U"' \cos\psi - V"' \sin\psi \\
&= U\,(-\cos\alpha\cos\beta\cos\psi + \sin\alpha\cos\theta\sin\psi \\
&\qquad + \cos\alpha\sin\beta\sin\theta\sin\psi) \\
&\quad + V\,(-\sin\alpha\cos\beta\cos\psi + \cos\alpha\cos\theta\sin\psi \\
&\qquad + \sin\alpha\sin\beta\sin\theta\sin\psi) \\
&\quad + W\,(-\sin\beta\cos\psi - \cos\beta\sin\theta\sin\psi) \\
U_p &= U"' \sin\psi + V"' \cos\psi \\
&= U\,(\cos\alpha\cos\beta\sin\psi + \sin\alpha\cos\theta\cos\psi \\
&\qquad + \cos\alpha\sin\beta\sin\theta\cos\psi) \\
&\quad + V\,(\sin\alpha\cos\beta\sin\psi - \cos\alpha\cos\theta\cos\psi \\
&\qquad + \sin\alpha\sin\beta\sin\theta\cos\psi) \\
&\quad + W\,(\sin\beta\sin\psi - \cos\beta\sin\theta\cos\psi) \\
U_n &= W"' \\
&= U\,(-\cos\alpha\sin\beta\cos\theta + \sin\alpha\sin\theta) \\
&\quad + V\,(-\sin\alpha\sin\beta\cos\theta - \cos\alpha\sin\theta) \\
&\quad + W\,(\cos\beta\cos\theta)
\end{aligned}
\qquad \text{(B19)}
$$

The relationship between the last step of transformation and any intermediate step can be obtained from

equation (B19) by substituting the angular rotation of all the previous steps equal to zero.

Thus, the relationship between the velocity components in the sensor frame of reference (TPN) and the probe frame of reference ($X_2Y_2Z_2$) are given by [substitute $\alpha = \beta = 0$ and $\psi = 45^\circ$ in equation (B19)],

$$\begin{aligned} U_t &= (-1/\sqrt{2})U_2 + (-\cos\theta/\sqrt{2})V_2 + (-\sin\theta/\sqrt{2})W_2 \\ U_p &= (1/\sqrt{2})U_2 + (-\cos\theta/\sqrt{2})V_2 + (-\sin\theta/\sqrt{2})W_2 \\ U_n &= (-\sin\theta)V_2 + (\cos\theta)W_2 \end{aligned} \qquad \text{(B20)}$$

The relationship between the velocity components in the probe frame of reference ($X_2Y_2Z_2$) and the model frame of reference ($X_1Y_1Z_1$) or the test section frame of reference (XYZ) can be obtained by substituting the appropriate values of α and β in equation (B17). Rearranging the equations and noting that $()'' = ()_2$:

$$\begin{aligned} U &= (\cos\alpha\cos\beta)U_2 + (-\sin\alpha)V_2 \\ &\quad + (-\cos\alpha\sin\beta)W_2 \end{aligned}$$

$$V = (\sin\alpha \cos\beta)U_2 + (\cos\alpha)V_2 + (-\sin\alpha \sin\beta)W2 \quad \text{(B21)}$$

$$W = (\sin\beta)U_2 + (\cos\beta)W_2$$

Equation (B21) also gives the direction cosines of the velocity components in the probe frame of reference $(X_2Y_2Z_2)$ and the model frame of reference $(X_1Y_1Z_1)$ or the test section frame of reference (XYZ) when the proper values for the angles α and β are substituted in the transformation matrix,

$$C_{ij} = \begin{bmatrix} \cos\alpha \cos\beta & -\sin\alpha & -\cos\alpha \sin\beta \\ \sin\alpha \cos\beta & \cos\alpha & -\sin\alpha \sin\beta \\ \sin\beta & 0 & \cos\beta \end{bmatrix} \quad \text{(B22)}$$

B.4 Computer Program to Solve the Hot Wire Equations

A listing of the computer program used to solve the hot wire equations, given in Chapter III, is presented in this section. The correction for fouling and variation in atmospheric pressure and temperature are incorporated in the program.

During execution the main program invokes the

following sub programs:

subroutine COEFA; to calculate coefficients A_{ij},

subroutine MEVEL; to calculate mean velocity components in the frame of reference of the probe,

subroutine COEFB; to calculate coefficients B_{ij},

subroutine MRCOTR; to convert the mean velocity components from MEVEL to the frame of reference of the model,

subroutine FLUCT; to calculate Reynolds stress tensor in the reference frame of the probe,

subroutine FRCOTR; to convert Reynolds stresses from FLUCT to the frame of reference of the model,

subroutine SSLAE; Gauss-Jordan elimination subroutine,

function URE; to calculate reference velocity from Kiel probe measurements.

```
$JOB            XX,TIME=060,PAGES=200
C       THIS PROGRAM IS WRITTEN TO CALCULATE THE MEAN VEL-
C       OCITY COMPONENTS AND REYNOLDS STRESS TENSOR FROM
C       MEASUREMENTS TAKEN AT EIGHT ANGULAR POSITIONS WITH
C       A 45 DEGREE INCLINED SINGLE SENSOR HOT WIRE.
C
C
       IMPLICIT REAL*8 (A-H,O-Z)
       DIMENSION EEM(8),EEF(8),UES(8),UM(5),VM(5),WM(5),
      8          UEFS(8),R(6),D(6,6),C(3,3),A(8,6),B(8,6),
      8          UEM(8),UEF(8),T(3,3),TM(3,3),XN(14),YN(14),
      8          ZN(14),UN(14),VN(14),WN(14),USN(14),VSN(
      8          14),WSN(14),UVN(14),UWN(14),VWN(14),TUV(14)
      8          ,TUW(14),TVW(14),UINT(14),RVU(14),RWU(14),
      8          CUV(14),CUW(14),CVW(14),TKE(14)
C
       DATA ALP,BET/23.000,30.000/
C
       DO 955 NN=1,12
C
       READ (5,10) SC,EO,RK,H,X,Z
10     FORMAT (1X,4F8.4,8X,2F8.4)
C
       CALL COEFA (RK,H,A)
C
       READ (5,20) HTI1,TR1,PO1,ER1,HTI2,TR2,PO2,ER2
20     FORMAT (1X,4F8.4/1X,4F8.4)
C
       URI=URE(HTI1,TR1,PO1)
       URF=URE(HTI2,TR2,PO2)
       UERI=URI/ER1
       UERF=URF/ER2
       DUER=(UERF-UERI)/14.000
       DHT=(HTI2-HTI1)/14.000
C
       DO 900 N=1,14
C
       UERN=UERI+N*DUER-0.500*DUER
       HTIN=HTI1+N*DHT-0.500*DHT
       CSL=SC*UERN
C
       READ (5,100) Y,PO,TR,(EEM(I),I=1,8),(EEF(I),I=1,8)
100    FORMAT (1X,3F8.4/1X,8F8.4/1X,8F8.4)
C
       UO=URE(HTIN,TR,PO)
       UOS=UO*UO
       DO 110 I=1,8
       UEM(I)=CSL*(EEM(I)-EO)
       UEF(I)=CSL*EEF(I)
110    CONTINUE
C
C
C
       WRITE (6,555) X,Y,Z,UO
555    FORMAT (////1X,'COORDINATES',5X,3F10.2,5X,
      8         'REF. VEL.',F10.3/)
C
```

```
C
C
      CALL MLVEL (PK,M,UEM,UMA,VMA,WMA)
C
      CUVW=DABS(UMA)+DALS(VMA)+DABS(WMA)
      IF (CUVW.EQ.0.000) GO TO 800
C
      CALL COEFB (A,UEM,UMA,VMA,WMA,B)
C
      CALL MRCOTR (ALP,EET,U,V,W,UMA,VMA,WMA,C)
C
C
C
      WRITE (6,556) U,V,W
556   FORMAT (1X,'AVARAGE MEAN IN MODEL FRAME'/1X,3D15.5//
     8         1X,'FLUCTUATING QUANTITIES IN MODEL FRAME')
C
C
C
      CALL FLUCT (B,C,UEF,T,TM,UOS)
C
      XN(N)=X
      YN(N)=Y
      ZN(N)=Z
      UN(N)=U/UO
      VN(N)=V/UO
      WN(N)=W/UO
      USN(N)=TM(1,1)
      VSN(N)=TM(2,2)
      WSN(N)=TM(3,3)
      UVN(N)=TM(1,2)
      UWN(N)=TM(1,3)
      VWN(N)=TM(2,3)
      TKE(N)=USN(N)+VSN(N)+WSN(N)
      GO TO 900
C
800   XN(N)=X
      YN(N)=Y
      ZN(N)=Z
      UN(N)=0.000
      VN(N)=0.000
      WN(N)=0.000
      USN(N)=0.000
      VSN(N)=0.000
      WSN(N)=0.000
      UVN(N)=0.000
      UWN(N)=0.000
      VWN(N)=0.000
      TKE(N)=0.000
      GO TO 900
C
900   CONTINUE
C
      WRITE (6,950) (XN(I),YN(I),ZN(I),UN(I),VN(I),WN(I),USN
     8      (I),VSN(I), WSN(I),UVN(I),UWN(I),VWN(I),I=1,14)
950   FORMAT ('1',1X,'X MM',3X, 'Y MM',3X,'Z MM',6X,'U/UO',
     8        6X,'V/UO',8X,'W/UO',6X,' UU/UOS',5X,' VV/UOS'
     8        ,5X,' W',W/UOS',5X,' UV/UOS',5X,' UW/UOS',5X,
     8        ' VW/UOS'//14(3(1X,F6.2),9D12.4/))
C
```

```
      PAI=4.000*DATAN(1.000)
      DO 700 I=1,14
      IF (UN(I).NE.0.000.AND.VN(I).NE.0.000) GO TO 650
      TUV(I)=999.99
      TUW(I)=999.99
      TVW(I)=999.99
      GO TO 660
650   TUV(I)=180.000*DATAN(VN(I)/UN(I))/PAI
      TUW(I)=180.000*DATAN(WN(I)/UN(I))/PAI
      TVW(I)=180.000*DATAN(WN(I)/VN(I))/PAI
C
660   IF (USN(I).LE.0.00.OR.VSN(I).LE.0.00.OR.WSN(I).LE.
     8                                        0.00)   GO TO 670
      UINT(I)=DSQRT(USN(I))
      RVU(I)=DSQRT(VSN(I)/USN(I))
      RWU(I)=DSQRT(WSN(I)/USN(I))
      CUV(I)=DABS(UVN(I)/DSQRT(USN(I)*VSN(I)))
      CUW(I)=DABS(UWN(I)/DSQRT(USN(I)*WSN(I)))
      CVW(I)=DABS(VWN(I)/DSQRT(VSN(I)*WSN(I)))
      GO TO 700
670   UINT(I)=9.9999
      RVU(I)=9.9999
      RWU(I)=9.9999
      CUV(I)=9.9999
      CUW(I)=9.9999
      CVW(I)=9.9999
C
700   CONTINUE
C
      WRITE (6,750) (XN(I),YN(I),ZN(I),TUV(I),TUW(I),TVW(I)
     8              ,UINT(I),RVU(I),RWU(I),CUV(I),CUW(I),
     8              CVW(I),TKE(I),I=1,14)
750   FORMAT (////3X,'X MM',3X,'Y MM',3X,'Z MM',5X,'TUV',6X
     8       ,'TUW',6X,'TVW',5X,'UINT',5X,'V/U',6X,'W/U',6X
     8       ,'CUV',6X,'CUW',6X,'CVW',6X,'TURB.K.E./K.E.'//
     8       14(3(1X,F6.2),3(3X,F6.2),6(3X,F6.4),4X,D14.5
     8       /)'1')
C
955   CONTINUE
C
      STOP
      END
C
C
      SUBROUTINE MEVEL (RK,M,UEM,UMA,VMA,WMA)
C
      IMPLICIT REAL*8 (A-H,O-Z)
      DIMENSION UES(8),UM(4),VM(4),WM(4),UEM(8)
C
      DO 10 I=1,8
      UES(I)=UEM(I)*UEM(I)
10    CONTINUE
C
      F1=UES(1)+UES(5)
      F2=UES(1)-UES(5)
      F3=UES(3)+UES(7)
      F4=UES(3)-UES(7)
      F5=UES(2)+UES(6)
      F6=UES(2)-UES(6)
      F7=UES(4)+UES(8)
```

```
      F8=UES(4)-UES(3)
C
      RK1=1.0D0+RK*RK
      RK2=1.0D0-RK*RK
      HS2=RK1-2.0D0*H*H
      K=0
      FD1=F5-F7
      IF (FD1.NE.0.0D0) GO TO 20
C
      GO TO 32
C
20    USQ=HS2/2.0D0/(RK2*RK2)*F2*F4/FD1
      IF (USQ.LE.0.0D0) GO TO 21
C
      K=K+1
      UM(1)=DSQRT(USQ)
      VM(1)=-F2/2.0D0/RK2/UM(1)
      WM(1)=-F4/2.0D0/RK2/UM(1)
      GO TO 22
21    UM(1)=0.0D0
      VM(1)=0.0D0
      WM(1)=0.0D0
C
22    USQ=HS2/2.0D0/DSQRT(2.0D0)/(RK2*RK2)/FD1*(F6+F8)*F2
      IF (USQ.LE.0.0D0) GO TO 23
C
      K=K+1
      UM(2)=DSQRT(USQ)
      VM(2)=-F2/2.0D0/RK2/UM(2)
      WM(2)=-(F6+F8)/2.0D0/DSQRT(2.0D0)/RK2/UM(2)
      GO TO 24
23    UM(2)=0.0D0
      VM(2)=0.0D0
      WM(2)=0.0D0
C
24    USQ=HS2/2.0D0/DSQRT(2.0D0)/(RK2*RK2)/FD1*(F6-F8)*F4
      IF (USQ.LE.0.0D0) GO TO 25
C
      K=K+1
      UM(3)=DSQRT(USQ)
      VM(3)=-(F6-F8)/2.0D0/DSQRT(2.0D0)/RK2/UM(3)
      WM(3)=-F4/2.0D0/RK2/UM(3)
      GO TO 26
25    UM(3)=0.0D0
      VM(3)=0.0D0
      WM(3)=0.0D0
C
26    USQ=HS2/4.0D0/(RK2*RK2)/FD1*(F6+F8)*(F6-F8)
      IF (USQ.LE.0.0D0) GO TO 27
C
      K=K+1
      UM(4)=DSQRT(USQ)
      VM(4)=-(F6-F8)/2.0D0/DSQRT(2.0D0)/UM(4)/RK2
      WM(4)=-(F6+F8)/2.0D0/DSQRT(2.0D0)/RK2/UM(4)
      GO TO 30
27    UM(4)=0.0D0
      VM(4)=0.0D0
      WM(4)=0.0D0
C
30    IF (K.EQ.0) GO TO 32
```

```
C
      UMA=(UM(1)+UM(2)+UM(3)+UM(4))/K
      VMA=(VM(1)+VM(2)+VM(3)+VM(4))/K
      WMA=(WM(1)+WM(2)+WM(3)+WM(4))/K
C
C
C
      WRITE (6,31) (UM(I),VM(I),WM(I),I=1,4),UMA,VMA,WMA
31    FORMAT (1X,'IN PROBE FRAME'/4(1X,3D15.5/)1X,
     8        'AVARAGE MEAN'/1X,3D15.5)
C
C
C
      GO TO 34
C
32    UMA=0.0D0
      VMA=0.0D0
      WMA=0.0D0
C
34    RETURN
      END
C
C
      SUBROUTINE COEFA (RK,H,A)
C
      IMPLICIT REAL*8 (A-H,O-Z)
      DIMENSION A(8,6)
C
      PAI=4.0D0*DATAN(1.0D0)
      DTH=45.0D0*PAI/180.0D0
      R1=1.0D0+RK*RK
      R2=1.0D0-RK*RK
      H1=R1-2.0D0*H*H
      DO 10 I=1,8
      RTH=(I-1)*DTH
      STH=DSIN(RTH)
      CTH=DCOS(RTH)
      A(I,1)=R1/2.0D0
      A(I,2)=(R1*CTH*CTH+2.0D0*H*H*STH*STH)/2.0D0
      A(I,3)=(R1*STH*STH+2.0D0*H*H*CTH*CTH)/2.0D0
      A(I,4)=-R2*CTH
      A(I,5)=-R2*STH
      A(I,6)=H1*STH*CTH
10    CONTINUE
C
      RETURN
      END
C
C
      SUBROUTINE COEFB (A,UEM,UMA,VMA,WMA,B)
C
      IMPLICIT REAL*8 (A-H,O-Z)
      DIMENSION A(8,6),B(8,6),UEM(8)
C
      DO 10 I=1,8
      B1=(2.0D0*A(I,1)*UMA+A(I,4)*VMA+A(I,5)*WMA)/UEM(I)
      B2=(2.0D0*A(I,2)*VMA+A(I,4)*UMA+A(I,6)*WMA)/UEM(I)
      B3=(2.0D0*A(I,3)*WMA+A(I,5)*UMA+A(I,6)*VMA)/UEM(I)
      B(I,1)=B1*B1/4.0D0
      B(I,2)=B2*B2/4.0D0
```

```
      B(I,3)=B3*B3/4.0D0
      B(I,4)=B1*B2/2.0D0
      B(I,5)=B1*B3/2.0D0
      B(I,6)=B2*B3/2.0D0
10    CONTINUE
C
      RETURN
      END
C
C
      SUBROUTINE FLUCT (B,C,UEF,T,TM,UDS)
C
      IMPLICIT REAL*8 (A-H,O-Z)
      DIMENSION UEFS(8),R(6),D(6,6),B(8,6),C(3,3),UEF(8),
     a          T(3,3),TM(3,3)
C
      DO 10 J=1,8
      UEFS(J)=UEF(J)*UEF(J)
10    CONTINUE
C
      KK=0
      II=0
      UFSC=0.000
      VFSC=0.000
      WFSC=0.000
      UVFC=0.000
      UWFC=0.000
      VWFC=0.000
C
      DO 201 N=1,7
      MM=8-N
      IF (N.EQ.1) GO TO 56
C
      K=N-1
      DO 55 I=1,K
      DO 50 J=1,6
      D(I,J)=B(I,J)
50    CONTINUE
      R(I)=UEFS(I)
55    CONTINUE
C
56    DO 201 M=1,MM
      IF (M.EQ.1) GO TO 66
C
      MN=M+N-2
      DO 65 I=N,MN
      K=I+1
      DO 60 J=1,6
      D(I,J)=B(K,J)
60    CONTINUE
      R(I)=UEFS(K)
65    CONTINUE
C
66    NN=M+N-1
      IF (NN.GT.6) GO TO 23
      DO 75 I=NN,6
      K=I+2
      DO 70 J=1,6
      D(I,J)=B(K,J)
70    CONTINUE
```

```
      R(I)=UEFS(K)
 75   CONTINUE
C
 23   KK=KK+1
      CALL SSLAE(A,D,6,1,1.0D-16,IER,36)
C
      T(1,1)=R(1)
      T(2,2)=R(2)
      T(3,3)=R(3)
      T(1,2)=R(4)
      T(1,3)=R(5)
      T(2,3)=R(6)
      T(2,1)=T(1,2)
      T(3,1)=T(1,3)
      T(3,2)=T(2,3)
C
C
      CALL FRCOTR(C,T,TM)
C
C
      CUM=DABS(TM(1,1))+DABS(TM(2,2))+DABS(TM(3,3))+
     8    DABS(TM(1,2))+DABS(TM(1,3))+DABS(TM(2,3))
C
C
      IF (CUM.GT.150.0DC) GO TO 201
      IF (TM(1,1).LT.0.CDC.OR.TM(2,2).LT.0.0D0.OR.TM(3,3).
     8            LT.0.CD0) GO TO 201
C
      II=II+1
C
      DO 99 I=1,3
      DO 99 J=1,3
      TM(I,J)=TM(I,J)/UCS
99    CONTINUE
C
      TM1=DSQRT(TM(1,1))*100.0D0
      TM2=DSQRT(TM(2,2))*100.0D0
      TM3=DSQRT(TM(3,3))*100.0D0
      T21=TM2/TM1
      T31=TM3/TM1
      SBN=(DABS(TM(1,2))+DABS(TM(1,3))+DABS(TM(2,3)))/
     8    (TM(1,1)+TM(2,2)+TM(3,3))
      TKE=TM(1,1)+TM(2,2)+TM(3,3)
C
      WRITE (6,111) II,KK,TM1,TM2,TM3,TM(1,2),TM(1,3),
     8              TM(2,3),T21,T31,SBN,TKE
111   FORMAT (1X,2(I2,5X),3(F6.3,2X),3D12.3,2X,
     8       3(F7.3,2X),D12.3)
C
C
C
      UFSC=UFSC+TM(1,1)
      VFSC=VFSC+TM(2,2)
      WFSC=WFSC+TM(3,3)
      UVFC=UVFC+TM(1,2)
      UWFC=UWFC+TM(1,3)
      VWFC=VWFC+TM(2,3)
C
201   CONTINUE
C
```

```
      IF (II.GT.1) GO TO 150
C
      UFSA=UFSC
      VFSA=VFSC
      WFSA=WFSC
      UVFA=UVFC
      UWFA=UWFC
      VWFA=VWFC
      GO TO 160
C
150   UFSA=UFSC/II
      VFSA=VFSC/II
      WFSA=WFSC/II
      UVFA=UVFC/II
      UWFA=UWFC/II
      VWFA=VWFC/II
C
      UFA=DSQRT(UFSA)
      VFA=DSQRT(VFSA)
      WFA=DSQRT(WFSA)
C
      WRITE (6,112) UFA,VFA,WFA,UVFA,UWFA,VWFA
112   FORMAT (/1X,'MEAN OF FLUCT',1X,3(F6.3,2X),3D15.5)
C
C
C
160   TM(1,1)=UFSA
      TM(2,2)=VFSA
      TM(3,3)=WFSA
      TM(1,2)=UVFA
      TM(1,3)=UWFA
      TM(2,3)=VWFA
      TM(2,1)=UVFA
      TM(3,1)=UWFA
      TM(3,2)=VWFA
C
      RETURN
      END
C
C
      SUBROUTINE MRCOTR (ALP,BET,U,V,W,UMA,VMA,WMA,C)
C
      IMPLICIT REAL*8 (A-H,O-Z)
      DIMENSION C(3,3)
C
      PAI=4.0D0*DATAN(1.0D0)
      RAL=ALP*PAI/180.0D0
      RBE=BET*PAI/180.0D0
      SAL=DSIN(RAL)
      CAL=DCOS(RAL)
      SBE=DSIN(RBE)
      CBE=DCOS(RBE)
      C(1,1)=CAL*CBE
      C(1,2)=-SAL
      C(1,3)=-CAL*SBE
      C(2,1)=SAL*CBE
      C(2,2)=CAL
      C(2,3)=-SAL*SBE
      C(3,1)=SBE
      C(3,2)=0.0D0
```

```
      C(3,3)=CBE
C
      U=UMA*C(1,1)+VMA*C(1,2)+WMA*C(1,3)
      V=UMA*C(2,1)+VMA*C(2,2)+WMA*C(2,3)
      W=UMA*C(3,1)+VMA*C(3,2)+WMA*C(3,3)
C
      RETURN
      END
C
C
      SUBROUTINE FRCOTR (C,T,TM)
C
      IMPLICIT REAL*8 (A-H,O-Z)
      DIMENSION C(3,3),T(3,3),TM(3,3)
C
C
      DO 20 I=1,3
      DO 20 J=1,3
C
      TM(I,J)=T(1,1)*C(I,1)*C(J,1)+T(1,2)*C(I,1)*C(J,2)
     8        +T(1,3)*C(I,1)*C(J,3)+T(2,1)*C(I,2)*C(J,1)
     8        +T(2,2)*C(I,2)*C(J,2)+T(2,3)*C(I,2)*C(J,3)
     8        +T(3,1)*C(I,3)*C(J,1)+T(3,2)*C(I,3)*C(J,2)
     8        +T(3,3)*C(I,3)*C(J,3)
C
20    CONTINUE
      RETURN
      END
C
C
      SUBROUTINE SSLAE(R,A,M,N,EPS,IER,NDIM2)
C
      IMPLICIT REAL*8 (A-H,O-Z)
      DIMENSION A(NDIM2),R(M)
C
      IF(M)23,23,1
    1 IER=0
      PIV=0.D0
      MM=M*M
      NM=N*M
      DO 3 L=1,MM
      TB=DABS(A(L))
      IF(TB-PIV)3,3,2
    2 PIV=TB
      I=L
    3 CONTINUE
      TOL=EPS*PIV
      LST=1
      DO 17 K=1,M
      IF(PIV)23,23,4
    4 IF(IER)7,5,7
    5 IF(PIV-TOL)6,6,7
    6 IER=K-1
    7 PIVI=1.D0/A(I)
      J=(I-1)/M
      I=I-J*M-K
      J=J+1-K
      DO 8 L=K,NM,M
      LL=L+1
      TB=PIVI*R(LL)
```

```
      R(LL)=R(L)
    8 R(L)=TB
      IF(K-M)9,18,18
    9 LEND=LST+M-K
      IF(J)12,12,10
   10 II=J+M
      DO 11 L=LST,LEND
      TB=A(L)
      LL=L+II
      A(L)=A(LL)
   11 A(LL)=TB
   12 DO 13 L=LST,MM,M
      LL=L+I
      TB=PIVI*A(LL)
      A(LL)=A(L)
   13 A(L)=TB
      A(LST)=J
      PIV=0.D0
      LST=LST+1
      J=0
      DO 16 II=LST,LEND
      PIVI=-A(II)
      IST=II+M
      J=J+1
      DO 15 L=IST,MM,M
      LL=L-J
      A(L)=A(L)+PIVI*A(LL)
      TB=DABS(A(L))
      IF(TB-PIV)15,15,14
   14 PIV=TB
      I=L
   15 CONTINUE
      DO 16 L=K,NM,M
      LL=L+J
   16 R(LL)=R(LL)+PIVI*R(L)
   17 LST=LST+M
   18 IF(M-1)23,22,19
   19 IST=MM+M
      LST=M+1
      DO 21 I=2,M
      II=LST-I
      IST=IST-LST
      L=IST-M
      L=A(L)+.5D0
      DO 21 J=II,NM,M
      TB=R(J)
      LL=J
      DO 20 K=IST,MM,M
      LL=LL+1
   20 TB=TB-A(K)*R(LL)
      K=J+L
      R(J)=R(K)
   21 R(K)=TB
   22 RETURN
   23 IER=-1
      RETURN
      END
C
C
      FUNCTION URE(HTI,TR,PU)
```

```
C
      IMPLICIT REAL*8 (A-H,O-Z)
C
      PR=0.4911540D0*HTI*(1.000-(9.0800*(TR-28.630D0)*1.00-5)/
     d   (1.000+1.01D0*(TR-32.000)*1.0D-4))
      ROE=53.245D0*PR/(459.670D0+TR)
      URE=22.315D0*DSQRT(2.41D0*PD/ROE)
C
      RETURN
      END
C
C
$ENTRY
```

APPENDIX C

ERROR ANALYSIS

The uncertainties in the results arise from the inaccuracy in the instruments used, inaccuracy in positioning the probes with respect to the model and the approximations made during the derivation of the hot wire equations.

C.1 Inaccuracy of the Instruments

Transducer:

Linearity: 0.5%.

Zero shift: 1% of full scale each 1000 psig.

Demodulator:

Shift in gain: 0.01% per degree F. The room temperature change over a year was 20 F therefore, the maximum possible change in gain was 0.2%.

Digital Integrating Voltmeter:

Maximum error: 0.5%

RMS Voltmeter:

RMS output: 1%

Attenuator: 0.2%

Frequency response: 10 - 104 Hz, 1%; 0 - 10 Hz, 7%

Spectrum Analyzer:

Maximum error in frequency calibration: 5%

Maximum scatter of data: 5%

Hot Wire Probe, Anemometer and Linearizer:

For accuracy of measurement, the hot wires were calibrated before and after each set of experiments. The cumulative effect of all the instrumentation errors of the equipments used; namely, hot wire probe, constant temperature anemometer, linearizer and the voltmeters are reflected in the value of sensitivity S. After correcting for drift and fouling of the probe as described in Appendix B, the maximum variation in sensitivity was found to be 1.5%.

C.2 Inaccuracy in Positioning the Probe

The inclined single sensor probe was carefully constructed so that the probes used had the slant angle ψ within $45^{\circ} \pm 1^{\circ}$.

The maximum eccentricity of the probe rotation was

kept below 0.05 mm during the experiments. However, the effect due to this eccentricity could not be calculated. All other angles associated with the measurements; namely, θ, α, and β could be set with an accuracy of $\pm$ 2°.

The effect of these errors in the final results were estimated by computing the results by changing the variables ψ, α, β and θ one by one to its maximum value while keeping the other quantities at the nominal values. The difference between the results with the nominal value and the results with the new values gave the maximum errors introduced by the errors in these variables.

The probe interference effect due to the hot wires was negligible in these experiments. The effect due to the total and static pressure probes were expected to be significant only in a very small region (dimension of the diameter of the probe) near the corner. The effect of probe interference was negligible beyond this region.

C.3 Effect of Approximations

Linearization of the hot wire equations by neglecting the second and higher order terms of the fluctuating quantities may introduce considerable errors if the turbulence levels are high. Muller [48] showed that this procedure does not introduce significant error till the

turbulence intensity exceed 20%. In the present series of experiments, the maximum value of turbulence encountered was less than 20%, thus, the effect was negligible.

The development of the equations warranted that the sensitivity coefficients k and h be constants. However, the angle β vary in the range of 15° to 75°. In this range the maximum value of k was 0.35. The maximum error introduced by variable k was estimated by running the computer program with k = 0.35 instead of the nominal value of 0.22. The difference in the values of the quantities calculated with these two values of k gave the maximum errors that may have been introduced.

The normal sensitivity coefficient h was evaluated separately for each wire and found to be constant over the velocity range investigated. However, over long period of use it changes slightly due to fouling and bending of the wire. The maximum change in h encountered was 0.5%. The errors introduced in the final results due to this variation were calculated by using the new values in the computer program and finding the difference between these results and the results with the nominal values.

C.4 Uncertainties

The maximum cumulative effect of the errors listed

above, on the final measured quantities are as follows:

Quantity		Uncertainty
$(\Delta P/P)_{max}$	=	$\pm$ 0.007
$(\Delta \bar{U}_\infty/\bar{U}_\infty)_{max}$	=	$\pm$ 0.004
$(\Delta \bar{U}_1/\bar{U}_\infty)_{max}$	=	$\pm$ 0.040
$(\Delta \bar{V}_1/\bar{U}_\infty)_{max}$	=	$\pm$ 0.030
$(\Delta \bar{W}_1/\bar{U}_\infty)_{max}$	=	$\pm$ 0.030
$(\Delta u_1'/\bar{U}_\infty)_{max}$	=	$\pm$ 0.005
$(\Delta v_1'/\bar{U}_\infty)_{max}$	=	$\pm$ 0.050
$(\Delta w_1'/\bar{U}_\infty)_{max}$	=	$\pm$ 0.010
$(\Delta \overline{u_1 v_1}/\bar{U}_\infty^2)_{max}$	=	$\pm$ 0.30x10^{-3}
$(\Delta \overline{u_1 w_1}/\bar{U}_\infty^2)_{max}$	=	$\pm$ 0.25x10^{-3}
$(\Delta \overline{v_1 w_1}/\bar{U}_\infty^2)_{max}$	=	$\pm$ 0.20x10^{-3}

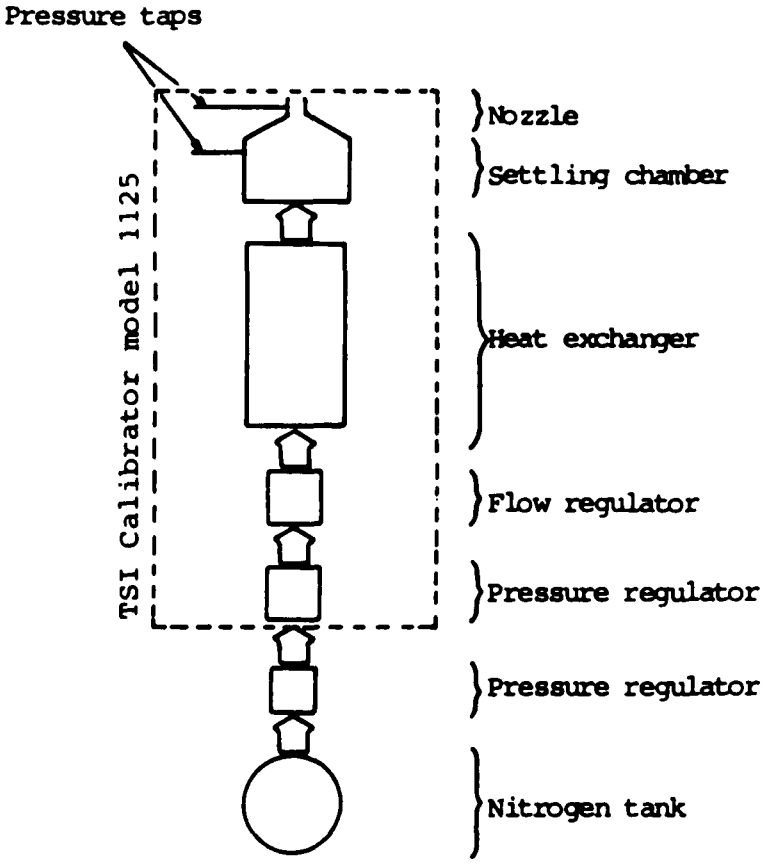

Fig. A1 Arrangement for Calibration

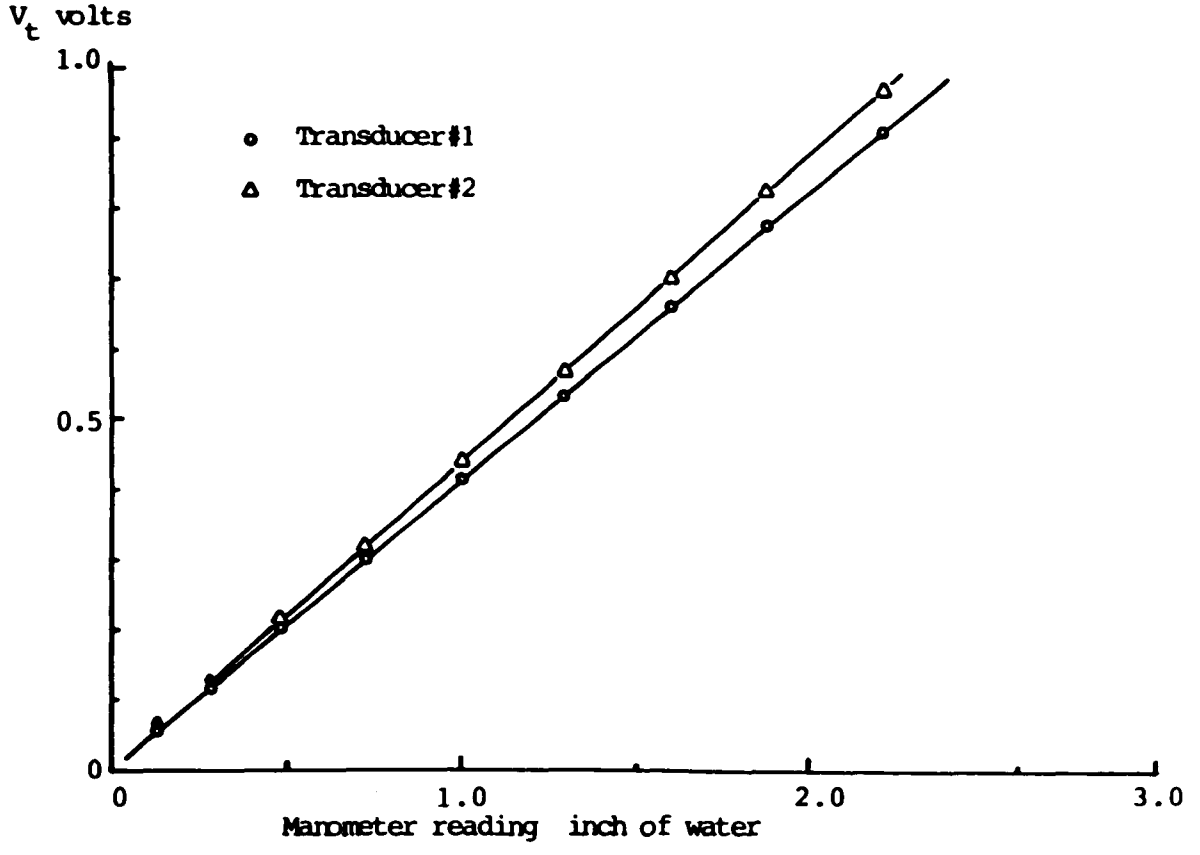

Fig. A2 Calibration Curve of Pressure Transducers

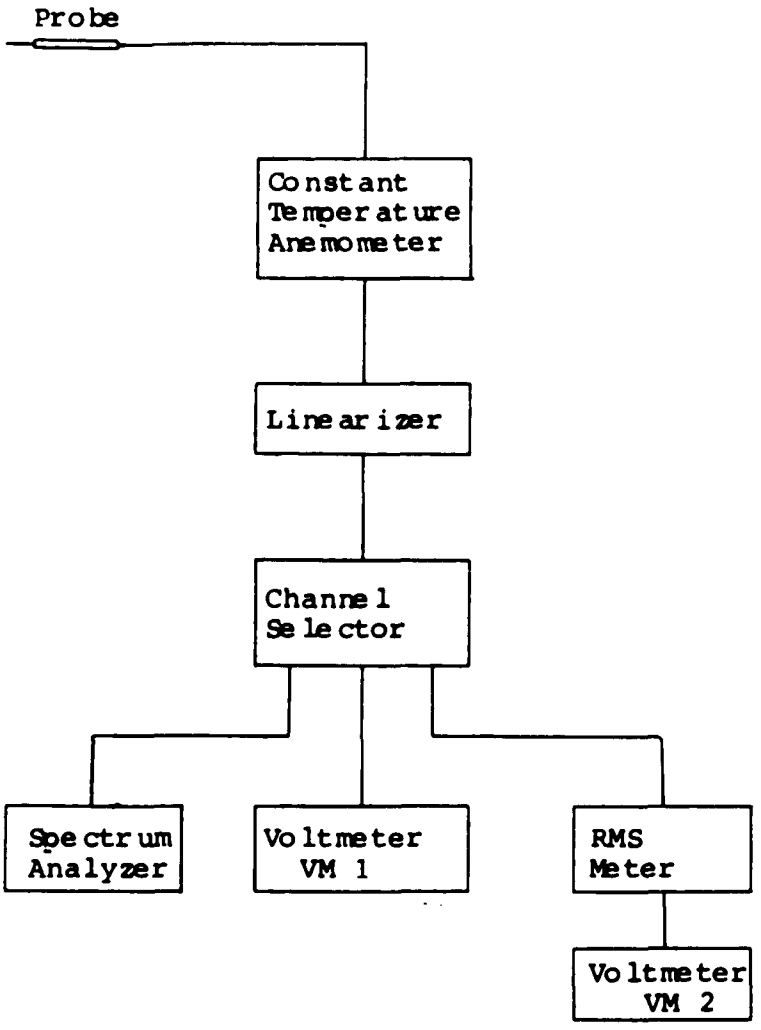

Fig. A3 Arrangement of Hot Wire Equipments

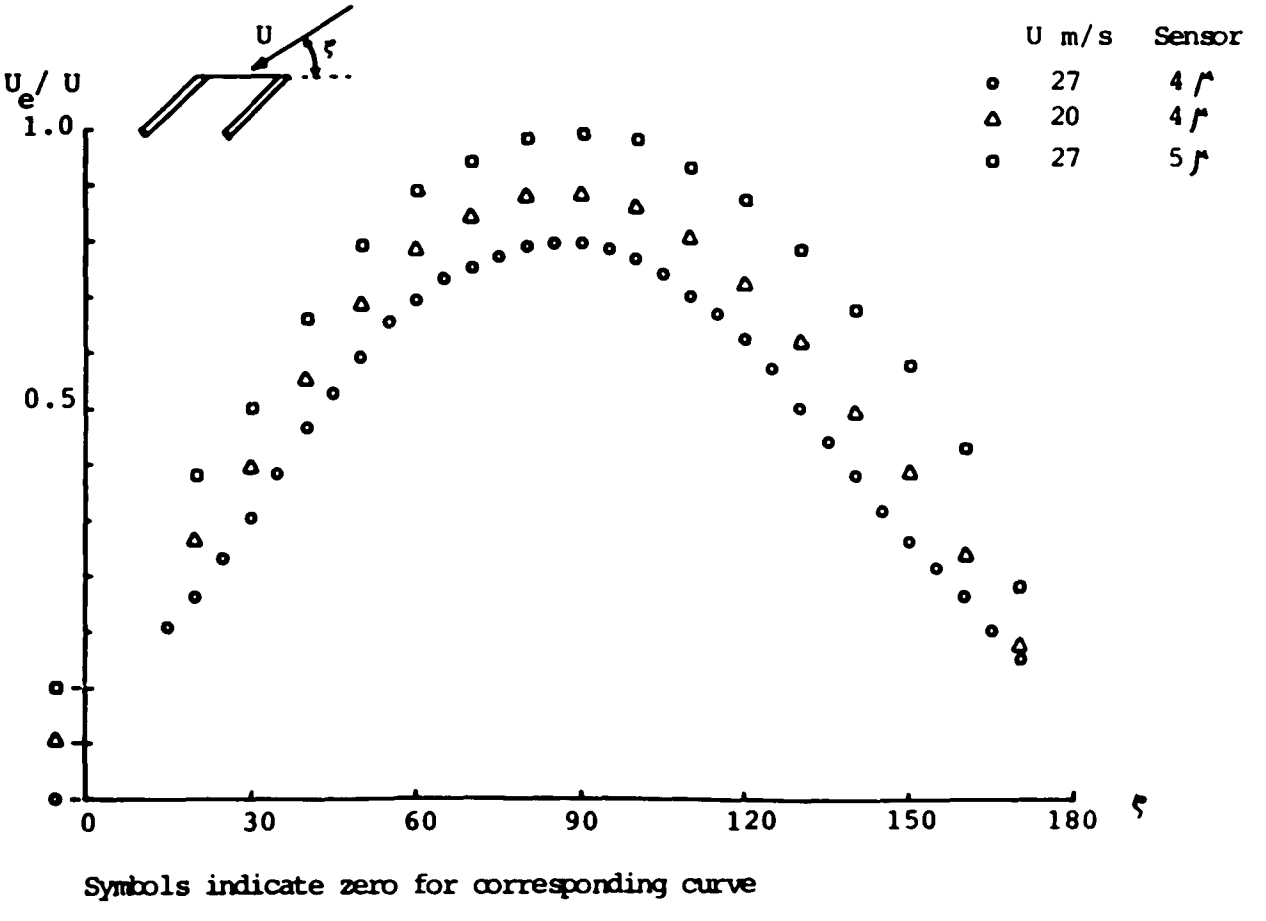

Fig. A4 Variation of Equivalent Cooling Velocity with Flow Angle

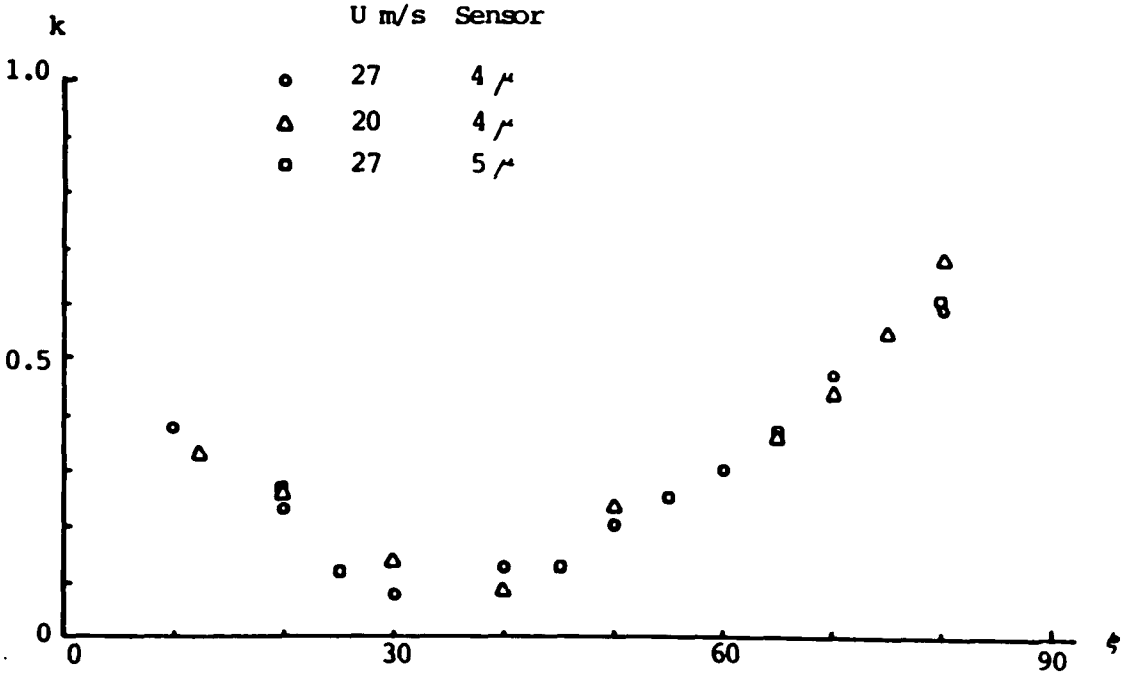

Fig. A5 Variation of Tangential Sensitivity Coefficient (k)

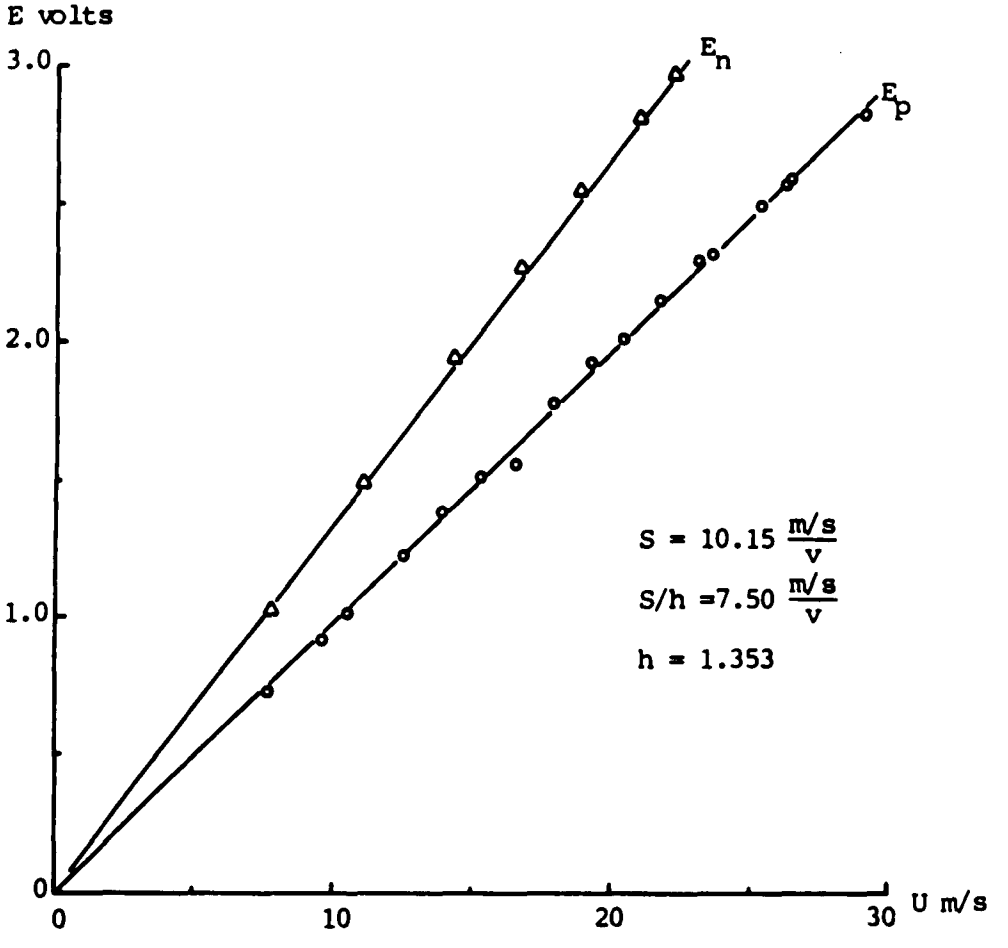

Fig. A6 Calibration With the Velocity Vector in N and P Directions

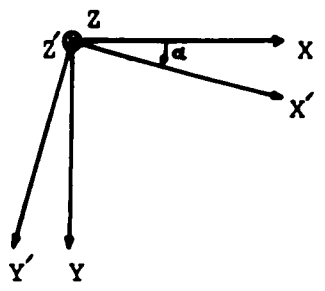

First transformation

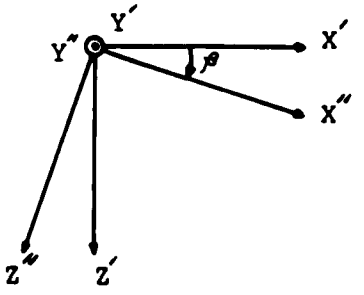

Second transformation

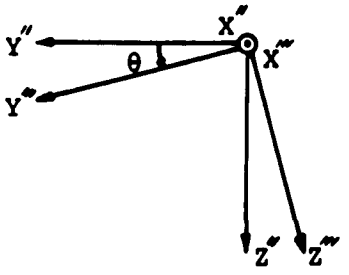

Third transformation

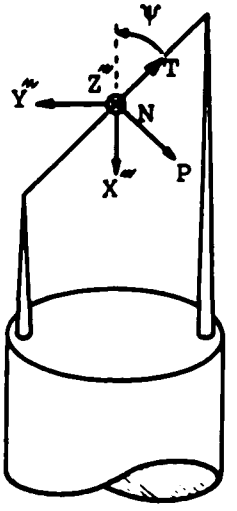

Fourth transformation

Fig. A7 Coordinate Transformations Required for Relationship Among Wind Tunnel, Model, Probe and Sensor Coordinates

REFERENCES

1. Barclay, W.H.,
"Experimental Investigatin of Laminar Flow Along a Straight 135° Corner", Aero. Quart., Vol. 24, 1973, p.147.

2. Binder, A. and Romey, R.,
"Secondary Flow Effects and Mixing of the Wake Behind a Turbine Stator", ASME Paper No. 82-GT-46.

3. Bradshaw, P.,
"An Introduction to Turbulence and its Measurement", Pergamon Press, First Edition, 1971.

4. Bradshaw, P., Cebeci, T. and Whitelaw, J.H.,
"Engineering Calculation Methods for Turbulent Flow", Academic Press, 1981.

5. Bragg, M.,
"The Turbulent Boundary Layer in a Corner", J.F.M., Vol.36, Part 3, 1969, p.485.

6. Brundrett, E. and Baines, W.D.,
"The Production and Diffusion of Vorticity in Duct Flow", J.F.M., Vol.19, Part 3, 1964, p.375.

7. Carrier, G.,
"The Boundary Layer in a Corner", Quart. of Appl. Math., Vol.4, No.4, 1947, p.367.

8. Chu, J.K. and Young, A.D.,
"A Further Investigation of Viscous Effects in a Wing Plate Junction", Queen Mary College Department Report, QMC ER-1003.

9. Dring, R.P.,
"A Momentum Integral Analysis of the Three Dimensional Turbine End Wall Boundary Layer", Trans.ASME , JEP, October 1971, p.386.

10. Dring, R.P., Joslyn, H.D. and Hardin, L.W.,
"An Investigation of Axial Compressor Rotor Aerodynamics", Trans. ASME, JEP, Vol.104, January 1982, p.84.

11. Dunham, J.,
"A Review of Cascade Data on Secondary Losses in Turbines", Journal of Mech. Engrg. Science, Vol.12, No.1, 1970, p.48.

12. East, L.F. and Hoxey, R.P.,

"Boundary Layer Effect in an Idealized Wing-Body Junction at Low Speed", RAE Tech. Report TR68161, 1968.

13. East, L.F. and Hoxey, R.P.,
"Low Speed Three-Dimensional Turbulent Boundary Layer Data - Part 2", RAE Tech Report TER69137, 1969.

14. Eichelbrenner, E.A. and Preston, J.H.,
"On the Role of Secondary Flow in Turbulent Boundary Layers and Corners (and Salients)", Journal de Me'canique, Vol.10, No.1, 1971, p.91.

15. Gessner, F.B. and Emery, A.F.,
"A Reynolds Stress Model for Turbulent Corner Flows - Part I:Development of the Model", Trans. ASME, J. of Fluid Engrg., Series I, Vol.98, 1976, p.261.

16. Gessner, F.B. and Emery, A.F.,
"A Length-Scale Model for Developing Turbulent Flow in a Rectangular Duct", Trans.ASME, J. of Fluid Engrg., June 1977, p.347.

17. Gessner, F.B. and Po, J.K.,
"A Reynolds Stress Model for Turbulent Corner Flows - Part II : Comparisons Between Theory and Experiment", Trans. ASME, J. of Fluids Engrg., Series I, Vol.98, p.269.

18. Ghia, K.N.,
"Incompressible Streamwise Flow Along an Unbounded Corner", AIAA Journal, Vol.13, No.7, 1975, p.902.

19. Ghia, K.N. and Davis, R.T.,
"A Study of Compressible Potential and Asymptotic Viscous Flows for Corner Region", AIAA Journal, Vol.12, No.3, 1974, p.355.

20. Goldstein, R.J. and Chen, H.P.,
"Film Cooling on a Gas Turbine Blade Near the End Wall", ASME Paper No.84-GT-42.

21. Gorski, J.J., Govindan, T.R. and Lakshminarayana, B.,
"Computation of Three-Dimensional Turbulent Shear Flows in Corners", AIAA Journal, Vol.23, No.5, May 1985, p.685.

22. Gurevich, Y.G.,
"Boundary Layer in the Neighborhood of a Concave Cylindrical Surface and a Plane", Izvestiya Akadimi Nauk SSSR, Mekhanika Zhidkosti iGaza, March-April, 1981, p.160.

23. Hah, C.,
"A Navier-Stokes Analysis of Three-Dimensional Turbulent Flows Inside Turbine Blade Rows at Design and Off-Design Conditions", ASME Paper No.83-GT-40.

24. Han, L.S., Ma, C and Rapp, J.R.,
"The Endwall Influence on Heat Transfer From a Single Cylinder (The Horseshoe Vortex Effect)", GTSJ/ASME, 1983 Tokyo International Gas Turbine Congress, Paper No.83-TOKYO-IGTC-3.

25. Hanjalic, H.Z. and Launder, B.E.,
"Reynolds Stress Model of Turbulence and its Application to Thin Shear Flows", J.F.M., Vol.52, Part 4, 1972, p.609.

26. Herzig, H.Z. and Hansen, A.G.,
"Visualization Studies of Secondary Flows with Applications to Turbomachines", Trans.ASME, Vol.77, 1955, p.249.

27. Hinze, J.O.,
"Turbulence", McGraw Hill Book Company, Second Edition, 1975.

28. Hornung, H.G. and Joubert, P.N.,
"The Mean Velocity Profile in Three-Dimensional Turbulent Boundary Layers", J.F.M., Vol.15, Part 3, p.368.

29. Hsing, Ting-Ding and Teng, Hsueh-Ying,
"Experimental Study of the Behavior of 3D-Turbulent Boundary Layer in a Simplified Wing/Body Junction", AIAA-84-1529.

30. Hunter, I.H.,
"Endwall Boundary Layer Flows and Losses in an Axial Turbine Stage", Trans.ASME, JEP, Vol.104, January 1984, p.184.

31. Hunter, I.H. and Cumpsty, N.A.,
"Casing Wall Boundary Layer Development Through an Isolated Compressor Rotor", ASME Paper No.82-GT-18.

32. Klebanoff, P.S.,
"Characteristics of Turbulence in a Boundary Layer with Zero Presure Gradient", NACA Report No.1247, 1955.

33. Kubendran, L.R.,
"Study of Turbulent Flow in a Wing-Fuselage Type Juncture", Ph.D. Thesis, Georgia Institute of Technology, 1983.

34. Lakshminarayana, B. and Horlock, J.H.,
"Review: Secondary Flows and Losses in Cascades and Axial Flow Turbomachines", Int. J.of Mech. Sci., Vol.5, 1963, p.287.

35. Lakshminarayana, B. and Pandya, A.,
"Investigation of the Tip Clearance Flow Inside and at the Exit of a Compressor Rotor Passage - Part I: Mean Velocity Field", ASME Paper No.82-GT-12.

36. Lakshminarayana, B. and Sitaram, N.,
"Wall Boundary Layer Development Near the Tip Region of an IGV of an Axial Flow Compressor", ASME Paper No.83-GT-171.

37. Langston, L.S.,
"Cross Flow in a Turbine Cascade Passage", Trans.ASME, JEP, Vol.102, No.4, 1980, p.866.

38. Langston, L.S. and Boyle, M.T.,
"A New Surface-Streamline Flow Visualization Technique", J.F.M., Vol.125, 1092, p.53.

39. Langston, L.S., Nice, M.L. and Hooper, R.M.,
"Three Dimensional Flow Within a Turbine Cascade Passage", ASME Paper No.76-GT-50.

40. Lasser, R. and Rouleau, W.T.,
"Measurements of Secondary Flows Within a Cascade of Curved Blade and in the Wake of the Cascade", ASME Paper No.83-GT-24.

41. Launder, B.E. and Ying, W.M.,
"Secondary Flows in Ducts of Square Cross - Section", J.F.M., Vol.54, Part 2, 1972, p.289.

42. Manor, D.,
"Low Aspect Ratio Wing/Body Vortex Interaction at Large Angles of Pitch and Yaws", Ph.D. Thesis, Wichita State University, 1983.

43. Marchal, Ph. and Sieverding, C.H.,
"Secondary Flows Within Turbomachinery Bladings", AGARD-CPP-214, 1977.

44. Mikhail, A.G. and Ghia, K.N.,
"Analysis and Asymptotic Solutions of Compressible Turbulent Corner Flow", ASME Paper No.81-GT-149.

45. Moore, J. and Ransmayr, A.,
"Flow in a Turbine Cascade, Part I: Losses and Leading-Edge Effects", ASME Paper No.83-GT-68.

46. Moore, J. and Smith, B.L.,
"Flow in a Turbine Cascade, Part II: Measurement of Flow Trajectories by Ethylene Detection", ASME Paper No.83-GT-69.

47. Muller, U.R.,
"Measurement of the Reynolds Stress and the Mean Flow Field in a Three-Dimensional Pressure-Driven Boundary Layer", J.F.M., Vol.119, 1982, p.121.

48. Muller, U.R.,
"On the Accuracy of Turbulence Measurements With Inclined Hot Wires", J.F.M., Vol.119, 1982, p.155.

49. Murray, J.C.,
"Incompressible Flow Past a Wing-Body Combination Using General Curvilinear Coordinates", Aero Quart., August 1979, p.451.

50. Nakayama, A., Chow, W.L. and Sharma, D.,
"Calculation of Fully Developed Turbulent Flows in Ducts of Arbitrary Cross-Section", J.F.M., Vol.128, 1983, p.199.

51. Oguz, Ergun Abdullah,
"An Experimental Investigation of the Turbulent Flow in the Junction of a Flat Plate and Body of Constant Thickness", Ph.D. Thesis, Georgia Institute of Technology, 1981.

52. Pal, A. and Rubin, S.G.,
"Asymptotic Features of the Viscous Flow Along a Corner", Quarterly of Applied Mathematics, Vol.29, 1971, p.91.

53. Pandya, A. and Lakshminarayana, B.,
"Investigation of the Tip Clearance Flow Inside and at the Exit of a Compressor Rotor Passage-Part II: Turbulence Properties", ASME Paper No.82-GT-13.

54. Papailiou, K., Flot, R. and Matheiu, J.,
"Secondary Flows in Compressor Bladings", ASME Paper No.76-GT-57.

55. Perkins, H.J.,
"The Formation of Streamwise Vorticity in Turbulent flow", J.F.M., Vol.44, Part 4, 1970, p.721.

56. Railly, J.W. and Sharma, P.B.,
"Treatment of the Annulus Wall Boundary Layer Using a Secondary Flow Hypothesis", ASME Paper No. 76-GT-52.

57. Rubin, S.G.,
"Incompressible Flow Along a Corner", J.F.M., Vol.26, Part I, 1966, p.97.

58. Rubin, S.G. and Grossman, B.,
"Viscous Flow Along a Corner:Numerical Solution of the Corner Layer Equation", Quart of App. Math., Vol.29, 1971, p.169.

59. Sepri, P.,
"An Investigation of the Flow in the Region of the Junction of a Wing and a Flat Surface Normal to the Wing Span", Queen Mary College, Dept. Report, QMC ER-1002, 1973.

60. Shabaka, I.M.M.A.,
"Turbulent Flow in an Idealized Wing-Body Junction", Ph.D. Thesis, University of London, 1979.

61. Shafir, M. and Rubin, S.G.,
"The Turbulent Boundary Layer Near a Corner", A.S.M.E. Journal of Applied Mechanics, December 1976, p.567.

62. Siverding, C.H.,
"Recent Progress in the Understanding of Basic Aspects of Secondary Flows in Turbine Blade Passages", ASME Paper No.84-GT-78.

63. Stanbrook, A.,
"Experimental Observation of Vortices in Wing-Body Junctions", RAE Aero. Report 2589.

64. Tennekes, H. and Lumley, J.L.,
"A First Course in Turbulence", Book, The M.I.T. Press, 1972.

65. Thomson, W.G.,
"A Study of Wing-Body Aerodynamic Interference of a Light Twin Aircraft Utilizing a Panel Method Potential Flow Program", Ph.D. Thesis, Wichita State University, 1982.

66. Vasant Ram, V.,
"Experimentelle Untersuchungen der Stronung Entlang Eines Rechtwinkligen Ecke Zuischen - Einem Profil und Efner ebonen Seitenwand", Institut fur Stromungsmechanick, Technische Hochschule Braunschweig Berichal 63/17, 1963.

67. Vasant Ram, V,
"Untersuchungen Uber die Eckengerenzschicht an Einem Kriszylinder mit Seitenwant", Institute of Fluid Mechanics, Technische Hochschule, 63/46

Braunscheweig, 1963.

68. Wagner, J.H., Dring, R.P. and Joslyn, H.D., "Inlet Boundary Layer Effects in an Axial Compressor Rotor:Part I - Blade-to-Blade Effects", ASME Paper No.84-GT-84.

69. Wagner, J.H., Dring, R.P. and Joslyn, H.D., "Inlet Boundary Layer Effects in an Axial Compressor Rotor:Part II - Throughflow Effects", ASME Paper No.84-GT-84.

70. Young, A.D., "Some Special Boundary Layer Problems", Z. Flugwis, Weltraumforsch 1, Heft 6, 1977, p.401.

71. Zamir, M., "On the Corner Boundary Layer with Favorable Pressure Gradient", Aero. Quart., Vol.23, 1972, p.161.

72. Zamir, M. "Further Solution of the Corner Boundary Layer Equations", Aero. Quart., Vol.26, 1973, p.219.

73. Zamir, M., "Boundary Layer Theory and Flow in a Streamwise Corner", Aeronautical Journal of the Royal Aeronautical Society, Vol.74, 1979, p.330.

74. Zamir, M and Young, A.D., "Experimental Investigation of the Boundary Layer in a Streamwise Corner", Aero. Quart., Vol.21, 1970, p.313.

75. Zamir, M. and Young, A.D., "Pressure Gradient and Leading Edge Effects on the Corner Boundary Layer", Aero. Quart., 1979, p.471.